Sede Amministrativa: Università degli Studi di Padova
Dipartimento di Fisica

DOTTORATO DI RICERCA IN FISICA

CICLO XIV

Perspectives for Higgs Boson Search in Full Hadronic Final States at CDF II

Coordinatore: Ch.mo Prof. Attilio Stella

Supervisore: Prof. Giovanni Busetto

Dottorando: Dr. Luca Scodellaro

31 Dicembre 2001

Contents

Introduction **1**

1 The Higgs Boson in the Standard Model **3**
1.1 Introduction to the Standard Model of the Elementary Particles . . . 3
1.2 The Higgs Sector in the Minimal Standard Model 5
1.2.1 The Higgs Mechanism 5
1.2.2 Mass Term Generation for Bosons and Fermions 7
1.2.3 Beyond the Standard Model 9
1.3 Higgs Phenomenology 10
1.3.1 Indirect Limits on Higgs Boson Mass 10
1.3.2 Total Width and Decay Modes of Higgs Boson 12
1.3.3 Higgs Production and Past Searches 13
1.4 Perspectives for Higgs Boson Search at the Tevatron Collider 16

2 Tevatron and CDF Upgrades **21**
2.1 The Accelerator Complex 21
2.1.1 Proton Production and Boosting 23
2.1.2 The Main Injector 23
2.1.3 Antiproton Production and Cooling 23
2.1.4 The Recycler Ring 23
2.1.5 The Tevatron 24
2.1.6 The Beam Monitors 24
2.2 Phenomenology and Detection of the Events at CDF II 24
2.3 The Tracking System 27
2.3.1 Track Reconstruction 30
2.3.2 Track Resolution 31
2.3.3 Primary Vertex Reconstruction 32
2.3.4 The Time of Flight 33
2.4 The Calorimetry System 34
2.4.1 Jet Reconstruction 37
2.4.2 Jet Energy Corrections 37
2.4.3 b-Jet Identification 39
2.4.4 Electron Identification 41
2.5 The Muon System 43
2.5.1 Muon Identification 44

2.6 The Trigger and Data Acquisition System 46
2.6.1 Level 1 Primitives 47
2.6.2 Level 2 Primitives 49

3 A Multijet Trigger for Higgs Associated Production 55
3.1 Introduction 55
3.2 Level 1 56
3.3 Level 2 57
3.3.1 Calorimetry Requirements 57
3.3.2 Study of SVT Performance 59
3.4 Level 3 92
3.4.1 Calorimetric Requirements 93
3.4.2 Level 3 Tracking Studies 93
3.4.3 Soft Lepton Based Trigger 94

4 Trigger Validation on Real Data 99
4.1 Level 1 and Level 2 Calorimetric Trigger 99
4.2 Study of SVT Requirements 102
4.2.1 Beam Position Correction 103
4.2.2 Extrapolation to the Complete Detector 104
4.2.3 Preliminary Estimate of the Rate after SVT Requirements . . 106

5 Jet Energy Corrections 109
5.1 Introduction 109
5.2 Strategy 111
5.3 Jet Corrections 113
5.3.1 SLT Corrections 113
5.3.2 Charged Fraction Corrections 114
5.3.3 E_T Corrections 116
5.4 Effects of the Corrections on Dijet Mass Spectra 120
5.5 Checks 126
5.5.1 Independence of the Corrections on the Input Mass 126
5.5.2 Independence of the Corrections on the Fragmentation Model 126
5.5.3 Effects of the Corrections on Backgrounds 126
5.5.4 Stability of the Corrections for Analysis Cuts 127
5.5.5 Effects of the Corrections on Real Data 134
5.6 Status of Jet Energy Corrections with CDF II Code 135
5.7 New Jet Energy Reconstruction Algorithm 136
5.8 Perspectives on Jet Energy Corrections at CDF II 137

6 Characterization of the Events 141
6.1 The Trigger Selected Sample 141
6.2 Signal Topology and Analysis Sample Selection 143
6.3 Studies of $HV \to b\bar{b}q\bar{q}^{(\prime)}$ Decay Reconstruction 148
6.4 Kinematical Characterization of the Events 151

7 Strategies for an Estimate of the Sensitivity on VH Production 163
7.1 Estimate of $S/\sqrt{B}$ 163
7.1.1 Standard Kinematical Selection 163
7.1.2 Neural Network Approach 168
7.2 Discussion of the Systematic Uncertainties 173
7.3 Preliminary Limits on the Cross Section of the VH Production . . . 174

Conclusions 177

Acknowledgements 179

A Introduction to Neural Networks 181
A.1 Neural Network Architecture 181
A.2 Training 182
A.3 Testing and Generalization 183

List of Figures 187

List of Tables 197

Introduction

Our present understanding of the fundamental physical processes is based on an elegant theory (the *Standard Model*) whose predictions found extraordinary confirmations at the high energy physics experiments in the past twenty years.

Among the main successes of the Standard Model, we remember the discovery of the $W^{\pm}$ and Z^0 bosons, carrying the weak interaction, the high precision measurements of electroweak observables and the most recent observation of the *top* quark. These results show the excellent descriptive power of the Standard Model at the electroweak energy scale, *id est* up to few hundreds of GeV.

However, the Standard Model itself predicts the existence of a particle, the *Higgs boson*, not yet observed experimentally, but required by the formal consistency of the theory.

In the next few years, remarkable efforts will be directed to the search in this sector of the high energy physics. In particular, the *Tevatron* collider and its detectors - CDF and D0 - have undergone major upgrades aimed at increasing sensitivity with respect to Higgs production and decays in the new phase of data taking that started in March 2001. The most promising channel for Higgs boson search turns out to be the associated production with a vector boson V. Preliminary studies show that, for an integrated (CDF and D0) luminosity of the order of 10 fb^{-1}, a 3σ Higgs evidence is at reach for Higgs boson mass $M_H \lesssim 130\ GeV/c^2$, while a 95% C.L. exclusion is achievable for $M_H \lesssim 190\ GeV/c^2$.

In this thesis, we investigate the feasibility for an Higgs boson search in the all hadronic decay channel $VH \rightarrow q\bar{q}^{(\prime)}b\bar{b}$ at the CDF II experiment. The motivations of this work are described in the **Chapter 1**, which provides the theoretical and experimental outline inside that this work have to be considered.

The main characteristics of the Tevatron collider and CDF detector are presented in the **Chapter 2**. In particular, the upgrades and their implications to the data collection and event reconstruction are described.

The high cross section for *background* events requires the design of a specific trigger that keeps the rate of recorded events compatible with the data acquisition system capability. The fully hadronic final states in VH events is characterized by a high jet multiplicity and the heavy flavour contents produced in Higgs decay. The calorimetric and the silicon tracking systems of CDF II are designed to operate and detect jets and secondary vertices also at trigger level. In the **Chapter 3**, we discuss a proposal for a *multijet+heavy flavour* trigger based on such features. Preliminary studies of the effectiveness of this trigger on real data are instead presented in the **Chapter 4**.

The collected data sample is expected to be dominated from competing events. The extraction of a VH signal is a very difficult task. The jet energy resolution has a fundamental importance in the recognition of the intermediate boson states, in particular for jets originated from b quark hadronization, since semileptonic decays of heavy flavour particles produce additional uncertainty. In the **Chapter 5**, we present a study of energy measurement corrections to improve the resolution on the invariant mass of two jet systems.

Furthermore, a characterization in terms of kinematics and heavy flavour contents of the events collected by the multijet + heavy flavour trigger is given in the **Chapter 6** to provide the tools for a background discrimination capable to increase the sensitivity on Higgs boson production. In the **Chapter 7**, we discuss some possible ways to achieve this task, based on a standard kinematical selection and also on a neural network approach. Finally, we draft preliminary conclusions on the possibility to search the Standard Model Higgs boson in full hadronic final states at CDF II.

Chapter 1

The Higgs Boson in the Standard Model

The search in the field of high energy physics changed radically in last 50 *years our vision of elementary components of matter and of fundamental principles of their interactions.*

In this chapter a brief review of our knowledge of elementary particles, summarized in a theory called Standard Model, *will be presented. In particular, we will focus onto the issue of Higgs physics, for which both a theoretical introduction, aimed at describing in detail the Higgs mechanism, and a phenomenological view, aimed at introducing the present state of the searches, will be provided. Finally, we will describe the perspectives of Higgs search at the Fermilab Tevatron collider for the beginning period of data taking.*

1.1 Introduction to the Standard Model of the Elementary Particles

The extraordinary predictive capability and the formal elegance that determined in the last 50 years the success of *quantum electro-dynamics* (QED), on which our present understanding of electromagnetic interactions is based, induced theoretical physicists to try to extend its formulation to an analogous gauge theory able to describe also the weak and strong nuclear interactions. These models are based on the simple idea that, by requiring a theory to be invariant under opportune local gauge transformations, fermionic fields describing ordinary matter can be *naturally* associated with gauge fields responsible of their interactions. The computation of physical quantities leads to divergences that can be reabsorbed in a finite number of measurable parameters (mass, charge, etc.). The success of this procedure, named *renormalization*, is assured by the invariance itself under gauge transformations of the theory.

In particular, in the Standard Model of elementary particles, the introduction of a group of symmetry $SU(2)_L \otimes U(1)_Y$[1] instead of $U(1)_{EM}$ on which QED is based allowed an unified description of electromagnetic and weak interactions. In this the-

Generation	1	2	3	T_L	T_L^3	Q
Leptons	$\begin{pmatrix} \nu_e \\ e \end{pmatrix}_L$	$\begin{pmatrix} \nu_\mu \\ \mu \end{pmatrix}_L$	$\begin{pmatrix} \nu_\tau \\ \tau \end{pmatrix}_L$	1/2 1/2	1/2 $-1/2$	0 -1
	e_R	μ_R	τ_R	0	0	-1
Quarks	$\begin{pmatrix} u \\ d \end{pmatrix}_L$	$\begin{pmatrix} c \\ s \end{pmatrix}_L$	$\begin{pmatrix} t \\ b \end{pmatrix}_L$	1/2 1/2	1/2 $-1/2$	$+2/3$ $-1/3$
	u_R d_R	c_R d_R	t_R b_R	0 0	0 0	$+2/3$ -1/3

Table 1.1: *Organization and characteristics of fermions in the Standard Model.*

ory, elementary fermions are divided in two classes, *quarks* and *leptons*, arranged in three families (*generations*) of doublets and characterized by the quantum numbers associated to the generators of the group of symmetry: the weak isospin, T_L, and the hypercharge, $Y = 2(Q - T_L^3)$. Tab. 1.1 summarizes the properties of the fermion particles described in the Standard Model; it has to be noted that left-handed fermions are doublets of weak isospin, $T_L = 1/2$, while right-handed fermions are singlets, $T_L = 0$. Such a difference is responsible for the observed parity violation in weak processes. The interactions between these particles are carried by a triplet of gauge field $\vec{W}_\mu$, associated to the group of symmetry $SU(2)_L$, with charge g and by a field B_μ, associated to $U(1)_Y$, with coupling constant $g'/2$.

The electroweak model is completed by a description of strong interactions, which are responsible for the stability of atomic nuclei, based on the gauge group $SU(3)$. Correspondingly with the generators of this group, a new quantum number, named *colour*, is assigned to quarks, whose strong interactions are then carried by an octet of gauge fields $G\mu$, corresponding to eight vector bosons called *gluons*.

The elegant formalism of the Standard Model is not yet sufficient to provide a complete description of the observed phenomenology: actually, the requirement of invariance of the theory under transformations associated to the group $SU(2)_L \otimes U(1)_Y$ forbids the explicit introduction of mass terms for fermions and bosons in the lagrangian density of the Standard Model, otherwise the renormalizability of the theory and, consequently, its predictive character would be lost. In order to overcome this difficulty and to obtain a theory predicting the existence of massive particles, the generation of a *spontaneous breaking*[2] of the symmetry through the introduction of a new field, named *Higgs field*, with non-null expectation value at the

ground state (the *vacuum*) has been proposed. In this way, the lagrangian density describing the system preserves its original invariance under transformations of the $SU(2)_L \otimes U(1)_Y$ group, while it gets a non-null minimum value in the vicinity of which a preferential direction breaking its symmetry[1] is established.

1.2 The Higgs Sector in the Minimal Standard Model

1.2.1 The Higgs Mechanism

At high energy, the elastic scattering amplitude of massive weakly interacting bosons W, $WW \to WW$, increases indefinitely with the energy for longitudinally polarized particles, due to the linear dependence of the longitudinal wave-function W_L on particle energy. In particular, the amplitude of the partial wave for angular momentum $J = 0$, $A_0 = G_F s/8\pi\sqrt{2}$, presents a quadratic divergence that violates the unitarity limit for elastic scattering amplitude if

$$s > 4\pi\sqrt{2}/G_F \sim (1.2\ TeV)^2. \tag{1.1}$$

Unitarity can be restored by introducing the exchange of a new scalar particle (see Fig. 1.1). To ensure that the contributions of the new diagrams cancel exactly the quadratic divergence at high energy, the coupling has to be proportional to the W boson mass squared. Similarly, the linear divergence in the $A(f\bar{f} \to W_L W_L) \sim g m_f \sqrt{s}$ for fermion-antifermion annihilation to massive gauge boson with longitudinal polarization can be cancelled by adding the exchange of a scalar particle to that of the gauge boson. In this case, the coupling has to be proportional to the mass of fermion f. A gauge theory with massive fermions and bosons suggests then that the Higgs field responsible for the breaking of the gauge symmetry of the $SU(2)_L \otimes U(1)_Y$ group in the Standard Model possesses a global symmetry as regards to $SU(2)_L$, with at least a scalar field in a doublet of $SU(2)_L$ with hypercharge $Y = +1$.

The minimal choice consists of a doublet of complex scalar fields ϕ^+ and ϕ^0 with hypercharge $Y = +1$ and electric charge $Q = +1$ and 0 respectively:

$$\phi = \begin{pmatrix} \phi^+ \\ \phi^0 \end{pmatrix} = \frac{1}{\sqrt{2}} \begin{pmatrix} \phi_1 + i\phi_2 \\ \phi_3 + i\phi_4 \end{pmatrix}. \tag{1.2}$$

In the electroweak lagrangian density, interaction terms of the Higgs field with itself and with fermionic and gauge fields have therefore to be added to the fermionic and gauge parts. The self-interaction potential can be written in the general form

$$V(\phi) = \mu^2 \phi^\dagger \phi + \lambda (\phi^\dagger \phi)^2, \tag{1.3}$$

that gets a minimum value for

$$\phi^\dagger \phi = -\frac{\mu^2}{\lambda} = \frac{v^2}{2}. \tag{1.4}$$

[1] In fact, it would be more appropriate to speak about hidden symmetry more than broken symmetry.

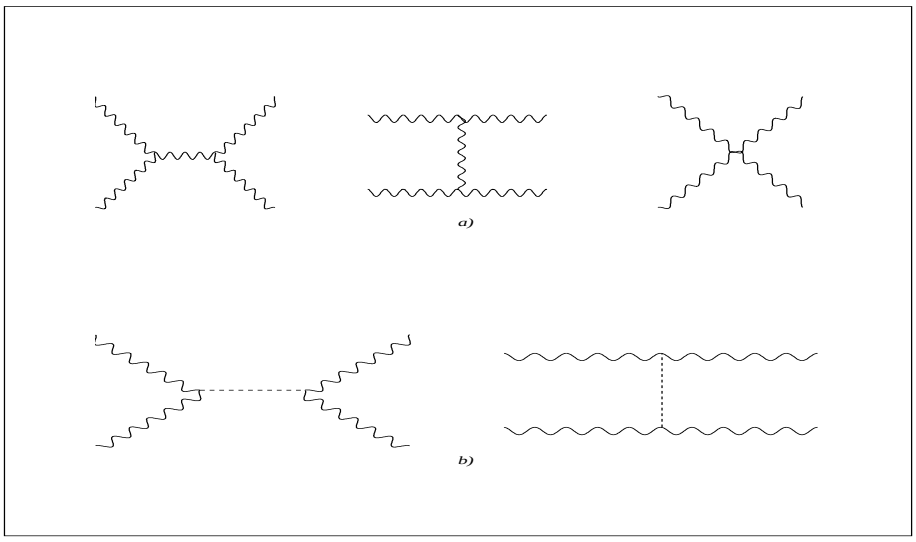

Figure 1.1: *Diagrams for WW elastic scattering: (a) mere dynamic of gauge bosons, (b) exchange of a scalar boson.*

The choice $\lambda > 0$ and $\mu^2 < 0$ guarantees this minimum exists and it is non-null, so that the symmetry breaking is achieved. Now, the photon, quantum of electromagnetic interaction, is massless: the vacuum state $\phi_0)$ has therefore to preserve the gauge invariance under transformations of the $U(1)_{EM}$ group, whose generator is

$$Q = T_L^3 + \frac{Y}{2}. \tag{1.5}$$

This suggests the choice

$$\phi_0 = \begin{pmatrix} 0 \\ v \end{pmatrix}. \tag{1.6}$$

for the ground state. The ϕ-field variations around the minimum ϕ_0 can then be parametrized as

$$\phi(x) = \frac{1}{\sqrt{2}} e^{i\sum_i \epsilon_i(x)\tau_i/v} \begin{pmatrix} 0 \\ v+h(x) \end{pmatrix} \tag{1.7}$$

by adjusting the value of the scalar fields $\epsilon_i(x)$. The number of these fields corresponds to the number of broken generators. They are known as '*would-be* Goldstone bosons' and do not represent physical fields. Actually, they can be gauged away by the $SU(2)_L$-transformation $U(x) = e^{-i\epsilon_i(x)\tau_i/v}$ thanks to the invariance of $V(\phi)$. In the so-called unitary gauge, we can therefore write

$$\phi_0 = \begin{pmatrix} 0 \\ v + h(x) \end{pmatrix}. \tag{1.8}$$

This is essentially the core of the Higgs mechanism [3]: among the four degrees of freedom associated to the initial scalar fields ϕ_i, three are absorbed in the would-be Goldstone bosons gauging procedure, to be returned in terms of longitudinal degrees of freedom of three gauge bosons, which in this way acquire mass. The

fourth degree of freedom is associated to the Higgs field $h(x)$, which represents the only physical scalar field of the model. Its mass is computed developing the self-interaction potential V around the vacuum state and results to be

$$M_H = \sqrt{2\lambda}v. \tag{1.9}$$

1.2.2 Mass Term Generation for Bosons and Fermions

We can get the explicit expression for the boson masses by computing the kinetic term $\mathcal{L}_K^\phi$ of the scalar field

$$\mathcal{L}_K^\phi = (D^\mu\phi)^\dagger(D_\mu\phi) \tag{1.10}$$

around the ground state. By recalling the covariant derivative

$$D^\mu = \partial^\mu + igW_a^\mu\tau_a/2 + ig'B^\mu 1/2, \tag{1.11}$$

we obtain

$$\begin{aligned}\mathcal{L}_K^\phi &= \tfrac{(v+h)^2}{8}[g^2(W_1^\mu + iW_2^\mu)(W_{1\mu} - iW_{2\mu}) + (g'B^\mu - gW_3^\mu)(g'B_\mu - gW_{3\mu})] \\ &= \tfrac{g^2}{4}v^2W_\mu^+W^{-\mu} + \tfrac{(g^2+g'^2)}{8}v^2Z_\mu^0Z^{0\mu} + \tfrac{g^2}{4}h^2W_\mu^+W^{-\mu} + \\ &+ \tfrac{g^2}{2}vhW_\mu^+W^{-\mu} + \tfrac{(g^2+g'^2)}{8}h^2Z_\mu^0Z^{0\mu} + \tfrac{(g^2+g'^2)}{4}vhZ_\mu^0Z^{0\mu}\ ,\end{aligned} \tag{1.12}$$

where we have introduced two charged bosons

$$W^{\pm\mu} = (W_1^\mu \mp W_2^\mu)/\sqrt{2} \tag{1.13}$$

and two neutral ones

$$\begin{aligned}Z^{0\mu} &= (g'B^\mu - gW^{3\mu})/\sqrt{g^2+g'^2} \\ A^\mu &= (gB^\mu + g'W_3^\mu)/\sqrt{g^2+g'^2}\ .\end{aligned} \tag{1.14}$$

The first two terms of expression 1.12 provides the mass spectrum of the vector bosons,

$$M_W = \frac{gv}{2} \tag{1.15}$$

$$M_Z = \frac{v}{2}\sqrt{g^2+g'^2} \tag{1.16}$$

$$M_A = 0\ , \tag{1.17}$$

while the others supply their coupling with the Higgs boson:

$$\begin{aligned}h\mathrm{Z}_\mu^0\mathrm{Z}_\nu^0 &\sim M_\mathrm{Z}^2 g_{\mu\nu}/v \\ h\mathrm{W}_\mu^+\mathrm{W}_\nu^- &\sim M_\mathrm{W}^2 g_{\mu\nu}/v \\ hh\mathrm{Z}_\mu^0\mathrm{Z}_\nu^0 &\sim M_\mathrm{Z}^2 g_{\mu\nu}/(2v^2) \\ hh\mathrm{W}_\mu^+\mathrm{W}_\nu^- &\sim M_\mathrm{W}^2 g_{\mu\nu}/(2v^2)\ .\end{aligned} \tag{1.18}$$

As previously mentioned, these couplings are proportional to the square of the boson masses. Now, we can identify the massless boson A with the photon γ and express Eq. 1.14 by means of a rotation in the gauge boson space

$$\begin{aligned}Z^{0\mu} &= sin\theta_W B^\mu - cos\theta_W W_3^\mu \\ A^\mu &= cos\theta_W B^\mu + sin\theta_W W_3^\mu\ ,\end{aligned} \tag{1.19}$$

Bosons	Spin	Q	Mass (GeV/c^2)
γ	1	0	0
$W^{\pm}$	1	± 1	80.419 ± 0.056
Z^0	1	0	91.188 ± 0.002

Table 1.2: *Vector bosons in the electroweak sector of the Standard Model.*

where the *Weinberg angle* θ_W is defined by the relation

$$tan\theta_W = g'/g \ . \tag{1.20}$$

The couplings of the neutral bosons to the fermions can then be written

$$\begin{aligned} Z^0 f\bar{f} &\sim (T_L^3 - sin^2\theta_W Q)g/cos\theta_W \\ Af\bar{f} &\sim gsin\theta_W Q = g\prime cos\theta_W Q = eQ \ , \end{aligned} \tag{1.21}$$

from which g, g' and θ_W can be measured. By comparing the low energy limit of the $Wf\bar{f}$ interaction to the Fermi's theory results, we find instead $v = (\sqrt{2}G_F)^{-1/2} \approx 246\ GeV$. Finally, the vector boson mass can be predicted. Their measured values (see Tab. 1.2) turn out to be very close to the theoretical predictions, providing one of the best confirmations to the Standard Model.

Mass terms for fermionic particles can be obtained by introducing a *Yukawa* interaction between the Higgs field and the fermions. The corresponding lagrangian density can be written

$$\mathcal{L}_{yuk} = -((\bar{\nu}_e^j, \bar{e}_L^j)\phi\Gamma^E_{j,i}e_R^i) - ((\bar{u}_L^j, \bar{d}_L^j)\phi\Gamma^D_{j,i}d_R^i - (\bar{u}_L^j, \bar{d}_L^j)\tilde{\phi}\Gamma^U_{j,i}u_R^i) + h.c. \ , \tag{1.22}$$

where $\tilde{\phi}$ is defined as the charged conjugate of ϕ:

$$\tilde{\phi} \equiv i\tau_2\phi^* = \begin{pmatrix} \varphi^{0^*} \\ -\varphi^- \end{pmatrix} \tag{1.23}$$

and Γ^E, Γ^D and Γ^U are generic 3×3 matrices in the generation space, since $SU(2)_L$ singlets and doublets carry the same quantun numbers across fermion generations. By developing $\mathcal{L}_{yuk}$ around the vacuum state, we obtain

$$\mathcal{L}_{yuk} = -\frac{1}{\sqrt{2}}(v+h)[(\bar{e}_L\Gamma^E e_R) + (\bar{d}_L\Gamma^D d_R + \bar{u}_L\Gamma^U u_R)] + h.c. \ , \tag{1.24}$$

from which mass and coupling matrices can be obtained:

$$\begin{aligned} M &= \Gamma v/\sqrt{2} \\ C &= \Gamma/\sqrt{2} = M/v \ . \end{aligned} \tag{1.25}$$

Again, the required proportionality between the mass of the fermions and their coupling to the Higgs boson has been satisfied. In order to obtain the explicit value of fermionic masses, M matrix have to be diagonalized. This leads to a rotation between mass and interaction eigenstates and to the introdution of the Cabibbo-Kobayashi-Maskawa (CKM) matrix [4, 5], describing the flavour changing in the charged currents.

1.2.3 Beyond the Standard Model

Despite the remarkable successes, as for example the discoveries of the $W^{\pm}$ and Z^0 bosons [6, 7, 8] and of the top quark [9], the Standard Model is not considered really the ultimate theory of elementary particles, since it leaves several unresolved questions, as these concerning unification and flavour. The unification problem is raised by the gauge interactions, whose pattern of group and representations appear to be complicated and arbitrary, while the flavour one is related to the Yukawa interactions, that introduce several arbitrary parameters in the theory.

Moreover, theoretical considerations suggest that the Standard Model can not be considered a fundamental theory. Actually, it does not provide a quantum description of gravitational interactions; besides, some of the Standard Model couplings are not asymptotically free.

The Standard Model has therefore to be seen as an effective field theory, valid up to some physical cut-off scale Λ. The most natural candidate value for Λ is $\Lambda_{Planck} \sim 10^{18}\ GeV$, as roughly suggested by the asymptotical behaviour of the measured strength of the fundamental interactions, pointing towards an unification at $\Lambda \sim 10^{14} \div 10^{16}\ GeV$. Moreover, at that energy the effects of gravitational interactions begin to be sensible and the Standard Model *must* lose its validity. However, a lower value for the cut-off scale seems to be suggested by the *naturalness* problem. In an effective theory, in fact, all parameters, such as masses and couplings, should be calculable in terms of a more fundamental theory, describing physics at the energy scale Λ: while all couplings and fermion masses are logarithmically sensitive to this scale, scalar squared masses result to have a quadratical dependence on Λ. On the other hand, arguments based on perturbative unitarity suggest that self-consistency of the Standard Model would be broken unless $M_H \lesssim 1\ TeV/c^2$ [10]. This is hard to reconcile with a contribute to the Higgs boson mass proportional to Λ_{Planck}, and seems to advise that the Standard Model has to be replaced by a new theory already at the electroweak symmetry breaking scale.

Two possible models have been studied. One of these, aimed at resolving the naturalness problem by substituting the Higgs mechanism through a dynamical breaking of the electroweak symmetry, has been inspired by the chiral symmetry breaking induced by quark condensates within the QCD framework. Models based on this idea, known as *Technicolour* models, require the introduction of new generation of fermions undergoing a new strong interaction at a scale $\Lambda \gtrsim \Lambda_{Fermi}$; however, their capability to formulate realistic predictions is still limited.

The other proposed solution to the naturalness problem consists in embedding the Standard Model within a theory characterized by a broken *supersymmetry* which connects fermion and boson masses and interactions[2]. Actually, the one loop corrections to the Higgs boson mass include two opposite signed contributions (see Fig. 1.2), controlled by the Yukawa coupling λ_F and by the quartic coupling λ_B respectively, so that

$$\delta M_{\mathrm{H}}^2 \sim (\lambda_B - \lambda_F^2)\Lambda^2 \ . \tag{1.26}$$

[2]Supersymmetry has to be broken since expected supersymmetric partners for fermions and bosons have not been observed yet.

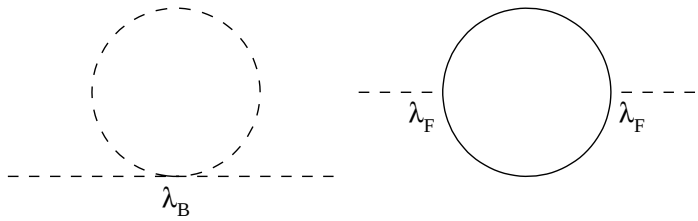

Figure 1.2: *One-loop contributions to Higgs boson mass within the* SM.

The (super)symmetry relating bosons and fermions enforce the vanishing of the coefficient of Λ^2 (not only at one loop, but also at higher orders) and allow to the theory to remain valid up to the Planck scale, while still being natural.

The simplest supersymmetric extension of the Standard Model is the Minimal Supersymmetric Standard Model (MSSM), in which a (supersymmetric) Higgs mechanism is also invoked to give mass to all particles, but two Higgs doublets are required to preserve the theory from anomalies. The Higgs sector contains then eight (scalar) degrees of freedom, three of which are absorbed and become the longitudinal components of the $W^{\pm}$ and Z^0 bosons after electroweak symmetry breaking. The remaining five physical Higgs fields correspond to a charged Higgs pair $H^{\pm}$, one CP-odd scalar A, and two CP-even scalars h^0 and H^0. The supersymmetric structure of the theory imposes constraints on the Higgs sector. In particular, at tree-level we find:

$$\begin{aligned} M_{\mathrm{H}^{\pm}} &= M_{\mathrm{W}^{\pm}} + M_{\mathrm{A}^0} \ , \\ M_{\mathrm{h}^0} \leqslant M_{\mathrm{Z}^0} \ , \ M_{\mathrm{A}^0} &\leqslant M_{\mathrm{H}^{\pm}} \ . \end{aligned} \tag{1.27}$$

However, radiative corrections enable to raise the upper limit on the lightest Higgs boson mass M_h up to $\sim 130\ GeV/c^2$. Since over a significant region of the MSSM parameter space the h^0 boson has SM-like properties [7], this results is an important hint to the search for Higgs boson in the mass range $M_H \lesssim 130\ GeV/c^2$.

1.3 Higgs Phenomenology

1.3.1 Indirect Limits on Higgs Boson Mass

The only unknown parameter in the scalar sector of the Standard Model is the Higgs boson mass M_H (see equation 1.9). After its determination, production modes and corresponding cross sections of the Higgs boson, as well as its lifetime and decay branching ratios, can be predicted.

Limits on Higgs boson mass can be derived from theoretical considerations and experimental observations:

- Unitarity requirement in high energy scattering of massive bosons weakly interacting leads to an upper limit of about $1\ TeV/c^2$ on M_H [10].

- Other limits can be established by hypotheses on the energy scale of cut-off Λ above which the coupling constant would increase too much and new

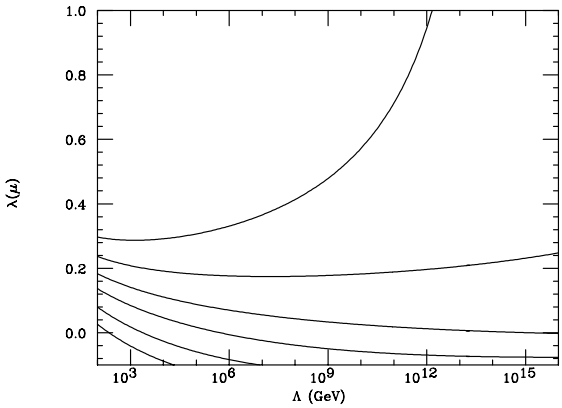

Figure 1.3: *Running of λ as a function of the energy scale Λ.*

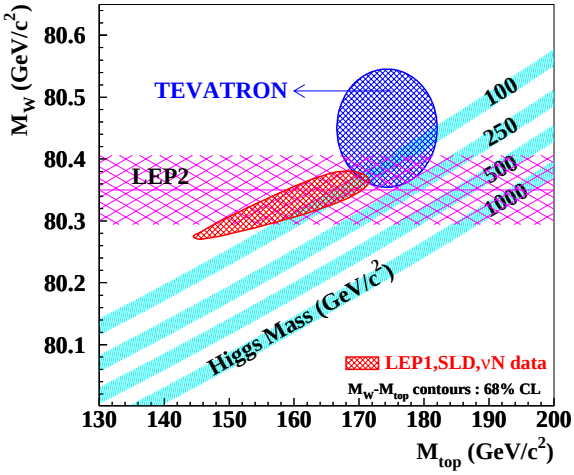

Figure 1.4: *Limits on Higgs boson mass from top quark and W boson mass measurements at* CDF, D0, LEP *and* SLC.

phenomena have to appear. The key of these limits is the running of the quartic coupling constant λ of the Higgs field as a function of the energy, due to the quantum fluctuations. The contributions are shown in Fig. 1.5. Diagrams with Higgs boson loops lead to an unlimited increase of the coupling (see Fig. 1.3. The condition $\lambda(\Lambda) < \infty$ gives

$$M_H^2 \leq \frac{8\pi^2 v^2}{3log\frac{\Lambda^2}{v^2}}. \tag{1.28}$$

The maximum value of M_H for the minimum cut-off $\Lambda \sim 1\ TeV$ is about $700\ GeV/c^2$. For $\Lambda \sim \Lambda_{Planck}$, the upper limit on M_H decrease to $\sim 190\ GeV/c^2$.

- A lower limit on Higgs boson mass can instead be derived from the requirement of vacuum stability. Actually, the contributions of top quark loops to the self-interaction of the Higgs field lead to negative values of λ as the energy increases; in such a case, the self-interaction potential 1.3 would lose its minimum and the vacuum state would no longer be stable. In order to avoid this situation, the Higgs boson must have a mass greater than a minimum value determined by the cut-off Λ. Tab. 1.3 summarizes the theoretical limits on M_H for two specific values of Λ. We note that if the Standard Model remains valid up to the Planck energy, the Higgs boson must have a mass between 130 and 190 GeV/c^2: a value of M_H outside this range would require the existence of new physics under the scale of Planck.

- Finally, indirect information on the Higgs boson mass can be obtained from high precision measurements of electroweak observables. Actually, since the Standard Model is renormalizable only by introducing the contributions of top quark and Higgs boson to the radiative corrections, such observables have to

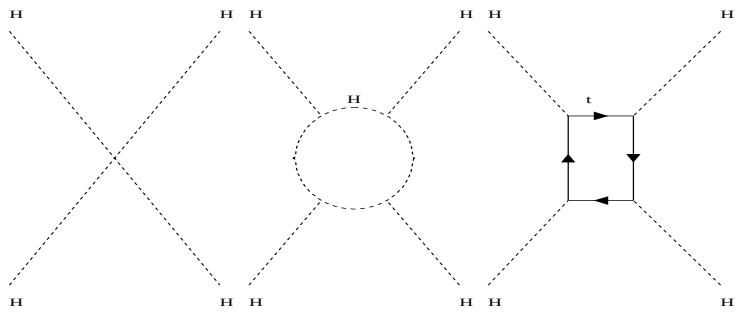

Figure 1.5: *Diagrams contributing to the running of the selfinteraction constant λ of the Higgs field.*

Λ	M_H
$1\ TeV$	$55\ GeV < M_H < 700\ GeV$
$10^{19}\ GeV$	$130\ GeV < M_H < 190\ GeV$

Table 1.3: *Theoretical limits on Higgs boson mass M_H for two specific values of the cut-off energy Λ.*

be sensitive to the masses of these particles [12, 13]. In particular, estimates and limits on M_H have been obtained from top quark and $W^{\pm}$ boson mass measurement at CDF, D0, LEP and SLC (see Fig. 1.4). Although the sensitivity on Higgs boson mass is only logarithmic, the high precision of the electroweak measurement has allowed to put an upper limit $M_H \leq 188\ GeV/c^2$ at 95% of confidence level.We remark that Standard Model predictions are compatible with these estimates.

1.3.2 Total Width and Decay Modes of Higgs Boson

The profile of the Higgs Boson is completely determined by the value of its mass. In particular, by establishing the coupling constant of the Higgs boson with fermions and bosons through equations 1.18 and 1.25, this parameter allows to compute the total width Γ_H and the branching ratios β of each specific decay channel (see Fig. 1.6 and 1.7).

In the region of low mass ($M_H \lesssim 130\ GeV/c^2$), the decay into vector bosons is suppressed by phase space and the Higgs boson decays mainly into $b\bar{b}$ pairs ($\beta_{b\bar{b}} \sim 0.5 \div 0.9$). Other significant decay modes in this mass range are those into $c\bar{c}$, gg and $\tau^+\tau^-$ pairs, with branching ratios close to 5%. Near 120 GeV/c^2, the decay into

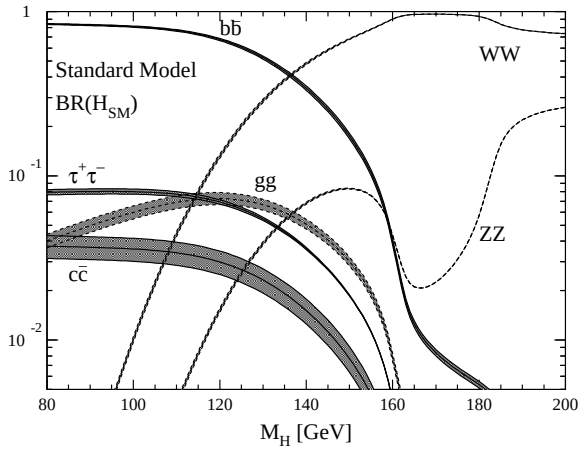

Figure 1.6: *Higgs branching ratios as a function of M_H. Shaded bands result from the uncertainties on input parameters (m_b, m_c, m_t, α_s).*

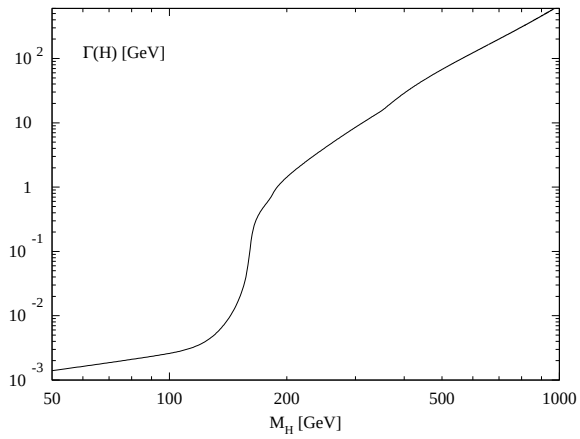

Figure 1.7: *Total width of the Higgs boson as a function of its mass.*

ZZ^* begins to be as much important, while the WW^* channel becomes the second more important one ($\beta \sim 0.2$). Finally, the Higgs boson can decay into $\gamma\gamma$ and $Z\gamma$ through top quark and W boson loops with $\beta \sim 0.001$.

For Higgs boson masses higher than 130 GeV/c^2, decay channels into $WW^{(*)}$ and $ZZ^{(*)}$ boson pairs become dominant due to the greater coupling between Higgs boson and vector boson. If $M_H \gtrsim 180$ GeV/c^2 ($= 2\ M_Z$), the Higgs boson decays exclusively in these channels, with branching ratios of about 2/3 and 1/3 for WW and ZZ respectively. The opening of the $t\bar{t}$ channel (near 350 GeV/c^2) does not change significantly this situation.

The Higgs total width remains very narrow ($\Gamma_H < 10$ MeV/c^2) up to $M_H <$ 130 GeV/c^2, but it increases rapidly after the opening of the decay channels into vector boson pairs and reaches the value of 1 GeV/c^2 when $M_H \sim 180$ GeV/c^2.

1.3.3 Higgs Production and Past Searches

Searches at LEP

The main production mode of Higgs boson at the e^+e^- LEP collider were the Higgsstrahlung from a virtual Z boson and the vector boson fusion (see Fig. 1.8), the former being largely dominant. The four LEP experiment (ALEPH, DELPHI, L3 and OPAL) performed detailed analyses on the ~ 120 pb^{-1} of integrated luminosity collected by each detector (at $\sqrt{s} \geq 206.5$ GeV) during the last year of data taking, by exploiting almost the whole final state spectrum permitted for Higgsstrahlung processes [14, 15, 16]. By considering all possible Z^0 decay channels and the dominant Higgs ones ($H \to b\bar{b}, \tau^+\tau^-$), four experimental signatures have been considered: the missing energy ($ZH \to \nu\bar{\nu}X$), the lepton pair ($ZH \to l^+l^-X$, $l = e,\mu$), the tau pair ($ZH \to q\bar{q}\tau^+\tau^-$ or $ZH \to \tau^+\tau^-X$) and the all hadronic ($ZH \to b\bar{b}q\bar{q}$). Each set of data collected by exploiting these signatures by the different LEP detectors has

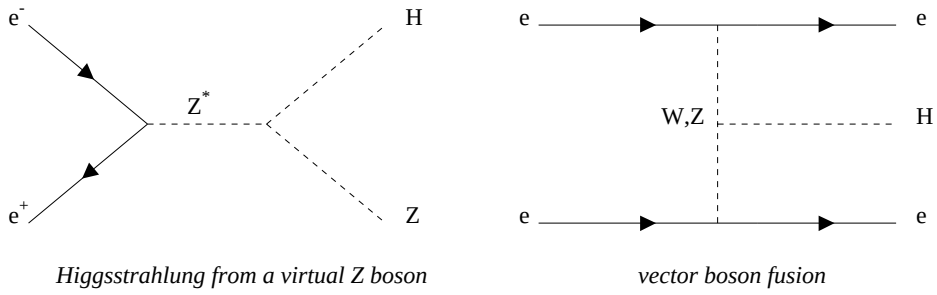

Figure 1.8: *Standard Model Higgs boson dominant production modes at the* LEP *collider.*

been subjected to two likelihood tests to verify its compatibility with being origined from an exclusive background production and with being enriched also by Standard Model Higgs boson production. Results have been combined in a likelihood ratio estimator, defined as a function of the Higgs boson mass M_H as:

$$Q(M_{\rm H}) = \frac{L_{s+b}(M_{\rm H})}{L_b(M_{\rm H})} = \frac{e^{-(s(M_{\rm H})+b)}}{e^{-b}} \prod_{j=1}^{N_{obs.}} \frac{s(M_{\rm H})S(M_{\rm H}, m_j^{rec.}) + bB(m_j^{rec.})}{bB(m_j^{rec.})} , \qquad (1.29)$$

where $N_{obs.}$, $s(M_H)$ and b are the number of observed signal and background events, while $S(M_H, m_j^{rec.})$ and $B(m_j^{rec.})$ are the distributions of the reconstructed mass $m^{rec.}$ expected for signal and background processes respectively. Finally, a conbination of the contributions from each different channel k has been computed as $Q(M_H) = \prod_k Q_k(M_H)$. The observed curve for $-2ln(Q(M_H))$ is shown in Fig. 1.9; green and yellow bands correspond to a 68 and 95% compatibility with an exclusive background production: a hint for Higgs boson production is pointed out by a dip in the observed behaviour of data for $M_H = 115.0^{+0.7}_{-0.3}\ GeV/c^2$. Another useful quantity is the probability CL_b of obtaining a lower value of Q function (corresponding to a more background-like behaviour of data) than the effectively observed one. Fig. 1.10 shows the found values of $1 - CL_b$ as a function of M_H; the significance of the observed excess is also given: for $M_H = 115.0\ GeV/c^2$ a maximum significance of 2.9 σ is obtained.

The collected statistics was not enough to provide an observation of the Higgs boson; however, a lower limit $M_H \gtrsim 113.5\ GeV/c^2$ at 95% C.L. has been established.

Searches at the Tevatron

Higgs boson production at the $p\bar{p}$ Tevatron collider can occur through several processes (see Fig. 1.12); the most important contributions are shown in Fig. 1.11:

- direct production by means of gluon fusion: $gg \to H$;
- vector boson fusion: $q\bar{q} \to q\bar{q}VV \to q\bar{q}H$;

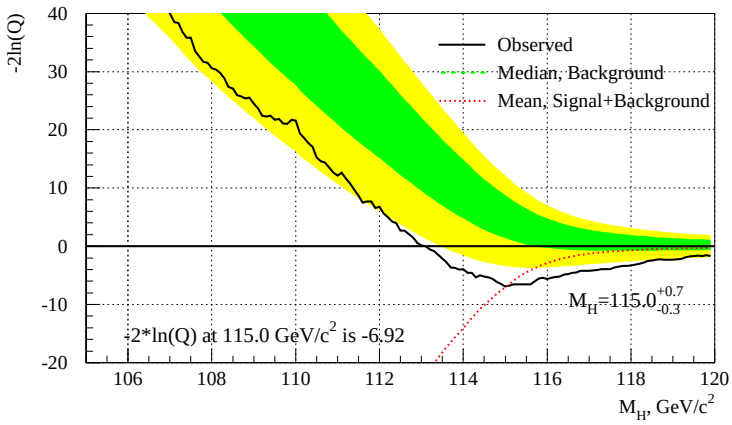

Figure 1.9: *Observed behaviour of* $-2ln(Q(M_H))$ *as a function of* M_H*; green and yellow bands correspond to a* 68% *and* 95% *compatibility with an exclusive background production.*

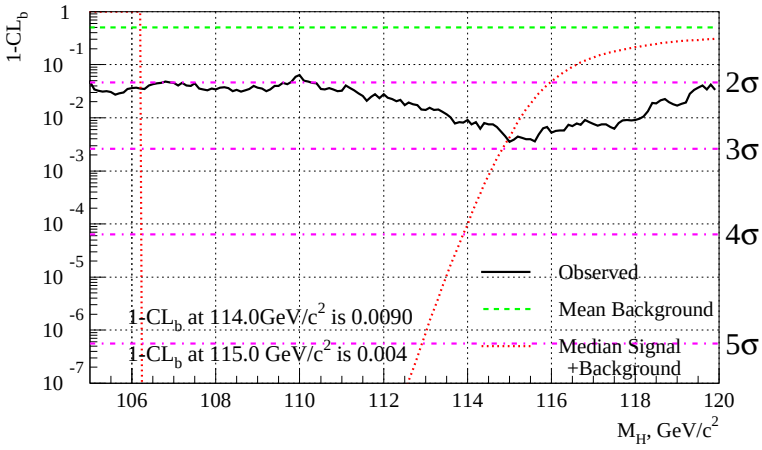

Figure 1.10: *Value of* $1-CL_b$ *as a function of* M_H *obtained by the four* LEP *experiment; excesses above the expected background are shown on the right axis.*

- associated production with a vector boson: $q\bar{q} \to VH$.

Although gluon fusion is the dominant production mode, with an expected cross section ranging from 1.17 to 0.15 *pb* for Higgs boson mass between 100 and 200 GeV/c^2, the presence of an overcoming background from QCD processes makes it hard to exploit. Vector boson fusion, on the other hand, is penalized by a low cross section and by the difficult detection of the outcoming quarks due to their direction almost parallel to the beam line. Higgs associated production results then to be the most promising channel since the presence of the vector boson allow to identify specific topologies to discriminate signal production from background processes.

Searches for Higgs associated production were already performed at the Tevatron collider on the data sample ($\sim$ 110 pb^{-1}) collected at $\sqrt{s} = 1.8\ TeV$ with the CDF detector from 1992 to 1995. Most decay channels of the vector boson were considered, while Higgs boson was required to decay into a $b\bar{b}$ pair. In these channel,

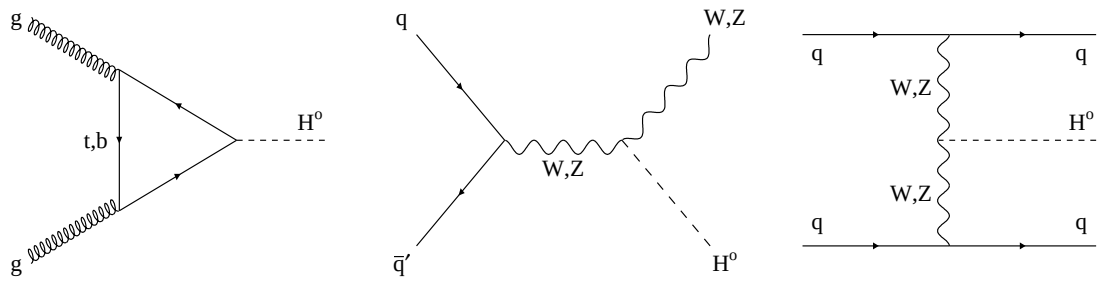

Figure 1.11: SM *Higgs boson dominant production processes at the Tevatron collider: from left to right, gluon fusion, Higgsstrahlung and vector boson fusion.*

b-tagging procedure could be used to identify events with at least an outcoming b quark, providing a powerful rejection of background processes. Further requirements were then established for each final state topology the different vector boson decays lead ($VH \to l^+l^-b\bar{b}$ [17], $\nu_l l b\bar{b}$ [18], $\nu\bar{\nu}b\bar{b}$ [19] and $q\bar{q}b\bar{b}$ [20], with $l = e,\mu$). Successively, invariant mass distribution of the candidate Higgs bosons was reconstructed and used as input for a maximum likelihood fit of expected signal and background distributions. The likelihood function [21] was defined as

$$L(M_{\mathrm{H}}) = \prod_{j}^{n_{bins}} \frac{\mu_j^{n_j}\, e^{-\mu_j}}{n_j!} \tag{1.30}$$

where n_j and μ_j were the number of observed and expected events in each bin j of the mass distribution; μ_j was written as

$$\mu_j = \sigma_{\mathrm{HV}} \mathcal{L}_{int.} \epsilon s_j(M_{\mathrm{H}}) + \sum_i B_k b_i \ , \tag{1.31}$$

where s and b_i were the predicted mass distributions of the $\sigma_{VH}\mathcal{L}_{int.}\epsilon$ signal[3] and B_i background events respectively (k runs on all the possible background sources). Finally, results obtained from each decay channel k were combined by considering an integrated likelihood $L(M_H) = \prod_k L_k(M_H)$.

The CDF collaboration quoted 95% C.L. exclusion curves for associated Higgs production cross section by integrating the negative log-likelihood function on σ_{VH} from 0 to the value which encloses an area underneath the $-lnL(M_H)$ curve equal to 0.95. Results are shown in Fig. 1.13.

1.4 Perspectives for Higgs Boson Search at the Tevatron Collider

The search for the Higgs boson is a basic point in the comprehension of the electroweak symmetry breaking mechanism. As previously mentioned, at the LEP

[3]Here, $\mathcal{L}_{int.}$ is the integrated luminosity, σ_{VH} is the cross section of VH production and ϵ the efficiency of signal detection and reconstruction.

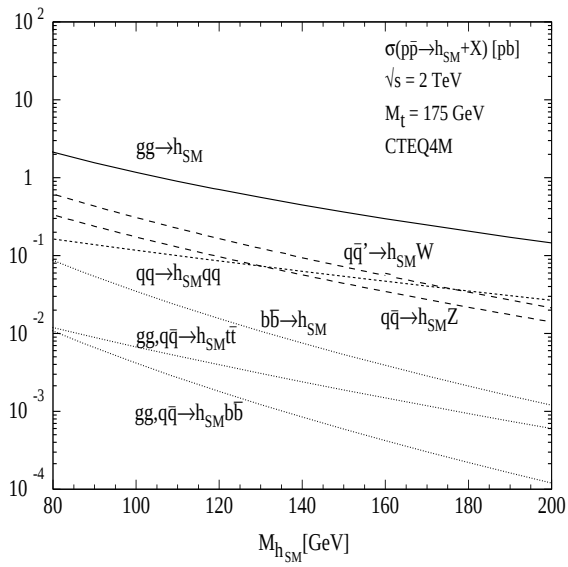

Figure 1.12: *Cross sections for* SM *Higgs boson production at the Tevatron collider.*

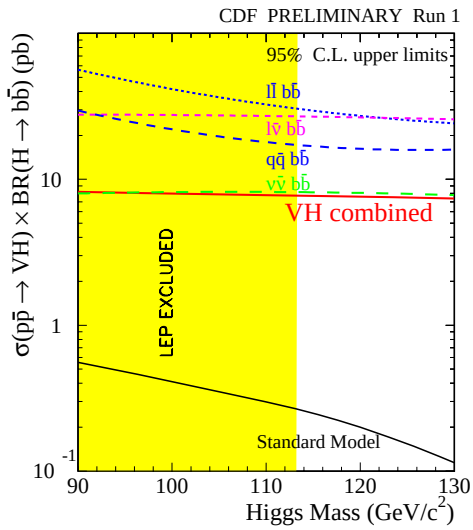

Figure 1.13: CDF *limits on the cross section for* SM *Higgs boson associated production [21].*

collider the production process $e^+e^- \rightarrow ZH$ has been studied up to an energy $\sqrt{s} \geq 206.5\ GeV$ and a lower limit on M_H has been set at 113.5 GeV/c^2 (95% C.L.). Higher mass region will be instead explored by the Large Hadron Collider (LHC) at the CERN laboratory starting from 2007: pp collisions at a center-of-mass energy $\sqrt{s} = 14\ TeV$ will make accessible the observation of the $gg \rightarrow H$ production process in the range $130 \lesssim M_H \lesssim 700\ GeV/c^2$. On the contrary, the region $M_H \approx 110 \div 130\ GeV/c^2$ will remain hard to explore at LHC. Actually, an inclusive W trigger would have a very high rate and QCD background will be dominant at that energy. An interesting channel will be instead provided by the Higgs decay into two photons. Also for this reason, LHC electromagnetic calorimeter has been designed to get high performances.

whose detectors are not able to reconstruct the Higgs boson decay into $b\bar{b}$ pair, that is dominant in this mass range.

The most suitable collider at the search for an Higgs boson with mass between 110 and 130 GeV/c^2 is therefore the Tevatron, which began to take new data on March 2001, after the accelerator and its detectors - CDF and D0 - have been undergone to several upgrades (see Chap. 2). Actually, the new center-of-mass energy ($\sqrt{s} = 2\ TeV$) allow the Higgs boson production in this mass region and its detectors have been projected on purpose to trigger, between the other things, on b quark production.

Two alternative scenarios are possible:

- $M_H \lesssim 130\ GeV/c^2$: as for the preceding data taking period, Higgs associated production with a vector boson is the most promising channel for experimental searches, thanks to the possibility to identify specific topologies due to the vector boson decays.

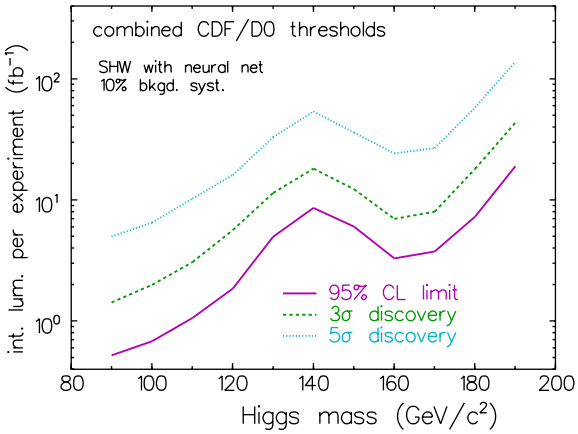

Figure 1.14: *Integrated luminosity thresholds for Standard Model Higgs boson discovery at the Tevatron collider.*

- $M_H \gtrsim 130\ GeV/c^2$: the opening of the Higgs boson decay channel into vector boson pairs allow to study the Higgs direct production through gluon fusion. In particular, full leptonic decay channels are possible, leading to extremely pure final states.

Preliminary studies have been performed to investigate the sensitivity of the two Tevatron detectors to Higgs boson production [7]. Results are shown in Fig. 1.14: the integrated luminosity required to either exclude Standard Model Higgs boson production at 95% C.L. or discover it at the 3 σ or 5 σ level of significance is plotted as a function of Higgs boson mass. Is is important to note that the integrated luminosity displayed is the delivered integrated luminosity *per* experiment, while the results are been obtained by combining the statistical power of *both* experiments for all the most promising channels: the required integrated luminosity thresholds for a single experiment are very close to a factor of two higher than those for the two combined experiments.

In conclusion, Higgs boson discovery at Tevatron collider will can be achieved only by integrating the capability of the two detectors and by combining the results of all the possible channels. Furthermore, the full detection power of the apparatus will have to be exploited; in particular, high b-tagging efficiency and $b\bar{b}$ mass resolution will be needed to reconstruct Higgs boson decays.

Bibliography

[1] S. Glashow, *Nucl. Phys.* 22 (1961) 579; S .Weinberg, *Phys. Rev. Lett.* 19 (1967) 1264; A. Salam, in *Elementary Particle Theory: Relativistic Groups and Analicity (Nobel Symposium No. 8)*, ed. N. Svartholm (Almqvist and Wiksell, Svezia 1968) 367.; G. 't Hooft, *Nucl. Phys.* B33 (1971) 167.

[2] P. W. Higgs, *Phys. Lett.* 12(1964) 132; 13(1964) 508; J. Goldstone, *Nuovo Cimento* 19(1961) 154; J. Goldstone, A. Salam, S. Weinberg, *Phys. Rev.*, 127(1962) 965.

[3] P. W. Higgs, *Phys. Lett.* **12**, 132 (1964); *Phys. Lett.* **13**, 508 (1964).

[4] N. Cabibbo, *Phys. Rev. Lett.* **10**, 531 (1963).

[5] M. Kobayashi, K. Maskawa, *Progr. Theor. Phys.* **49**, 652 (1973).

[6] G. Arnison et al. (UA1 Collaboration), *Phys. Lett.* **122 B**, 103 (1982).

[7] M. Banner et al. (UA2 Collaboration), *Phys. Lett.* **122 B**, 476 (1982).

[8] C. Rubbia, Nobel Lecture, *Rev. Mod. Phys.* **57**, 699 (1985).

[9] F. Abe et al. (CDF Collaboration), *Phys. Rev. Lett.* **74**, 2626 (1995).

[10] M. Spira, P. M. Zerwas, *Electroweak Symmetry Breaking and Higgs Physics*, HEP-PH/9803257, Dec 1997.

[11] M. Carena, J. S. Conway, H. E. Haber, J. D. Hobbs, et al. (The Fermilab Higgs Working Group), *Report of the Tevatron Higgs Working Group*, HEP-PH/0010338, Oct 2000.

[12] H. Spieseberger, M. Spira, P. M. Zerwas, *The Standard Model: Physical Basis and Scattering Experiments*, HEP-PH/0011255, Nov 2000.

[13] The LEP Electroweak Working Group, `http://lepewwg.web.cern.ch/LEPEWWG/`.

[14] The ALEPH, DELPHI, L3 and OPAL (The LEP Higgs Working Group), *Searches for Higgs bosons: Preliminary combined results using* LEP *data collected at energies up to 209GeV/c^2*, contribution to ICHEP'2000, Osaka, Japan, July 27 - Aug 2, 2000.

[15] R. Barate et al. (The ALEPH Collaboration), *Observation of an Excess in the Search for the Standard Model Higgs Boson at ALEPH*, CERN-EP/2000-138, Nov 2000.

[16] The LEP Higgs Working Group, `http://lepewwg.web.cern.ch/LEPHIGGS/`.

[17] M. Kruse, W. Yao, *Search for* $\mathrm{ZH} \to \ell^+\ell^-\mathrm{b}\overline{\mathrm{b}}$ *in Run I*, CDF internal note 4827, Jan 1999.

[18] F. Abe et al. (CDF Collaboration), *Search for New Particles Decaying into* $b\bar{b}$ *and produced in Association with* W *Bosons Decaying into* $e\nu$ *or* $\mu\nu$ *at the Tevatron*, *Phys. Rev. Lett.* **79**, 3819 (1997).

[19] W. Bokhari, C. Holck, W. Yao, *Search for* $\mathrm{ZH} \to \nu\overline{\nu}\mathrm{b}\overline{\mathrm{b}}$ *production*, CDF internal note 4663, Apr 1999.

[20] J. Troconiz et al., *Update in the Search for a Neutral Heavy Scalar in the Multijet Data Sample*, CDF internal note 4129, Apr 1998.

[21] M. Kruse, J. Valls, W. Yao (CDF Higgs Working Group), *Combined* CDF VH *production cross section limits for Run I*, CDF internal note 4985, Apr 2000. Submitted to *Phys. Rev. Lett.*

Chapter 2

Tevatron and CDF Upgrades

The analysis of experimental data collected at the Tevatron detectors - CDF *and* D0 *- during the last ten years yielded to a lot of important results, such as the first experimental evidence for the top quark [1][2][3], and the measurement of average lifetime for several b hadrons [4].*

However, the machine and detectors setup for such a period of data collection (called Run I*) were not optimal for many searches of new physics, leading to a low statistics for achieving enough sensitivity on processes whose limited production cross sections essentially reflect the smallness of the electroweak coupling constant and the high mass of the new particles involved. For this reason, since the shutdown in* 1996*, the Tevatron and its detectors have undergone major upgrades, making the actual physics run (named* Run II*) the best opportunity for new physics discoveries after the shutdown of* LEP *(occurred at the beginning of November 2000) and until* LHC *starts to run.*

In this chapter, we describe the whole of the production and the detection of the events at CDF II *experiment, with particular attention to the contributions of accelerator and detector upgrades.*

2.1 The Accelerator Complex

The number of events which are expected to be collected for a specific process is given by the expression:

$$N_{evts} = \sigma \cdot \epsilon \cdot \int \mathrm{d}t \mathcal{L} \ ,$$

where σ is the cross section of the considered process, ϵ the efficiency of his detection and $\mathcal{L}$ is the instantaneous luminosity achievable by the experiment; therefore, N_{evts} can be increased in four ways:

1. performing the experiment in the situation that maximizes σ;

2. increasing the experiment instantaneous luminosity;

3. augmenting the running time of the experiment;

4. increasing the detector's acceptance and trigger's efficiency.

The first three steps, and the partial reconstruction of the Tevatron they implied, are the topic of this section, while the last one, together with the consequences on readout and triggering procedures an high luminosity requires, will be discussed in the next ones.

In order to augmenth the cross section of the interesting processes, the p-$\bar{p}$ center of mass energy at Tevatron has been increased to 2 TeV, some 10% higher than in Run I; this provides an increase in the collected sample size: for example, the H^0V and $t\bar{t}$ production cross sections will grow by $\sim$ 30% and $\sim$ 40% respectively, with respect to Run I.

In order to understand how the instantaneous luminosity can be increased, let us express it in terms of:

$$\mathcal{L} \propto \frac{f B N_{\mathrm{p}} N_{\overline{\mathrm{p}}}}{2\pi(\sigma_{\mathrm{p}}^2 + \sigma_{\overline{\mathrm{p}}}^2)} ,$$

where f is the revolution frequency, B the number of bunches in each beam, N_{p} and $N_{\overline{\mathrm{p}}}$ the number of protons and antiprotons per bunch, σ_{p} and $\sigma_{\overline{\mathrm{p}}}$ the transverse beam sizes (RMS) at the interaction point, while the proportionality is provided by a form factor depending on the beam longitudinal size and on its dispersion in phase space.

A limiting factor in the augmenting of the number of colliding particles per bunch is the superposition of multiple elementary p-$\bar{p}$ interactions within the same bunch crossing. At high luminosity, this superposition increases the complexity of the event, making its reconstruction more difficult. The average number of superimposed interactions is shown in Fig. 2.1 as a function of luminosity for different values of the number of bunches. As suggested in such a figure, the most effective improvement in luminosity is obtained by increasing the number of bunches per beam from 6 to 36, and then to 108, while maintaining the number of protons/antiprotons per bunch at roughly the same value used in Run I.

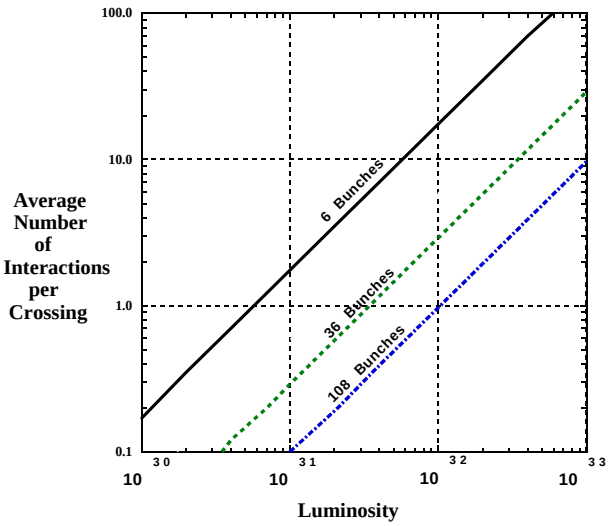

Figure 2.1: *Average number of interactions per beam cross for various beam conditions.*

Finally, the running time of the experiment can be increased mainly by improving the $\bar{p}$ accumulating and recycling, which suffered a certain inefficiency during Run I.

In the following, a description of the steps needed to achieve such results is provided.

2.1.1 Proton Production and Boosting

The proton production begins by ionizing gaseous hydrogen in H^- ions, whose energy is increased to 750 KeV by ba Cockcroft-Walton accelerator and successively to 400 MeV through a drift tubes linear accelerator (*Linac*). The beam of ions is then focalized on a thin sheet of graphite to strip the electrons; the so-obtained protons are accelerated to 8 GeV by a small synchrotron having a diameter of 150 m, the *Booster*. The use of radio-frequency cavities allows to collect the protons into bunches, that can be injected into the *Main Injector*, a newly built circular pre-accelerator that replaces the older Main Ring.

2.1.2 The Main Injector

The Main Ring was originally built to provide 400 GeV protons to Fermilab's fixed target experiments; later on, it was converted to act as an injector to the Tevatron. The new operational requirements for the Main Ring did not match its original design due to its low phase space acceptance.

The Main Injector was designed to solve this problem, while providing further benefits: it is a 3 km synchrotron, which accelerates protons and antiprotons to an energy of 150 GeV with acceptance large enough to accommodate particle bunches from the Booster. Another feature of the Main Injector consists in its capability of decelerating antiprotons, a functionality which reveals very useful for recovering unused antiprotons when Tevatron is not in colliding mode.

2.1.3 Antiproton Production and Cooling

Antiprotons are produced by dumping onto a nickel target a 120 GeV proton bunch extracted from the Main Injector. A lithium lens helps collecting the antiprotons produced in the collision at energies close to 8 GeV. The antiproton bunches are then fed into the *Debuncher Ring*, where they are collected as a continuous beam and stochastically cooled, and then into the *Accumulator*, where they are further cooled. The antiproton stacking rate will increase from $7 \cdot 10^{10}$ to $\sim 20 \div 30 \cdot 10^{10}$ $\bar{p}/hour$ thanks to Run II upgrades, such as antiproton cooling and lithium lens improving. When a sufficiently high number of antiprotons is available, they are cooled into a bunch and this is injected into the *Recycler Ring*.

2.1.4 The Recycler Ring

As previously pointed out, antiproton production was one of the limiting factors in the luminosity achieved by the Tevatron during Run I. In fact, on one hand, the frequent power losses distressing the antiproton accumulation led to the loss of the store approximately once a week, while on the other, the antiprotons remaining at the end of a run used to be dumped.

The Recycler Ring is a new accumulation ring built in the same cavity hosting the Main Injector in order to avoid these limitations: thanks to the use of permanent magnets, it can store the bunches of antiprotons produced by the Accumulator

without the risk of losing the beam as a consequence of power losses; besides, the Recycler Ring can recycle the antiprotons slowed down by the Tevatron and Main Injector at the end of a run, providing an increase on the average integrated luminosity by a factor of two.

2.1.5 The Tevatron

The Tevatron is a 6 km circular collider, where protons and antiprotons arranged to circulate in opposite directions within the same beam pipe, are accelerated from 150 GeV to 1 TeV before beams are crossed and collisions take place[1]. Making use of the upgrades developed for each component of the accelerator chain, the Tevatron will be able of producing $p\bar{p}$ collisions at a center of mass energy $\sqrt{s} = 2\ TeV$ with a luminosity that should increase up to $2 \cdot 10^{32}\ cm^{-2}s^{-1}$ after a fine tuning of the machine. It would allow to collect 2 fb^{-1} of data within approximately two years.

2.1.6 The Beam Monitors

The quality of the beams colliding at the Tevatron requires a constant monitoring of beam position and luminosity in order to have effective control of the physics processes taking place in the detectors.

The luminosity monitor is based on the same technology used during Run I, since, as mentioned in Section 2.1, the increase of instantaneous luminosity is obtained by augmenting the number of bunches per beam, but keeping the average luminosity per bunch almost the same with respect to Run I. In pratic, two arrays of scintillators (*beam-beam counters*) are placed on both sides of the interaction region: time-coincidences between particles moving away from the interaction point, both in the p and $\bar{p}$ directions, are used to measure the luminosity, while time-coincidences due to bunches of particles moving through the interaction region in a single direction, without a coincident bunch in the opposite direction, give an estimate of beam losses.

Finally, the beam position and transverse profile are measured by the tracking devices of the detectors themselves at the beginning of each data-taking. These informations are used by the Tevatron control crew in order to optimize the accelerator performance.

2.2 Phenomenology and Detection of the Events at CDF II

Proton-antiproton interactions at the center of mass energy available at the Tevatron are interpreted in terms of collisions between the elementary partons constituting them. At this level, the phenomenology is usually described in the framework of a gauge theory based on the $SU(3)$ group, called *Quantum Chromo-Dynamics* (QCD).

[1]There are twelve possible beam cross points: ten are avoided by means of electrostatic separators; in the remaining two, the CDF and D0 detectors are situated.

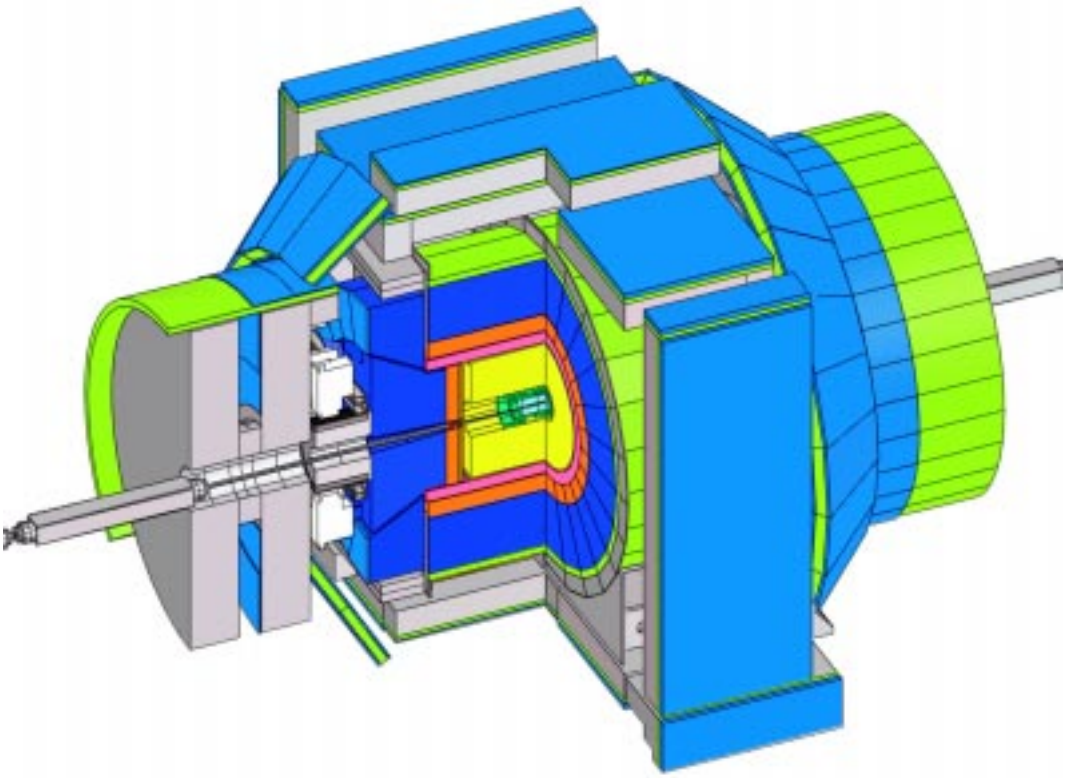

Figure 2.2: CDF II *detector section.*

In such a theory, the interactions are carried by massless gauge bosons, the *gluons*, whose coupling to fermions is expressed in terms of three kinds of charge named *colour* (by convention red, green and blue). The interaction potential grows linearly with the distance between the outgoing partons, until the creation of new colour singlet hadronic states becomes energetically favorable. At the end of this process, called *hadronization*, collimated *jets* of particles emerge, whose energies and directions carry a reminiscence of initial partons' ones. The colour radiation emitted from partons departing from the interaction center can lead to the creation of new jets or be included in the original one. In this case, the transverse expansion of the jet is limited by an effect known as *colour coherence*: the angle between quark and emitted gluon decreases at every subsequent emission; in fact, the effects of interference between all the possible emission diagrams are destructives at the order of the main logarithm outside this region of angular ordering.

The *Collider Detector at Fermilab* (see Fig. 2.2) [5] has been designed in order to perform precise measurement of energy and momentum of the jets and charged leptons produced by the $p\bar{p}$ collisions, as well as the missing energy due to the neutrinos created in W decays. Besides, it has been studied to provide a first identification of the produced particles, particularly of the ones with relatively long lifetime coming from heavy quarks hadronization.

The event reconstruction begins with the identification of jets: this is a task of a calorimetry system, essentially based on the search of clusters of calorimetric

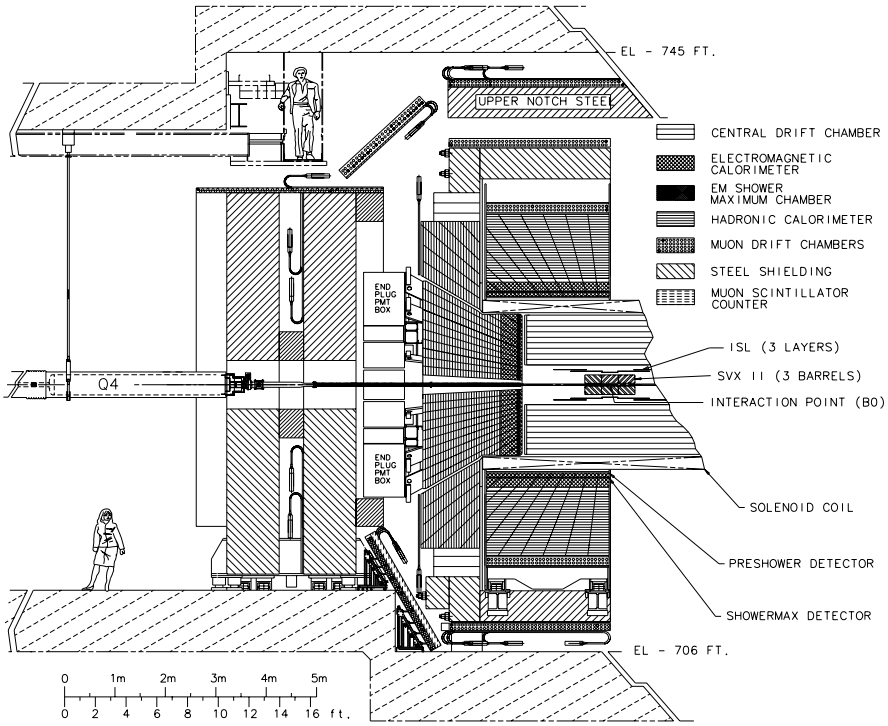

Figure 2.3: *$r-\phi$ view of one half of the* CDF II *detector.*

towers with energy above a certain threshold. In order to determine the direction of the jet momentum a precise measurement of the event interaction center is needed; besides, the identification of the jets originated by heavy quarks requires an accurate reconstruction of the secondary vertices. These measurements take advantage of the presence in the jets of charged particles, whose transverse momentum and trajectories can be reconstructed by a tracking system situated between the beam pipe and the calorimeter. Calorimetric and tracking informations are also used to identify electrons produced in the event. Outside the detector, a complex of drift chambers for muon identification is arranged. In fact, these particles are very penetrating and do not leave an appreciable quantity of energy in the calorimeter: in order to identify them, tracks with high transverse momentum are extrapolated and matched to low energy calorimetric deposition and to stubs reconstructed in the external chambers.

In the following of this chapter, the detection and the reconstruction of the events at CDF II experiment will be examined in detail. In particular, in the next section the devices and the algorithms used to reconstruct the tracks will be described, while the successive ones will be dedicated to calorimetry system and jets and electron identification (Section 2.4) and to external drift chamber and muon reconstruction (Section 2.5). Finally, in the last section we will summarize the principal techniques of data triggering and recording.

The description of CDF II subdetectors given in the following sections uses a cartesian coordinate system centered in the nominal point of interaction, with the z axis coincident with the beamline and oriented parallel to the motion of protons

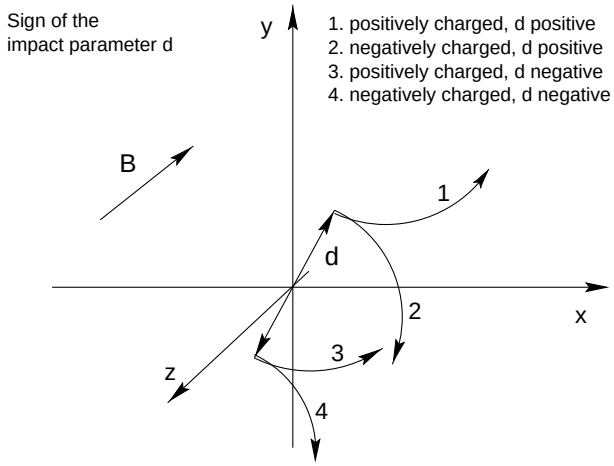

Figure 2.4: *Convention for the sign of impact parameter.*

and the x axis radial, and a polar coordinate system, with the azimuthal angle ϕ measured in the xy plane starting from the x axis, being positive in the anti-clockwise direction, polar angle θ measured from the positive direction of the z axis, and r defining the transverse distance from the z axis. Finally, we define the *pseudorapidity* as:

$$\eta = -\ln\left(\tan(\theta/2)\right) \ .$$

This coordinate is usually preferred to θ at hadron collider, where events are boosted along the beamline, since it transforms linearly under Lorentz-boosts.

2.3 The Tracking System

The detection and reconstruction of the charged particles are essentially based on the effect of a Lorentz force: an electric charge qe (where e denotes the positron charge) moving with a velocity $\vec{v}$ in a homogeneous magnetic field $\vec{B}$ experiences a force

$$\vec{F} = qe\vec{v} \wedge \vec{B}$$

that constrains it to a helicoidal trajectory, whose radius, measured in the plane transverse to $\vec{B}$, is directly related to its transverse momentum P_T according to the relation:

$$\rho = \frac{P_T}{|q|eB} \ .$$

Such a trajectory can be completely described by five parameters [6]:

- $\cot\theta$: cotangent of polar angle of helix measured at minimum approach to beam axis;
- C : signed half curvature (same sign of q);
- z_0 : z-coordinate of minimum approach to beam axis;
- φ_0 : azimuthal angle of helix at minimum approach to beam axis;
- d_0 : impact parameter (minimum distance of helix from beam axis with sign defined according to fig. 2.4).

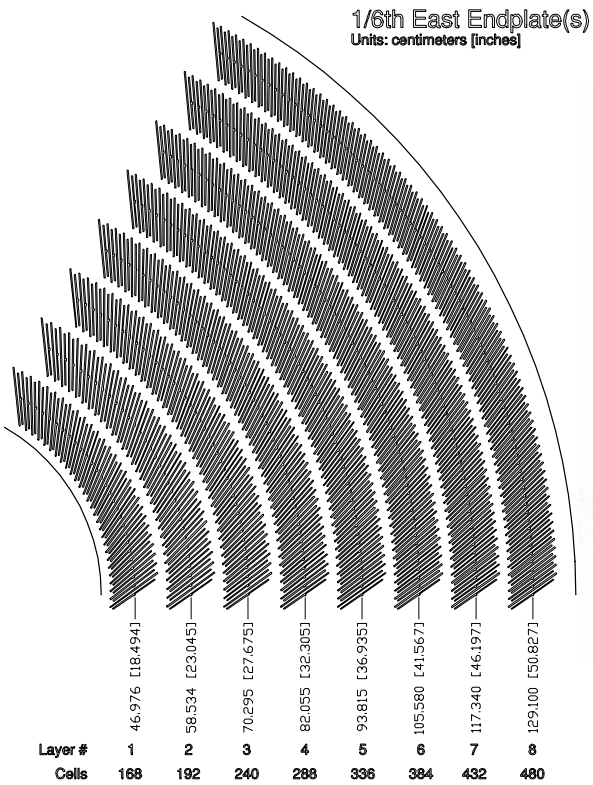

Figure 2.5: *Sector of* COT *($\Delta\phi = 60°$).*

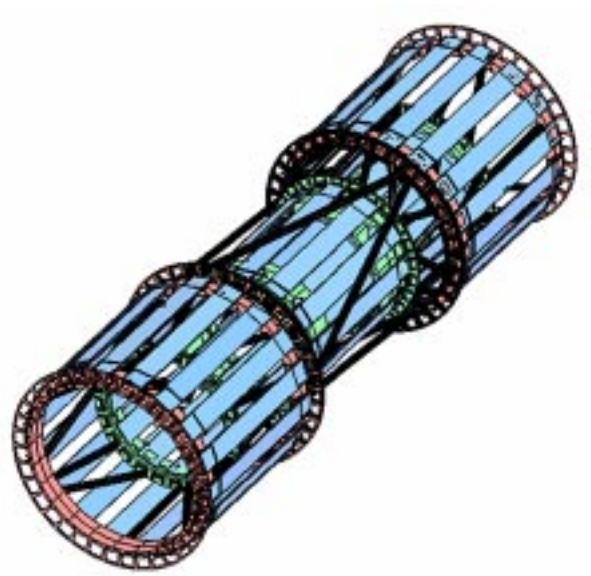

Figure 2.6: *Perspective view of* ISL.

In order to measure such parameters, the innermost part of the CDF II detector has been equipped with four devices enclosed in a superconducting solenoid providing a uniform magnetic field of 1.5 TeV, parallel to the beamline:

- The **C**entral **O**uter **T**racker (COT), arranged at a distance between 40 and 138 cm from the beam, is a new open-cell drift chamber, able of tracking in the $|\eta| < 1$ region, provided that the transverse momentum of the particle traversing its volume is at least 300 MeV/c. The COT replaces the old Central Tracking Chamber (CTC), that would have been unable to work with the occupancy and event rate expected during Run II.

  The COT is constituted of eight superlayers of cells, each containing an array of 12 sense wires. Axial superlayers alternate with stereo superlayers (whose wires are tilted of $\pm 3^o$ with respect to the axial direction), thus providing both r-ϕ and r-z measurements for each track. Double stereo sampling with respect to Run I configuration improves sensibly three-dimensional tracking efficiency.

  In order to solve the problem of occupancy, the cell size has been reduced by a factor of four and each cell is tilted with respect to the radial direction (as shown in Fig. 2.5) by an angle which minimizes the drift time. Moreover, the usage of a faster gas mixture (Argon-Ethane-CF_4 instead of Argon-Ethane) further reduces the maximum drift time to 100 ns. This makes the COT immune from event pile-up even at the highest collision rate (1/132 ns).

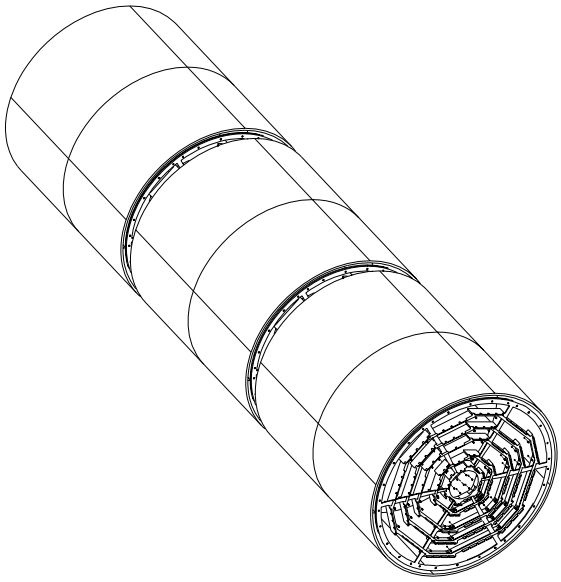

Figure 2.7: *Perspective view of* SVX II.

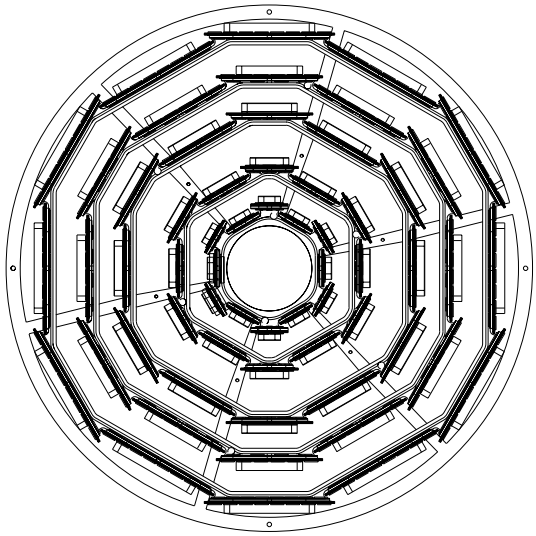

Figure 2.8: $r-\phi$ *view of* SVX II.

- The **I**ntermediate **S**ilicon **L**ayers (ISL) consists of double-sided silicon crystals: one side has axial microstrips to provide measurements in the r-ϕ plane, while the other one supplies z information by means of stereo strips.

  The arrangement of this device, shown in Fig. 2.6, varies according to the η range: in the central region ($|\eta| < 1$) it consists of a single layer placed at ~ 22 *cm* from the beam line, while for $1 < |\eta| < 2$ ISL is constituted of two layers placed respectively at $r = 20$ and 29 *cm*.

  In both regions, the stereo sampling of ISL enables a full three-dimensional stand-alone silicon tracking.

- The **S**ilicon **V**erte**X** detector II (SVX II) consists of three barrels of five silicon layers (see Fig. 2.7), similar to those in ISL, aligned along the beam line up to 45 *cm* on either side of the interaction point. The silicon layers are divided in 12 ϕ sectors (*wedges*) and placed at a distance from the beam line ranging from 2.5 to 10.6 *cm*, as shown in Fig. 2.8. Like in ISL, the sides of SVX II layers alternate axial and stereo microstrips, providing a three-dimensional information of particle position.

- The **L**ayer **00** (L00) is the most recent addition to the tracking system. It is a single-sided, radiation-hard layer of silicon crystals, placed at $r \sim 1.5$ *cm*. It can supply measurement in the r-ϕ plane only, but, being very close to the interaction point (see Figs. 2.9 and 2.10), it is the perfect tool for improving the resolution on the track impact parameter d_0.

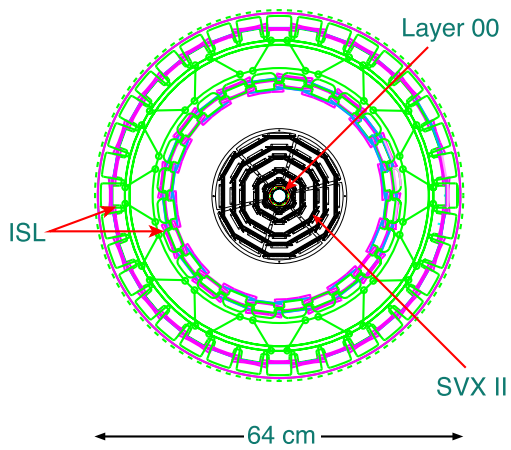

Figure 2.9: *$r-\phi$ view of silicon detectors.*

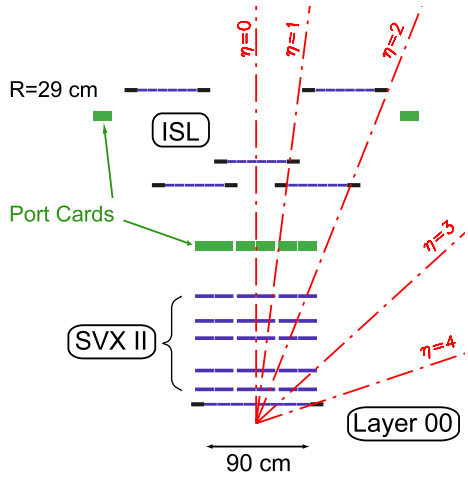

Figure 2.10: *$r-z$ view of silicon detectors.*

2.3.1 Track Reconstruction

During Run I, charged track reconstruction began by fitting the points detected in the CTC; the so-found tracks were then extrapolated to the inner region of the detector and linked to the charge depositions (*hits*) in the SVX′. This procedure, although improving the resolution achievable on track parameters, was affected by different problems, which were later taken into account in the development of the CDF II tracking system.

The main source of tracking inefficiency in Run I was the limited polar coverage of the CTC, that was almost the same as the one of the COT, shown in Fig. 2.11. Since an extension of the drift chamber would have been limited by the calorimeter, in order to increase tracking efficiency in Run II the inner silicon detectors have been improved, making them capable of a full three-dimensional track reconstruction. First of all, the length of SVX II has been increased from 51 to 90 *cm* with respect to SVX′, which covered only $\sim 60\%$ of the acceptance. A full coverage up to $|\eta| < 2$ is also provided by the new ISL detector. Besides, these devices have been equipped with double-sided layers, in order to supply also z measurements in addition to the usual r-ϕ information. Moreover, the combination of LAYER00, CDF II and ISL guarantees up to eight points for each fiducial track, providing a higher efficiency with respect to the four silicon layers of SVX′. Finally, the lever arm of the silicon system increases from ~ 5 *cm* during Run I to ~ 26 *cm*, supplying a precision of $\delta P_T/P_T^2 \sim 0.4\%$ on P_T measurement also with a

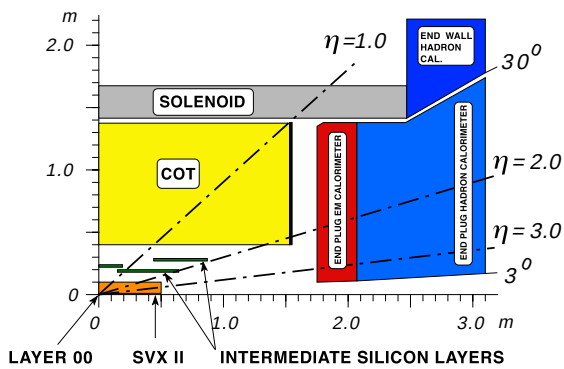

Figure 2.11: *$r-z$ view of* CDF.

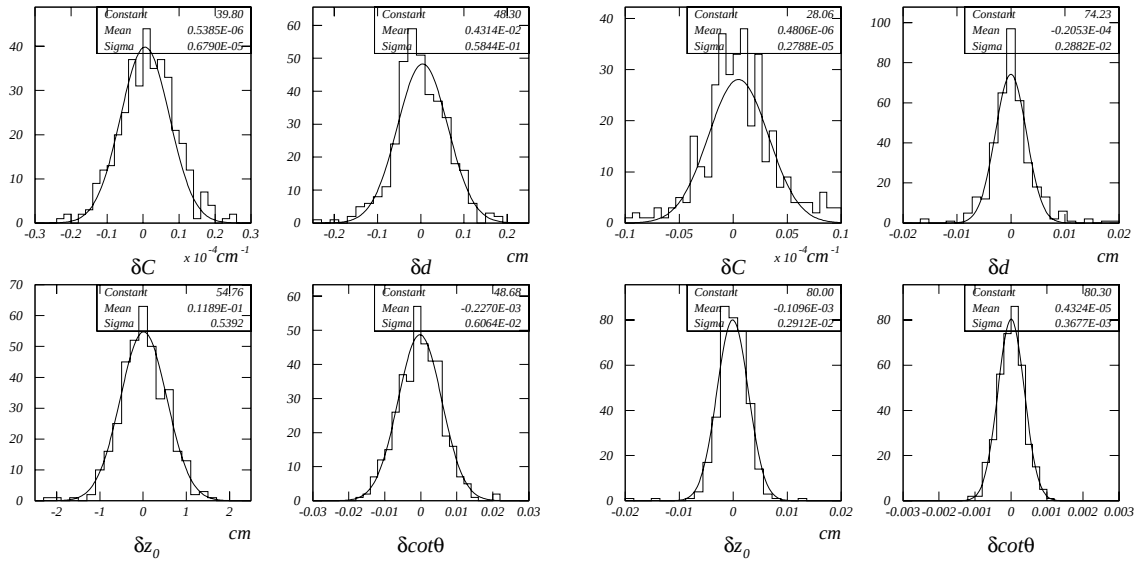

Figure 2.12: *Expected resolutions on tracking parameters achievable with stand-alone* COT *(left) and integrated (right) tracking procedures.*

stand-alone silicon tracking procedure.

2.3.2 Track Resolution

The new tracking system has been developed in order to achieve optimal performances even in a high luminosity scenario. This led to the introduction of more material around the interaction point (more silicon layers and COT stereo superlayers). The impact that luminosity changes and multiple scattering phenomena induce on the resolution of the tracking parameters has been studied in the dense b-jets environment of simulated $t\bar{t}$ events. Resolutions on the parameters of the charged particles' trajectories are computed as the difference between the parameters measured after a simulation of the tracking detector and reconstruction and the corresponding generated quantities. Results are shown in Fig. 2.12 for a low luminosity scenario. Degradations due to multiple interactions are studied by mixing $t\bar{t}$ events with a variable number of simulated minimum bias events (see Fig. 2.13) and show a weak dependence on luminosity, of the order of 10% for luminosities ranging from 1(3) to 2(6)$\cdot 10^{32}$ $cm^{-2}s^{-1}$ for Tevatron running with 36(108) bunches.

The contribution of the silicon tracking system is also stressed in Figs. 2.12 and 2.13, showing a comparison of the tracking resolution achievable by means of a stand-alone COT and integrated tracking procedures [5]: the increased number of silicon layer and their shorter distance from the beam line result in high precision measurement, in particular on d_0 and z_0, while their greater arm lever supplies a best resolution on P_T. Tab. 2.1 summarizes the track resolutions achievable in Run II, comparing them to tracking performances in Run I.

The determination of the absolute momentum scale is usually obtained by measuring a clean and well known signal. In the case of CDF experiment the decay

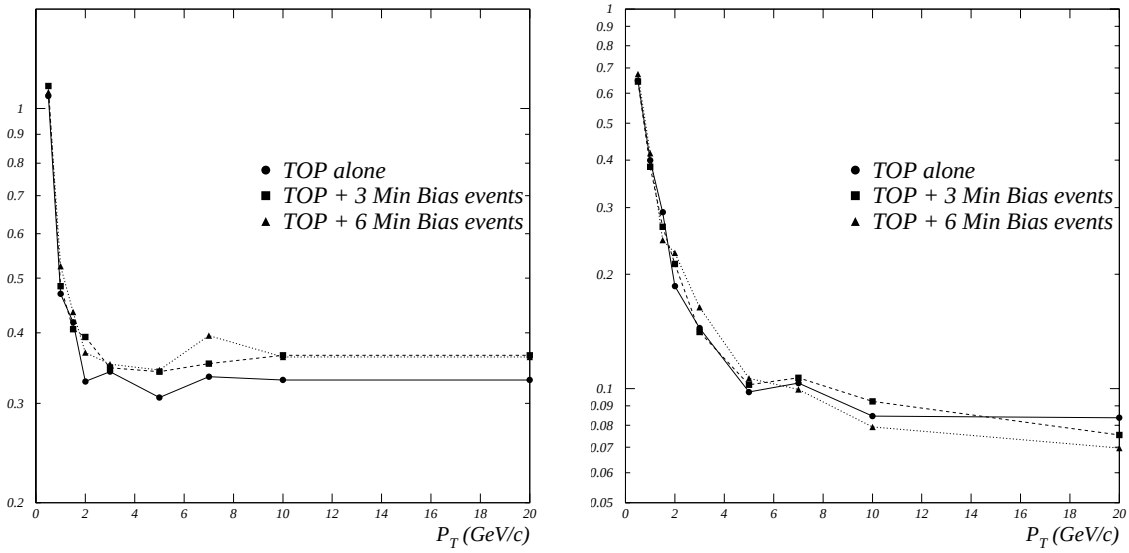

Figure 2.13: *Expected P_T resolutions for stand-alone* COT *(left) and integrated (right) tracking procedures.*

Resolution	Run I		Run II	
	CTC	CTC+SVX′	COT	COT+SVXII+ISL
$\delta P_T/P_T^2\,[(GeV/c)^{-1}]$	2×10^{-3}	1×10^{-3}	3×10^{-3}	1×10^{-3}
$\delta d\,[\mu\mathrm{m}]$	340	15	600	30
$\delta z_0\,[\mu\mathrm{m}]$			5×10^{3}	30
$\delta\cot\theta$			6×10^{-3}	4×10^{-4}

Table 2.1: *Summary of resolutions on various track parameters as obtained in Run I and as expected in Run II.*

$J/\psi\to\mu^+\mu^-$ is studied; the estimate of the momentum scale is performed by renormalizing the observed $J/\psi(1s)$ peak to the world average.

2.3.3 Primary Vertex Reconstruction

Primary vertex reconstruction proceeds through an iterative algorithm that combines all the information on reconstructed tracks: a P_T-weighted fit is performed and tracks with large impact parameter with respect to the candidate vertex are discarded. The procedure is repeated until stability is reached. The fitting algorithm can be based on x-y informations only as during Run I [7] or take advantage of tracking upgrades and perform a three-dimansional reconstruction. The resulting resolution on the primary vertex position in the transverse plane ranges from 6 to 26 μm, depending on the topology of the event and on the number of tracks used in the fit. It is a significant improvement over the beam spot information alone, and it provides the benchmark to secondary vertex searches for heavy flavour jets

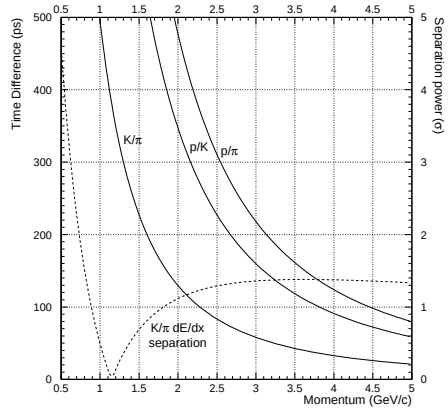

Figure 2.14: Time of flight difference as a function of particle type and momentum. The dashed line indicates the COT dE/dX separation power for $K\pi$: TOF and COT complement each other in different p regions.

tagging. Finally, the z coordinate of the primary vertex is used to define the actual pseudorapidity of each physics object reconstructed in the event.

2.3.4 The Time of Flight

Immediately outside the tracking system a **T**ime-**O**f-**F**light detector (TOF) [8] has been added for Run II. It consists of an array of scintillator bars three meters long, matching the COT active volume. The thickness of the bars (4 cm) is limited by the space remained available between COT and solenoid, while their width (4 cm) has been determined by occupancy and resolution considerations. Finally, the section of the bars has a trapezoidal shape, in order to minimize the uninstrumented regions (*cracks*).

Photomultiplier tubes, attached to both ends of each bar, provide time and pulse-height measurements; the comparison of the readings performed at each end provides an estimate of the instant when a particle crossed the scintillator and the z coordinate of the intersection. Time resolution is expected to be ~ 100 ps. The time of flight is then computed as the time interval between the interaction and the signal in the scintillators, and can be used quite effectively in particle identification, as shown in Fig. 2.14. Finally, the z coordinate can be used for matching the time of flight determination to a track reconstructed by the inner tracking system.

	Central	Plug
Electromagnetic:		
Thickness	19 X_0, 1 λ	21 X_0, 1 λ
– per sample (abs.)	0.6 X_0	0.8 X_0
– per sample (scint.)	5 mm	4.5 mm
Light yield	160 p.e./GeV	300 p.e./GeV
Sampling resolution	11.6% / $\sqrt{E[GeV]}$	14% / $\sqrt{E[GeV]}$
Stochastic resolution	14% / $\sqrt{E[GeV]}$	16% / $\sqrt{E[GeV]}$
Hadronic:		
Thickness	4.5 λ	7 λ
– per sample (abs.)	1 in (central) 2 in (end wall)	2 in
– per sample (scint.)	6 mm	6 mm
Light yield	40 p.e./GeV	39 p.e./GeV
Resolution	$75\%/\sqrt{E[GeV]} \oplus 3\%$	$80\%/\sqrt{E[GeV]} \oplus 5\%$

Table 2.2: Characteristics of the CDF II calorimeter.

2.4 The Calorimetry System

The CDF calorimetry system has been designed to measure energy and direction of neutral and charged particles leaving the tracking region. In particular, it is devoted to jet reconstruction and it is also used to measure the missing transverse energy associated to neutrinos.

Particles hitting the calorimeter can be divided in two classes, according to their interaction with the detector: electromagnetically interacting particles, such as electron and photon, and hadronically interacting particles, such as mesons producted in hadronization processes. To detect these classes of particles, two different calorimetric parts have been developed: an inner electromagnetic and an outer hadronic section, providing coverage up to $|\eta| < 3.64$. In order to supply information on particle position, the calorimeter is also segmented in towers projecting towards the geometrical center of the detector. Each tower consists of alternating layers of passive material and scintillator tiles. The signal is read via wavelength shifters WLS embedded in the scintillator; light from the WLS is then carried by light guides to photomultiplier tubes. The central sector of the calorimeter ($|\eta| < 1.1$) was recycled from Run I, while the plug one ($1.1 < |\eta| < 3.64$) has been built anew, since the old gas calorimeter used in Run I would not be able to work at the increased event rate of Run II.

In the following, a detailed description of the various calorimeter sectors is provided. Tab. 2.2 summarizes their most important characteristics.

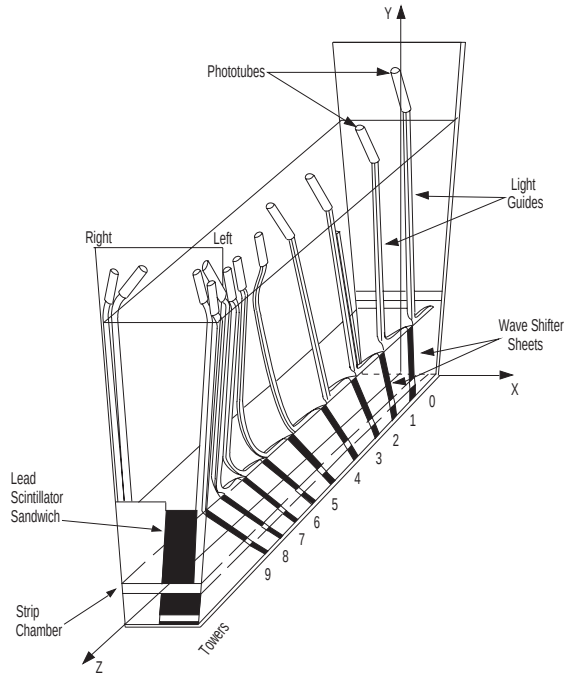

Figure 2.15: *Perspective view of a* CEM *module.*

The Central Calorimeter

Apart some upgrades on the readout electronics, the central calorimeter is almost the same used during Run I. The **C**entral **E**lectro-**M**agnetic calorimeter CEM is segmented in $\Delta\eta \times \Delta\phi = 0.11 \times 15^o$ projective towers consistings of alternating layers of lead and scintillator, while the **C**entral and the End **W**all **HA**dronic calorimeters (CHA and WHA respectively), whose geometry matches the tower segmentation of CEM, use iron layers as radiator. A perspective view of a central electromagnetic calorimeter module (*wedge*) is shown in Fig 2.15, where both the arrangement in projective towers and the light-gathering system are visible.

Two position detectors are embedded in each wedge of CEM:

- The **C**entral **E**lectromagnetic **S**trip chamber (CES) is a two-dimensional strip-wire chambers arranged in correspondence to maximum shower development ($\sim 5.9\ X_0$). It measure the charge deposition of the electromagnetic showers, providing information on their pulse-height and position with a finer azimuthal segmentation than calorimeter towers. This results in an increased purity on electromagnetic object reconstruction (see Subsection 2.4.4).

- The **C**entral **P**re-**R**adiator (CPR) consists of two wire chamber modules placed immediately in front of the calorimeter. It acts as a pre-shower detector by using the tracker and the solenoid coil material as radiators, resulting to be a very useful tool in rejection of electron and photon background.

Calorimeter response is fast enough to match the time requirements imposed by Run II. However, wire chambers associated to CES and CPR may need to be integrated over several beam crossings; this will not be a problem since the high granularity of these devices guarantees a low detector occupancy.

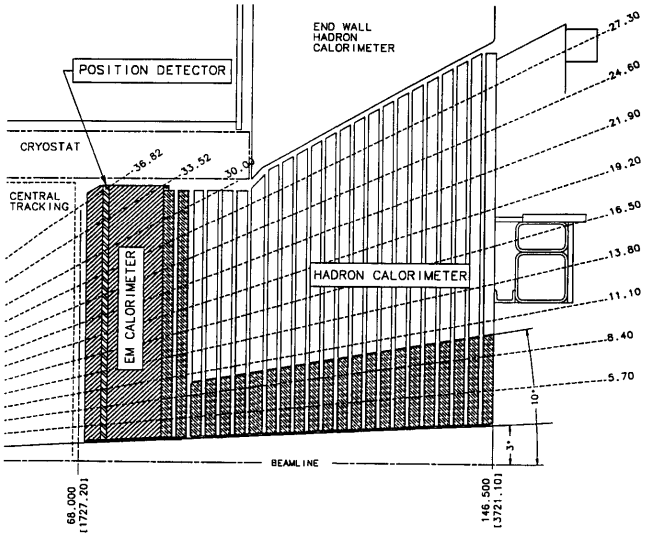

Figure 2.16: *$r-z$ view of the plug calorimeter.*

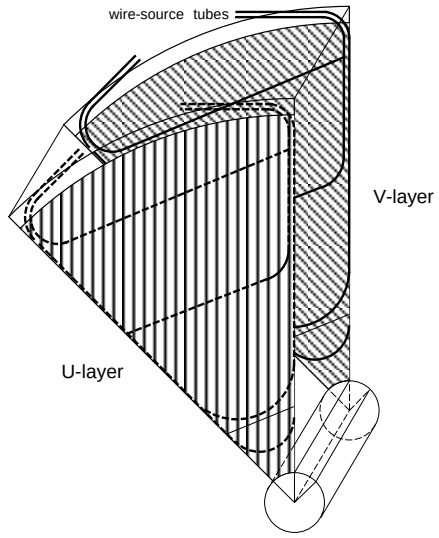

Figure 2.17: *Perspective view of* SMD.

The Plug Calorimeter

The plug calorimeter, shown in Fig. 2.16, covers the η region from 1.1 to 3.64. The new configuration, based on the same principles as the central calorimeter, allows the detector to operate in the Run II environment and make experimental data more homogeneous. Both electromagnetic and hadronic sectors are divided in 12 concentric η regions, with $\Delta\eta$ ranging from 0.10 to 0.64 according to increasing pseudorapidity, each segmented in 48 or 24 (for $|\eta| < 2.11$ or $|\eta| > 2.11$ respectively) projective towers. The actual size of these towers was chosen so that the identification of electron in b-jets would be optimized.

Projective towers consist of alternating layers of absorbing material (lead and iron for electromagnetic and hadronic sector respectively) and scintillator tiles. The first layer of the electromagnetic calorimeter acts as a pre-shower detector; to this scope, the first scintillator tile is thicker (10 mm instead of 6 mm) and made of a brighter material.

As in the central calorimeter, a **S**hower **M**aximum **D**etector (SMD) is also included in the plug electromagnetic calorimeter, at a radial depth of $\sim 6\ X_0$. The SMD consists of eight 45° azimuthal sectors, each covering six (or three) calorimetric towers in ϕ. Furthermore, each sector is segmented in two η regions in order to reduce detector occupancy. Within each region, 5 mm pitch scintillating strips are arranged on two layers (called U and V). Being parallel to either boundary of the sector, U and V strips form an angle of 45° among them (see Fig. 2.17), providing a two-dimensional measurement of the shower. The SMD is an useful tool to discriminate photons and electrons from pion background.

2.4.1 Jet Reconstruction

The jet reconstruction algorithm at CDF uses the energy depositions in the calorimetric towers in a *fixed opening cone* procedure, in compliance with the directives of the Snowmass conference (1990) for a common operating description of jets in $p\bar{p}$ collisions. The opening of the cone is usually defined in terms of a radius in the $\eta - \phi$ plane and has to be chosen accordingly with the characteristics of the physical process under study; as an example, in high multiplicity events a lower radius (typically 0.4) is preferred, in order to avoid jet overlapping.

The reconstruction starts by assigning to each tower a vector in the $r\eta\phi$ space, with module equal to tower transverse energy, origin in the interaction point, and pointing towards the energy baricenter of the tower. The baricenter is defined assuming that all energy has been released at the average depth computed for CDF calorimeter (6 radiation lengths X_0 and 1.5 interaction lengths λ for electromagnetic and hadronic sector respectively).

Towers with $E_T > 1\ GeV$ are ranked according to a decreasing magnitude order; the adjacent towers are then grouped in *pre-clusters*, which will be used as *seeds* for jet reconstruction. Around to each pre-cluster, a cone is drawn with fixed radius R and axis the vector associated to the maximum energy tower. All vectors falling inside a cone are summed to re-estimate its axis and the process is iterated until all vectors are assigned to a cone. Successively, remaining vectors with $E_T > 0.1\ GeV$ are associated to the cone containing them and the axis is re-estimated until no new vector is found inside the cone.

It may happen that two cones overlap; in this case, if more than 75% of the transverse energy of the less energetic one is common, the two cone are replaced by a single one, centered around the sum of their resultants. Otherwise, they are kept distinguished, and common vectors are assigned to the closest cone in the η-ϕ plane.

Finally, quadrimomenta of the jets are computed by interpreting each vector as a massless particle whose direction and energy are given by vector direction and associated tower energy respectively. The cones that remain at the end of the procedure are identified with jets if their energy is large enough (typically 10 or 15 GeV) to guarantee their unambiguous interpretation in terms of partons.

2.4.2 Jet Energy Corrections

According to CDF definition, jets emerge from a vector sum of the momenta associated to calorimeter towers enclosed in a certain region (cone), under the assumption that all tower contributions come from massless particles originated in the primary vertex and detected in the energy baricenter of each tower. However, a lot of factors contribute to a bad estimate of the real parton energies:

- Due to the transversal dimension of the physical jet, some particles can fall outside the cone of the reconstructed jet (*out-of-cone energy*).

- Very penetrating particles can be present in the jet, such as muons or neutrinos, whose energy is not detected in the calorimeter.

- Contribution of low-P_T charged particles can also be lost due to the deflection they suffer in the tracking magnetic field.

- Imperfect calorimeter coverage and detector cracks, in particular at boundaries between the central and plug regions, also contributes in degrading energy measurements.

- Calorimeter response could be non-homogeneous for particles hitting different regions of the detector. This was an important factor during Run I, due to different detection techniques in central and plug calorimeters. However, it should be substantially reduced in Run II, thanks to the plug calorimeter upgrades.

- Strong interactions involving beam remnants (*underlying event*) can introduce a flux of hadrons that can interfere with the jet definition, since some particles generated in the underlying event can be included in the clustering procedure.

- The same phenomenon can happen when more events occur during the same beam crossing (*multiple interactions*).

In order to take in to account all these effects, specific procedures have been studied [9] during Run I. Correction algorithms are functions of E_T and η of the jet and have been optimized to estimate the corrected average energy, but not to reduce the fluctuations around this value. During Run I, the uncertainty on the corrected jet energy ranging from 5% at $E_T = 20\ GeV$ to 3% at 300 GeV.

The most general form for the corrections to be applied to the P_T of a jet reconstructed with a cone of radius R is the following [10]:

$$P_T(R) = (P_T^{unc.}(R) \times f_{rel} - UEM(R)) \times f_{abs}(R) - UE(R) + OC(R) \ ,$$

where f_{rel} and f_{abs} are the relative and absolute energy scale factor, the first correcting for non-uniformities in the detector response and the second rescaling the jet energy into the average corrected jet energy, while $UEM(R)$, $UE(R)$ and $OC(R)$ are corrections for multiple interactions, underlying event and out-of-cone losses respectively.

The absolute calorimetric energy scale can be estimated by means of a two-step procedure. First, the electromagnetic energy scale can be determined using a sample of $J/\psi \rightarrow e^+e^-$ or $Z^0 \rightarrow e^+e^-$ events; this can be done exactly as for setting the momentum scale of the tracking system by renormalizing the observed $J/\psi(1s)$ and Z^0 peaks to the corresponding world average values. Hence, this information can be used for calibrating the response of the hadronic calorimeter: once the process $Z^0 \rightarrow e^+e^- + 1\ jet$ is considered, the hadronic energy scale can be determined by renormalizing the energy of the single jet to the energy measured for the recoiling leptons.

2.4.3 b-Jet Identification

The high resolution of the silicon vertex detector can be exploited to identify secondary vertices originated inside a jet by decays of long lifetime particles produced in heavy quark hadronization. This approach has been followed by the SECondary VerTeX (SECVTX) tagging algorithm [5, 6] and results to provide a great discrimination of high P_T b-jets from jets originated by light quarks or gluons.

The B hadrons produced by bottom quark hadronization have a lifetime of the order of the picosecond [13]. At the typical energy of the bottom quark originating by Higgs boson decay, they travel some mm before decaying. During Run I, SECVTX algorithm was then based on the selection of tracks whose trajectories were incompatible with coming from the primary vertex of the interaction, while converging to a secondary vertex, as shown in Fig. 2.18.

The tracks were selected according to the transverse momentum P_T, the impact parameter significance S_d[2] and the quality the track was reconstructed with. In particular, they were classified in:

- *loose tracks*: tracks reconstructed with hits in at least three layers of the SVX, $P_T \geq 0.5\ GeV/c$ and $S_d \geq 2.5$. These requirements are modified to two layers and $P_T \geq 1.5\ GeV/c$ if the acceptance of the silicon detector does not allow the reconstruction of further hits.

- *tight tracks*: tracks reconstructed with hits in at least three layers of the SVX, $P_T \geq 1.5\ GeV/c$ and $S_d \geq 4.0$.

The selected tracks were ranked according to their transverse momentum and impact parameter significance: the two *best* tracks were used to identify a common vertex, located where the their trajectories cross in the transverse plane. Successively, it was used as *seed* for a vertex reconstruction involving all the other tracks. Worse track was then discarded and the fit was repeated until $\chi^2 < 50$. The so obtained vertex was chosen as secondary vertex candidate if at least three tracks resulted to have an impact parameter significance $S_d < 3$ with respect to it. In the opposite case, the procedure was iterated starting from an other pair of tracks. If no candidate vertex was found, tight tracks were used for a new iteration, with only two tracks required to define a vertex.

Once a secondary vertex candidate was found, its distance L_{xy} from the primary vertex on the transverse plane was computed. The typical resolution on this distance was $\sigma_{L_{xy}} \sim 130\ \mu m$. A sign was also associated to L_{xy}, according to the scalar product between its direction and the axis of the jet the vertex was found in. Actually, jets produced from heavy quarks were expected to have secondary vertices with positive L_{xy}, while those originated by light quarks could indifferently present vertices with positive or negative L_{xy} [14]. Finally, a jet was identified as produced by heavy quark hadronization (*tagged jet*) if

[2]This quantity is defined as the ratio $S_d = d/\sigma_d$ between the track impact parameter d with respect to the primary vertex of the interaction, and the uncertainty σ_d in its determination, obtained from the uncertainty in the track parameters and the resolution on the location of the primary vertex itself in the transverse plane.

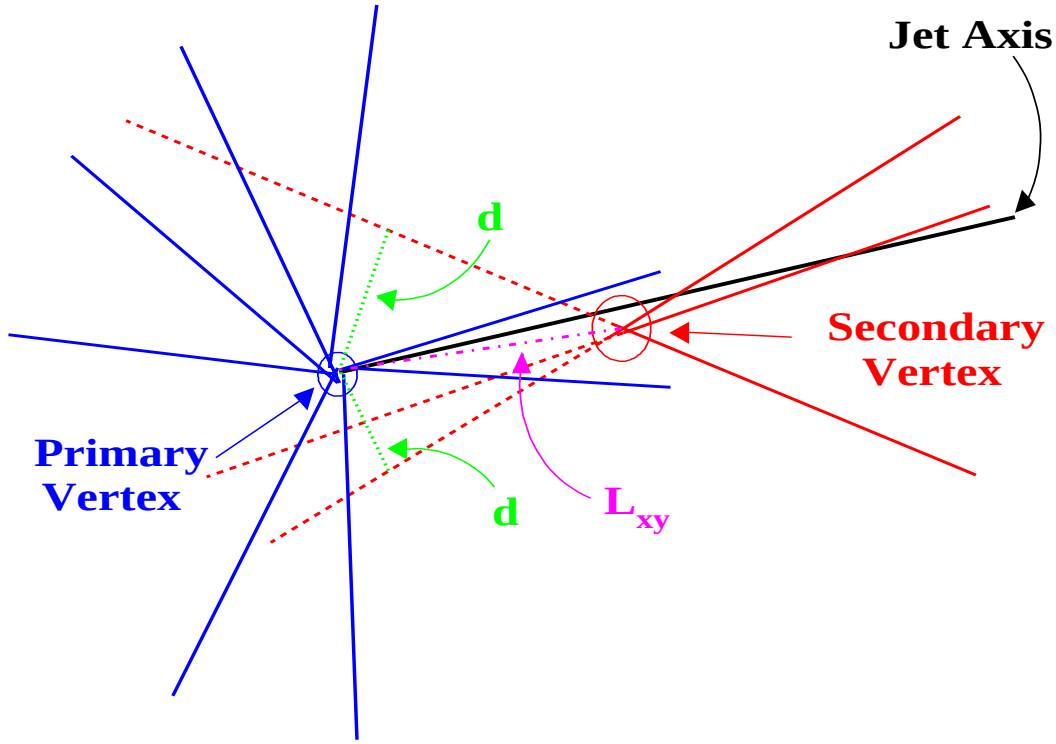

Figure 2.18: *Reconstruction of the primary and secondary vertices in the r-ϕ plane. The impact parameter d for some representative tracks and the distance L_{xy} between the vertices on the transverse plane are shown.*

- $|L_{xy}| < 2.5\ cm$;
- $|L_{xy}/\sigma_{L_{xy}}| \geq 3$;
- $L_{xy} > 0$.

The SECVTX tagging algorithm was optimized to identify jets originated by high-P_T bottom quarks, while it resulted less effective for those produced by charm quarks. The tagging efficiencies were determined by combining measurements on data and studies on Monte Carlo simulation and resulted to be $\sim 33\%$ and $\sim 11\%$ for b-jets and c-jets respectively, while the *mistag* probability (*id est* the probability to tag a jet originated by light quark or gluon hadronization) was found to be $\lesssim 1\%$.

2.4.4 Electron Identification

The energy depositions in the electromagnetic towers are also the basis for electron reconstruction. According to kinematical characteristics and production mechanisms of electrons, different identification procedures have been developed at CDF, that can be roughly divided in *cluster-based* and *track-based* procedures.

Cluster-based algorithms start from energy depositions in the electromagnetic calorimeter. These procedures tend to average energy contributions coming from adjacent towers and need a lot of isolation requirements, resulting to be a powerful tool to identify isolated electrons, but rather inefficient in the detection of low-P_T electrons produced in the semileptonic decay of bottom or charmed hadrons inside a jet.

Several requirements are used in cluster-based procedures to keep background under control:

- To reject background from photons, a reconstructed track extrapolating to the electromagnetic deposit, fitting to the known E/P electron behavior is required.

- Background from isolated hadrons performing showering before reaching the hadronic calorimeter can be reduced with an upper cut on E_{had}/E_{em} ratio. Such a variable can be computed on jet, cluster or single tower topologies, according to the electron production mode. An other useful variable is the lateral shower shape χ^2, L_{shr}, coming from a fit of the observed calorimeter lateral shower profile to test-beam electrons.

- High granularity of the CES chambers is exploited to reject casual matching between non-electron tracks and calorimetric deposition due to surrounding soft particles. Strips (wires) detecting an energy grater than 0.5 GeV or matched by an extrapolated track are used as seeds to cluster a fixed number n of strips (wires). Powerful cuts are then set on th total energy (*pulse-height*) either of the strips or wires clustered (E_{s_n}, E_{w_n}), on the spatial mismatches (Δx and Δz[3]) between the position of cluster centroids and the track extrapolation, and on the χ^2 of cluster profile fits to test beam electrons both in strip (χ^2_{strip}) and wire (χ^2_{wire}) plane.

The CDF standard electron selection cuts are summarized in Tab. 2.3.

As previously mentioned, cluster-based procedures are not able to reconstruct soft electrons inside a jet with acceptable efficiency. For this reason, during Run I the CDF collaboration developed a track-based algorithm to tag soft electron [15]. Instead of beginning from an deposition in the electromagnetic calorimeter, this algorithm starts by searching candidate tracks extrapolating to a fiducial region of the calorimeter after a loose quality selection. A set of requirements is then applied to these tracks, exploiting two further informations:

[3] x and z are local coordinates of the CEM modules, see Fig. 2.15.

Variable	Std. electron cuts	Soft electron cuts
$(E_T)_{em}$	$>7.5GeV$	–
P_T	$>6GeV/c$	$\geqslant 2GeV/c$
E_{em}/P	–	$\geqslant 0.7,\ \leqslant 1.5$
E_{had}/E_{em}	<0.04	<0.1
L_{shr}	<0.2	–
$E_{s_5}/P,\ E_{w_5}/P$	–	$\geqslant \min\{0.6, 0.24+0.03P\}GeV$
$\lvert\Delta x\rvert$	<1.5 cm	$\leqslant \max\{0.7, 1.82-0.1867P\}$ cm
$\lvert\Delta z\rvert$	<3 cm	$\leqslant 2$ cm
$\chi^2_{strip}/6$	<10	$\leqslant 16$
$\chi^2_{wire}/6$	<10	$\leqslant 16$
Q_{CPR}	–	$\geqslant 4744-11592(P/P_T)+7923(P/P_T)^2$
Q_{CTC}	–	$\geqslant 29.15+e^{1.671-0.08P},\ P\leqslant 15GeV/c$

Table 2.3: *Standard and soft electron requirements for Run I (P and P_T are expressed in GeV/c).*

- The total energy deposited in a three-wire cluster around the point the track extrapolates to in the central preradiator (Q_{CPR}): due to the thicker layers of material crossed by the particles travelling at high η values, energy deposition in CPR exhibits a $P/P_T = 1/sin\ \theta$ dependence that can be used to perform a rough z matching between the track and the CPR deposition itself.

- The specific energy loss $\mathrm{d}E/\mathrm{d}x$ suffered by the candidate particle in traversing the CTC: due to their low mass, $\mathrm{d}E/\mathrm{d}x$ experienced by the electrons is essentially momentum independent within the range of interest, while particles contributing to the background, like muons or light charged hadrons, exhibit a strong momentum dependence. The energy loss (Q_{CTC}) is therefore required to fit the expected electron behaviour if $P \leq 15\ GeV/c$.

The soft electron selection has been optimized to tag electrons coming from b-quark decays. The main requirements are summed up in Tab. 2.3. A serious source of background for tagging b-jets comes from photons converting into electron-positron pairs in detector material. To reject tagging arising from this source, a veto is applied to all pairs of tracks compatible with coming from a common vertex, constrained to lay within 50 cm from the beam line, and having an invariant mass lower than 0.5 GeV/c^2. Finally, the selection achieves an average efficiency of $\sim 70\%$ on electron tracks, while suffering a fake rate of $\lesssim 0.4\%$ per track [16].

The soft electron tagging procedure was developed as a part of a more general **S**oft **L**eptons **T**agging algorithm (SLT), and resulted a powerful tool in offline analysis involving b-jet identification, like for example $t\bar{t}$ event reconstruction [17]. In Run II, the new tracking capabilities and the performances of the new plug calorimeter should enable an extension of soft electron tagging to the $1 < |\eta| < 2$ region; however, a Run II-based algorithm has yet to be developed and predictions are not easy to make.

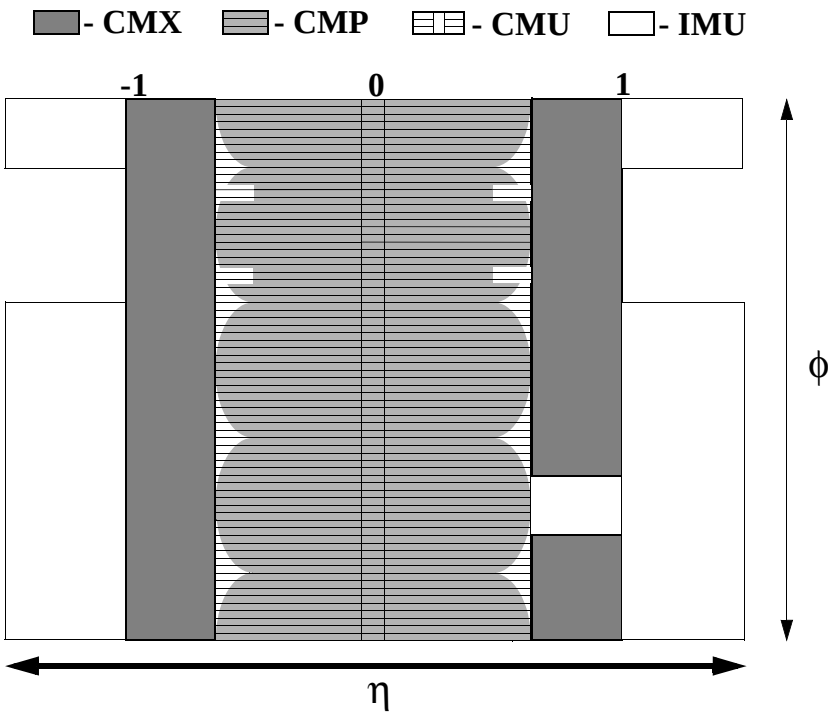

Figure 2.19: *η-ϕ coverage of the Run II muon system.*

2.5 The Muon System

Thanks to their high penetration power, muons are separated from surrounding particles by the calorimeter, that acts as a shield on electromagnetic and hadronic matter. Muon identification can therefore be performed by extrapolating the tracks outside the calorimeter and matching them to track segments (*stub*) reconstructed in an external muon detector.

To this purpose, muon system has been equipped with several devices:

- **C**entral **MU**on Detector (CMU) consists of a set of 144 modules, each containing four layers of four rectangular drift cells, operating in proportional mode. It is placed immediately outside the calorimeter and supplies a global coverage up to $|\eta| \lesssim 0.6$: ϕ measurement of muon position is guaranteed by azimuthal segmentation of the detector, while z coordinate is estimated on the basis of charge division.

- **C**entral **M**uon u**P**grade (CMP) consists of four layers of single-wire proportional drift tubes staggered by half cell per layer and shielded by an additional 60 *cm* steel layer. It is arranged in a square box around the CMU, providing a ϕ-dependent η coverage (see Fig. 2.19) according to the cylindrical structure of the inner detector. Contray to CMU, this device supplies only ϕ information. For Run II, CMP benefits an increased acceptance of $\sim 17\%$.

- **C**entral **S**cintillator u**P**grade (CSP) is a layer of rectangular scintillator counters placed on the outer surface of CMP.

- **C**entral **M**uon e**X**tension (CMX) consists of a stack of eight proportional drift tubes, arranged in conical sections to extend the CMU/CMP coverage in the $0.6 \lesssim |\eta| \lesssim 1$ region. Azimuthal acceptance has been improved by 45% for Run II; only a 30° ϕ-gap remains to be used by the solenoid cryogenic system.

- **C**entral **S**cintillator e**X**tension (CSX) consists of a layer of scintillator counters on both side of CMX. Thanks to scintillator timing, this device complete with z information the measurement of ϕ position of muons provided by CMX.

- **I**ntermediate **M**uon Detector (IMU) replaces the old Forward Muon Detector (FMU) to exploit the improved tracking capabilities and perform muon momentum measurement based only on the central solenoid field. In fact, during Run I the momentum of forward muons had to be mearured by the FMU itself through a toroidal magnet; steel toroids are now used to supply mechanical support and shielding to new detector. IMU consists of four staggered layers of proportional drift tubes and two layers of scintillator tiles, arranged as for the CMP/CSP system to extend triggering and identification of muons up to $|\eta| \leq 1.5$ and $|\eta| \leq 2$ respectively.

Due to their slow response, muon chambers are not able to work within the Run II interbunch interval of 400 or 132 ns. However, detector occupancy is expected to be strongly reduced with respect to Run I thanks to the accelerator upgrades[3] and to stronger shielding from beam halo. Together with the high granularity of the muon devices, it should allow to integrate the collected signals over several beam crosses.

2.5.1 Muon Identification

As soft electron tagging, the identification of low-P_T muons begins by extrapolating tracks passing a loose quality selection to fiducial regions of the muon system. After extrapolation, the distances from the edges of each detector and expected multiple scattering distance σ_{MS}[4] are computed and used to classify the track into four fiducial types:

- CMUP type: the track must have $P_T > 3\ GeV/c$ and extrapolate to within both CMU and CMP. Besides, it must be more than 3 σ_{MS} or 2 cm from the nearest boundary of CMU and more than 3 σ_{MS} or 5 cm from the nearest boundary of CMP. The momentum requirement insures that the muon should reach the CMP, the other cuts insure that stubs should be present both in CMU and CMP.

- CMP type: the track must have $P_T > 3\ GeV/c$ and extrapolate to within the CMP. Besides, it must be more than 3 σ_{MS} or 5 cm from the nearest boundary of the muon chamber. The track must not be qualified as CMUP type.

[3]More than 95% of the ionization detected in the muon system during Run I resulted to be originated by the Main Ring, that has been replaced by the Main Injector.

[4]The multiple scattering distance supplies an estimate of the uncertainty on the muon position due to the effect of multiple scattering in the inner detector. It has been measured as a function of track P_T and η using simulated samples of muons.

Variable	Soft muon requirements			
	CMUP	CMU	CMP	CMX
P_T	$\geqslant 3GeV/c$	$\geqslant 2GeV/c$	$\geqslant 3GeV/c$	$\geqslant 2GeV/c$
$\lvert\Delta z\rvert$	$<\max\{3\sigma, 8\,\mathrm{cm}\}$	$<\max\{3\sigma, 8\,\mathrm{cm}\}$	–	–
$\lvert\Delta x\rvert$	$<\max\{3\sigma, 2\,\mathrm{cm}\}$	$<\max\{3\sigma, 2\,\mathrm{cm}\}$	$<\max\{3\sigma, 5\,\mathrm{cm}\}$	–
$\lvert\Delta\phi\rvert$	–	–	$<0.1\,\mathrm{rad}$	$<0.1\,\mathrm{rad}$
$\chi^2_{\Delta\phi\Delta x}$	–	<10	<10	<9
$\chi^2_{\Delta x}$	–	–	–	<9
$\chi^2_{\Delta z}$	–	–	–	<9
$CMCLUS$	–	≤ 5	–	–
$E_{had}-\Sigma_p^{0.2}$	$<6GeV$	$<6GeV$	$<6GeV$	–

Table 2.4: *Soft muon requirements for Run I.*

- CMU type: the track must extrapolate to within the CMU boundaries, and not have been flagged of CMUP or CMP type.

- CMX type: the track must extrapolate to within the boundaries of the CMX chambers.

In order to match the tracks to muon stubs, some matching variables are defined: the point the track extrapolates to at the inner radius of the muon detector is used to compute distances between the stub and the track itself in the beam line direction (Δz) and in the transverse plane (Δx); a $\Delta\phi$ mismatch is also defined as the difference between the ϕ-direction of the extrapolated track and the stub slope. Moreover, from expected mismatch, χ^2 quantities are constructed for each matching variables; in particular, $\chi^2_{\Delta\phi\Delta x}$ is computed to take into account the correlation between Δx and $\Delta\phi$. Matching requirements are described in Tab. 2.4 for each class of candidate tracks.

The major source of background expected for muon tagging arises from secondary charged pion leakage through the outermost layer of the calorimeter (*punch-through*). This problem plagues especially the CMU. In order to keep it under control, an upper limit on the number CMCLUS of drift tubes involved in the CMU stub definition is applied.

Finally, since muons with $P_T \geq 6\ GeV/c$ are expected to deposit less energy in the calorimeter than hadrons, a loose minimum ionizing cut on $E_{had} - \Sigma_p^{0.2}$ is also applied for all non-CMX candidate tracks having transverse momentum above this value. E_{had} is the energy in the tower of CHA the track extrapolates to, while $\Sigma_p^{0.2}$ is defined as the sum of the momenta of all tracks reconstructed within a cone of radius $R = 0.2$ around the candidate track.

The soft muon tagging algorithm results to have an efficiency over 90% for muon in the fiducial region of the muon system, while the fake rate is less than 1% per track. The acceptance for soft muon detection is expected to be extended at CDF II experiment both for tracking and muon chambers upgrades. However, a Run II-based soft muon tagging algorithm has not been developed yet.

2.6 The Trigger and Data Acquisition System

The trigger plays an important role in hadron collider experiments because the collision rate is much higher than the rate at which data can be stored on tape. At CDF II, the predicted inelastic cross section for $p\bar{p}$ scattering is 56 mb, which, for a typical instantaneous luminosity of 10^{32} $cm^{-2}s^{-1}$, results in a collision rate of 5.6 MHz, while the tape writing speed is only of $\sim$ 50 events per second. The role of the trigger is to efficiently select the most interesting physics events from the large number of *minimum bias* events. Events selected by the trigger system are saved permanently on a mass storage and subsequently fully reconstructed offline.

Due to the accelerator and detector upgrades, the CDF trigger system had to be replaced for Run II. The primary reason for this replacing is the reduction in the accelerator bunch spacing from 3.5 μs to 132-396 ns. Moreover, the increased instantaneous luminosity regime needs more sophisticated trigger requirements to provide effective rate reduction, while maintaining high efficiency for the broad range of interesting physics processes the machine can access to. As a result, while in the past signals from the detector were processed and the trigger decision were sent back to the detector before the successive beam crossing, so that data from only one crossing needed to be stored on the detector, in the Run II scenario this will not be possible. In addition, most of the old triggers were incompatible with new or upgraded detector elements.

The CDF trigger system has a three level architecture with each level providing a rate reduction sufficient to allow a more sophisticated event processing in the next level with minimal deadtime. To allow time for transmission and processing of the detector signals to make the trigger decision, a Level 1 latency time of 5.5 μs has been chosen; each detector element has been provided of a local data buffering for the 42 event (at 132 ns separation) that are expected to occur during such a period. Events passing the Level 1 trigger requirements are then moved to one of four on-board Level 2 buffers. This is sufficient to allow a 40 kHz Level 1 accept rate with $\leq$ 10% deadtime for the successive 20 μs Level 2 processing time. Each separate Level 2 buffer is connected to a two-step pipeline, each step having a latency time of 10 μs: in step one, single detector signals are analyzed, while in step two the combination of the outcome of step one are merged and trigger decisions are made. The data acquisition system will allow the Level 2 trigger a $\sim$ 300 Hz accept rate. Events are then transferred to the Level 3 trigger processor farm where the they are reconstructed and filtered using the complete event data, with $\leq$ 50 event per second written to permanent storage. Fig. 2.20 summarizes the CDF three level pipelined and buffered trigger architecture.

According to the signal one wants to isolate, specific sets of requirements are established by exploiting the physics objects (*primitives*) available for each trigger level. Successively, links across different levels are established by defining *trigger paths*: a trigger path identifies a unique combination of a Level 1, a Level 2 and a Level 3 trigger; in other words, a trigger path establishes a logic AND between selection procedures at different levels. Datasets (or data streams) are then formed by merging the data samples collected via different trigger paths; hence, datasets

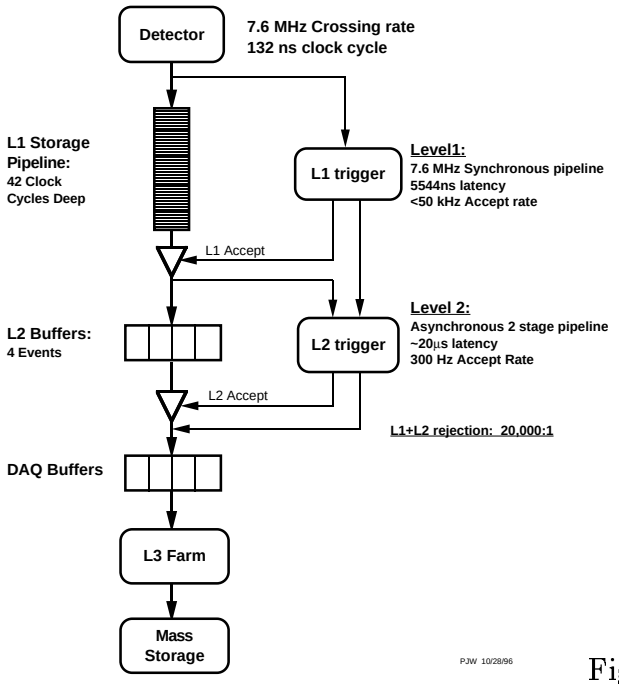

Figure 2.20: CDF *three level pipelined and buffered trigger architecture.*

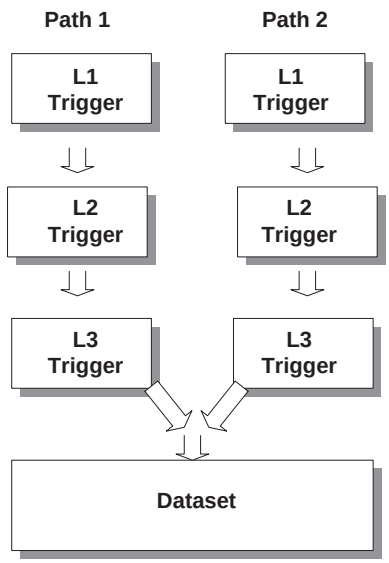

Figure 2.21: *Schematic diagram of trigger paths and datasets.*

are defined by a logic OR between trigger paths. A graphical representation of the CDF trigger layout is depicted in fig. 2.21.

In the following, CDF trigger primitives available for each of the three trigger levels will be shortly presented. A particular emphasis will be given to primitives having greater importance in our studies.

2.6.1 Level 1 Primitives

Tracks

Both Level 1 and Level 2 trigger systems (see Fig. 2.22) has been provided with detector information not available during Run I. The most significant improvement for Level 1 is the possibility of track finding by means of a new hardwired algorithm named e**X**tremely **F**ast **T**racker (XFT). It replaces the Central Fast Tracker (CFT), a similar device used during Run I for identifying high-momentum tracks in the CTC. These were then used in the Level 2 trigger. The XFT has been projected to work with COT signals at the high collision rate expected in Run II, returning track P_T and ϕ_0 by means of a fast r-ϕ reconstruction. These results are then sent to an extrapolation unit (XTRP), whose task consists in extrapolating XFT tracks to the central calorimeter wedges and to the muon chambers (CMU and CMX). This allows a track to be matched to an electromagnetic calorimeter cluster for better electron identification, a track to be matched to a stub on the muon detectors for improved muon reconstruction, and tracks to be used alone for specific trigger.

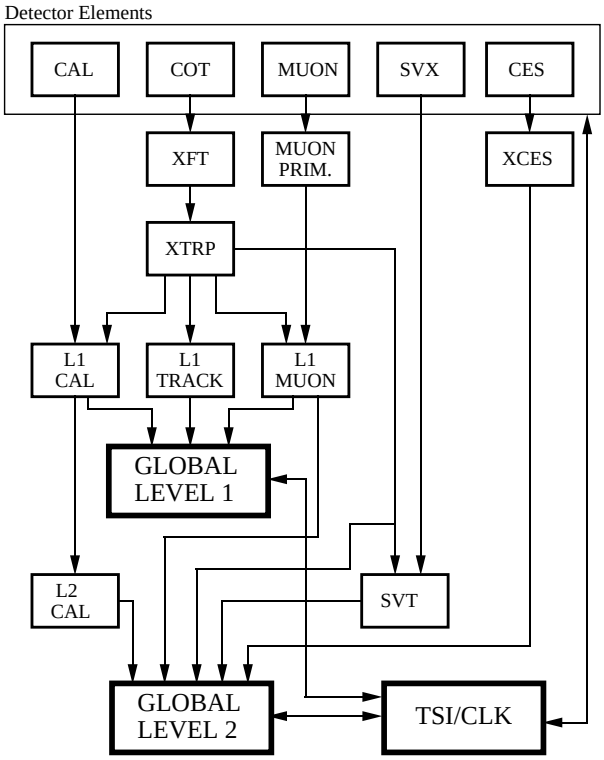

Figure 2.22: *The RunII trigger system block diagram.*

Calorimetric Primitives

At Level 1, calorimetric towers are merged in pairs along η to define *trigger towers*, which are the basis for two type of primitives:

- object primitives: electromagnetic and total transverse energy contribution are used to define electron/photon and jet primitives respectively;
- global primitives: transverse energy deposits in all trigger towers above 1 GeV are summed to compute event ΣE_T and $\not{E}_T$.

Correspondingly, object and global triggers can be defined by appling a threshold to the rispettive primitives. In turn, the object trigger can be divided in single-object triggers and di-object triggers according to the number of trigger towers above threshold needed to generate a Level 1 accept.

Leptons

Level 1 muon and electron triggers are obtained by matching a XFT track to a corresponding primitive: for electrons, primitives are essentially the calorimetric trigger towers described above, while for muons they are obtained from clusters of hits in the muon chambers.

2.6.2 Level 2 Primitives

Since jets are expected not to be fully contained into a single trigger tower, the energy threshold on Level 1 jet primitives must be set much lower than the typical jet energy in order to conseve high efficiency. As a consequence, jet trigger rate are too high to be fed directly into Level 3. An effective rate reduction can be obtained at Level 2 by triggering both on multiplicity and transverse energy of trigger tower clusters. The algorithm for cluster finding, essentially unchanged from Run I, is based on the four-step procedure described in Fig. 2.23:

- Electromagnetic and hadronic transverse energy of the trigger towers are checked to see if they are above predetermined *seed* and *shoulder* thresholds.
- All trigger towers whose energy has been found above the seed threshold are ordered according to increasing ϕ and η values.
- Cluster finding begins with the first seed tower. The four orthogonal nearest towers are considered: if their energy is above the shoulder threshold, they are merged to the cluster and their orthogonal neighbors are in turn considered.
- Tower merged in the cluster are disabled from being merged in another cluster. When no-other tower is found to add to the cluster, tower energy values are summed to define cluster ΣE_T and a new clustering procedure starts with the successive seed tower.

Different sets of thresholds can be used in according to the physics objects (typically electrons or jets) one want to trigger on. To define a jet cluster, seed and shoulder thresholds are set to 3.0 and 1.0 GeV respectively both for electromagnetic and hadronic tower.

Level 2 clusters can be used to built object triggers by appling a cut on their transverse energy and position (provided from η-ϕ adress of the seed towers), and global triggers by selecting on number and ΣE_T of clusters.

SVT tracks

The most significant addition to the Level 2 trigger system is the **S**ilicon **V**ertex **T**racker (SVT) [18] which, for the first time in a hadron collider experiment, exploits the potential of a high precision silicon vertex detector to trigger on tracks with large impact parameter. This can make accessible a large number of important processes involving decays of b-hadrons with a long lifetime. For example, SVT will allow to study CP-violation on B-decay channels that during Run I were undetectable (*e. g.* $B^0 \to \pi^+\pi^-$) [19]. Triggering on impact parameters offers remarkable improvements also to jet physics. For example, it can provide a $Z \to b\bar{b}$ signal, whose dijet mass peak can be used to measure resolution and mass-scale systematics on top-quark mass determination. Finally, hopes are that SVT can ability an high-efficiency collection of $HV \to b\bar{b}q\bar{q}^{(\prime)}$ events. We will discuss this extensively in Cap. 3.

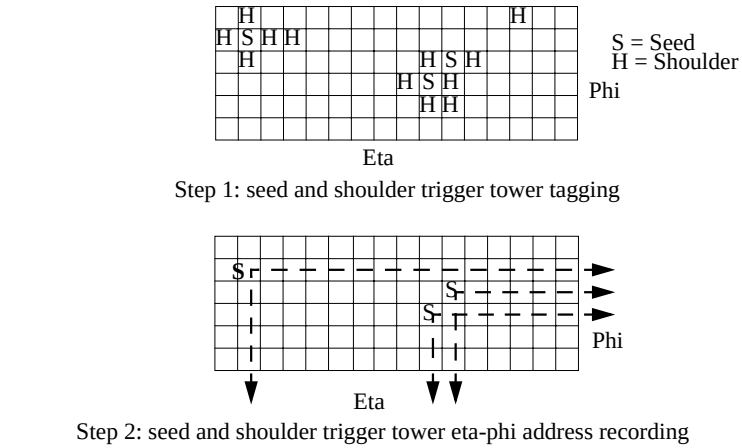

Figure 2.23: *Cluster finding procedure.*

The overall architecture of SVT is shown in Fig. 2.24. First, each of 72 SVX II sectors (12 ϕ-wedges $\times$ 6 semi-barrel) is read out by an *Hit Finder*, that perform a hit clustering on each layer contained in the sector. For each cluster found, the Hit Finder computes the centroid, representing the most probable intersection point between the trajectory of a particle and the layer that cluster belongs to. The outputs from the Hit Finders of each SVX II wedge are merged into one stream and fed both into an *Associative Memory* (AM) and an *Hit Buffer*, together with tracks from XFT. The task of the Associative Memory is to perform the first stage of the pattern recognition: cluster centroids from the Hit Finders are mapped in *superstrips*; then, all possible combinations of stacks of superstrips and XFT tracks are compared to a pre-established set of admissible combinations (*roads*), each corresponding to a set of four SVX II superstrips and an outer XFT track. Superstrips size results from a compromise between a small size which would provide a precise pattern recognition but require a large memory, and a large size that would output a lot of fake track candidates but require a small memory. The present choice is 300 μm. At the same time the clusters and XFT tracks are sent to the Associative Memory, they are also sent to the *Hit Buffer*, where they are stored by superstrip number. Successively, Hit Buffer board receives the road number of candidate tracks and finds the superstrips and the XFT track corresponding to each road. These sets of information, called *track packets*, are sent to the *Track Fitters*, where they are fitted by means of a linear approximated algorithm, consisting of a set of scalar products. For each track, P_T, ϕ_0 and d_0 are computed.

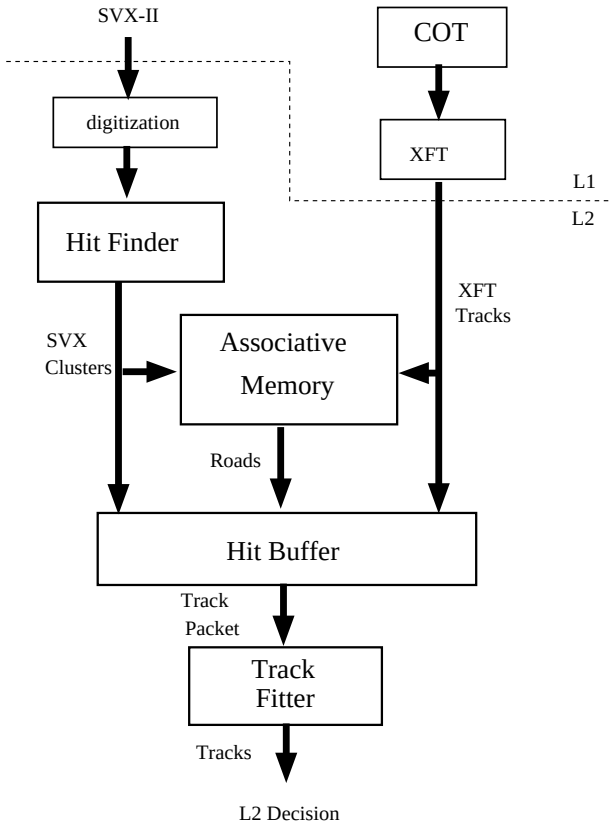

Figure 2.24: *The* SVT *architecture.*

Early simulations of SVT showed that for tracks with $P_T > 2\ GeV/c$ the resolutions were $\sigma_{d_0} \simeq 35\ \mu m$, $\sigma_\phi \simeq 1\ mrad$ and $\sigma_{P_T} \simeq 0.3\%$ (with $[P_T] = GeV/c$). Two problems can degrade SVT performance, the first concerns the mechanical alignment of SVX II, which has to be collinearly aligned with the beam line within 100 μm in order to keep into account that SVT does not have access to z information. Early analyses with the first data collected al CDF II seem to show a worse resolution on the impact parameter $\sigma_{d_0} \sim 50\ \mu m$. The other problem is the time required by SVT processing for high track multiplicity events, that could exceed the typical time

interval between two events at Level 2 ($\sim 20\ \mu s$) and introduce a high deadtime in trigger operations.

Leptons

Level 2 muon primitives are essentially unchanged with respect to Level 1, the only difference consisting in an improved ϕ-matching (within 1.25^o) between XFT tracks and stubs. In the case of electrons, a finer ϕ-matching can be instead performed at Level 2 thanks to the information from central and plug shower maximum detectors.

Level 3 Primitives

Events in input to Level 3 are loaded into a Linux PC farm, where they are almost fully reconstructed. In particular, jets, COT tracks and leptons are identified. The algorithms used for the reconstruction are the same used in offline analysis. Some variables, like global kinematic event observables, cannot be computed due to the long processing time required; Other tasks, like a full track reconstruction, could be possible only on subsets of data passing low-rate triggers.

If the event passes a Level 3 trigger, it is permanently stored to tape. An further offline processing is then performed on the selected events.

Bibliography

[1] F. Abe et al. (CDF Collaboration), *Evidence for Top Production in $p\bar{p}$ Collisions at $\sqrt{s}$ = 1.8 TeV*, Phys. Rev. Lett. **73**, 225 (1994).

[2] F. Abe et al. (CDF Collaboration), *Evidence for Top Quark Production in $p\bar{b}$ Collisions at $\sqrt{s}$ = 1.8 TeV*, Phys. Rev. **D50**, 2966 (1994).

[3] F. Abe et al. (CDF Collaboration), *Kinematic evidence for top quark pair production in W+multijet events in $p\bar{p}$ collisions at $\sqrt{s}$ = 1.8 TeV*, Phys. Rev. **D51**, 4623 (1995).

[4] M. Paulini , *B Lifetimes, Mixing and CP Violation at CDF*, Int. J. Mod. Phys. **A14**, 2791 (1999).

[5] F. Abe et al. (CDF II Collaboration), *The CDF II Detector Technical Design Report*, FERMILAB-PUB-96-390-E, Oct 1996.

[6] H. Wenzel, *Tracking in the SVX*, CDF internal note 1790, May 1998.

[7] S. Dell'Agnello et al., *A Primary Vertex Finding Package*, CDF internal note 1789, Jul 1992.

[8] The CDF Collaboration, *A Time of Flight System for CDF*, CDF internal note 2573, Feb 1994.

[9] F.Abe et al., *Phys. Rev.*, **D45**, 5(1992) 1449.

[10] T. Affolder et al. (CDF Collaboration), *Measurement of the Top Quark Mass with the Collider Detector at Fermilab*, HEP-EX/0006028, Jun 2000.

[11] D. Glenzinsky et al., *A detailed study of the SECVTX algorithm*, CDF internal note 2925, Dec 1994.

[12] C. Cmiao et al., *Update of SECVTX tagging on Run 1B data*, CDF internal note 3178, Jun 1995.

[13] M. Paulini, emphB Lifetimes, Mixing and CP Violation at CDF, Int. J. Mod. Phys. **A14**, 2791 (1999).

[14] F. Abe et al., *Phys. Rev.*, D50(1994) 2966.

[15] C. Campagnari et al., *Review of the SLT Algorithm for Run Ib*, CDF internal note 3682, May 1996.

[16] C. Campagnari et al., *The SLT tags and backgrounds for 110pb*$^{-1}$, CDF internal note 3582, May 1996.

[17] G. Apollinari et al., *Measurement of the* $t\bar{t}$ *production cross section using SLT tags*, CDF internal note 3861, Nov 1996.

[18] S. Belforte et al., *SVT – Silicon Vertex Tracker – Technical Design Report*, CDF internal note 3108, Oct 1996.

[19] S. Donati et al., $B^0 \to \pi\pi$ *Trigger Studies with Run Ia Data*, CDF internal note 3167, Jun 1995.

Chapter 3

A Multijet Trigger for Higgs Associated Production

The search for the Higgs boson is one of the main purposes of the CDF II *experiment: as pointed out in Sec. 1.4, a* 3σ *Higgs evidence is at reach for* $M_{\mathrm{H}} \lesssim 130\ GeV/c^2$ *for an integrated (*CDF *and* D0*) luminosity of the order of* $10\ fb^{-1}$*. Despite the very high background rates, hope are that the all-hadronic final state of associated* VH *production (where* V *denotes a vector boson) could contribute to the setting of mass limits or to the significance of a signal; in fact, the limits set by the analysis of these events in Run I has surprisingly proven to be competitive to those obtained with the leptonic channels (see Sec. 1.4).*

In this chapter, we study a specific set of trigger requirements to select associated VH *production events in all-hadronic final states. Besides calorimetric quantities, we exploit the presence of heavy flavoured hadrons with large lifetime in b-jets from Higgs decays. In particular, we discuss the use of the new Silicon Vertex Tracker for a Level 2 selection based on high impact parameter tracks.*

3.1 Introduction

The CDF I experiment developed a trigger for multijet final states [1], consisting of the following requirements:

- LEVEL 1: single trigger tower with transverse energy $E_T \geq 20\ GeV$;
- LEVEL 2: at least four hadronic clusters with $E_T^{cl.} \geq 15\ GeV$ and $\sum E_T^{cl.} \geq 125\ GeV$;
- LEVEL 3: at least four jets (reconstructed with cone radius $R = 0.4$) with with $E_T^{jet} \geq 15\ GeV$ and $\sum E_T^{jet} \geq 125\ GeV$.

This selection was designed to study the all hadronic decays of the $t\bar{t}$ production, that are expected to lead to final states with six jets. Efficiency on these events was about 90%, while the limited trigger cross section ($\sim 5\ nb$) guaranteed a low event

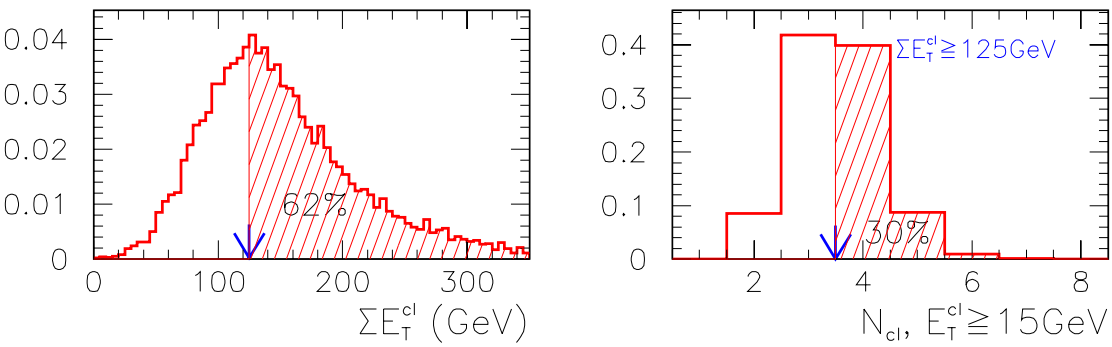

Figure 3.1: *Run I multijet trigger efficiency for Level 2 calorimetric requirements on* $\mathrm{HV} \to \mathrm{b\bar{b}q\bar{q}}^{(\prime)}$ *($M_{\mathrm{H}} = 120 GeV/c^2$) sample. The distribution of the number of clusters is shown after the requirement on* $\sum E_T^{cl}$.

rate. Finally, the sample collected during Run I allowed eventually the top quark observation in this final state [2].

A subsequent search for the Standard Model Higgs boson was also performed [3], but the multijet trigger requirements resulted to be unsuitable for the Higgs associated production detection: the only Level 2 selection, for example, was found to lose $\sim 70\%$ of the events (see Fig. 3.1).

In the following sections, we describe some studies for a new multijet trigger, aimed at selecting $VH \to q\bar{q}^{(\prime)}b\bar{b}$ events for improved Higgs boson search during the Run II data taking. The guideline of these studies is to loose the calorimetric requirements in order to recover efficiency, while keeping under control the trigger rate by exploiting the presence of heavy quarks in the final states. Two strategies can then be followed. The first one is aimed at searching for electrons or muons originated in the semileptonic decays of b or c quarks. A trigger path based on this idea has been recently proposed [4]. The second strategy exploits the decay of long lifetime particles produced in heavy quark hadronization, where tracks with large impact parameters are produced; in particular, the new Silicon Vertex Tracker (SVT) (see Subsec. 2.6.2) allows to study this trigger requirement already at Level 2. In this chapter, we investigate the feasibility of such a strategy. Calorimetric requirements will be maintained the same as in [4], in order to allow a future integration of the two triggers.

3.2 Level 1

Trigger rates are usually dominated by background events, and need to be estimated on real data. Samples of Run I data collected with loose triggers are used to study the effect of more selective criteria. The extrapolation to the Run II CDF detector was then performed with a parametrization of the increased acceptance, as discussed in [8], and rescaling to the expected luminosity and higher Tevatron energy. In

the following, all the quoted rates will be referred at an instantaneous luminosity $\mathcal{L} = 10^{-32} cm^{-2} s^{-1}$. To compute trigger efficiency, we use the trigger simulation on a sample of about $10,000$ $p\bar{p} \rightarrow VHX \rightarrow q\bar{q}^{(\prime)} b\bar{b} X$ processes generated at a center of mass energy $\sqrt{s} = 2\ TeV$ with the PYTHIA 6.129 [1] Monte Carlo. The CTEQ3M parametrization of the structure functions has been used and a full simulation of the CDF detector has been applied to the generated events.

The Level 1 calorimetric primitive has been taken from the QCD inclusive jet path, which requires a single trigger tower with transverse energy above a certain threshold. Two threshold values are so far available (5 and 10 GeV [7]), but only the highest one is interesting for this study. This is because loose requirements, leading to higher rates, can be incompatible with the allowed trigger bandwidths, in which case the acceptance rate is artificially limited by means of a prescaler. The same rejection, however, affects signal efficiency, which makes prescaled trigger paths particularly inconvenient for rare processes.

The requirement of a single trigger tower with $E_T \geq 10\ GeV$, on the other hand, results to be almost fully efficient ($\gtrsim 98\%$) on signal events. The rate has been estimed to be about 2.7 Hz [7] on a sample of events collected during Run I with a *minimum bias* trigger, that requires a coincidence between two beam-beam counters located in opposite sides of the detector (see Sec. 2.1.6).

3.3 Level 2

3.3.1 Calorimetry Requirements

Rate estimates for Level 2 calorimetric requirements are based on a Run I data sample selected by the JET20 trigger path, whose only physical requirements was a single Level 2 cluster with $E_T \geq 20\ GeV$, while applying a simple event prescale at Level 1 and Level 3. The efficiencies have been computed on the simulated VH sample we described in the last section.

The initial modification towards an Higgs-optimized multijet trigger has been motivated by topological considerations on the signal: $HV \rightarrow$ *had* events are expected[1] to produce four jets in the final state; taking into account the eventuality of losing one jet or merging two of them, the possibility of requiring only three clusters at Level 2 has been considered, which, according to fig. 3.1 (right plot), would guarantee a significant efficiency increase.

At this point, two parameters still need to be fixed: the threshold on E_T of the required clusters and the one on the sum of the transverse energy of all the hadronic clusters with energy content above a certain threshold. In the following, only two cases are considered:

- $\diamond$ $\Sigma E_T 3 \equiv \Sigma E_T^{cl}$ where $E_T^{cl} \geqslant 3 GeV$;
- $\diamond$ $\Sigma E_T 10 \equiv \Sigma E_T^{cl}$ where $E_T^{cl} \geqslant 10 GeV$.

[1]Disregarding initial and final state radiation processes at this time.

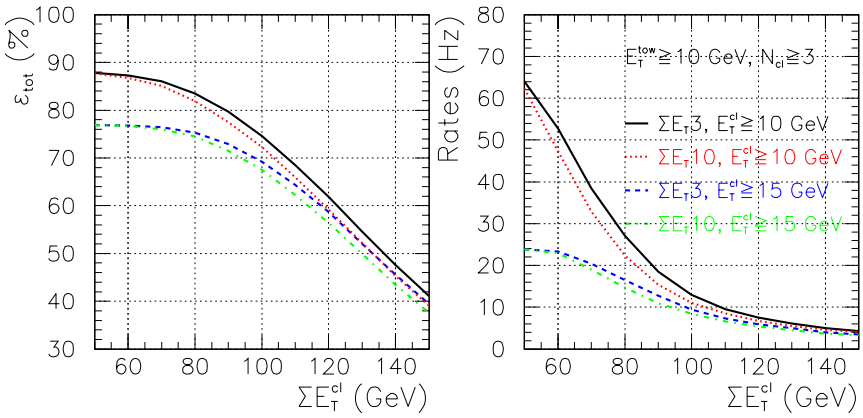

Figure 3.2: *Level 2 efficiencies (left) and rates (right) for different calorimetric requirements as functions of the corresponding* ΣE_T^{cl} *primitives. Efficiencies and rates are computed on* $\mathrm{HV} \to \mathrm{b\overline{b}q\overline{q}}^{(\prime)}$ *(*$M_{\mathrm{H}} = 120 GeV/c^2$*) and* JET20 *respectively.*

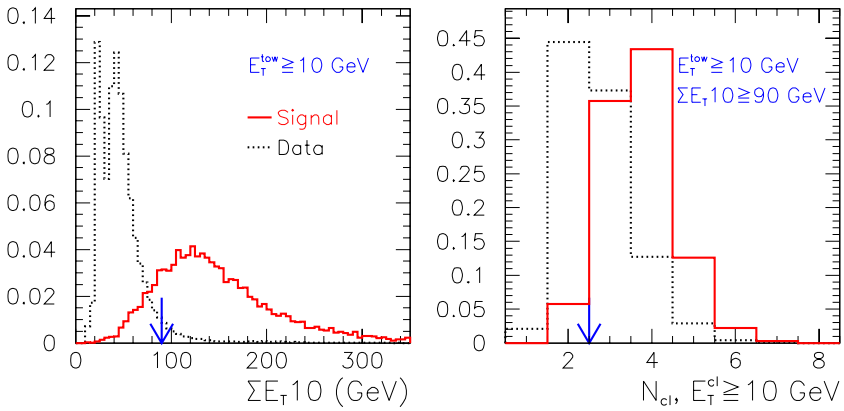

Figure 3.3: $\Sigma E_T 10$ *(left) and number of clusters with* $E_T^{cl} \geqslant 10 GeV$ *(right) distributions as functions of* $\Sigma E_T 10$ *for* $\mathrm{HV} \to \mathrm{b\overline{b}q\overline{q}}^{(\prime)}$ *(*$M_{\mathrm{H}} = 120 GeV/c^2$*) signal and* JET20 *background.*

The $E_T^{cl} \geq 3$ requirement is just above the threshold for the cluster definition, while $E_T^{cl} \geq 10$ is the threshold that will be used successively to define a jet.

In order to take into account the natural correlation between the ΣE_T^{cl} and the number of clusters, the behaviour of different combinations of ΣE_T^{cl} primitives and cluster E_T thresholds has been studied; the results are shown in fig. 3.2.
The choice of the optimal Level 2 primitive is performed on the basis of efficiency maximization. A rate level of ~ 15 Hz is compatible with the total Level 2 bandwidth, accounting to 300 Hz(see Sec. 2.6); therefore the requirements:

$$\Sigma E_T 10 \geqslant 90 GeV, \; N_{cl}(E_T^{cl} \geqslant 10 GeV) \geqslant 3,$$

corresponding to an efficiency of $(77.6 \pm 0.5)\%$ and a rate of (15.4 ± 0.8) Hz, will be applied at Level 2 (errors are statistical only).

A graphical representation of the Level 2 calorimetric selection is shown in fig. 3.3,

where the distributions of the calorimetric quantities at Level 2 for signal and data are compared.

3.3.2 Study of SVT Performance

SVT has been designed and optimized as a B-physics-specific tool[8], and its tracking capability has been demonstrated only for the low-P_T b-production events most interesting for B physics. However, hopes are that its output can also be effectively used for the collection of events suitable for Higgs searches and other processes yielding final states with large track multiplicity and high-P_T b-jets.

In principle, the extreme versatility of SVT may allow the simultaneous use of several sets of the non-hardware-specific optimization parameters: wild-card hits can be input to SVT to allow the selection on the fly –for instance, depending on which Level 1 trigger the event has fired– of different sets of patterns, χ^2 cuts, and other settings. However, these powerful characteristics have not been studied in detail to date to our knowledge.

When discussing the possibility of using the SVT output for the selection of a high-P_T process such as associated VH production (where V denotes a W or Z boson), one needs to first ascertain that these events are indeed reconstructable by SVT, given the current settings of the device, the available information, and the decision time at trigger level 2.

After a brief description of the datasets and the SVT simulation used for our studies, we investigate how to use at best the SVT output at level 2 to select multijet events due to VH production and reduce the huge QCD background. Successively, we discuss how those results vary as a function of the χ^2 cut on the fitted tracks, and how they depend on the amount of noise in input to SVT from the silicon microstrips. Finally, we discuss a simple timing model for SVT operation, which yields an estimate of the processing time needed for the reconstruction of these busy events.

The Datasets

SVT is a new device specifically designed for the Run II data taking. Since Run I data are not supplied with track information analogous to that provided by SVT, the method we previously used for estimate event rates after calorimetric requirements can be no longer employed. Therefore, we perform our studies on samples simulated with the Run II offline software. VH events have been generated through the PYTHIA V6.129 Monte Carlo. The Higgs boson mass was set at 120 GeV/c^2, and the creation of a multijet final state was induced by forcing hadronic decays of the W and Z bosons, and $b\bar{b}$ decays of the Higgs particle. A full simulation of the CDF II detector has been then applied to the generated events. Four samples of about $2,000$ events were generated to scan four different values of the fraction of noisy strips in the silicon detector[2]: 0.0%, 0.5%, 1.0% and 2.0% (see Sec. 3.3.2).

[2]Random noise is added to the silicon strips of the SVX detector such that a fraction of these yields a signal above the ADC threshold. Of course, this random addition of charge also affects

In order to study the background behaviour, some samples of QCD $2 \rightarrow 2$ processes were generated using the PYTHIA V6.129 Monte Carlo and successively reconstructed by means of a full CDF II detector simulation. Four samples were selected with Level 1 requirements (see Sec. 3.2) for timing studies ($\sim$ 5000 events with noise level set to 0.5% and $\sim$ 1000 events with noise level set to 0.0%, 1.0% and 2.0% respectively), while other four samples were filtered with Level 2 calorimetric requirements to test the SVT performance in background rejection ($\sim$ 700 events with noise level set to 0.5% and $\sim$ 300 events with noise level set to 0.0%, 1.0% and 2.0% respectively).

The SVT Simulation

To simulate the action of SVT on these events we use a stand-alone simulation named SVTSIM. This package, that contains a detailed description of the SVT hardware, was written and used to verify the performances of the system. We use it in the so-called "4/4" Associative Memory (AM) mode, where at least one hit is required in each of four silicon layers in order to reconstruct a track in a given SVX II sector[3]. The four input layers can be chosen among the five SVX II layers plus LAYER00 (see Sec. 2.3). For our studies we use the standard choice of the four inner layers of SVX II as input planes; we therefore did not investigate the improvements in impact parameter resolution which may be possible by substituting one of those layers with the LAYER00, or, conversely, the probable reduction of fake tracks when using layer 4 as a substitute of one of the inner layers[4]. These improvements may be the subject of a future study. Other details of the chosen configuration involve the superstrip size, which has been set to $300\mu m$, and the number of patterns stored in each memory bank, set to 32,768. The default value of the cut on the fit χ^2 has been set at 12.6, but this latter figure has been later varied to study its effect on our datasets.

Preselection of good SVT tracks

Reconstructed tracks passing the χ^2 cut and with a P_T greater than 2.0 GeV/c are the output of SVT: for each track, impact parameter (d), curvature (c), and azimuthal angle at the origin (ϕ_0) are available to the Level 2 processors. However, knowledge of the functioning of the extremely fast tracker (XFT) processor (see Subsec. 2.6.1) may allow a cleanup of this set of data, as is explained below.

XFT yields to the SVT hit finders and mergers two numbers per track: the curvature and the azimuthal position at the radius of the third axial COT superlayer (SL6). Although the latter is measured with a precision of 0.156 degrees, no more than one track is considered through each of 288 azimuthal slices, each 1.25 degrees

the reconstructed position of the centroid of clusters due to real particles.

[3]We use a terminology where a SVX II sector identifies a half-barrel and 30 degrees in azimuth: there is thus a total of 72 such sectors (see Sec. 2.3 and 2.6.2).

[4]It appears that L4 strips are on average much less noisy than the L3 ones. Of course, layer 4 is also expected to have a lower occupancy than the inner layers.

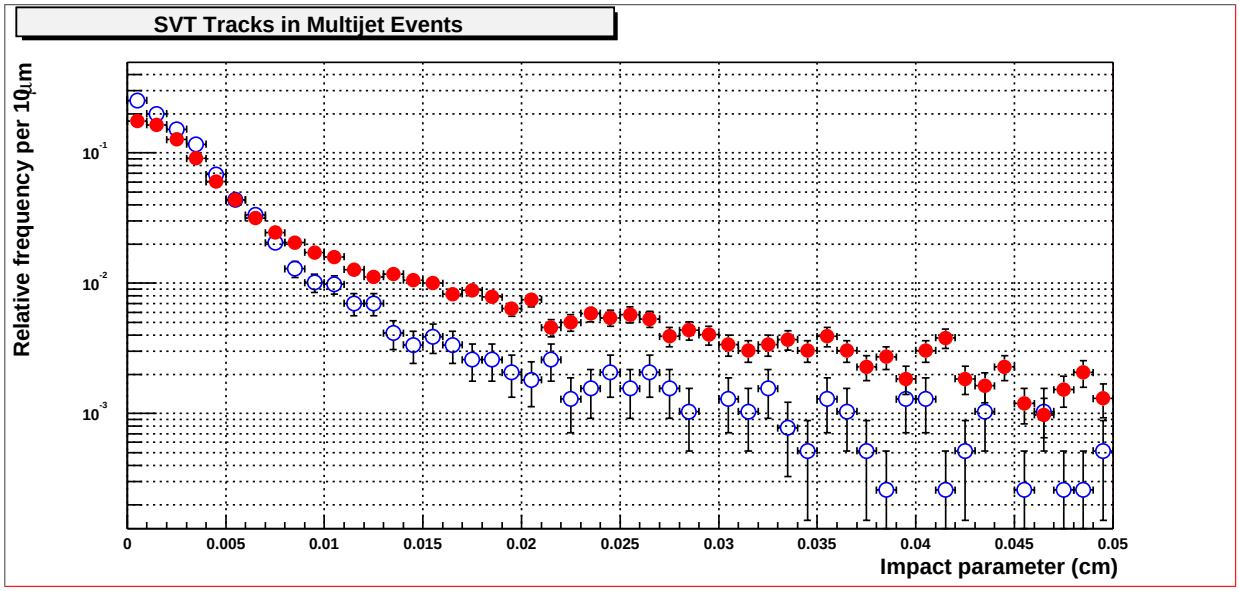

Figure 3.4: *Impact parameter distribution of good* SVT *tracks in multijet events, for the default simulation (*0.5% *of noisy silicon strips,* χ^2 *cut set at 12.6). In dark (open circles) tracks in* QCD *events; in red (full circles) tracks in HV events.*

wide. This information can be used with success in combination with the SVT output, particularly in the case of a very crowded and/or noisy environment: SVT has in fact the freedom to use the same XFT seed to find any track compatible with the hits found in the corresponding 30° sector (with the sole constraint that all hits belong to the same half-barrel), due to the lack of longitudinal information from XFT. Of course, if occupancy is high, a lot of fake tracks can be generated from the same XFT seed; it could become mandatory to discard these fakes. This can be accomplished by performing a simple linear extrapolation of SVT coordinates to the radius of SL6: if ϕ_0 and c are angle and curvature measured in the SVT for each track, we can require that no more than one track possesses the same value[5] of

$$\phi_{extr} \sim \phi_0 + 105.575 * c, \tag{3.1}$$

or, more precisely, the same value of

$$int((\phi_{extr} - 0.625^\circ)/1.25^\circ). \tag{3.2}$$

Such linear extrapolations are not needed by the Level 2 processors, since the SVT output does include, for each track, the XFT azimuthal measurement received in input[9], which automatically defines track multiplets; we have however verified that the two methods are equivalent.

We obviously need a sound prescription to choose the right track among all the identified candidates fitted using the same XFT seed, if we wish to avoid paying the

[5] 105.575 is the radius of the center of SL6 in cm, and we adopt a convention according to which curvature is the inverse of the track helix diameter, measured in cm^{-1}.

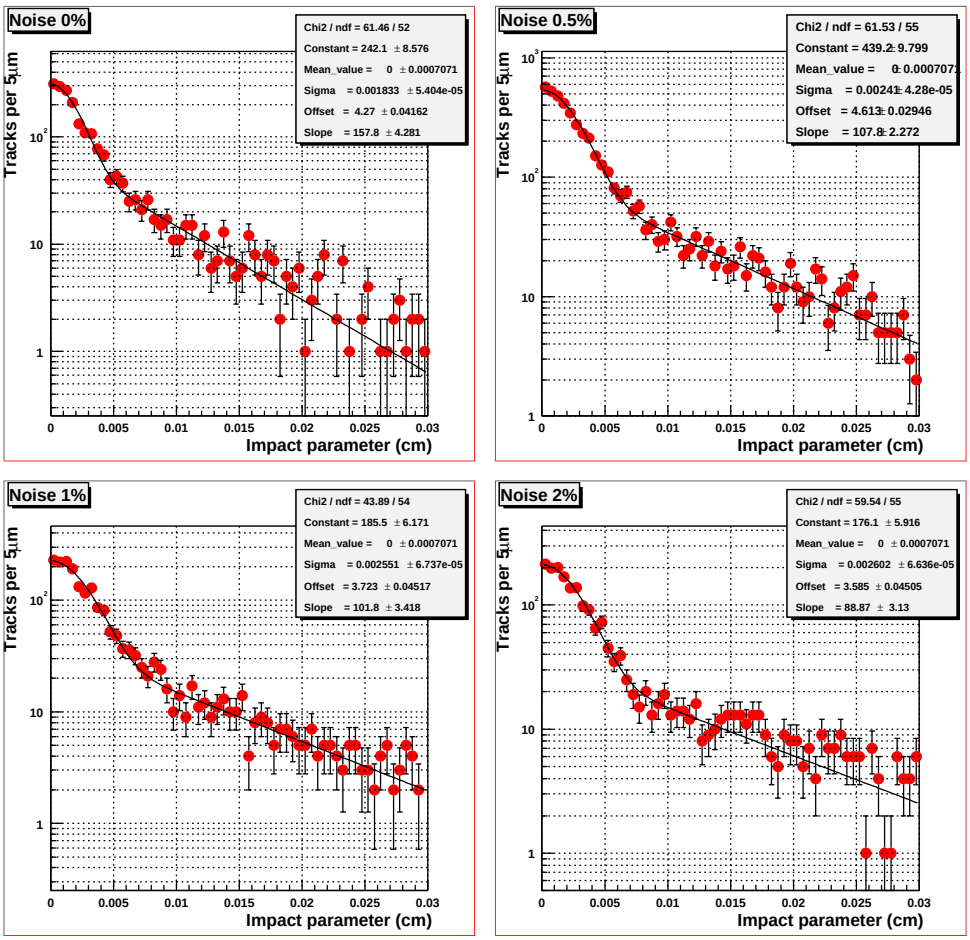

Figure 3.5: *Impact parameter distributions of* SVT *tracks in* QCD *events, for the default* χ^2 *cut and four different noise levels in the silicon microstrips; the rejection of multiple tracks from the same* XFT *seed described in Sec. 3.3.2 is not applied, and no beam spot smearing is operated. Notice the worsening of prompt track IP resolution as the noise level increases. A summary of the impact parameter resolutions fitted from these curves is presented in Fig. 3.17.*

price of discarding all of them. Our choice is to pick the track with smallest impact parameter: given that fake tracks have a very broad impact parameter distribution (Figs. 3.5, 3.7), this choice should select the correct track in most cases, while preserving the discriminating power of those other (single) tracks which are genuinely displaced from the primary vertex.

A comparison of the impact parameter distribution of tracks rescued from a multiplet by the above prescription with the I.P. distribution of the discarded tracks is shown in Fig. 3.6: indeed, tracks rescued from a multiplet and single tracks exhibit the very same distribution of impact parameter, confirming the soundness of our prescription. Further, Fig. 3.7 shows that the removal does make a huge difference in the effectiveness of IP-based selections; this can be also verified by comparing Fig. 3.11 to Fig. 3.12 (see Subsec. 3.3.2).

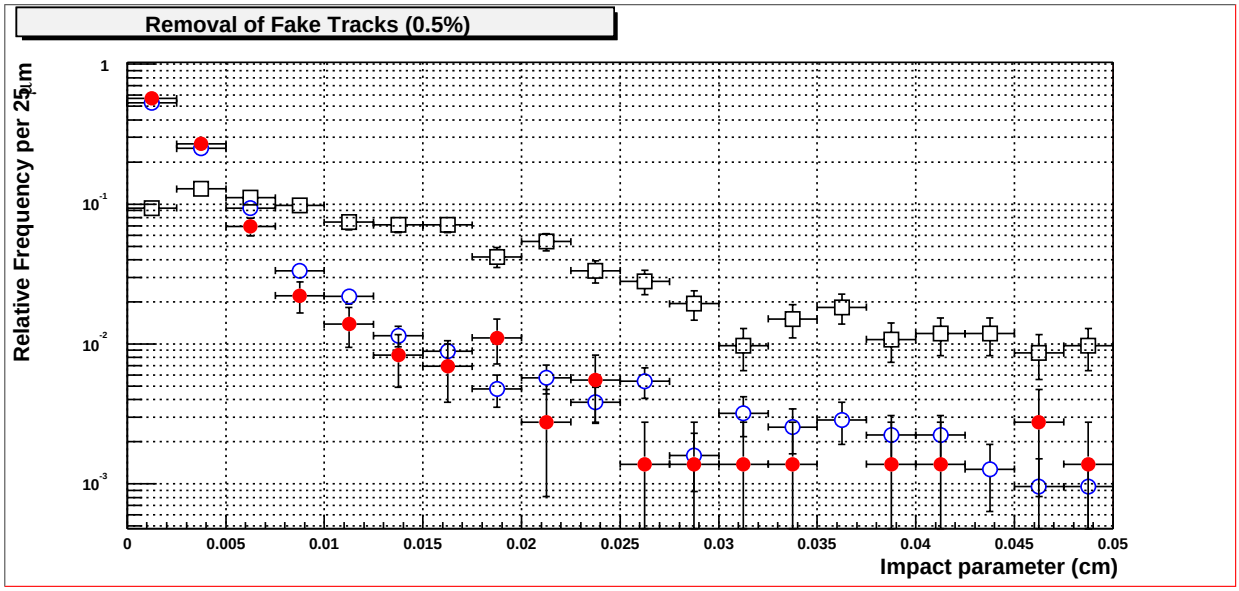

Figure 3.6: *Impact parameter distributions of* SVT *tracks belonging to three different categories: tracks univocally associated to an* XFT *seed (open dark circles), tracks belonging to a multiplet associated to the same seed that have been selected as the right one by the prescription discussed in Sec. 3.3.2 (full red circles), and tracks belonging to a multiplet that have been discarded by the prescription (open black squares). For this plot,* QCD *events and a 2% noise level (see Sec. 3.3.2) have been used; the* χ^2 *cut was set at its default value; a finite beam spot was simulated as discussed in the text.*

Currently, a custom board (*Ghostbuster board*) is being designed to select the *right* track in a multiplet without making explicit use of the track's impact parameter.

Other technicalities

In order to study resolutions, no beam-spot spread in the transverse plane is applied at generation level: all prompt tracks do come from the origin of coordinates, while a 29 *cm* z-spread is included in the detector simulation. For the study of IP-based selections, however, we do need to take into account the effect of a finite beam spot size. This is taken care of by a simple random extraction of a gaussian-distributed radial deviation r_v, of $30\mu m$ width, and an azimuthal angle ϕ_v, once per event. The effect on track impact parameters is then included by linearly adding to the measured value d the quantity

$$d_v = r_v sin(\phi_t - \phi_v). \tag{3.3}$$

The effect of this smearing is shown in Fig. 3.8. As expected, almost no variation is observed in the tails of the distribution, which are the regions we wish to study.

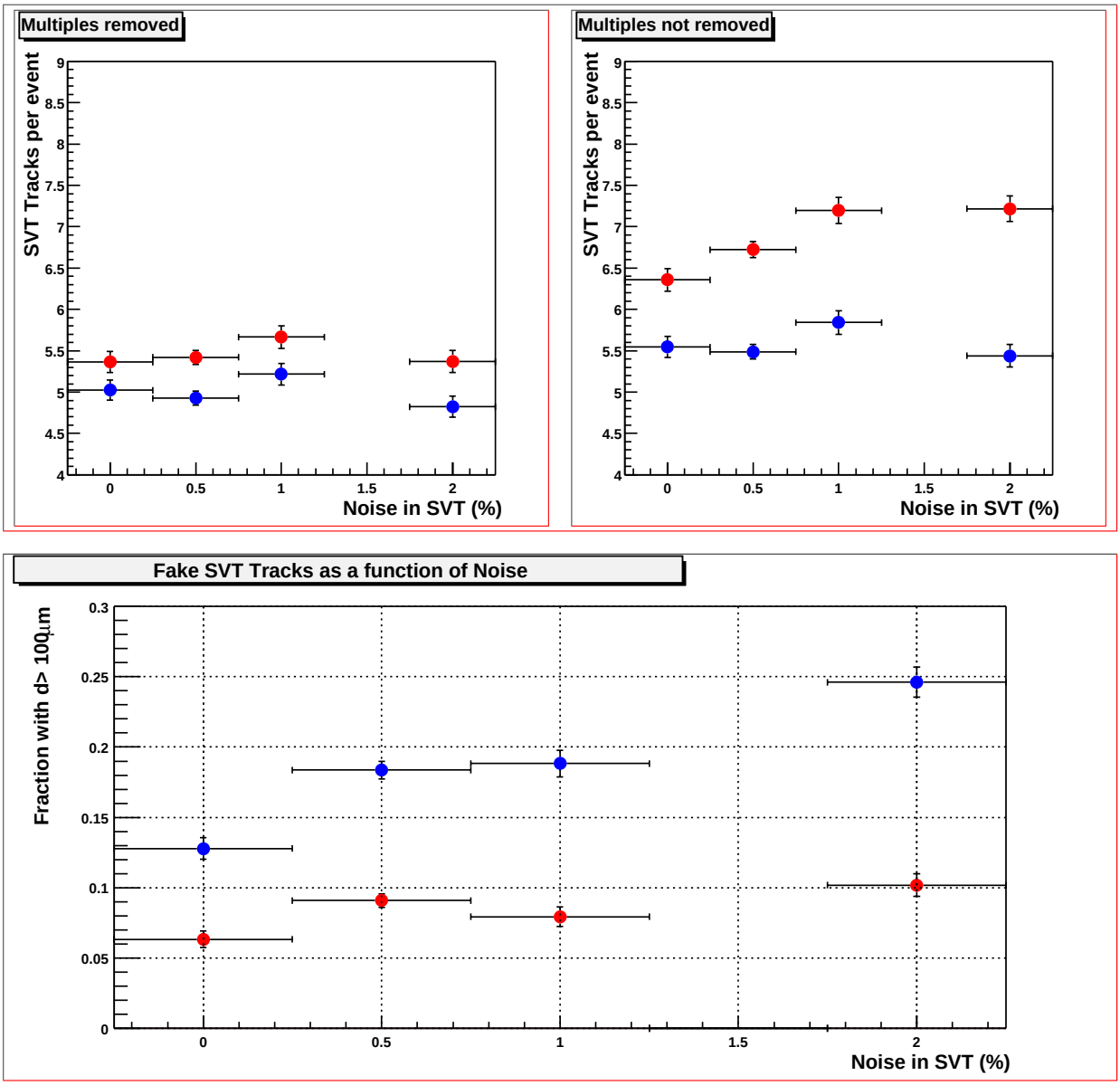

Figure 3.7: *Average number of* SVT *tracks as a function of SVX noise with and without multiple track removal. Top left: average number of tracks (red) and tracks with* $|d| < 100\mu m$ *(dark) when the prescription for the removal of multiple tracks is applied. Top right: same when no removal is operated. Bottom: comparison of the fraction of displaced tracks* ($|d| > 100\mu m$) *as a function of noise before (black) and after (magenta) the removal.*

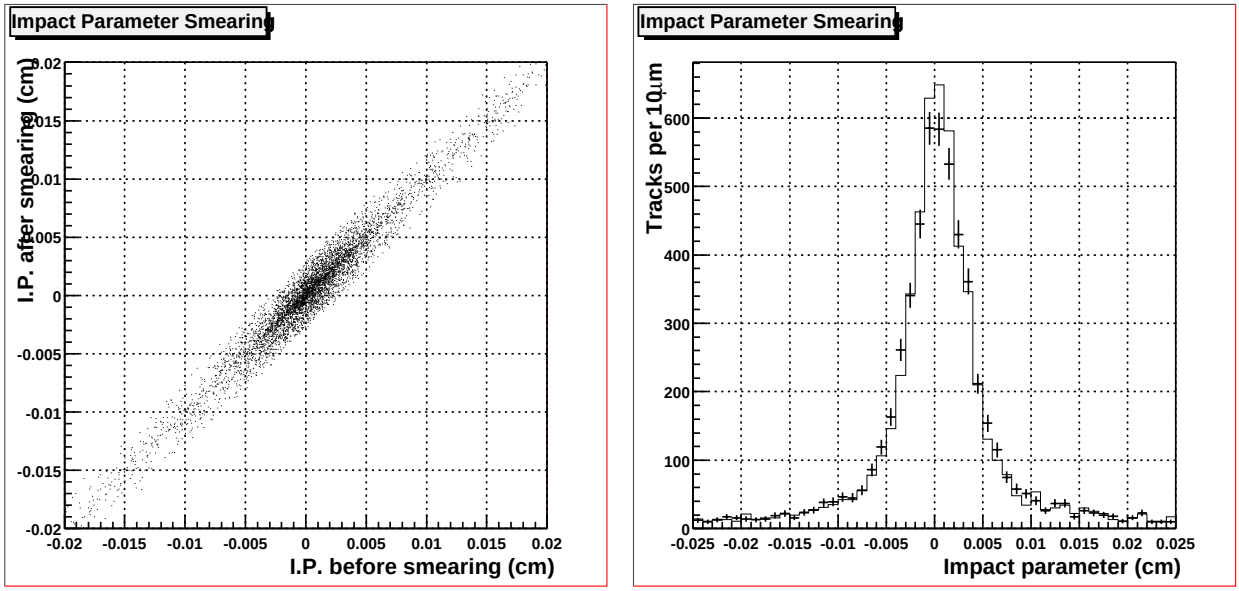

Figure 3.8: *Effect of the simulation of a finite beam spot size on track impact parameters. Left: impact parameter of tracks before vs after the smearing; right: the same quantities are overlayed. For this plot,* QCD *events and the default values of noise and* χ^2 *cut have been used.*

Optimization of Level 2 Requirements

We wish to determine how much use can be made of the tracking information provided by SVT at Level 2 for the discrimination of $VH \to q\bar{q}^{(\prime)}b\bar{b}$ events from generic 4-jet events produced by QCD processes after calorimetric requirements. The latter are dominated by light quark and gluon jets, and produce tracks that originate from the primary interaction vertex. Their discrimination should therefore be easy in principle, by just requiring that events contain some tracks with significant impact parameter. However, as we have already noted, the SVT has not been proven effective on the very complicated, high-multiplicity and high-P_T tracks that originate from a 4-jet interaction. Its effectiveness must in fact be demonstrated by comparing impact parameter spectra of signal and background events. We expect that the impact parameter distribution in background events will be dominated by prompt tracks peaking at zero, with a small, wide tail due to mismeasured tracks and fake tracks resulting from a random combination of noise hits; real tracks due to early decay of K_s^0 particles will also be contributing to this tail.

All these effects are of course also present in signal events, but how much signal and background distributions differ, and just how many displaced tracks the signal yields (once acceptance, XFT efficiency, and $P_T > 2\ GeV/c$ cut are taken into account), is what we set out to study.

The aim of this study is to find the SVT requirements that can lower the rate after calorimetric requirements have been applied, maintaining the efficiency as high as possible. A maximum bandwidth of 1.5 Hz at $\mathcal{L} = 10^{32} cm^{-2} s^{-1}$ is available for this trigger path.

We have already shown in Fig. 3.4 the impact parameter distribution of all tracks with $P_T > 2\ GeV$ reconstructed by SVT and passing the default cut ($\chi^2 < 12.6$) on the fit χ^2 obtained by the simulated track fitter boards, for QCD and HV events. The distributions are indeed different, reflecting the long lifetime of b-quarks from H decay. Ordering these tracks event-by-event by their impact parameter allows to plot the largest and second-largest IP in the event in Fig. 3.9.

We may perform a simple cut-optimization study on the basis of these and similar other histograms. Defining the signal efficiency $\epsilon_s(x)$ as the number of events where the largest-IP track has $|d|_{max} > x$, and accordingly for the background acceptance $\epsilon_b(x)$, we may compute the shape of the *quality factor*

$$Q(x) = \epsilon_s^2(x)/\epsilon_b(x) \tag{3.4}$$

(Fig. 3.10). A simple selection requiring $|d|_{max} > 120\ \mu m$ appears to increase this figure of merit by about 80%, while reducing the background rate by a factor of four. However, if we want to reduce the rate at about 1.0-1.5 Hz, we have to require $|d|_{max} > 350$-$500\ \mu m$, with an efficiency of about 35-23% respectively.

In the case of a selection based on the second-largest track IP, d_{2nd}, a cut at around 100-150 μm maximizes Q and reduces the rate to the wanted values, with an efficiency of about 50-38% (Fig. 3.11). This variable appears the most promising for a selection of good events in the sample, since it not only provides the best background reduction, but it also selects events that will very likely allow the reconstruction of

one or two displaced secondary vertices, since they possess two very good seed tracks (see Sec. 2.4.3). Fig. 3.12 points out the importance of the multiple SVT tracks removal for this selection: without removal, we find a worsening in the efficiency of about 5-10% at the same rate level.

The high multiplicity of multijet events suggests an examination of the impact parameter of the third track as well. The quality factor Q reaches in that case values close to the ones seen above, but with a lower efficiency (Fig. 3.13).

Another idea might be that of computing per each event the sum of all impact parameters of those $P_T > 2\ GeV/c$ tracks which have $|d| > 50\ \mu m$, *id est* tracks that appear only marginally consistent (more than 1σ away) with the hypothesis of coming from the primary event vertex (see Fig. 3.14). Such a selection appears less promising than the ones described above, and less straightforward to implement within the strict processing times allotted to the Level 2 processors.

Finally, we examine in Fig. 3.15 the outcome of a hypothetical seletion based on the quadrature sum $N = \sqrt{\sum_i {s_i}^2}$ of impact parameter significance of all SVT tracks in the event, where $s = |d|/0.0025$ is just defined as the impact parameter measured in 25 μm units, with the prescription that $s = 10$ if $|d| \geq 250\ \mu m$. Surprisingly, this approach does not yield better results than the ordinary selection based on $|d_{2^{nd}}|$: a cut $N > 12$ gives a rate of $\sim 1\ Hz$ for a $\sim 40\%$ signal efficiency. These latter exotic approaches may be worth another look only if a significant degradation in impact parameter resolution occurs during data-taking, or in case of other significant changes.

Finally, a requirement of two SVT tracks with impact parameter $|d| \geq 100\ \mu m$ turns out to be the most effectively choice for a Level 2 trigger. Event rate results to be reduced to $(1.7 \pm 0.2)\ Hz$, while signal efficiency after calorimetric requirements is kept at $(50 \pm 2)\%$.

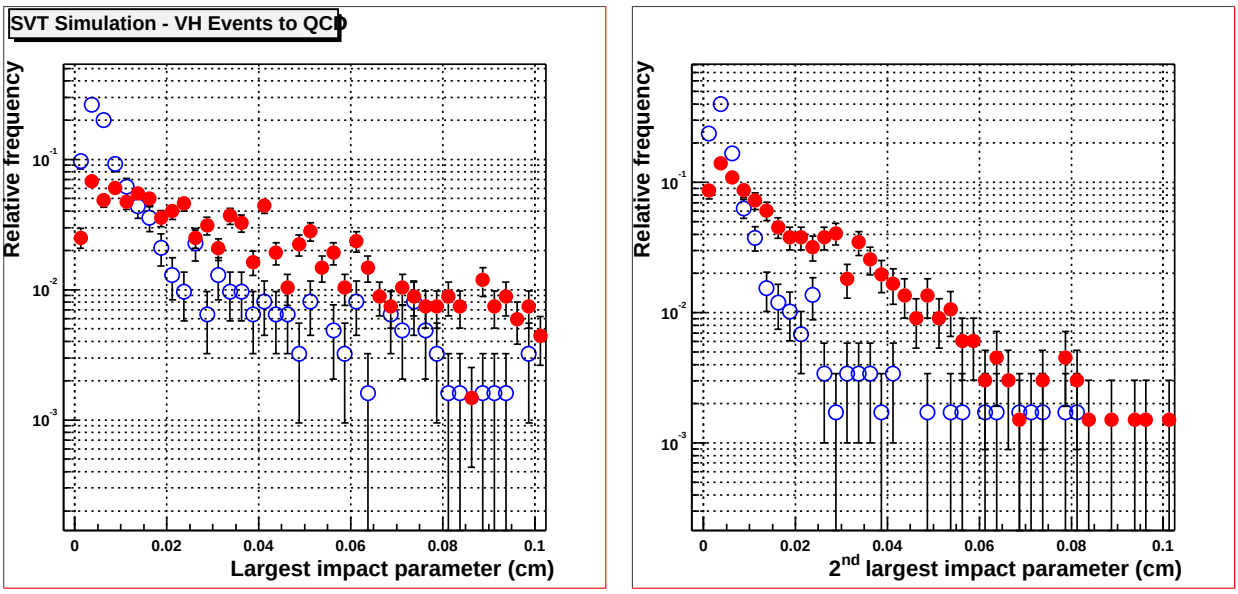

Figure 3.9: *Distribution of the largest (left) and second-largest (right) impact parameter in VH (open light circles) and* QCD *events (dark circles). The default values of χ^2 cut and noise level have been used; track impact parameters have been smeared with a finite beam spot size (see Sec. 3.3.2).*

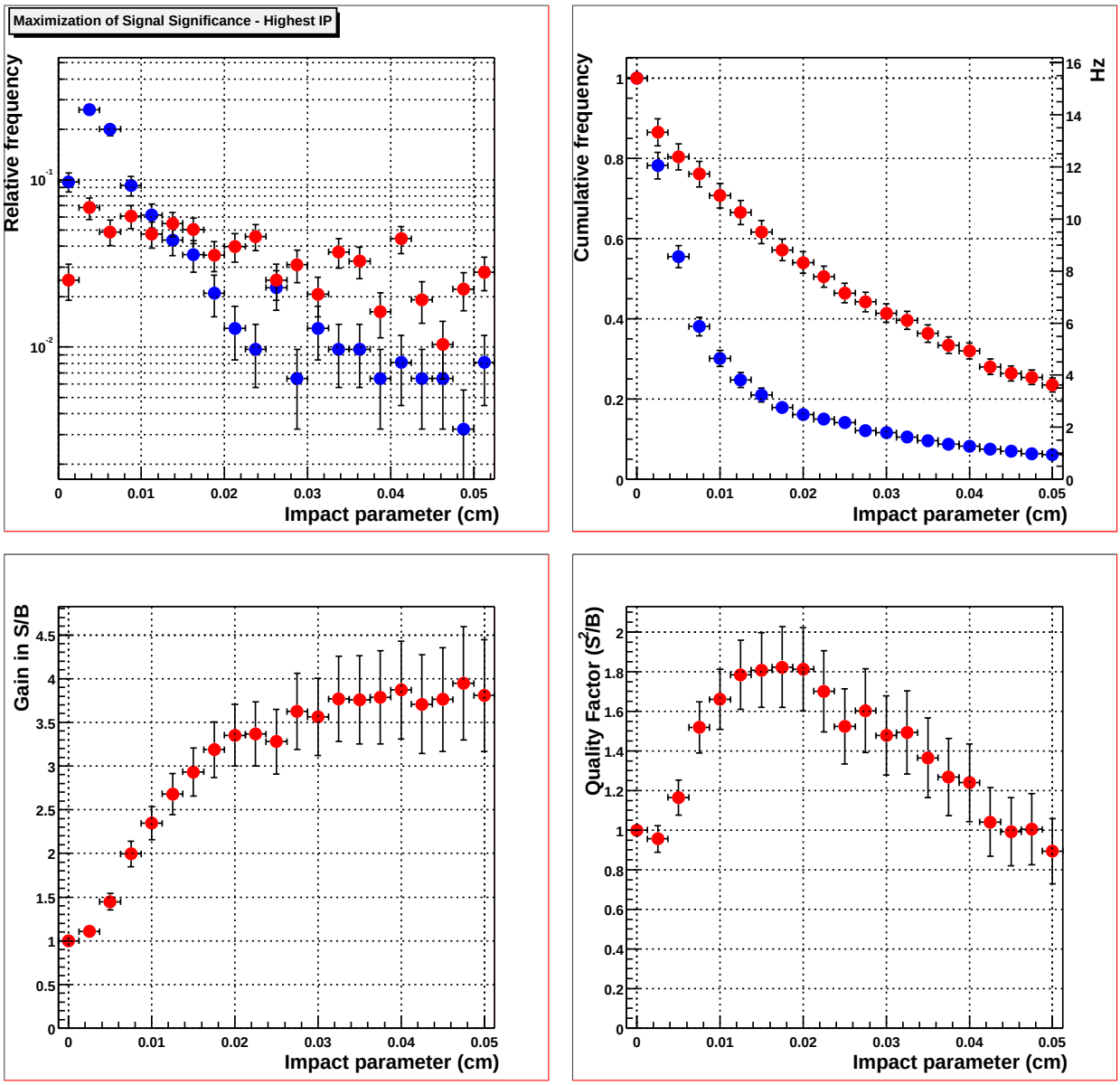

Figure 3.10: *Optimization of the selection based on the highest-IP track in the event. Top left: highest impact parameter in* QCD *(dark) and HV (light) events. Top right: efficiency as a function of the cut on the highest IP. Bottom left: ratio between signal and background efficiency. Bottom right: quality factor (see text). The default values of* χ^2 *cut and noise level have been used.*

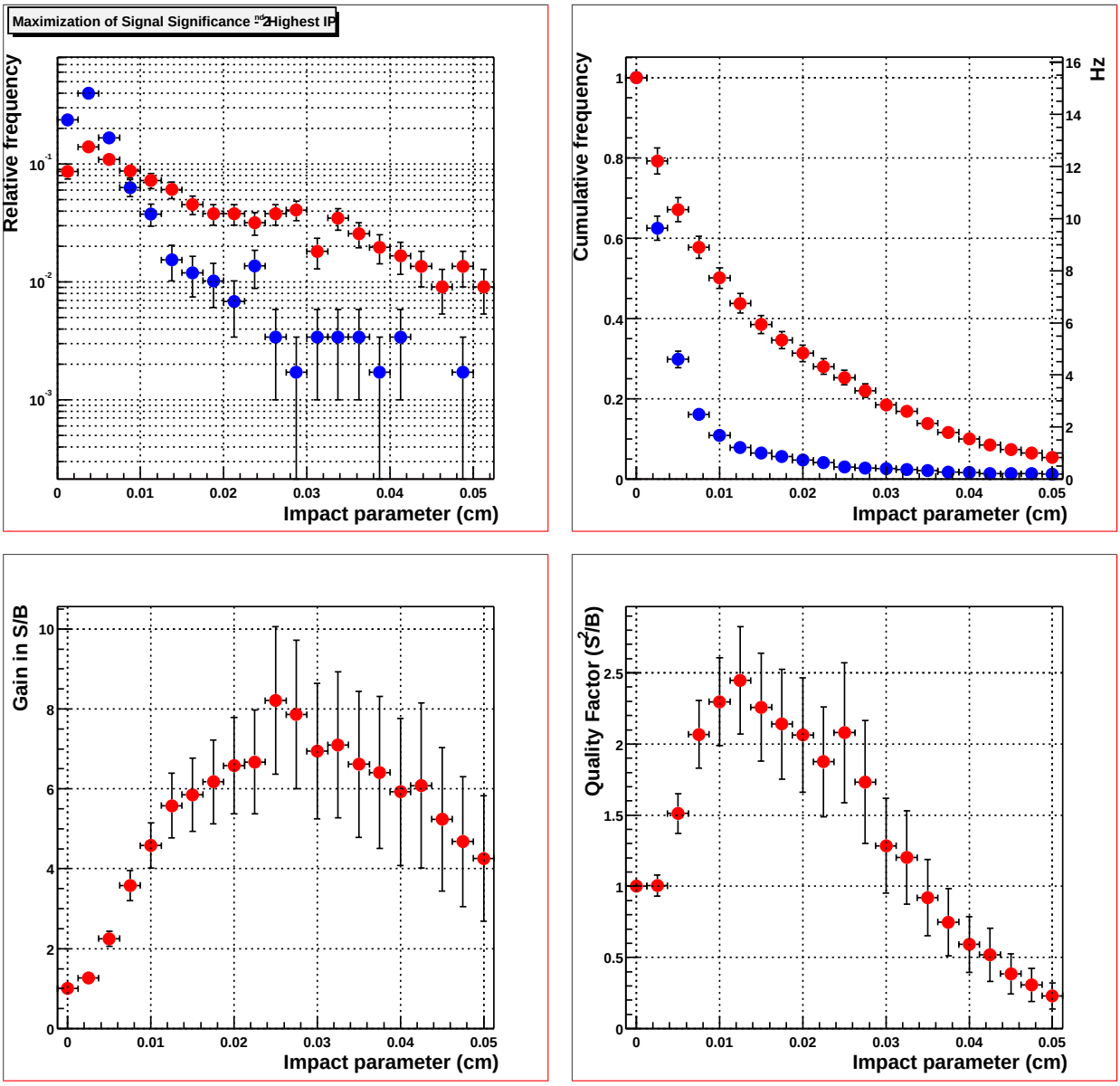

Figure 3.11: *Optimization of the selection based on the second-highest-IP track in the event. Top left: 2nd-highest impact parameter in* QCD *(dark) and HV (light) events. Top right: efficiency as a function of the cut on the 2nd-highest IP. Bottom left: ratio between signal and background efficiency. Bottom right: quality factor (see text). The default values of χ^2 cut and noise level have been used.*

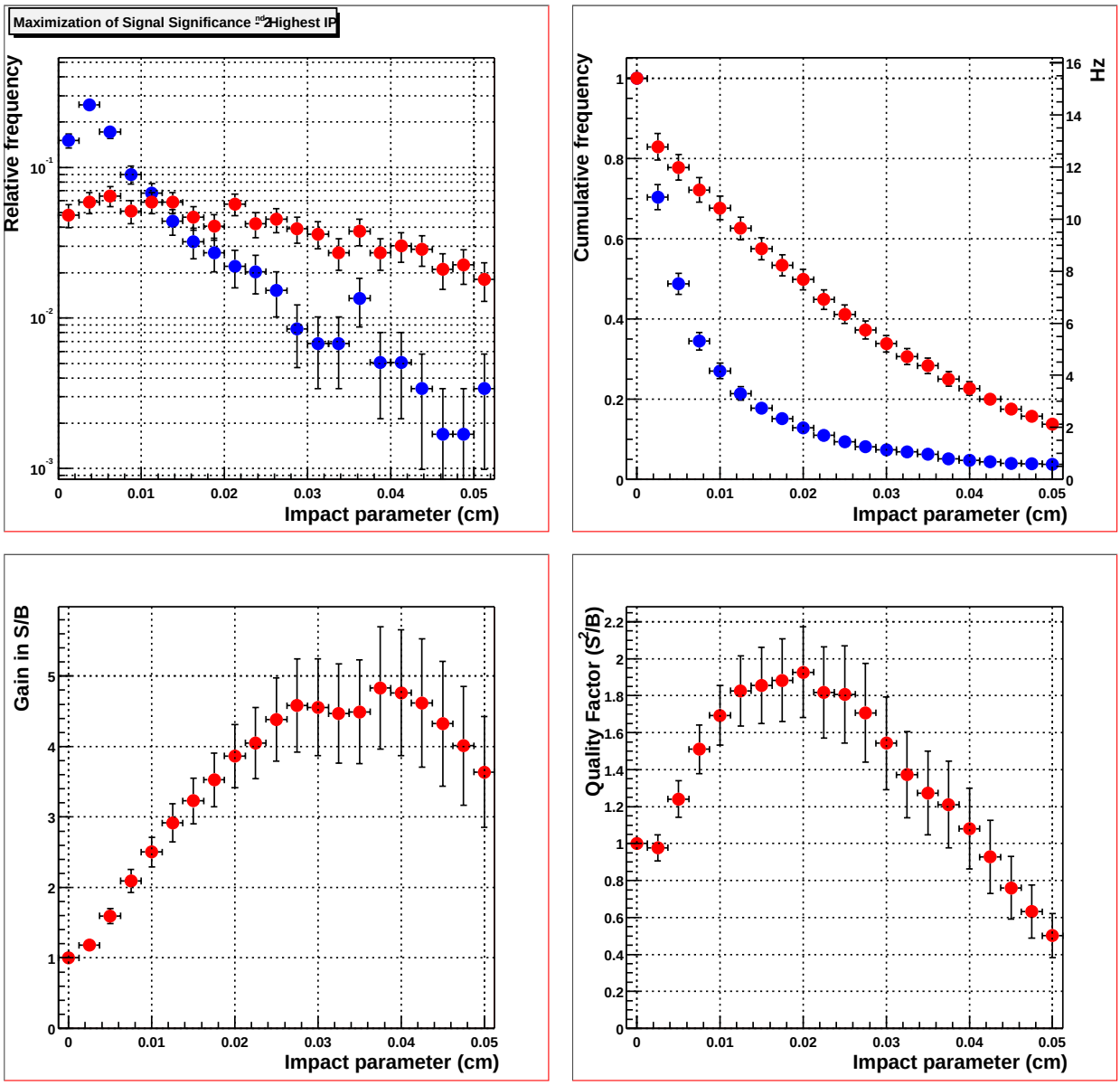

Figure 3.12: *Optimization of the selection based on the second-highest-IP track in the event, when no removal of multiple* SVT *tracks extrapolating to the same azimuth on* SL6 *is performed. Top left: 2nd-highest impact parameter in* QCD *(dark) and HV (light) events. Top right: efficiency as a function of the cut on the 2nd-highest IP. Bottom left: ratio between signal and background efficiency. Bottom right: quality factor (see text). The default values of χ^2 cut and noise level have been used.*

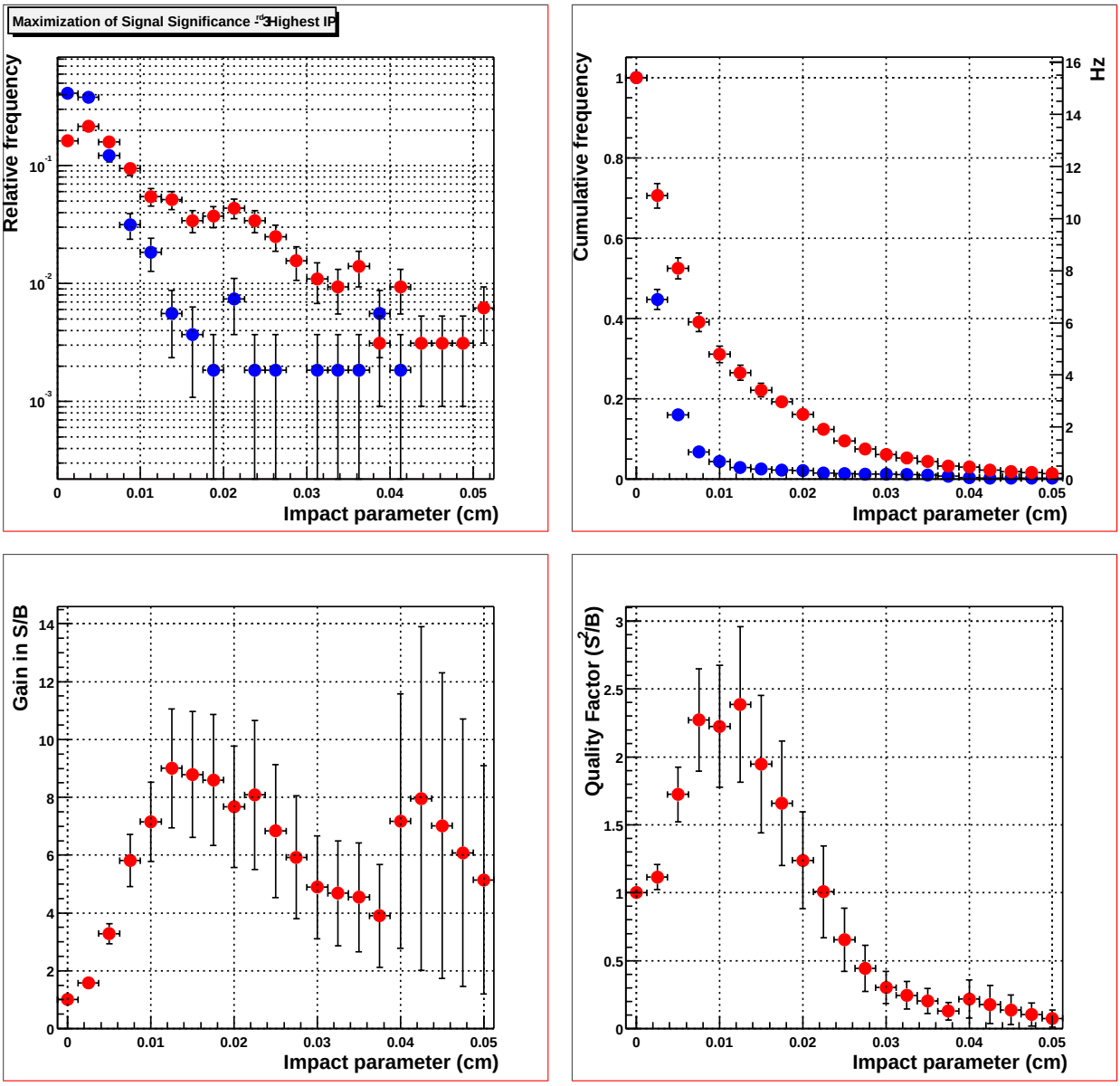

Figure 3.13: *Optimization of the selection based on the third-highest-IP track in the event. Top left:* 3rd*-highest impact parameter in* QCD *(dark) and HV (light) events. Top right: efficiency as a function of the cut on the* 3rd*-highest I.P.. Bottom left: ratio between signal and background efficiency. Bottom right: quality factor (see text). The default values of* χ^2 *cut and noise level have been used.*

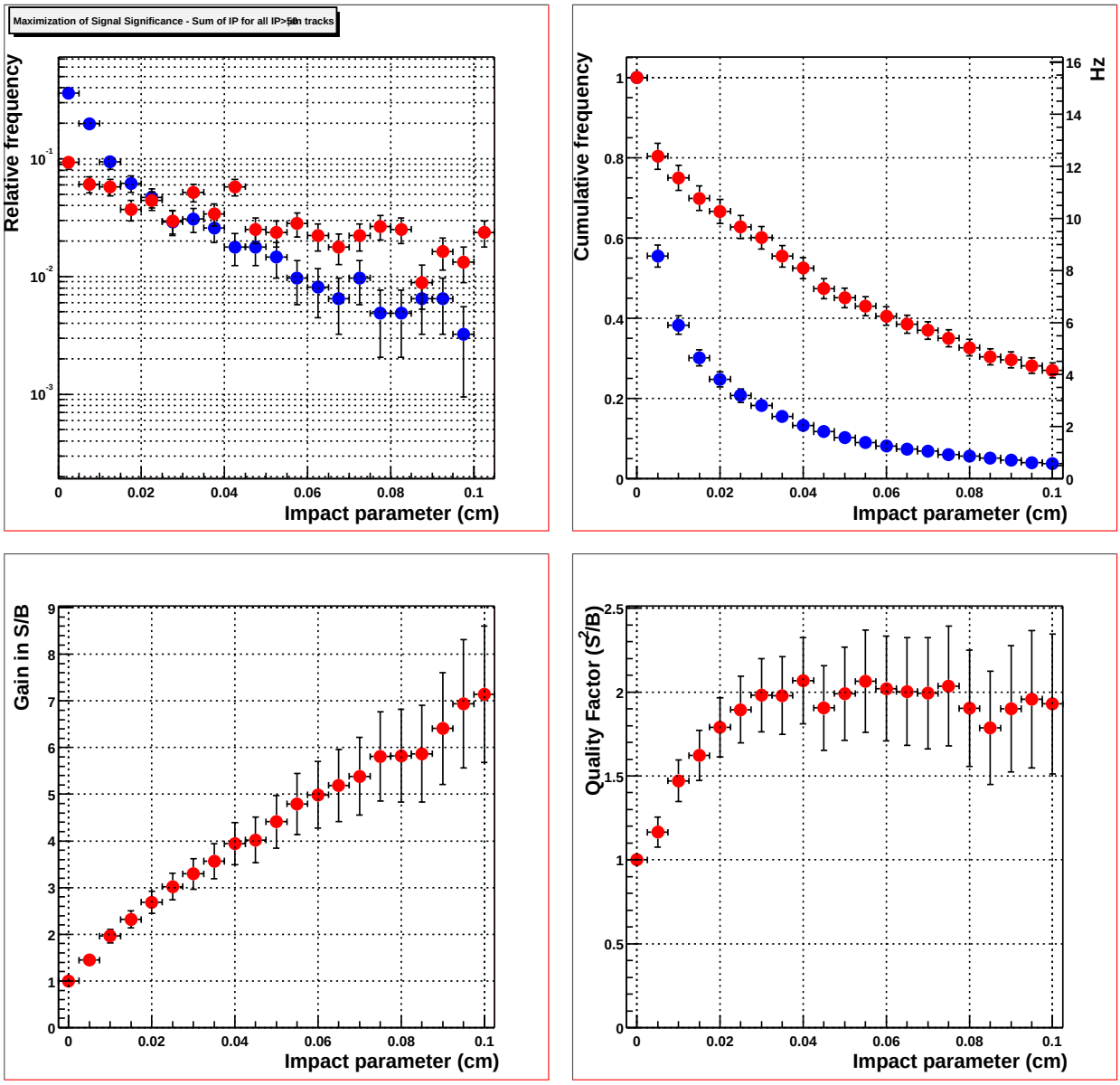

Figure 3.14: *Optimization of the selection based on the sum of impact parameters of all tracks with $d > 50$ μm. Top left: sum of impact parameters in* QCD *(dark) and HV (light) events. Top right: efficiency as a function of the cut on the sum. Bottom left: ratio between signal and background efficiency. Bottom right: quality factor (see text). The default values of χ^2 cut and noise level have been used.*

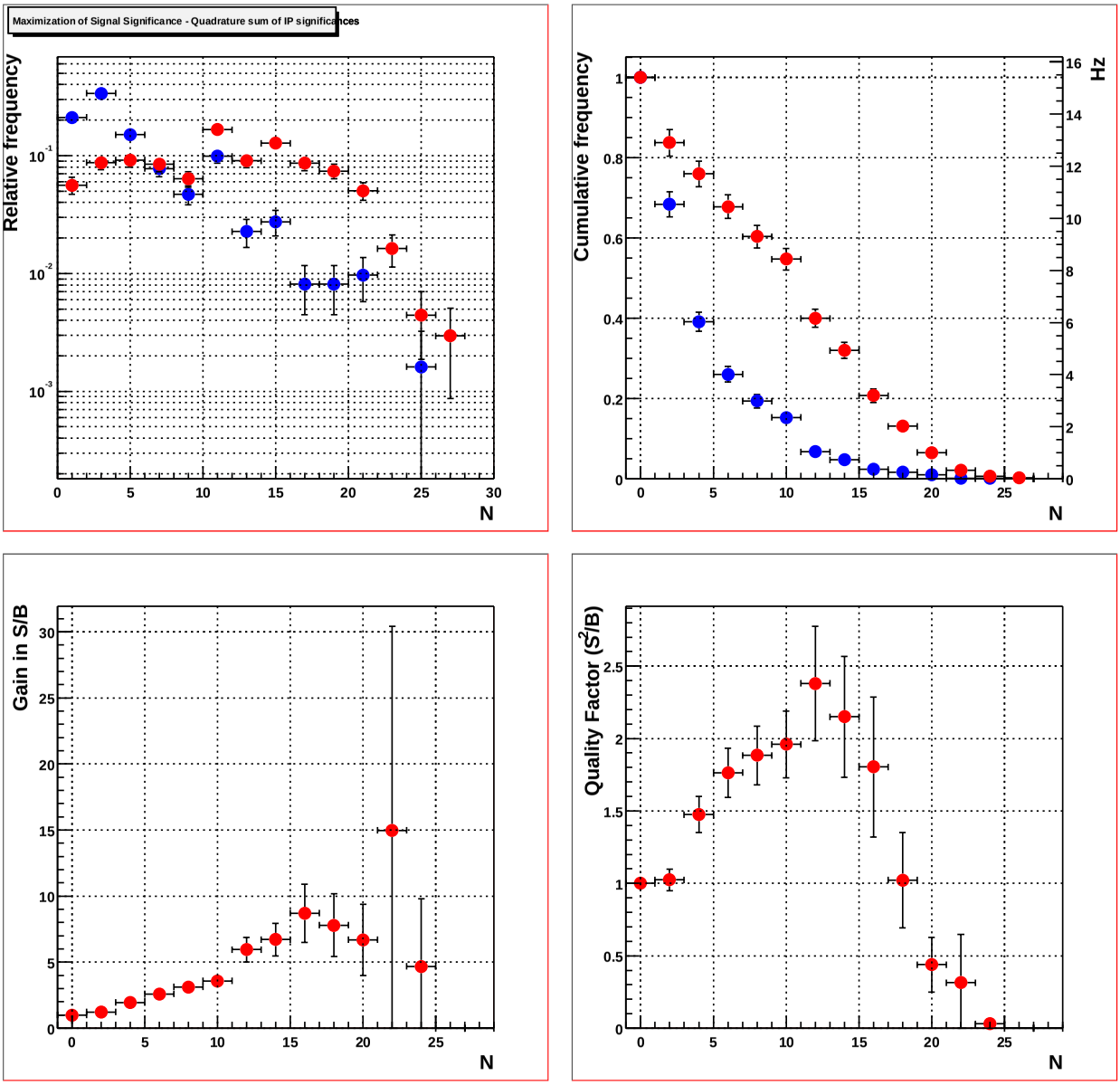

Figure 3.15: *Optimization of a selection based on the quadrature sum of impact parameter significances of* SVT *tracks (see text). The quality factor attainable is not larger than those obtained with simpler approaches.*

Effect of χ^2 Cut and Noise

Variations with the χ^2 cut

The track fitters in SVT operate a selection of good tracks based on the χ^2 of the fit to hit positions in the four SVXII layers plus the XFT track coordinates. The default cut is typically set to 12.6, a value that corresponds to a $\geq 99\%$ acceptance for real tracks and which appears to suit to events of interest for B physics, where track reconstruction efficiency is critical and occupancy is not very high. Of course, in the much more crowded environment caused by the multijet events, this cut might be not the optimal one, so we set out to study how efficiency and rate are affected by a change of its value.

We scan seven values of the χ^2 cut for all our simulations: 6, 8, 10, 12.6 (the default value), 15, 20, and 50. For each value of the cut we reprocess the data with the SVT simulation: that allows a comparison of efficiencies and gains as a function of the selections already discussed in the previous section.

Fig. 3.18 shows how the quality factor changes depending on the choice of χ^2 and IP cut. It could appear that a tighter cut on the fit χ^2 would improve the discrimination between signal and noise, particularly in the case of a tight impact parameter cut (see Fig.3.16). However, the effect around the critical range if the rate (1-1.5 Hz) is not very large, so that a tighter χ^2 cut is a useful option only if background rates become a critical issue.

The same study can be repeated for the various level of noise in the silicon strips, yielding similar results: in all cases, a tighter χ^2 has been found to slightly improve background rejection (see Fig. 3.19 for the case of 2.0% of noisy strips).

Variations with the noise level

In a given silicon strip on average a real signal from a minimum ionizing particle amounts to roughly 20,000 electrons, equivalent to about 30 ADC counts. The average amount of electronic noise varies half-ladder by half-ladder throughout the detector but is seldom larger than a few ADC counts; the readout thresholds to suppress it have been set to $2.5 - 3.0$ standard deviations of its value. However, noisy strips exist in all ladders of the detector, and they may have a definite impact in the performance of the SVT, particularly for the crowded topology we are focusing on here. It is necessary to note that the superstrip size chosen for this simulation (300 μm) implies that even a 2% of noisy strips amounts to 9.6% of fake single-strip hits in input to SVT, a number that is already able to confuse the track-hit matching with a certain frequency (see Fig. 3.17). Moreover, it has been shown[10] that noise in the inner layers is particularly bad for impact parameter reconstruction, because an accidental hit chosen by the Associative Memory in the inner SVX silicon layer in place of the real one will significantly degrade the I.P. resolution σ_d; however, even when the electronic noise does not cause the identification of an independent fake hit, it can worsen appreciably the resolution.

The fraction of noisy and dead silicon strips in the silicon layers has been mea-

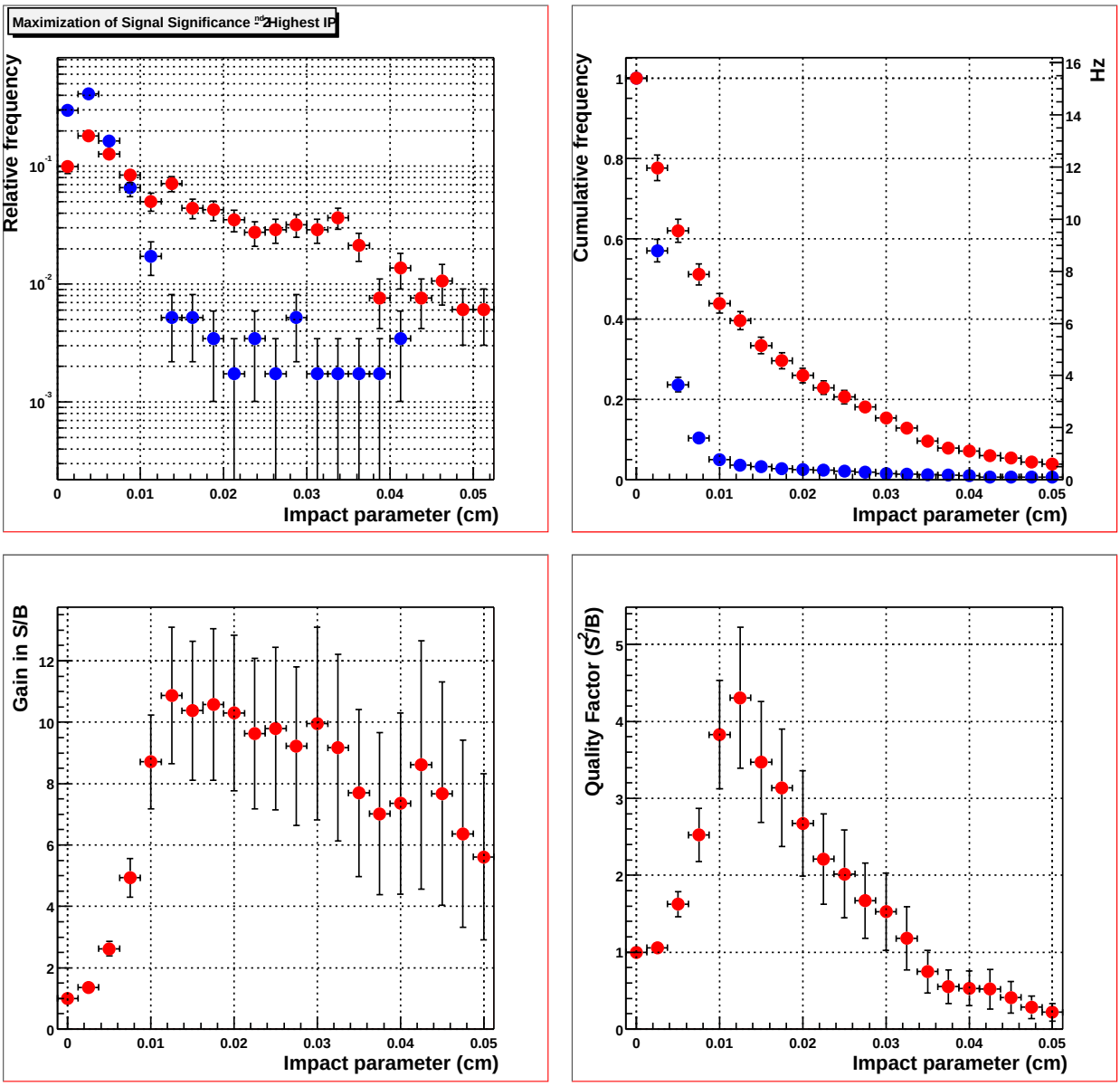

Figure 3.16: *Optimization of the selection based on the second-highest-IP track in the event, for tracks selected by* SVT *with a* χ^2 *cut at 8. Top left:* 2nd*-highest impact parameter in* QCD *(dark) and HV (light) events. Top right: efficiency as a function of the cut on the* 2nd*-highest IP. Bottom left: ratio between signal and background efficiency. Bottom right: quality factor (see text). The default value of noise level has been used.*

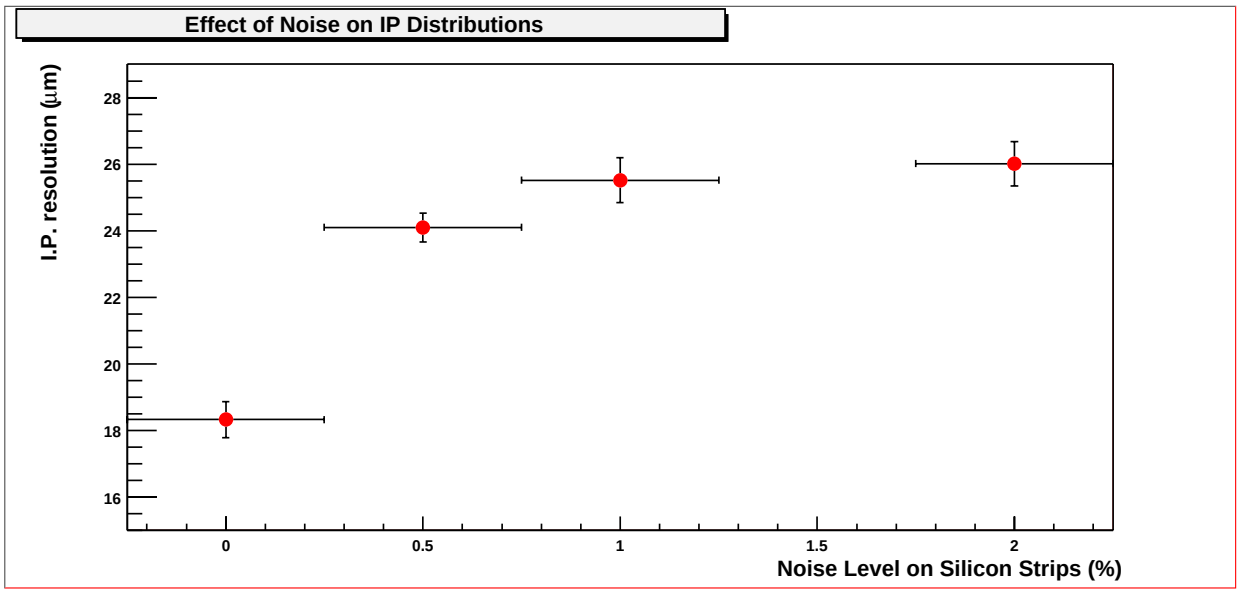

Figure 3.17: *Impact parameter resolution of prompt tracks reconstructed by* SVT *as a function of the noise level in the silicon.* QCD *events have been used (see the fits in Fig. 3.5).*

sured and is known in detail in each of the 360 half-ladders that constitute the SVX II detector. In principle, one could use the map of noisy and dead channels for a detailed simulation of the SVX II output in the study of the SVT response; however, the information is only available in the form of an Excel spreadsheet at the time of writing, and the task of converting it to a format suitable for consumption by GEANT3 has not been undertaken. We rather use a uniform value of noise in the detector. A random amount of electronic noise is generated by adding ADC counts to the strips, such that a given fraction of them surpasses the readout threshold. We set this fraction at 0.0%, 0.5%, 1.0% and 2.0% to study how it affects the number of reconstructed tracks, the resolution of the track parameters, and the signal efficiency and background rejection. The 0.5% figure should be close to the situation of our real detector. As noted above, this noise does not only affect SVX II occupancy, but also the resolution in the position measurement for multiple-strip clusters caused by real particles, since the smearing affects the computed cluster centroid.

We have measured the impact of the noise level by comparing efficiency and acceptance of each considered selection strategy for the four considered percentages of noisy strips. A performance degradation is observed in all cases with the increase of noise level: the acceptance for background events increases much more rapidly than that of the signal.

In the case of a straightforward selection requiring two displaced tracks with $|d| > 100\ \mu m$, signal acceptance remains approximately constant when the fraction of noisy strip goes from zero to 2%, in the face of a doubling of the background, from 6 (correspondent to $\sim 0.9\ Hz$) to 13% (correspondent to $\sim 2\ Hz$); the quality factor thus decreases considerably (see Fig. 3.20). A noise level of 2% or larger would

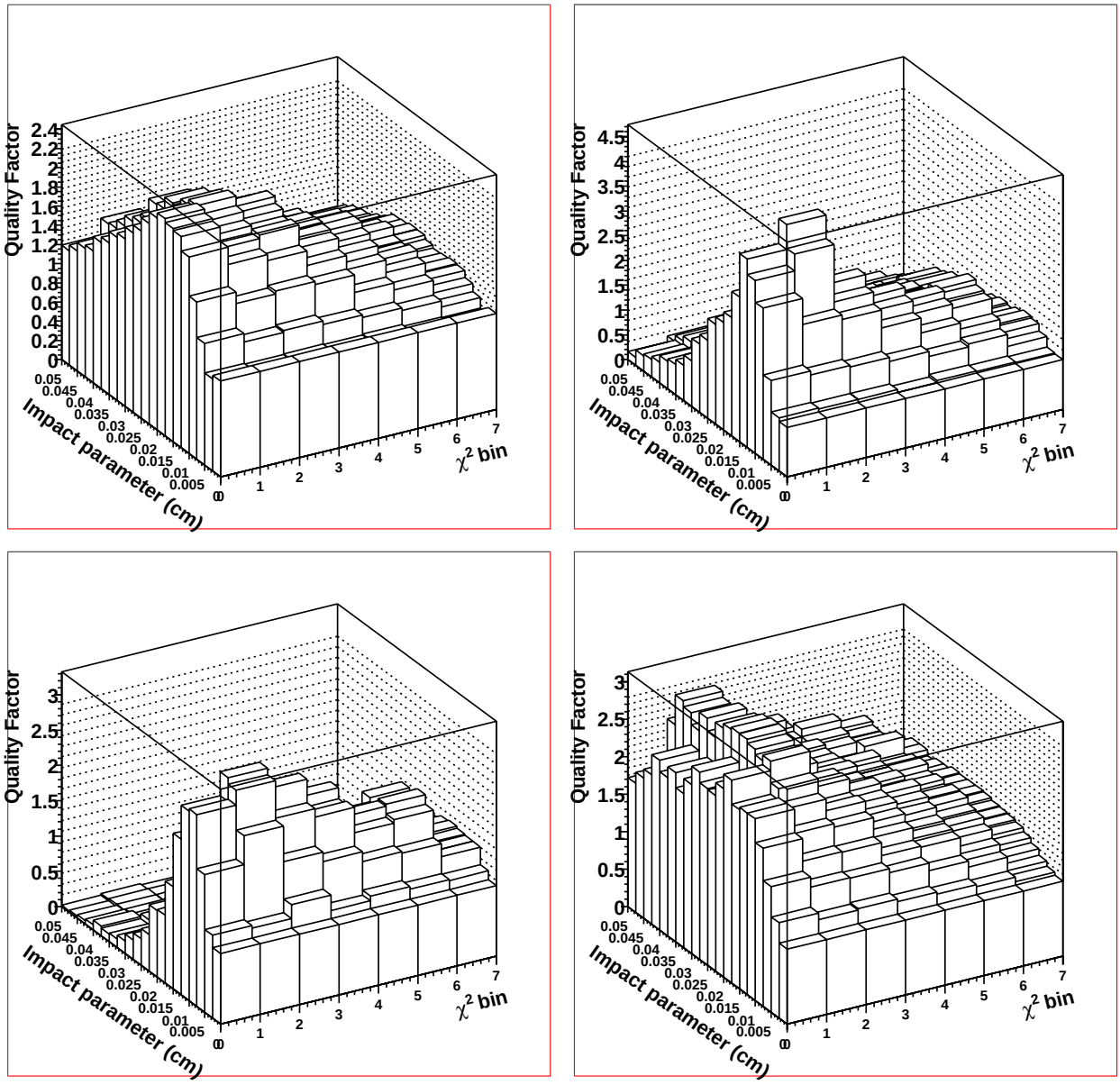

Figure 3.18: *Variation of quality factor with the choice of the χ^2 cut on* SVT *tracks. Bins 1 to 7 in the abscissa denote cuts at 6, 8, 10, 12.6, 15, 20 and 50, respectively. Top left: quality factor for a selection based on the impact parameter of the highest-IP track. Top right: Q values for a selection based on the impact parameter of the second-highest-IP track. Bottom left: Q values for a selection based on the impact parameter of the 2nd-highest-IP track for events having at least one track with $|d| > 100$ μm. Bottom right: Q values for a selection based on the sum of impact parameters of all tracks with $|d| > 50$ μm. The default value of noise (0.5%) has been used for all plots.*

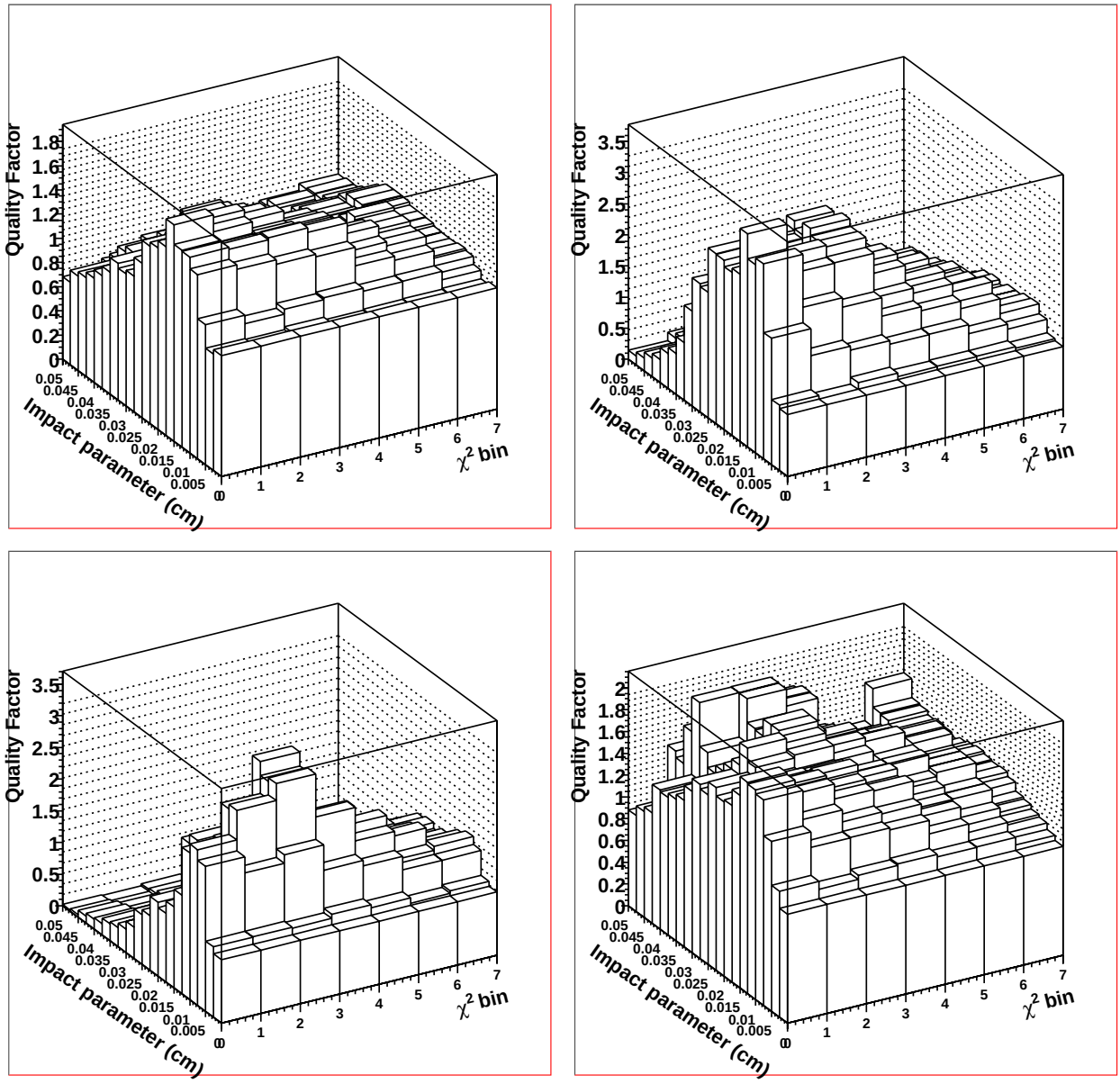

Figure 3.19: *Variation of quality factor with the choice of the χ^2 cut on* SVT *tracks. Bins 1 to 7 in the abscissa denote cuts at 6, 8, 10, 12.6, 15, 20 and 50, respectively. Top left: quality factor for a selection based on the impact parameter of the highest-IP track. Top right: Q values for a selection based on the impact parameter of the second-highest-IP track. Bottom left: Q values for a selection based on the impact parameter of the 2nd-highest-IP track for events having at least one track with $|d| > 100$ μm. Bottom right: Q values for a selection based on the sum of impact parameters of all tracks with $|d| > 50$ μm. The highest value of noise (2.0%) has been used for all plots.*

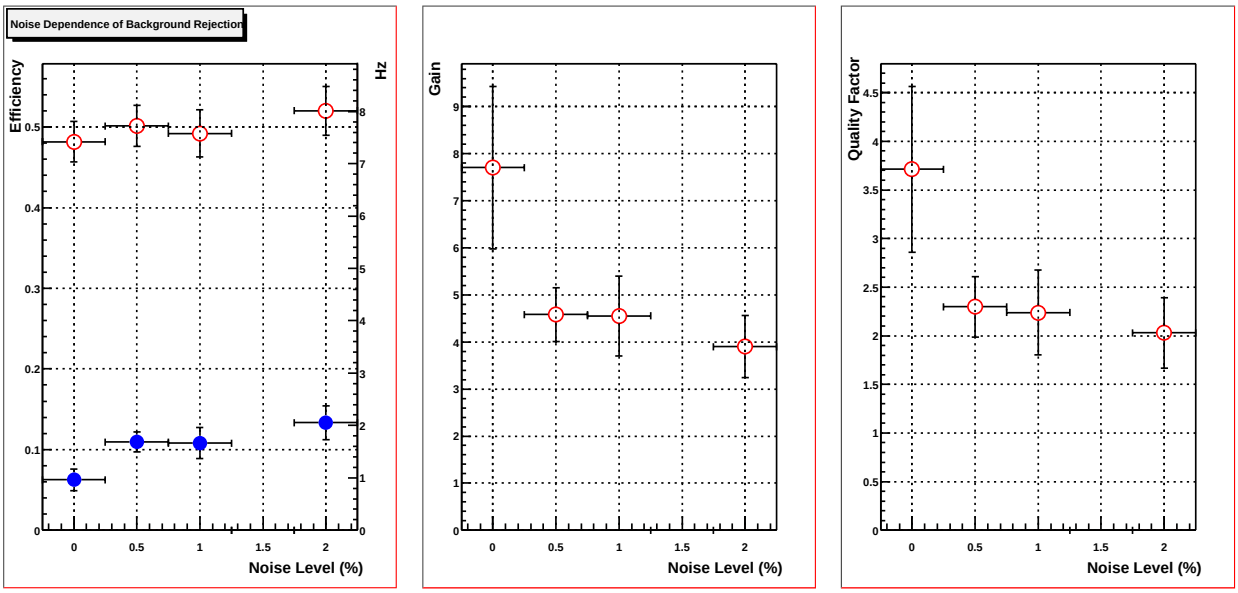

Figure 3.20: *Degradation of the effectiveness of a selection based on the 2nd-largest impact parameter in VH events ($|d_{2nd}| > 100$ μm) with the noise level in the silicon strips. Left: signal efficiency (light) and background acceptance (dark); center: gain of the selection (S/N); right: quality factor.*

decrease the utility of SVT in the discrimination of heavy flavors in the multijet data sample; however, in that case a smaller superstrip size -if applicable- could probably restore the discrimination power.

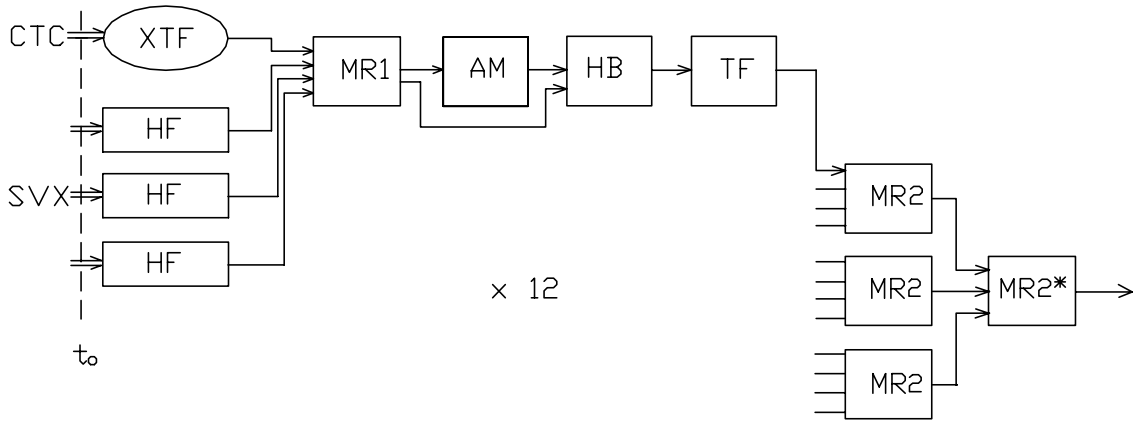

Figure 3.21: *A schematic view of the block model of the* SVT *system used for timing estimates (from Ref. [11]).*

Timing Issues

Timing is critical at trigger Level 2. On average, in a matter of less than 20 microseconds (see Sec. 2.6) from Level 1 accept the raw data from the detector components has to be analyzed, such that the Level 2 processors can decide whether to pass the event to Level 3. The SVT has been shown to be able to achieve that aim well within the allotted time with the typical events interesting for B-physics issues[11], using a simple timing model. We reproduce that study here for the more complicated $VH \to q\bar{q}^{(\prime)}b\bar{b}$ and possible background events we are interested in.

The timing model

The SVT system can be thought as a set of 12 parallel data streams, each composed of a few functional blocks connected by cables. Blocks identify the hit finders (HF), the first mergers (MR1), the associative memory boards (AM), the hit buffers (HB), the track fitters (TF), and the final mergers (MR2). Each block receives data relative to a single 30° slice of SVX II[6], processes it, and distributes it to one or more blocks downstream. The final information is then merged and output to the Level 2 processors in the form of a track list (see Fig. 3.21).

For timing estimations, one can model the data flow through each block with a few constants (partly measured on real prototypes and partly estimated with simulations [11]) which describe the cable delay, the processing time, and the time required to input and output each data word. We adopt here the terminology of Ref. [11], where t_1^{in}, t_1^{out}, t_2^{in}, and t_2^{out} are the times when the first (1) or last (2) dataword appears in input or output to each block. Given the constants per each block, the total SVT processing time (t_2^{out} for the last block in the chain) can be then estimated using the number of datawords flowing through each block. To those numbers one should add a 1.5 to 2.0 μs delay from Level 1 accept, to account for the digitization

[6]That is, data from all ladders at the same ϕ.

of the data.

Processing time for multijet events

As before, we consider as our default data the simulation with 0.5% of noisy SVX II strips. The distribution of total processing time for VH events into all hadronic final state after Level 1 calorimetric requirement is shown in Fig. 3.22, while a breakdown of the individual contribution of each functional block is presented in Fig. 3.23 and in Tab. 3.1. Because of the 12-fold parallel architecture of the considered model, the delays introduced by the blocks do not add up to the total processing time; instead, one may define each block's delay as

$$\Delta t_i = max_{j=1}^{12}(t_2^{out})_{i,j} - max_{j=1}^{12}(t_2^{out})_{i-1,j} \tag{3.5}$$

where j runs on the twelve 30° slices, and i denotes the considered block. Thus defined, the individual delays will add up to the total processing time.

From a first inspection of the plots, one notices that the bulk of the events take less than 20 microseconds to be processed, but a significant fraction exceeds that value considerably. The blocks most responsible for the long processing time are the track fitters, although hit buffers also take a relatively long time to process the data; the latter are also more sensitive to the number of reconstructed hits.

A more detailed look at the individual contributions to the processing time for signal can be illustrated by Fig. 3.24 and for background by Fig. 3.25 . Here the average value of the t_1^{in}, t_2^{out}, $min(t_1^{in})$, and $max(t_2^{out})$ values are presented for each block in cascade, to highlight the effects of parallelism.

Given the long tails of the total SVT processing time for $VH \rightarrow q\bar{q}^{(\prime)}b\bar{b}$ events, a number of special interest for the Level 2 trigger is the time necessary to process a given fraction of the considered events. Fig. 3.26, Fig. 3.27 and Tab. 3.2 and 3.3 show the time after which 85%, 90%, 95%, and 99% of the events of signal and background have been output by SVT. It appears obvious that a $20 \sim 30$ μs cutoff by the Level 2 processors would significantly hinder the collection of this category of events; on the other hand, the overhead in dead time caused by a delayed Level 2 decision appears small, given the relatively small rate of this kind of events: given the trigger rate for Level 1 (2.7 kHz), and given that the average time to process background events is less that 8 μs, we infer that SVT would the busy for about 2% of its time to process this kind of events. A more sophisticated analysis, taking into account several different classes of events, would be required for an estimate of the dead time introduced by a non-time-limited SVT output. We believe this will be better accomplished once we start collecting data.

Dependence on the noise level

As already noted, the processing time of some of SVT's functional blocks depends strictly on the number of hits reconstructed from strips above ADC threshold, while for others the dependence is only indirect, through the increased number of roads and tracks that can be reconstructed. The clearest example is given by the time needed by the MR1 and MR2 blocks: the processing time of the former depends

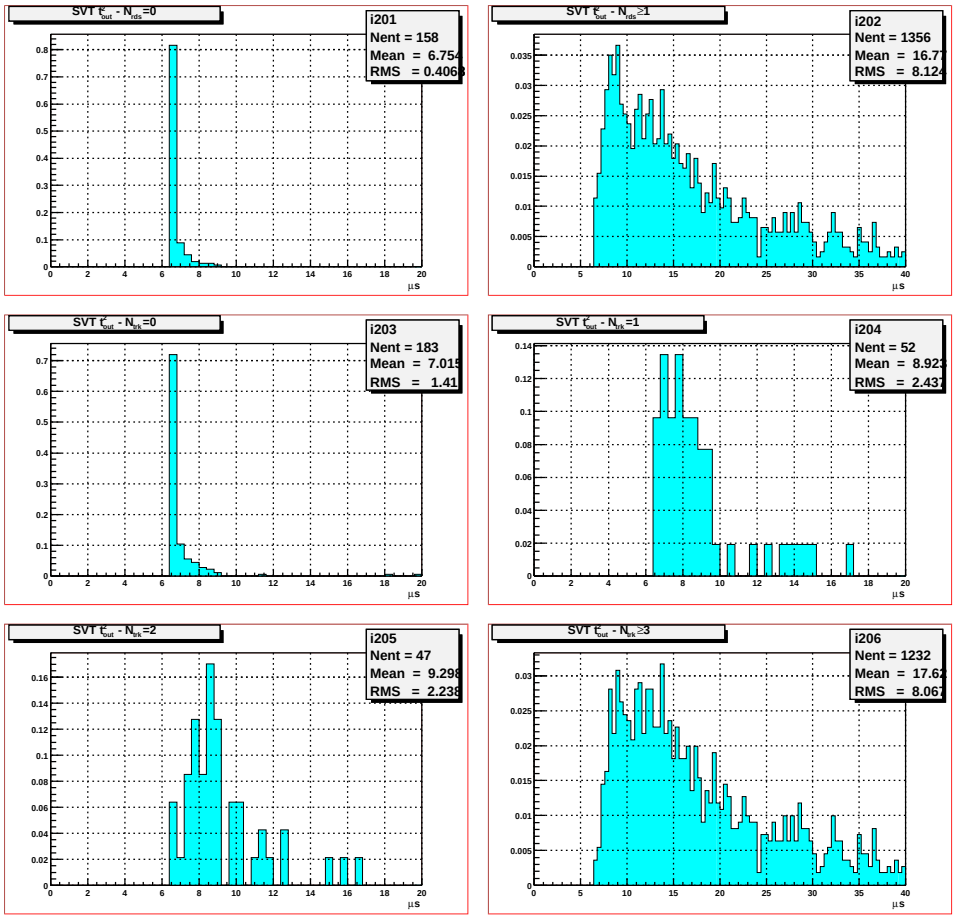

Figure 3.22: *Total processing time for different categories of* SVT *output. Top row: events with no found roads (left); events with at least one found road (right). Middle row: events with zero found* SVT *track (left); events with one found track (right). Bottom row: events with two found* SVT *tracks (left); events with three or more found tracks (right). The default value of noise level has been used.*

linearly on the number of hits, and it increases by an order of magnitude as the noise level increases from 0% to 2%; the processing time of the latter is basically a constant, being dominated by its internal delay. Fig. 3.28 affects the average processing time of each block for VH events; the individual numbers for signal and background events are provided in Tab. 3.2 and Tab. 3.3 respectively.

We should note that the level of noisy strips in the SVX II strongly affects the processing time for background events, taking it near to the critical threshold of 20-30 μs. It would be very important to keep under control this variable during the collection of data.

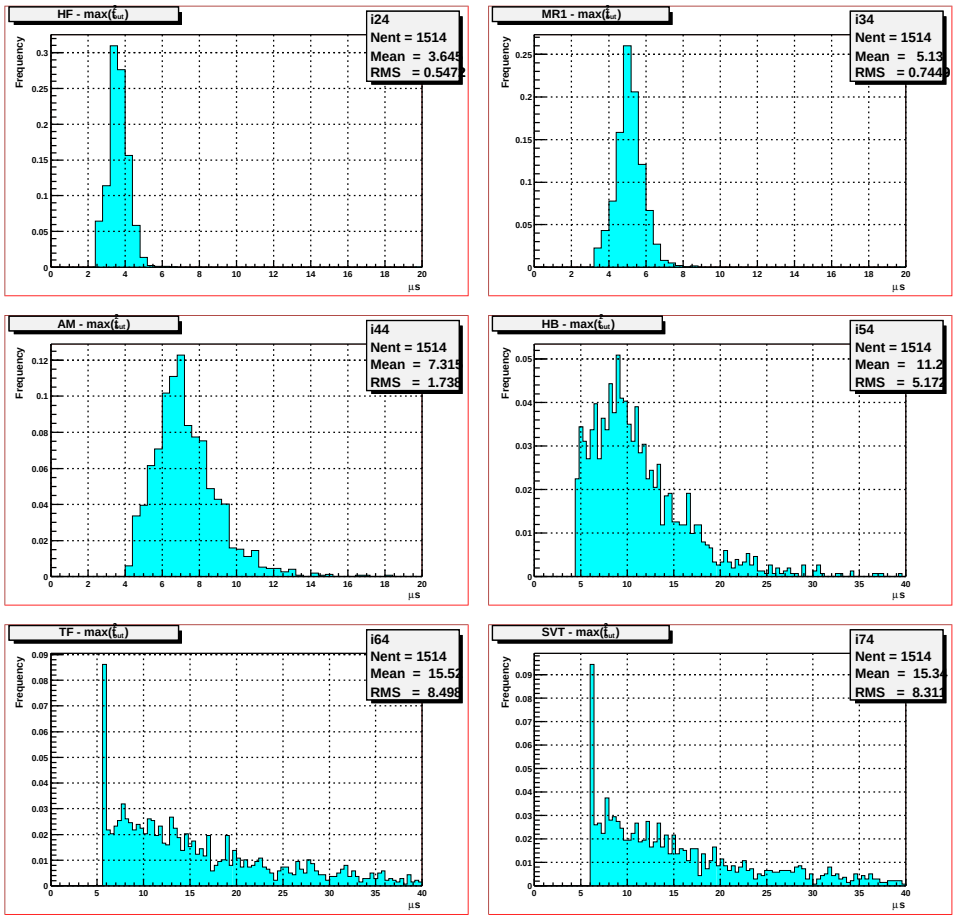

Figure 3.23: *Cumulative processing time of each* SVT *functional block for* $VH \rightarrow q\bar{q}^{(\prime)}b\bar{b}$ *events. The default value of noise level has been used.*

Data sample	HF (μs)	MR1 (μs)	AM (μs)	HB (μs)	TF (μs)	MR2 (μs)	MR2* (μs)	SVT (μs)
VH ($M_H = 120\ GeV$)	3.64	1.50	2.18	3.93	7.68	0.36	0.29	18.87
B-20 (Ref. [11])	3.52	2.56	1.45	1.51	1.74	0.30	0.30	11.39
B-10 (Ref. [11])	3.31	2.44	1.15	0.67	0.92	0.30	0.30	9.06

Table 3.1: *Average processing time of each* SVT *functional block for different datasets: all hadronic decays of* WH *and* ZH *events (with* $M_H = 120\ GeV$*), and* B *production simulations at* $P_T^{min} = 10\ GeV$ *and* $20\ GeV$ *from Ref. [11]. Note: noise in the silicon strips was generated differently in the studies of Ref. [11]; therefore, the values most dependent on the total number of hits in the silicon strips (MR1 in particular) do not warrant a direct comparison. See below for a description of noise effects on the timing.*

$VH \to q\bar{q}^{(\prime)}b\bar{b}$	HF (μs)	MR1 (μs)	AM (μs)	HB (μs)	TF (μs)	MR2 (μs)	SVT (μs)
0.0%	2.89	0.47	1.98	2.87	4.85	0.12	13.25
0.5%	3.64	1.50	2.18	3.93	7.68	0.36	18.87
1.0%	4.33	2.65	2.36	5.11	8.57	0.34	23.00
2.0%	5.66	4.90	2.75	7.42	10.45	0.50	31.00

Table 3.2: *Average processing time of each* SVT *functional block for 4-jet decays of WH and ZH events ($M_H = 120\ GeV/c^2$), for the four different noise levels. See also Fig. 3.28.*

Background	HF (μs)	MR1 (μs)	AM (μs)	HB (μs)	TF (μs)	MR2 (μs)	SVT (μs)
0.0%	2.55	0.33	1.18	0.60	1.18	0.21	6.37
0.5%	2.11	1.26	1.15	0.76	1.08	0.17	7.85
1.0%	3.79	2.42	1.16	1.34	1.18	0.20	10.41
2.0%	5.16	4.68	1.25	2.85	1.53	0.10	15.88

Table 3.3: *Average processing time of each* SVT *functional block for* QCD *background events for the four different noise levels.*

	t(85%) (μs)	t(90%) (μs)	t(95%) (μs)	t(99%) (μs)
SIGNAL				
0.0%	20.8	24.8	32.0	56.0
0.5%	30.4	36.0	48.8	76.0
1.0%	37.6	43.6	56.4	78.0
2.0%	48.0	54.0	66.0	88.4
QCD				
0.0%	7.2	7.6	8.0	12.8
0.5%	9.6	10.0	12.0	19.2
1.0%	12.0	12.8	14.8	24.4
2.0%	18.8	20.0	22.4	34.8

Table 3.4: *Total time necessary to process a given fraction of VH events of signal with $M_H = 120\ GeV/c^2$ or of* QCD *background passing Level 1 calorimetric requirements as a function of the noise level.*

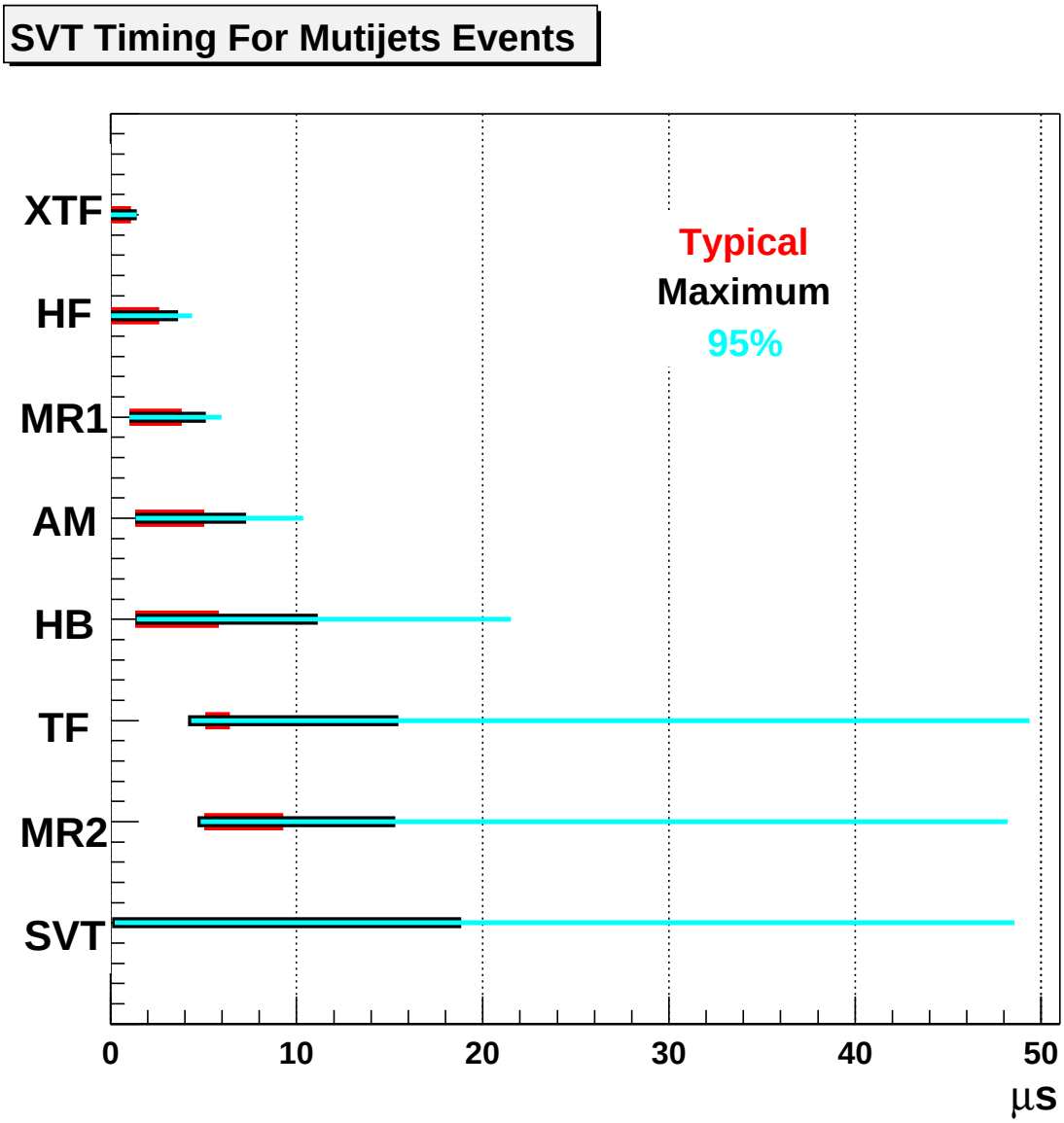

Figure 3.24: *This bar chart shows which* SVT *block is processing signal events as a function of time from Level 1 accept. Each thick red bar has extrema at the average value of* t_1^{in} *and* t_2^{out} *(see text), while the dark bar extends to the minimum and maximum of those values among the 12 parallel streams. The thin magenta line extends to the point when events have a 95% chance of having been finished processing from each block. A 0.5% electronic noise has been used.*

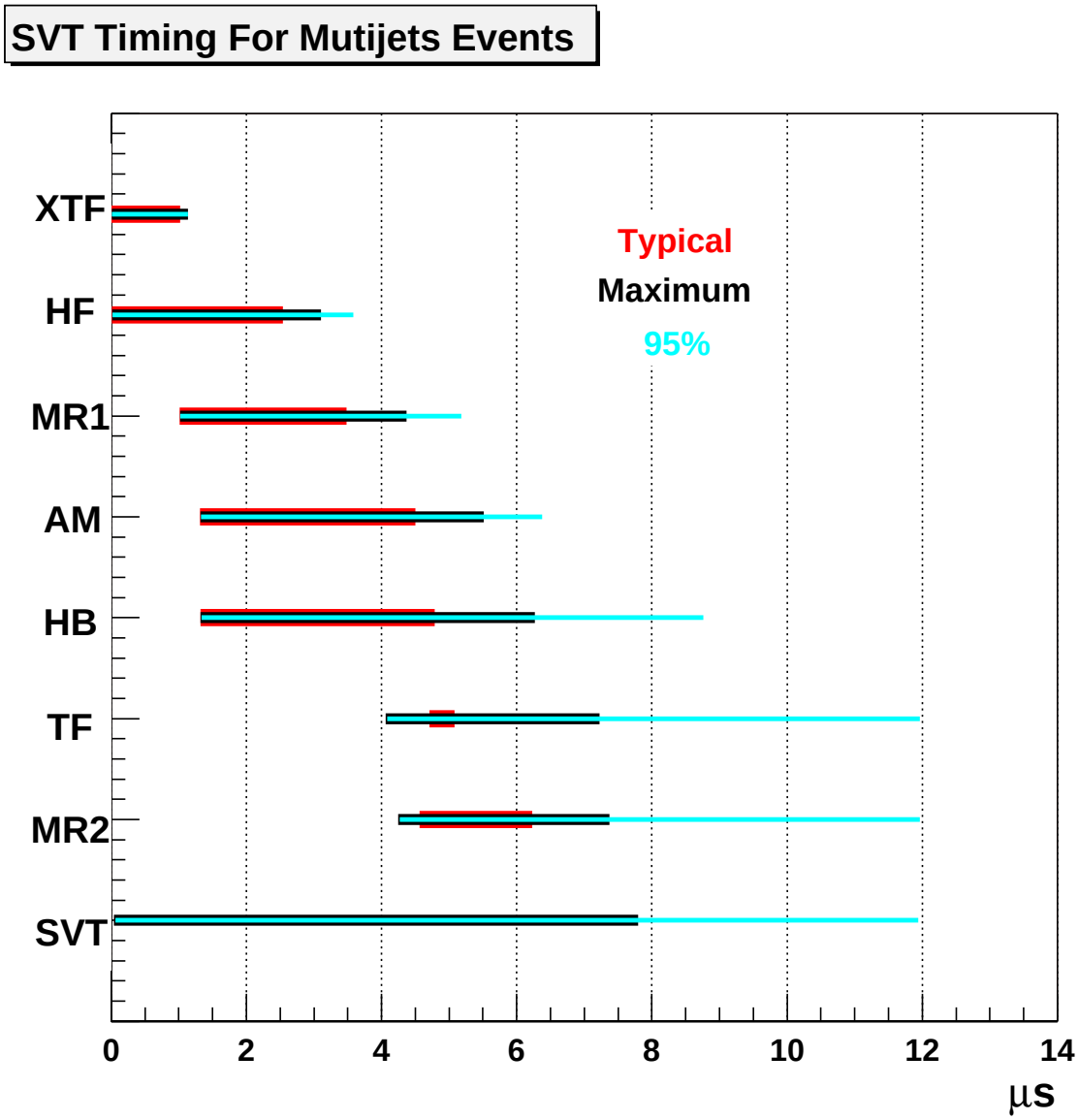

Figure 3.25: *This bar chart shows which* SVT *block is processing background events as a function of time from Level 1 accept. Each thick red bar has extrema at the average value of* t_1^{in} *and* t_2^{out} *(see text), while the dark bar extends to the minimum and maximum of those values among the 12 parallel streams. The thin magenta line extends to the point when events have a 95% chance of having been finished processing from each block. A 0.5% electronic noise has been used.*

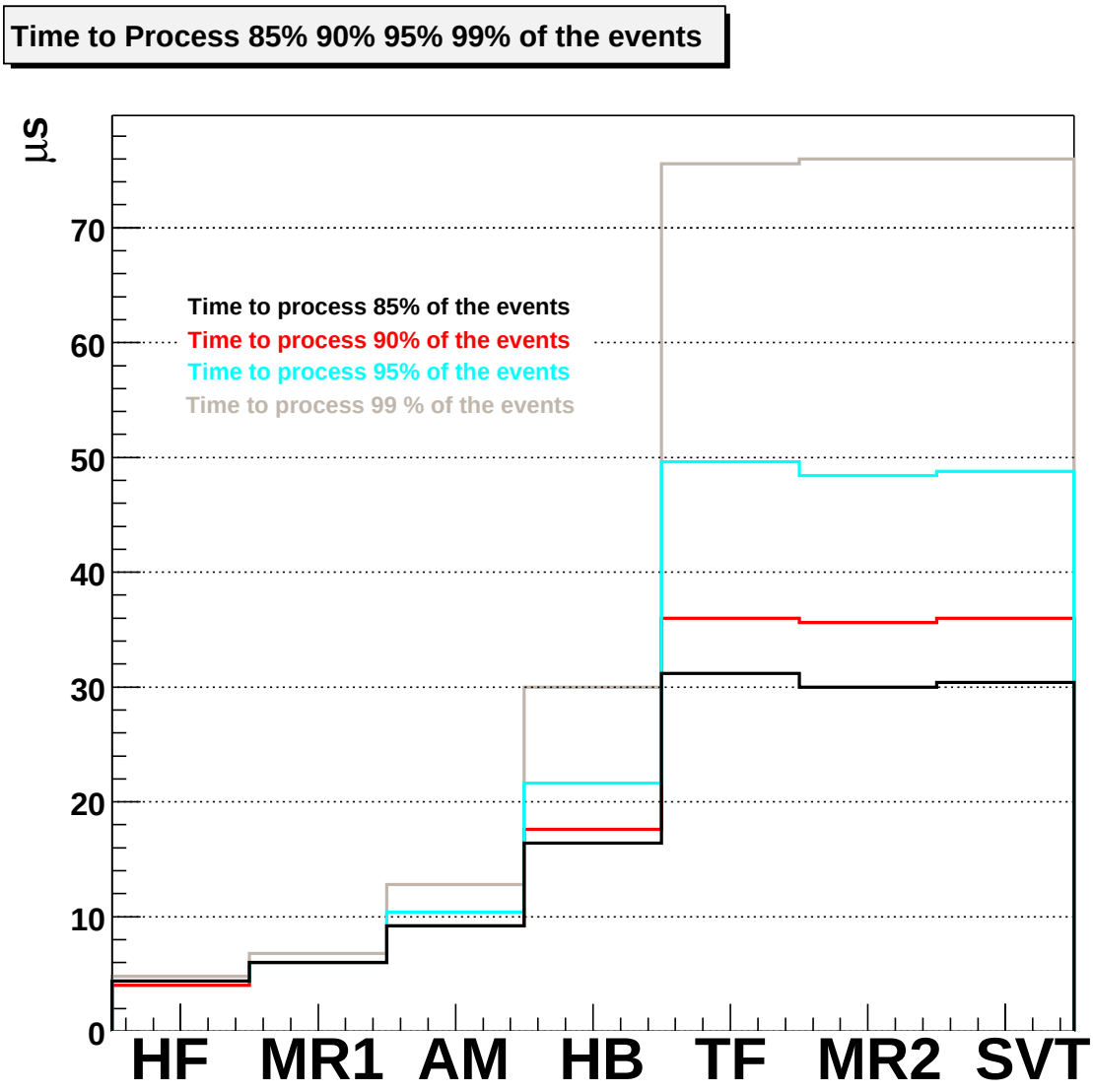

Figure 3.26: *Cumulative time necessary to process signal events through the various blocks of* SVT *a given fraction of the events. The default value of noise in the silicon strips has been used.*

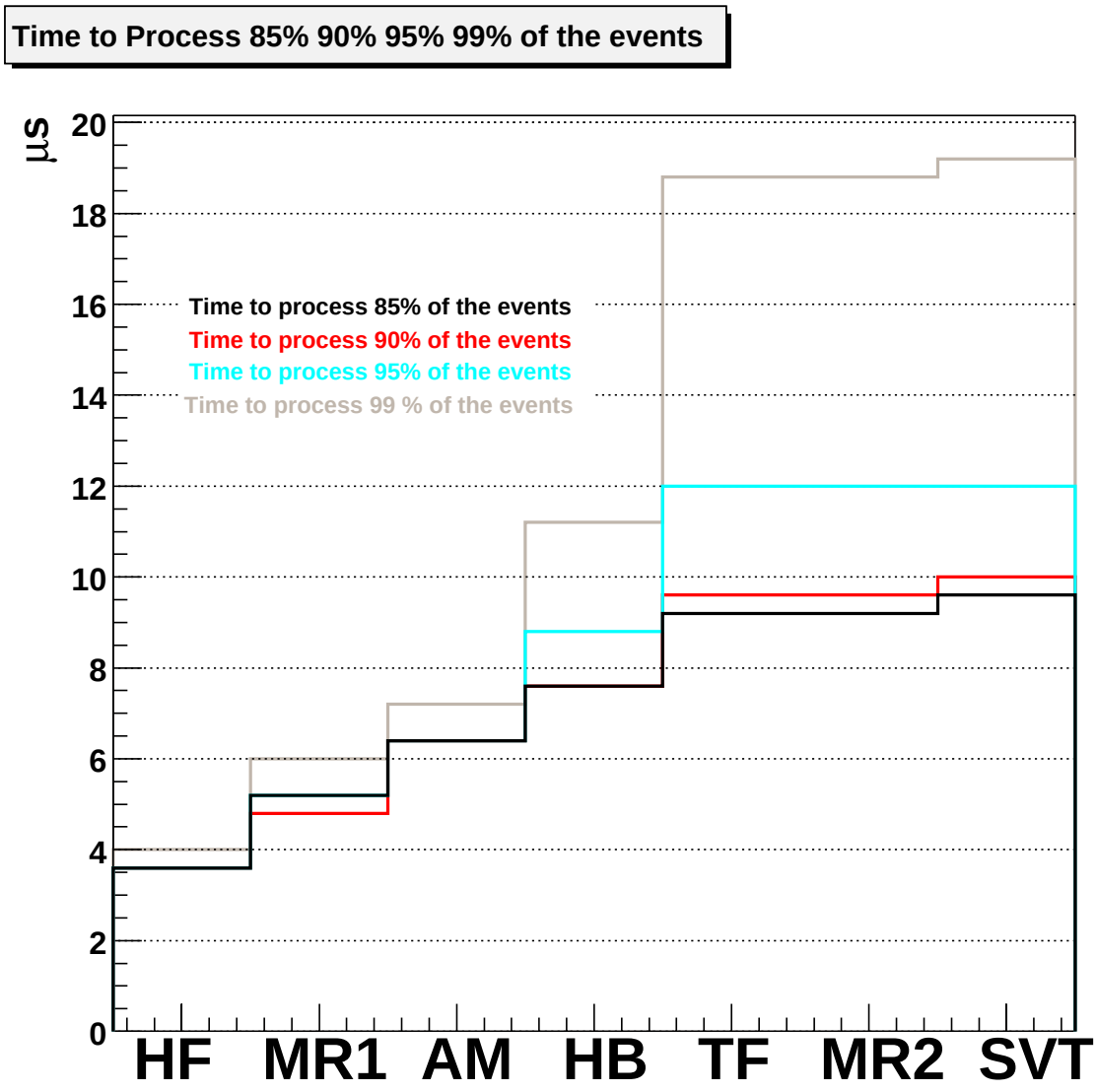

Figure 3.27: *Cumulative time necessary to process background events through the various blocks of* SVT *a given fraction of the events. The default value of noise in the silicon strips has been used.*

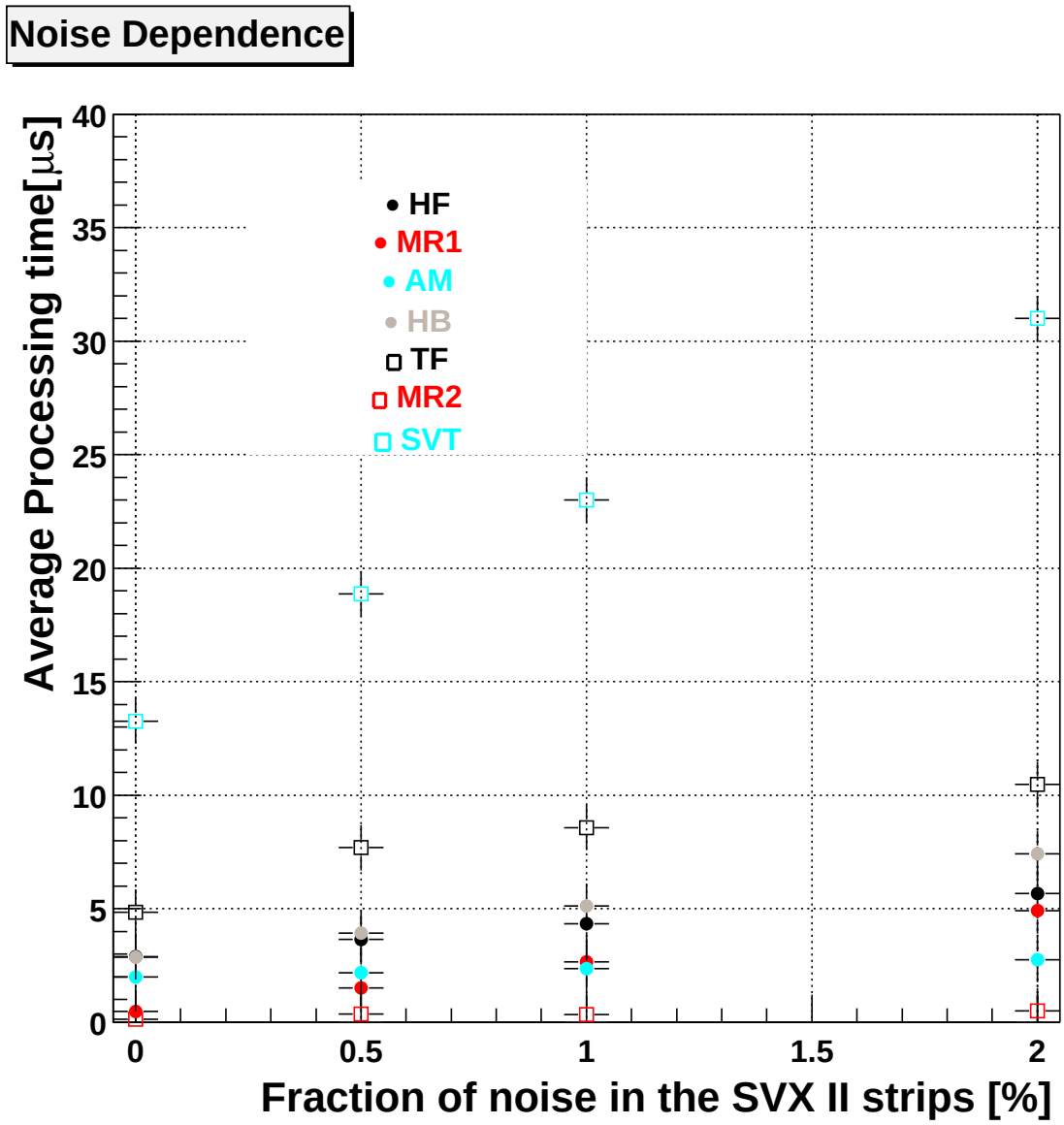

Figure 3.28: *Dependence of the average processing time of* SVT *on the amount of hits due to electronic noise in the silicon microstrips. VH events have been used.*

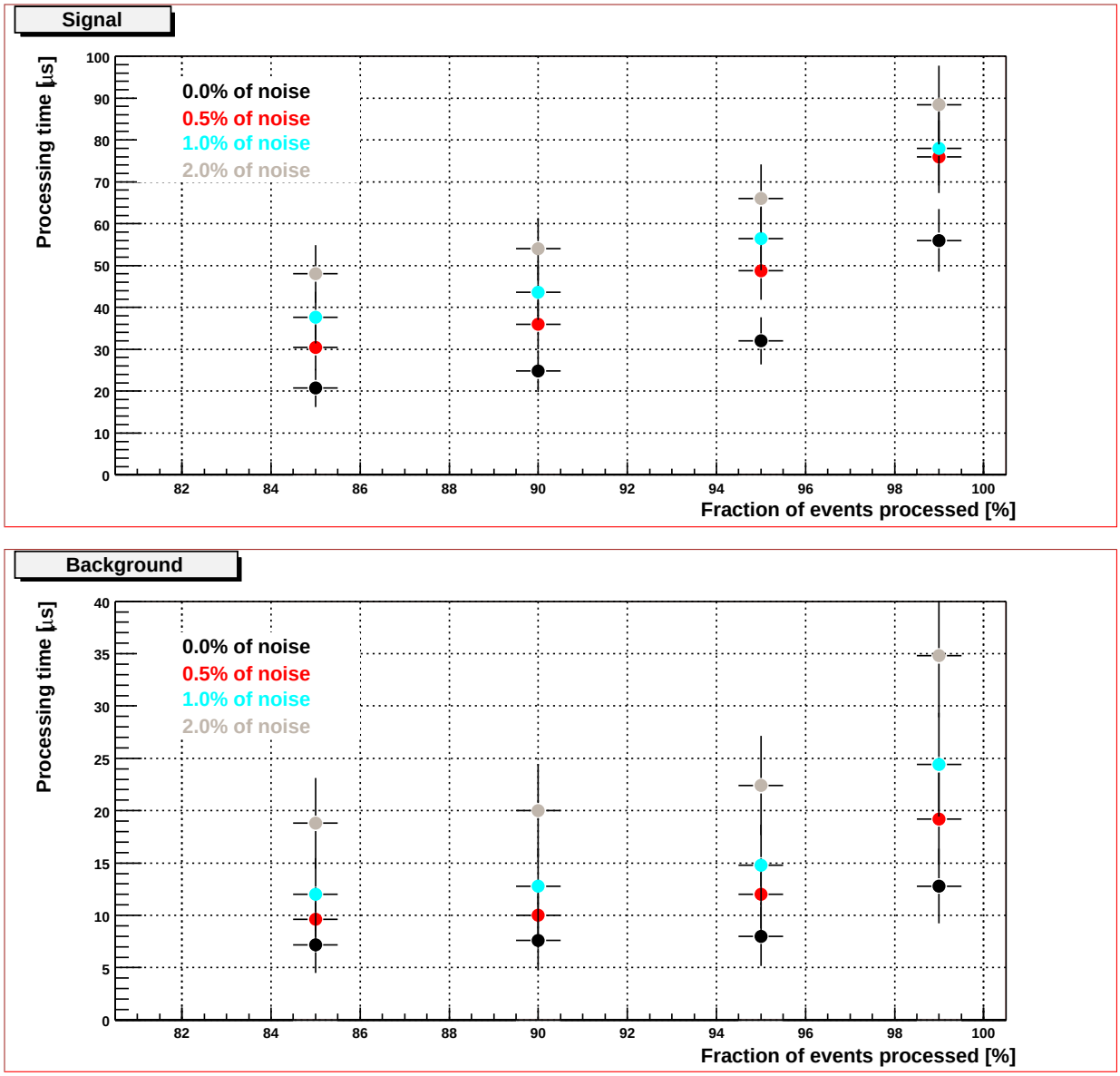

Figure 3.29: *These plots show the total time to process a given fraction of VH signal with $M_H = 120\ GeV/c^2$ (on the top), and a given fraction of background events (on the bottom), as a function of the noise set on the silicon strips.*

Proposal of SVT Requirements for the Multijet Trigger

We have studied the feasibility to use the new Silicon Vertex Tracker for a Level 2 selection based on high impact parameter tracks in a multijet environment. We found a selection requiring two SVT tracks with impact parameter larger than 100 μm appears a stable, conservative method to collect heavy flavor decays; the efficiency on all hadronic final states of Higgs associated production events results to be $(50 \pm 2)\%$ after calorimetric requirements, while background is reduced at (1.7 ± 0.2) Hz. A larger-than-estimated amount of noise in the silicon microstrips does not seem to have a large impact in the effectiveness of this selection criteria, although it does produce a non-negligible increase in background rates. In those conditions, if rates become an issue, a stricter cut on the fit χ^2 of SVT tracks (lowered from 12.6 to 10 or even 8) could be considered a valid choice.

It appears critical to perform a cleanup of the set of identified SVT tracks to reject multiplets of fakes extrapolating to the same XFT slice on COT superlayer 6. Given the availability of the information on the XFT seed of each found SVT track, we propose a very simple prescription for that task, which performs very well in our simulations; however, the possibility of implementing it needs verification. In the absence of such a cleanup, the effectiveness of impact-parameter-based selections on multijet events seems dubious.

Multijet events take on average 8 μs to be tracked by SVT; this number depends strongly on the noise level in the silicon. The distribution of processing time has long tails: these imply that a cutoff in the time available to SVT before a decision is taken by the Level 2 processors would have a dangerous impact on the efficiency on VH events, which take ~ 76 μs to be tracked at 99%. However, thanks to the reduced rate of events passing Level 1 requirement (~ 2.7 kHz), dead time caused by a delayed Level 2 decision appears to be small.

3.4 Level 3

Level 2 rate obtained by requiring at least two SVT tracks with impact parameter $|d| \geq 100$ μm is already compatible with the Level 3 bandwidth (see Sec. 2.6). Consequently, Level 3 requirements are aimed at keeping an high efficiency on signal events, and possibly at improving the purity of the multijet+heavy flavour collected sample. An high capability of background rejection could eventually allow to loose the Level 2 requirements, and recover in such way efficiency on VH production. We deal with these topics in the next two subsections.

Finally, in the last subsection we describe the results obtained by means of a different strategy of heavy flavour tagging, essentially based on the search for electrons and muons produced in the semileptonic decays of heavy quarks. As mentioned in Sec. 3.1, it represents a complementary approach to that we investigeted in this chapter.

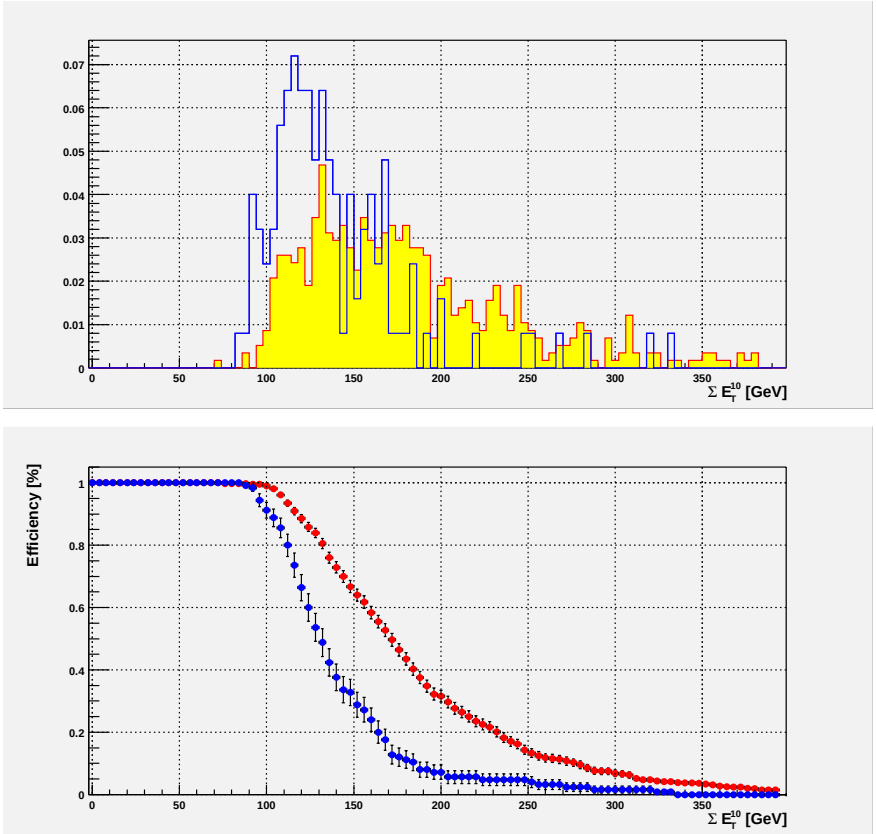

Figure 3.30: *Top: ΣE_T distribution for signal (shaded histogram) and background (white) events. Bottom: Efficiencies of the requirements $\Sigma E_T \geq$ cut on VH (light bullets) and* QCD *(dark) production as a function of the cut value.*

3.4.1 Calorimetric Requirements

At Level 3, calorimetry requirements essentially are aimed at confirming the Level 2 requirements; in particular, the events passing the Level 3 should have at least 3 jets reconstructed with a cone $R = 0.4$ and with a transverse energy $E_T \geq 10\ GeV$. Similarly, a requirement on ΣE_T^{jet} is set. Fig. 3.30 shows the efficiencies on signal and background events as a function of the cut value on the total transverse energy. We find a $\Sigma E_T^{jet} \geq 100\ GeV$ requirement is fully efficient on VH production, while allowing to slightly reduce the rate.

3.4.2 Level 3 Tracking Studies

We have studied the feasibility of a Level 3 confirmation of the SVT tracking requirements. It would be expected to clean the trigger selected sample from events passing Level 2 due to fake tracks. So far, the available software for Level 3 track reconstruction suffer a too long processing time to be effectively used in a trigger procedure. However, tracks reconstructed by using only COT hits should be available at Level 3. Study for a Level 3 confirmation of the SVT tracking requirements

Rate	Efficiency				
	110 GeV/c^2	115 GeV/c^2	120 GeV/c^2	125 GeV/c^2	130 GeV/c^2
(1.5 ± 0.2) Hz	$(31 \pm 2)\%$	$(33 \pm 2)\%$	$(34 \pm 2)\%$	$(35 \pm 2)\%$	$(37 \pm 2)\%$

Table 3.5: *Trigger rate and efficiency on VH production for some values of the Higgs boson mass M_H. Errors are statistical only.*

by means of COT tracks are in progress. For the time being, the multijet+ heavy flavour trigger has been implemented at the CDF II experiment with the following requirements:

- LEVEL 1: single trigger tower with transverse energy $E_T \geq 10$ GeV;
- LEVEL 2: at least three hadronic clusters with $E_T^{cl.} \geq 10$ GeV and $\sum E_T^{cl.} \geq 90$ GeV AND at least two SVT with impact parameter $|d| \geq 100$ μm;
- LEVEL 3: at least three jets (reconstructed with cone radius $R = 0.4$) with $E_T^{jet} \geq 10$ GeV and $\sum E_T^{jet} \geq 100$ GeV.

Expected trigger rate and efficiencies are summarized in Tab. 3.6. Efficiencies have been computed on $VH \to q\bar{q}^{(\prime)}b\bar{b}$ events with an Higgs boson mass M_H ranging from 110 to 130 GeV/c^2. The samples used consist of about 1,500 events generated with the same prescriptions we described in the Subsec. 5.2.

3.4.3 Soft Lepton Based Trigger

A multijet+heavy flavour trigger based on the search for low P_T leptons produced in the semileptonic decays of heavy quarks has been proposed [4]. The calorimetric requirements are the same we discussed in this chapter. Instead of Level 2 requirements on SVT tracks, a reconstructed lepton is required at Level 3. The identification of the lepton is based on the soft lepton tagging algorithm (SLT) described in the Subsec. 2.4.4 and 2.5.1.

Fig. 3.31 shows rate and efficiency achievable through this trigger as a function of the requirement on $\sum E_T^{jet}$. Both a single and a double lepton requirements have been considered. As for the SVT-based trigger, a cut $\sum E_T^{jet} \geq 100$ GeV has been established. Final proposal for the multijet+SLT trigger is:

- LEVEL 1: single trigger tower with transverse energy $E_T \geq 10$ GeV;
- LEVEL 2: at least three hadronic clusters with $E_T^{cl.} \geq 10$ GeV and $\sum E_T^{cl.} \geq 90$ GeV;
- LEVEL 3: at least three jets (reconstructed with cone radius $R = 0.4$) with $E_T^{jet} \geq 10$ GeV and $\sum E_T^{jet} \geq 100$ GeV AND at least one soft lepton tag.

Rate	Efficiency		
	110 GeV/c^2	120 GeV/c^2	130 GeV/c^2
1.43 Hz	14.3%	16.2%	17.3%

Table 3.6: *Trigger rate and efficiency on VH production for some values of the Higgs boson mass M_H. Errors are statistical only.*

Tab. 3.6 summarizes the expected rate and efficiencies for this trigger.

The studies presented here have been performed with the CDF I software, the estimates of the trigger rates are based on a JET20 data sample collected during Run I (see Sec. 3.3.1), and soft lepton tagging algorithm used has been developed and optimized for the old CDF detector. Actually, a SLT algorithm based on the CDF II software framework has not been implemented yet. In the following of this work, we will refer to the multijet+heavy flavour trigger as the SVT-based one. Future plans are to exploit both trigger strategies to improve the efficiency on the Higgs boson associated production.

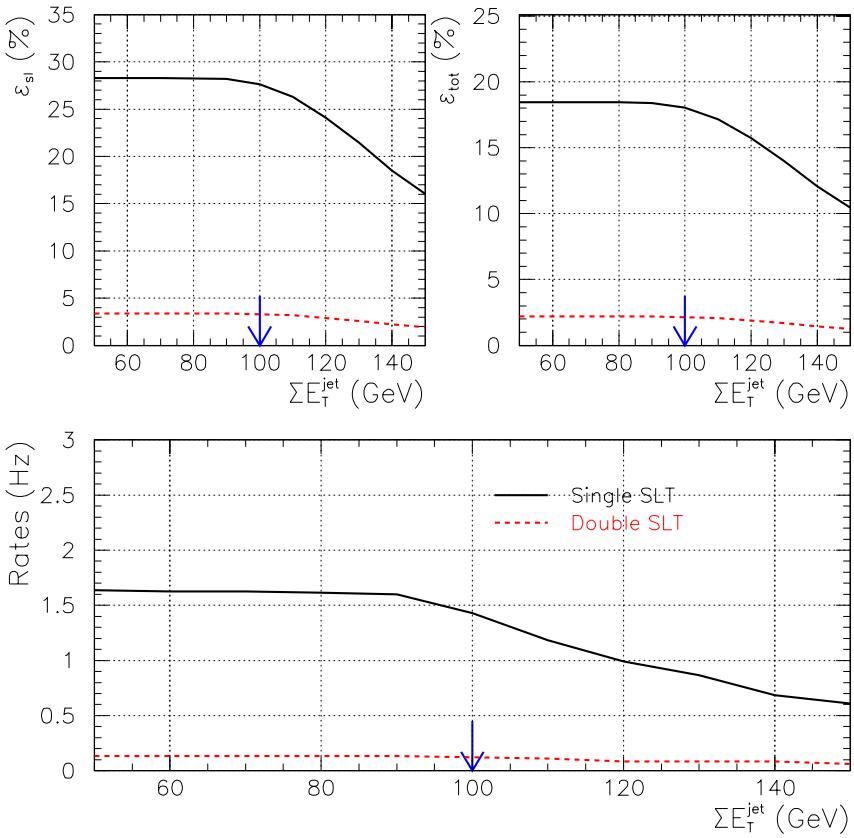

Figure 3.31: *Top: Efficiency of single (full line) and double (hatched) soft lepton requirement on VH events where a semileptonic decay occurred (left) and on all the all hadronic final state events. Bottom: expected rate after single (full line) and double (hatched) soft lepton requirement. Efficiency and rates are shown as a function of the requirements on the $\sum E_T$.*

Bibliography

[1] J. Benlloch et al., *The multijet data sample*, CDF internal note 2916, Dec 1994.

[2] F. Abe et al. (The CDF Collaboration), *Evidence for top quark production in $p\bar{p}$ collisions at $\sqrt{s}=2\ TeV$*, Phys. Rev. **D 50**, 2966 (1994).

[3] J. Troconiz et al., *Search for Higgs Bosons Produced in Association with a Vector Boson in $p\bar{p}$ Collisions at* 1.8 *GeV*, Phys. Rev. Lett. **81**, 5748 (1998).

[4] M. P. Giordani, *A Run II Trigger Design for Higgs Boson Search at CDF*, Ph.D. thesis, Dec 2000.

[5] J. Lewis et al., *Guide to Run II Trigger Simulations*, CDF internal note 4321, Sep 1997.

[6] `http://www.thep.lu.se/tf2/staff/torbjorn/Pythia.html`.

[7] M. Albrow et al. (The CDF Trigger and Datasets Working Group), *Run-II Trigger Table and Datasets Plan*, CDF internal note 4718, Aug 1998.

[8] S. Belforte et al., *Silicon Vertex Tracker Technical Design Report*, CDF internal note 3108, Apr 1995.

[9] S. Belforte et al., *Specification of the XTRP,* SVT*, and Level 2 Interfaces*, CDF internal note 4578, May 1998.

[10] G. Busetto, D. Lucchesi, G. Punzi, *Performances Comparison of* SVT *in the Baseline Configuration and with Layer 00*, CDF internal note 5134, Sep 1999.

[11] G. Chlachidze, V. Glagolev, G. Punzi, *Timing for the* SVT *Trigger*, CDF internal note 5021, May 1999.

Chapter 4

Trigger Validation on Real Data

The CDF II *experiment began to take data in March* 2001. *During this time, the Tevatron collider operated at low instantaneous luminosity* ($\mathcal{L} < 10^{31}\ cm^{-2}s^{-1}$) *and only* $\sim 14\ pb^{-1}$ *of data have been collected. Besides, a lot of elements of the* CDF *detector were not yet fully operational and several working conditions changed with the different data taking periods* (runs). *However, collected data can be effectively used for useful tests on detector and trigger devices.*

In this chapter, a study of collected data to confirm the trigger rate estimates of the last chapter is presented.

4.1 Level 1 and Level 2 Calorimetric Trigger

In order to check calorimetric trigger rates we use a sample of data selected with a trigger path named *SingleTower10*, which requires at Level 1 only a single trigger tower with $E_T \geq 10\ GeV$, *id est* the same requirement of the multijet trigger we proposed. At Level 2, the *SingleTower10* trigger path makes no requirement, while at Level 3 events are prescaled by a factor of 50, in order to limit the high rate of the data. In this way, no biases are introduced on the Level 1 selected events, that result to be the most natural sample to study the performance of the multijet trigger.

For each level, rates are monitored directly during tha data taking and recorded at each run on a database. Cross sections can be then computed by dividing the measured rates by the average instantaneous luminosity of the run. Fig. 4.1 (top left) shows the so obtained cross section of the multijet Level 1 trigger for a set of runs collected from August to the beginning of October 2001. The rates extrapolated to the project luminosity of $10^{32}\ cm^{-2}s^{-1}$ turn out to have an average value $R_{L_1} \sim 2.3 \pm 0.1\ kHz$, rather close to the expected rate of about $2.7\ kHz$ (see Sec. 3.2).

Due to the event superposition, calorimetric cross section could increase with the instantaneous luminosity. To monitor this effect, we look at the cross section as a function of the luminosity. Result is shown in Fig. 4.1 (top right). A fit to a straight line has been performed. The Level 1 cross section seems to increase with the instantaneous luminosity. However, we note a sharp increase of the cross section starting from the run 126730 (collected in September 15th). This suggests

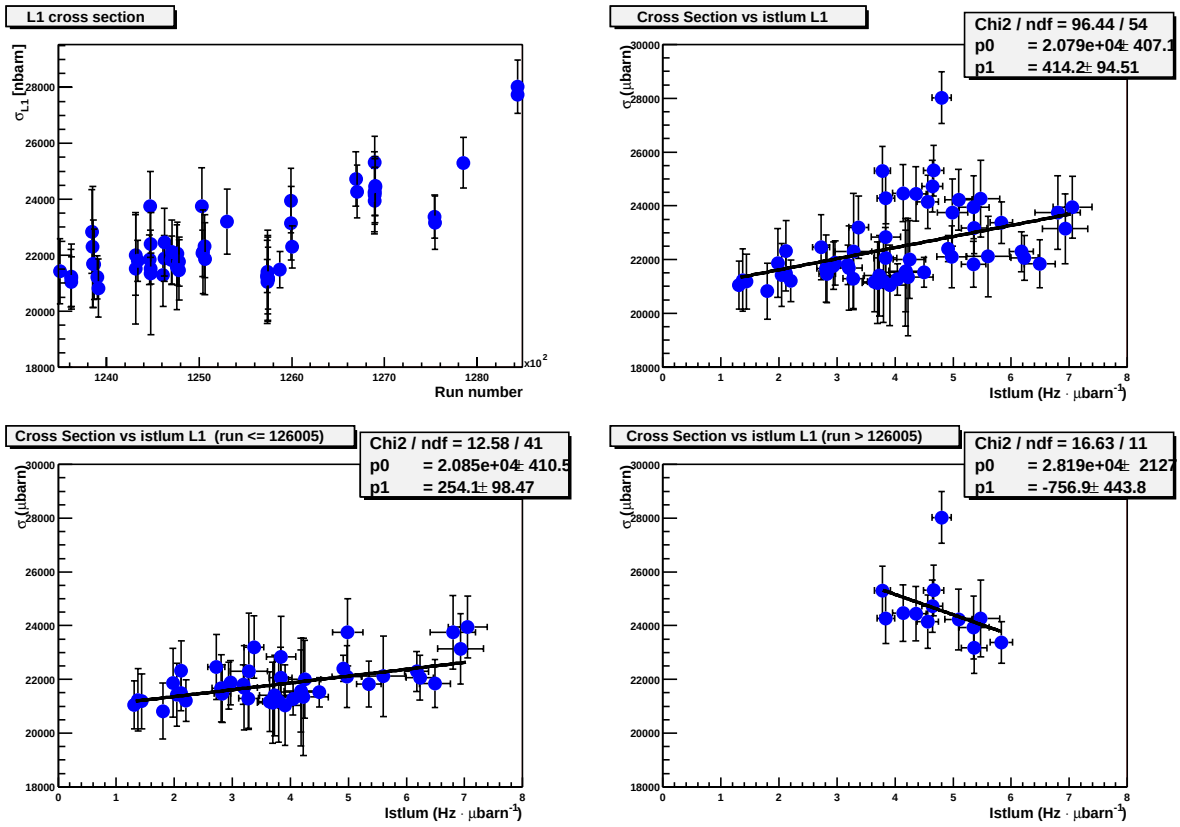

Figure 4.1: *Top: Level 1 cross section as a function of the run number N_{run} (left) and of the instantaneous luminosity (right). Bottom: Level 1 cross section as a function of the instantaneous luminosity for $N_{run} <= 126005$ (left) and for $N_{run} > 126005$ (right).*

the observed increase of cross section is due to a changing in the run conditions. Actually, several problems was found in the calorimetric trigger banks of the events colleted during August: some primitives showed a slight mismatch with the trigger response. In particular, the distributions of trigger tower transverse energy for events collected with *minimum bias* trigger paths[1] exhibited a certain inconsistency with the information stored in the trigger banks. This problems were afterwards solved. However, they could have biased our data. Fig. 4.1 (bottom) show the Level 1 cross section as a function of the luminosity for run after and before the run 126730 separately. We find a very different behaviour for the two classes. Cross section measured in runs collected after the September 15th are definitely higher than the preceding ones. We fit them to a costant and take the result as estimate of the Level 1 cross section for the multijet trigger. It predicts a rate $R_{L_1} \sim 2.46 \pm 0.03\ kHz$ at the project luminosity.

[1]The minimum bias trigger paths make requirements only on the coincidence between the signal of beam-beam counters located in opposite sides of the detector (see Sec. 2.1.6).

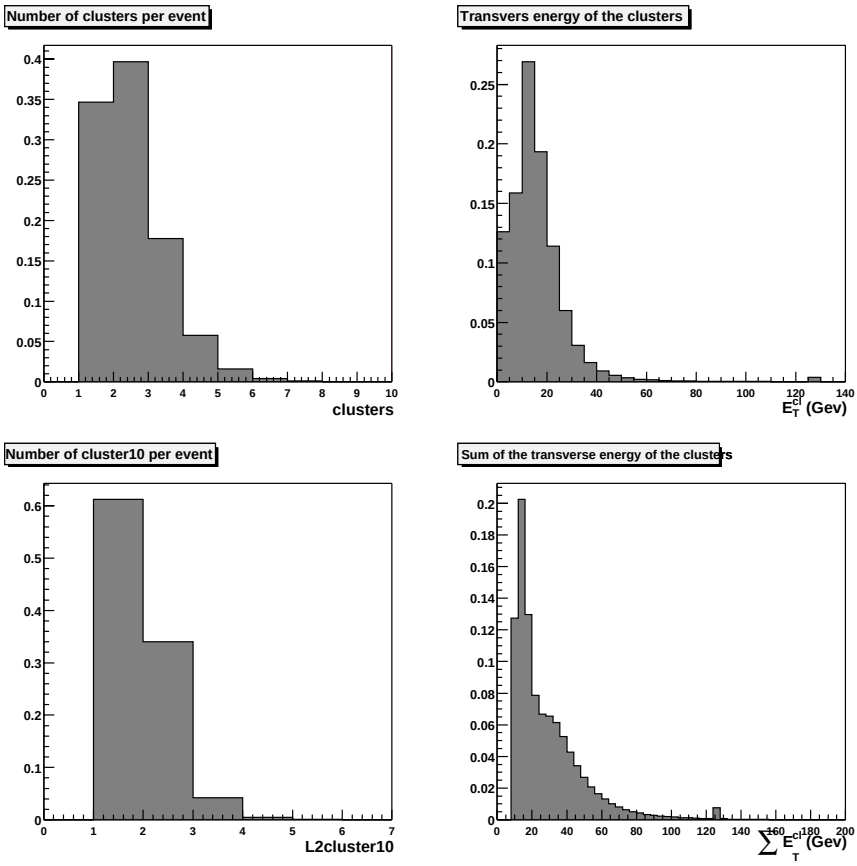

Figure 4.2: *Level 2 calorimetric primitive distributions for events selected by the* SingleTower10 *trigger path. From top left clockwise: number of Level 2 clusters in the event, transverse energy of the clusters, number of clusters with* $E_T \leq 10\ GeV$ *in the event, and sum of their transverse energy.*

During this first period of data taking, Level 2 hardware devices have met a lot of problems. In particular, Level 2 calorimetric primitives were not available. In order to perform our studies, we have therefore to simulate them by applying offline the clustering algorithm to the data. We use the events collected by the *SingleTower10* trigger path. Results are shown in Fig. 4.2. For each run, we compute the Level 2 cross section of the multijet trigger by rescaling the Level 1 cross section by the relative efficiency of its calorimetric requirements[2] (see Fig. 4.2. We obtain $\sigma_{L_2} \sim 149 \pm 4\ \mu b$, that results in a Level 2 calorimetric rate $R_{L_2} \sim 14.9 \pm 0.4\ Hz$ for $\mathcal{L} = 10^{32}\ cm^{-2}s^{-1}$ (see Fig. 4.2, top right). It is in very good agreement with the value we estimed in Chap. 3 ($\sim 15.4 \pm 0.8\ Hz$). However, we have to study the effect of the bias we found for Level 1 primitives on this estimate. We look at the cross section as a function of the luminosity: the result we find (see Fig. 4.3, top left) seems to indicate a slight dependence of the Level 2 calorimetric rate on the luminosity, even if it is compatible with a null dependence within 3σ. Fig. 4.3

[2]To recall it: ≥ 3 clusters with $E_T \geq 10\ GeV$ and $\Sigma E_T \geq 90\ GeV$.

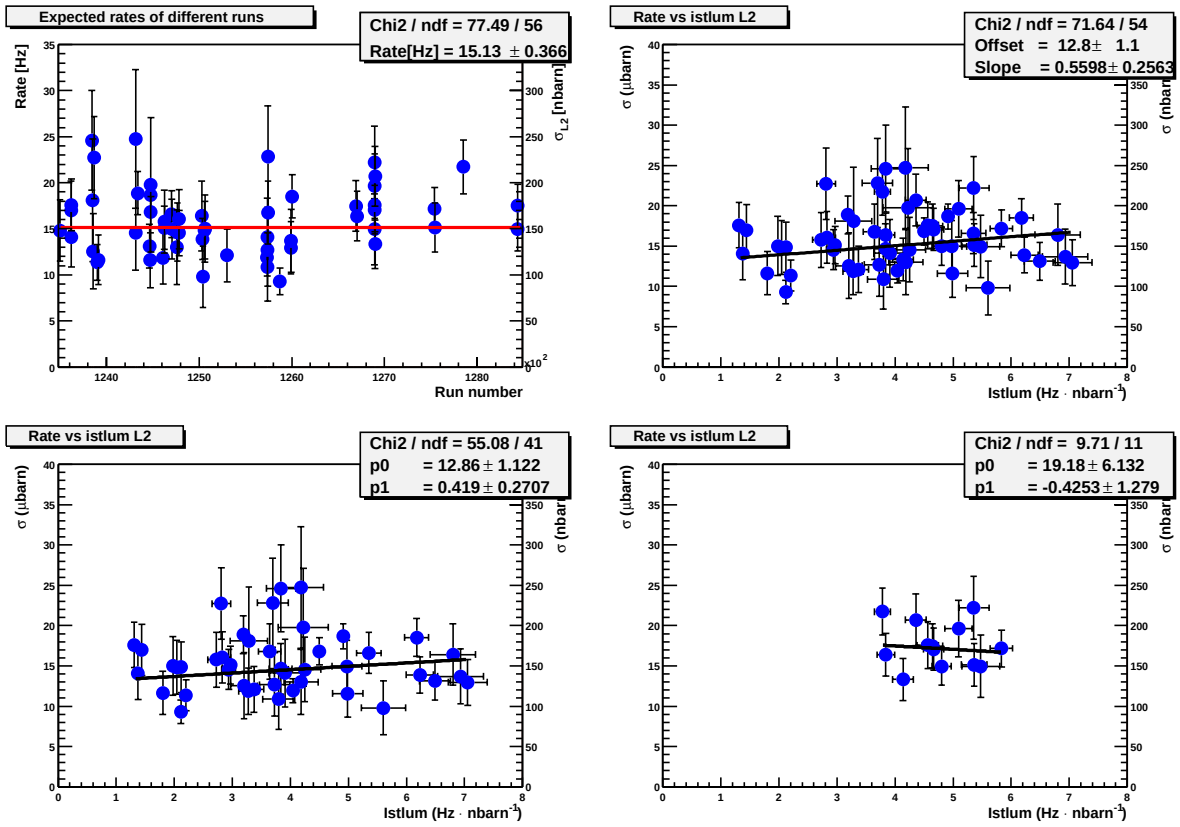

Figure 4.3: *Top: Level 2 cross section and extrapolated rate as a function of the run number N_{run} (left) and of the instantaneous luminosity (right). Bottom: Level 2 cross section and extrapolated rate as a function of the instantaneous luminosity for $N_{run} <= 126005$ (left) and for $N_{run} > 126005$ (right).*

(bottom) shows Level 2 cross section and rate as a function of the luminosity for run after and before the run 126730 separately. No significant dependence on the luminosity is exhibited. The two classes of run predict a Level 2 rate value of $R_{L_2} \sim 14.5 \pm 0.4$ and $R_{L_2} \sim 17.2 \pm 0.8$ Hz at the project luminosity respectively. The two estimate are quite different. We take the second one (runs collected after September 15th) as final estimate of the Level 2 multijet trigger rate.

4.2 Study of SVT Requirements

A lot of problems affected SVT performances during the first period of data taking:

- not all the SVX layers were active;
- beams alignment with the geometrical detector axis was not optimized and on-line correction system had yet to be tested;

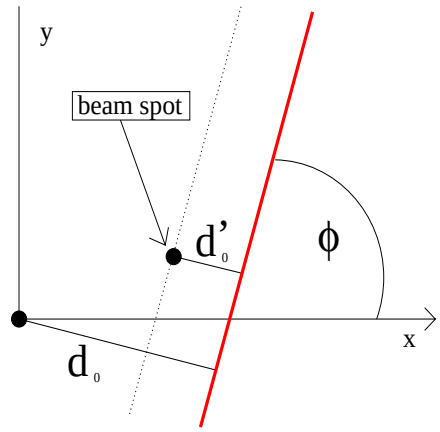

Figure 4.4: *Effect of a beam displacement from the z axis on impact parameter determination.*

- SVT system was not working at its full capability. In particular, superstrip size in the associative memory was increased to 500 μm instead of 300 μm;
- SVT reconstruction efficiency was estimated to be about 70% of the expected value due to not yet full understood problems in the arrangement of various SVT devices.

Furthermore, working conditions were continually changing so that different set of runs need to be treated separately. In the following, we describe the solutions we adopted to get *reasonable* estimate of the effect our SVT requirements have on the level 2 trigger rate.

In order to get more statistics, we use data collected by the *Jet_20_No_L2* trigger path, which requires 2 trigger towers with $E_T \geq 5\ GeV$ at level 1 and a jet with $E_T \geq 20\ GeV$ at level 3. Events are then prescaled by a factor of 20 instead of 50 like for *SingleTower10* trigger path. This results in a ~ 3 times larger sample after our level 2 calorimetric requirements. No biases are expected to be introduced on the selected events.

4.2.1 Beam Position Correction

SVT measures track parameters by supposing the beam along the geometrical axis of the detector. In particular, the impact parameter d_0 is computed with respect to such axis. A misalignment between beam direction and z axis results therefore in a wrong measurement of this parameter. The situation is shown in Fig. 4.4.

In order to get more accurate values of d_0, an on-line correction system has been provided to SVT. The task of this device consists in monitoring the beam position by measuring its x and y coordinates at the center of each SVX semibarrel. Impact

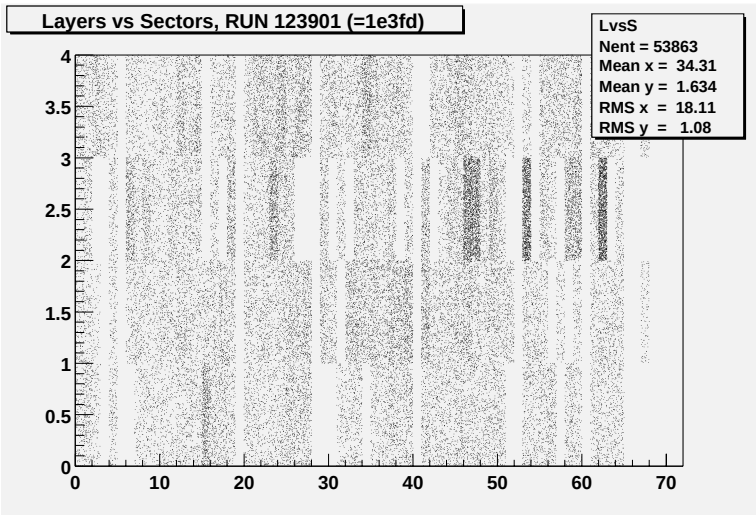

Figure 4.5: *Distribution of the reconstructed hits in the* SVX II *detector for a specific run (*123901*). The x (y) axis shows the number of* SVX II *sector (layer) where the hit has been detected. The active layers are well recognizable.*

parameters can then be corrected according to the relation

$$d_0^{corr} = d_0^{SVT} + x_B sin\phi - y_B cos\phi \ , \tag{4.1}$$

where ϕ is the azimuthal angle of the track as measured by SVT and x_B (y_B) the x (y) beam position in correspondence to the semibarrel B the track has been reconstructed in.

The correction system was not fully operative for long time during this first data taking period, therefore only a poor event sample is available. It has been collected from the mid-September to the end of October. After multijet calorimetric requirements, we have about 2000 events to analyze.

4.2.2 Extrapolation to the Complete Detector

A map of the active silicon region can be obtained by plotting the number of layer vs the number of sector[3] for all the reconstructed hits. Fig. 4.5 shows an example of this map for a specific run. Only SVX layers used by the active SVT configuration are shown.

Since SVT requires hit on each layer of a single sector to reconstruct a track, we develop the following procedure to extrapolate its results to a fully working detector regime:

- each sector has been considered *active* only if all its four silicon layers were active;
- the fraction f_B of active sectors in each semibarrel B has been computed;

[3]We remember that a sector is a ϕ-wedge of a specific SVX semibarrel. See also Sec. 2.6.2.

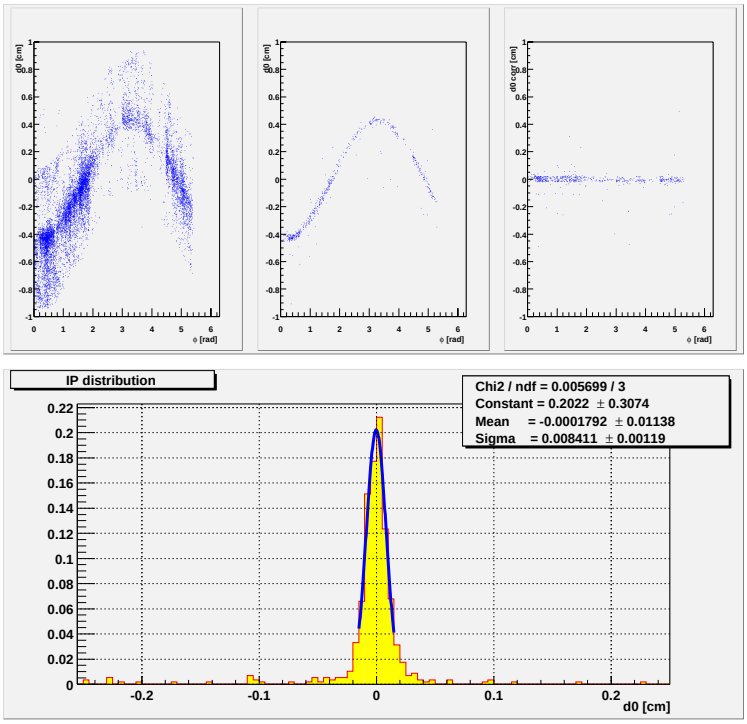

Figure 4.6: *Impact parameter correction for the considered runs. Top: correlation between impact parameter d_0 and azimuthal angle ϕ of the* SVT *tracks. On the left, all the track have been considered. In the middle, only tracks reconstructed with $\chi^2 < 12.6$ and $P_T \geq 2$ GeV/c are shown. On the right, same as the middle plot after the correction on the impact parameter. Bottom: distribution of the corrected impact parameters.*

- the expected number of lost tracks N_{lost} in each semibarrel has been determined event by event as
$$N_{lost} = N_{obs.}(1 - f_B)/f_B \ , \tag{4.2}$$
where $N_{obs.}$ is the number of tracks reconstructed in the semibarrel;

- the number $N_{add.}$ of tracks to add to the reconstructed ones has been computed by extracting a random number according to a poissonian distribution with mean N_{lost};

- an impact parameter has been assigned to each of the $N_{add.}$ tracks according to the d_0 distribution of the tracks reconstructed in the semibarrel, and the results have been used to make trigger decision.

The map of the SVX active region has been updated at each run. This is an approximated procedure. It assumes that the number of lost tracks is proportional to the not active fraction of SVX sectors. This is a reasonable hypothesis on average, but it does not takes into account the possible correlations in the distribution of the

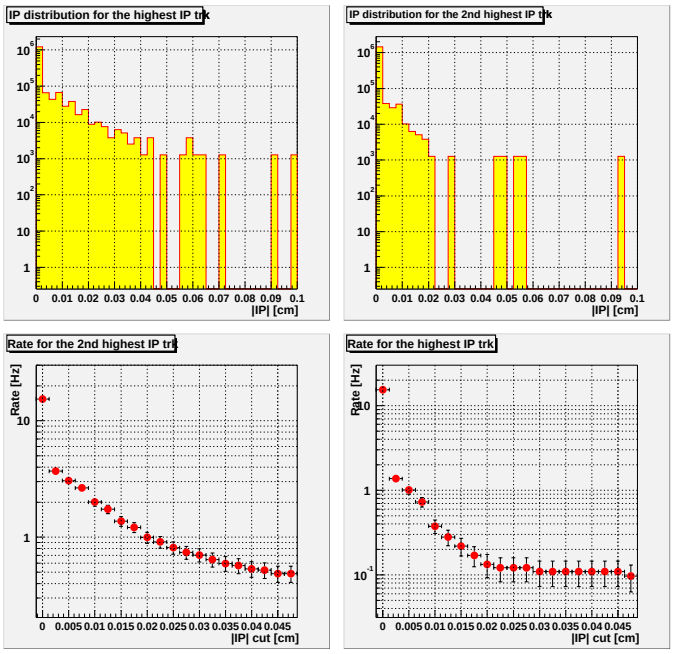

Figure 4.7: *Estimated Level 2 rate on real data. The extrapolation to the complete detector has been performed. Top: distributions of the highest (left) and 2nd highest (right) track impact parameter in the event. Bottom: expected Level 2 rate as a function of the requirement on the highest (left) ans 2nd highest (right) track impact parameter.*

azimuthal angle ϕ of the SVT tracks in the same event. The results quoted in the following section have therefore to be considered as preliminary.

4.2.3 Preliminary Estimate of the Rate after SVT Requirements

The Level 2 multijet trigger requires at least two tracks with transverse momentum $P_T \geq 2\ GeV/c$ and impact parameter $d_0 \geq 100\ \mu m$. In this section, we consider also the possibility to require only one SVT track. Actually, multijet requirements were established by means of Monte Carlo simulation, but eventual differences between simulation and real data have to be studied.

Fig. 4.6 (bottom) shows the distribution of track impact parameters. We fit to a gaussian in order to measure the resolution on d_0. The tails of the distribution are excluded from the fit by requiring that bins contain more then 20% of the entries of the most populated bin. We find a resolution $\sigma = 84 \pm 11 \mu m$. Also shown (top of the figure) is the correlation between impact parameter and azimuthal angle of the tracks before and after the d_0 correction.

Finally, Fig. 4.7 shows the distributions of the highest and 2nd highest track impact parameter in the event (top of the fugure) and the Level 2 rate extrapolated to the project luminosity as a function of the requirement on the impact parameters.

The obtained rates are significantly lower than the expected ones (see Sec. 3.3.2). For example, a requirement $|d_0^{nd}| \geq 100\ \mu m$ on the 2nd highest impact parameter in the event leads to a Level 2 rate $R_{L_2} \sim 0.37 \pm 0.06\ Hz$ instead of $R_{L_2} \sim 1.7 \pm 0.2\ Hz$ as predicted through simulation studies. Several factors can contribute to this result. Due to not yet fully understood problems in the arrangement of various SVT devices, SVT reconstruction efficiency was estimated to be about 70% of the expected value in this first period of data taking. Besides, extrapolation procedure could underestimate the rate due to not considered correlations in ϕ distribution of the SVT tracks. Starting from January, multijet trigger will be used to collect data at the CDF II experiment. The higher statistics provided and the improved status of the SVX detector and SVT device should allow more effective studies of the SVT performances.

Chapter 5

Jet Energy Corrections

The limits set on the Higgs boson production by the analysis of the all-hadronic final states in Run I has surprisingly proven to be competitive to those of the leptonic channels (see Sec. 1.4). Hope are that the all-hadronic decay channel of associated VH production could contribute to the setting of mass limits or to the significance of a signal.

However, the extraction of a VH signal is a very difficult task, needing a lot of work and specific analysis tools. One of the most distinctive characteristics of VH events is the reconstructed mass of the b-$\bar{b}$ pair coming from Higgs decay. An improvement on dijet mass resolution is therefore an important tool in the search of Higgs production.

In the present chapter we show that it is possible to devise an ad hoc *set of jet energy corrections for these events, and improve the relative dijet mass resolution of a Higgs boson decay by more than 30%, with the use of very simple characteristics of the jets, such as the P_T of soft leptons tagged inside the jet, the jet charged fraction, and the jet E_T itself. Since we are interested to increase the sensitivity on the Higgs production through a narrow dijet mass peak, these corrections have been optimized to reduce the fluctuations around the corrected jet energy.*

Finally, a short exposure of new generic jet energy corrections currently to the study at the CDF II *experiment will be given.*

5.1 Introduction

During Run I, CDF collaboration developed effective procedures to improve the resolution on jet energy measurements. We talked shortly about them in Subsection 2.4.2. Although correction parameters and algorithms have not been re-optimized with the upgraded CDF II calorimeter again, they result to work satisfactoryly even on Run II jets (see Fig. 5.1).

Beyond to that, a lot of improvements on jet energy resolution have being studied. In particular, CDF II collaboration are developing a new algorithm to compute calorimetric tower energy, exploiting for the first time the full granularity of the calorimeter and the performances of the tracking system. Preliminary results on

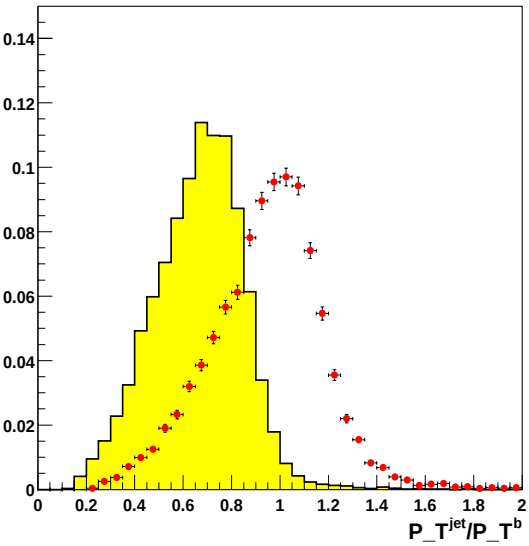

Figure 5.1: *Ratio between transverse momentum of jet and originating b-quark before (histogram) and after (bullets) standard jet corrections are applied. Events were generated with* $M_H = 120\ GeV/c^2$.

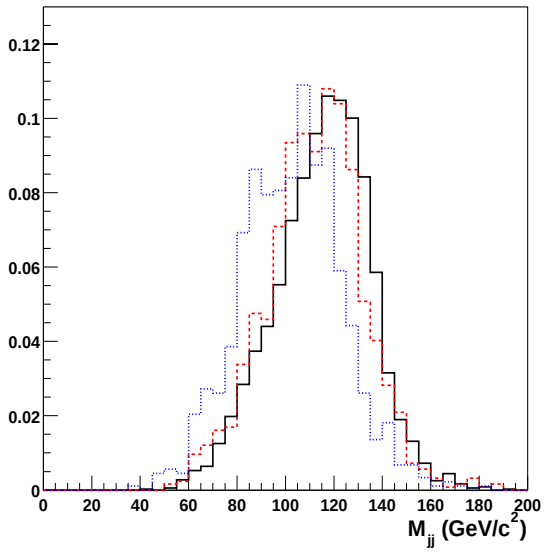

Figure 5.2: *Comparison between reconstructed Higgs mass distribution when a muon (pointed histogram), an electron (hatched) or no lepton (full) is found inside Higgs jet.*

Run I data stress the potentiality of such a strategy. We report shortly about this in Section 5.7.

However, b-jets originating from Higgs decays need of more specific corrections because of energy losses due to muon and neutrinos produced in the decay of heavy flavoured hadrons inside the jet. Fig. 5.2 points out the effects such energy losses have on reconstructed mass of Higgs boson. Worsening is expected in a data sample collected with a soft lepton requirement at level 3.

In conclusion, our studies are focused on b-jet specific corrections, capable to reduce jet uncertainties due to penetrating particles. Unfortunately, status of the software does not allow to performe the proposed work in a CDF II environment: a Run II soft lepton tagging algorithm has not been studied yet, and the lepton simulation itself has again being developed. We decide therefore to use the Run I software to performe our studies. Actually, detector upgrades are not expected to introduce significant differences on jet definition.

In Section 5.2 we describe discuss the general method employed to correct jet energies and the datasets used for the present study. In Section 5.3 we describe in detail the corrections step by step for each of the various categories of events we found useful to define. In Section 5.4 we study the effect of our jet corrections on the Higgs boson resonance. Some checks we performed on the validity of our procedure are described in Section 5.5. In Section 5.8 we present the status of our jet correction studies in a CDF II environment.

5.2 Strategy

The procedure we follow to generate our set of corrections consists of the following steps:

- reconstruct jets with $R = 0.4$ and apply CDF standard jet corrections with out-of-cone and no underlying event corrections[1], requiring an uncorrected transverse energy $E_T \geqslant 10\ GeV$ to define a good jet;
- associate to the b quarks from Higgs boson decays the closest jet in the η-ϕ plane, within a radius $R = 0.4$;
- look for measurable quantities sensitive to the difference Δ between jet energies at detector and generator level;
- look at the distribution of Δ values in bins of the measurable quantity;
- retrieve the mean value of the distribution in each of the bins and plot it;
- fit the mean values as a function of the measurable quantity with a simple functional form;
- invert the relation and apply it to jet variables in order to remove any offset from the true value and reduce their spread.

We perform this analysis using a mixture of five $H^0 + Z^0/W^{\pm}$ samples together, generated using different values of Higgs mass, in order to avoid any sensitivity to the input value of M_H and focus on the full mass range where a $H \to b\bar{b}$ decay may be detectable in Run II.

Only jets reconstructed in a cone of radius $R = 0.2$ around the direction of b quarks from Higgs decays are used in the development of the jet corrections, in order to avoid biases due to the loss of information arising from uncontrollable effects such as, for example, hard gluon radiation or detector cracks. Actually, in those situations no variable is sensitive to the jet energy mismeasurement. The ΔR spectrum is shown in Fig. 5.3. Following the same argument, we compute the average difference in the second step of our procedure twice, the second time using only data within 2 standard deviations from the first result. In this way we are insensitive to the tails of the distributions.

Fig. 5.4 points out the different behavior of the energy mismeasurement of jets with a soft muon tag (referred to as *μ-jets* in the following), jets with a soft electron tag (*e-jets*) and jets with no soft lepton tag (*generic jets*). These are due to the loss of muons and neutrinos in the calorimeter. Therefore we have to develop our corrections independently for these categories of jets. Neutrinos will also be present in a non-negligible amount of generic jets, due to the low efficiency of the soft lepton tagging algorithm. This efficiency could in principle be increased by loosening the lepton identification criteria, if we wished to reduce their contamination to the class of generic jets; however, the scshapeslt requirement is central in the definition of

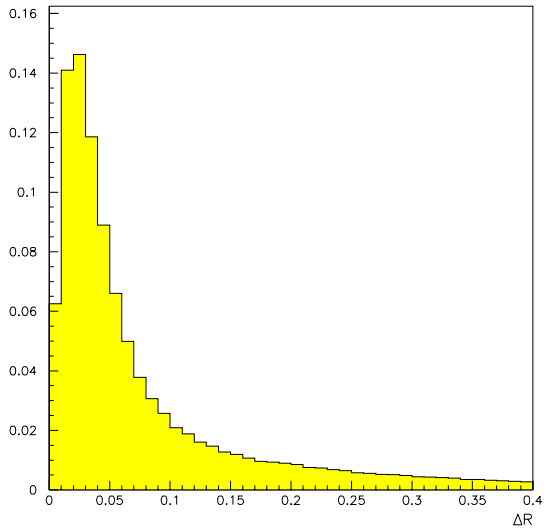

Figure 5.3: *ΔR spectrum of b-quarks from Higgs decays and their nearest jet.*

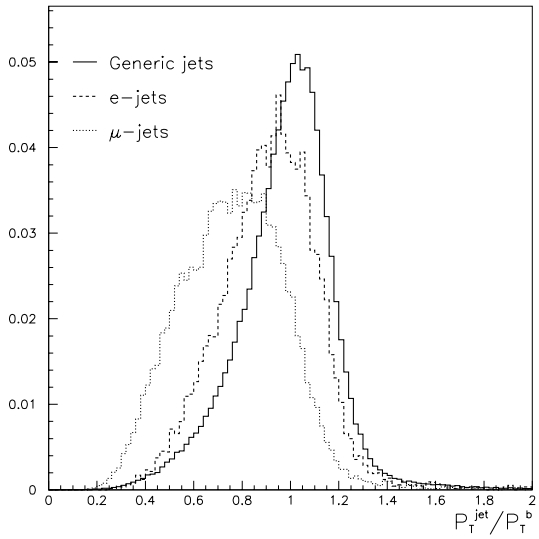

Figure 5.4: *Comparison of P_T^{jet}/P_T^b ratio for generic jets, e-jets and μ-jets.*

a possible trigger level 3 [4] requirement and in the reconstruction of the $H \to b\bar{b}$ decay, so we prefer to keep it unchanged for our corrections.

Finally, following the suggestions of [5] and [6], we look at the momentum P of the tracks tagged by scshapeslt and at the charged fraction and transverse energy of the jets.

Datasets

We use five samples of about 15,000 Higgs associated production (forcing the $H^0 + Z^0/W^\pm \to b\bar{b} + q'\bar{q}$ decays) events each generated at $\sqrt{s} = 2\ TeV$ with the PYTHIA 6.115 [1] Monte Carlo. The Higgs boson mass is set to 110, 115, 120, 125, and 130 GeV/c^2, respectively. A detector simulation is applied to the generated events, then we filter on calorimetric variables simulated through the parametrization of the Run II acceptance (see Sec. 3.2) to simulate calorimetric trigger selection.

We also generate about 2,400,000 events of QCD $2 \to 2$ processes at $\sqrt{s} = 2\ TeV$ with the PYTHIA 6.115 Monte Carlo for some checks on background behavior. After a detector simulation, events are filtered on the calorimetric variables. In the end, we have 18,000 events.

In order to test the independence of our corrections on the fragmentation model chosen, we use also a sample of about 5,000 Higgs direct production events (where the $H^0 \to b\bar{b}$ decay is forced and Higgs mass input M_H is set to 120 GeV/c^2) generated at $\sqrt{s} = 2\ TeV$ with the HERWIG 5.6 [9] Monte Carlo. After the generation, a detector simulation is applied to the events.

Finally, we use two additional samples for some preliminary study on the effects of our corrections on real data: the standard Run I W+JETS sample selected by

the requirements used in the top analysis, amounting to 225 events with $\geqslant 3$ jets and a SLT or SECVTX tag, and a sample of about $24,000$ $t\bar{t}$ events obtained with the PYTHIA 6.115 Monte Carlo (using $\sqrt{s} = 1.8\ TeV$), and selected by the top requirements after a full detector simulation.

5.3 Jet Corrections

5.3.1 SLT Corrections

Muon jets

The muon coming from the semileptonic decay of a B hadron carries almost as much information on the parent momentum vector as the hadronic jet does. First of all, we need to correct the jet direction in order to obtain the best estimate of its parent b quark direction: following again the suggestions of [5], we take as a corrected jet direction the direction of the vector sum of muon and jet momenta.

Successively, we correct the value of jet momentum by studing its mismeasurement $\Delta P = P_b - P_{jet}$ as a function of the momentum P_μ of the track tagged as a muon[1]. Fig. 5.5 shows the result of fitting ΔP to the function

$$-e^{p1+p2\cdot P_\mu} + p3.$$

In order to evaluate the effect of these corrections we compute the improvement on the resolution of jet transverse momentum P_T by fitting the P_T^{jet}/P_T^b ratio before and after corrections (see Fig. 5.5), excluding from the fit the tails of the distributions by requiring that bins contain more then 20% of the entries of the most populated bin. The resolution is defined as the gaussian σ and the improvements corresponds to the relative decrease in σ. Finally, we find that the P_T resolution decreases from $0.232 \cdot P_T^b$ to $0.179 \cdot P_T^b$, i.e. a net improvement of about 23%.

Electron jets

The electron energy is generally well measured in the EM calorimeter, so we do not expect that the electron track P_T measure carries information on the jet energy mismeasurement. However, it could bring some information about the neutrino momentum P_ν. Actually, the only other obvious variable correlated to P_ν, i.e. the missing transverse energy E_T, is very hard to exploit in a multijet environment, due to its very poor resolution. Therefore we try to correct e-jets by looking at the $\Delta P = P_b - P_{jet}$ as a function of the electron momentum P_e, just as we did for μ-jets. Results are reported in Fig. 5.6. We find an improvement in the mean value of jet P_T, which centers closer to the real value, but a worsening of the P_T resolution, which increases from $0.194 \cdot P_T^b$ to $0.195 \cdot P_T^b$. Therefore, we decide to

[1]THE MC_TAGGER module, used to find soft muon candidates in our simulations, only looks at tracks associated to true generated muons. In fact, there could be fake soft muons in the data too. We have found only $\sim 4\%$ of the SLT candidates to be fake in the MC events, therefore we can neglect the effects of the fake soft muons.

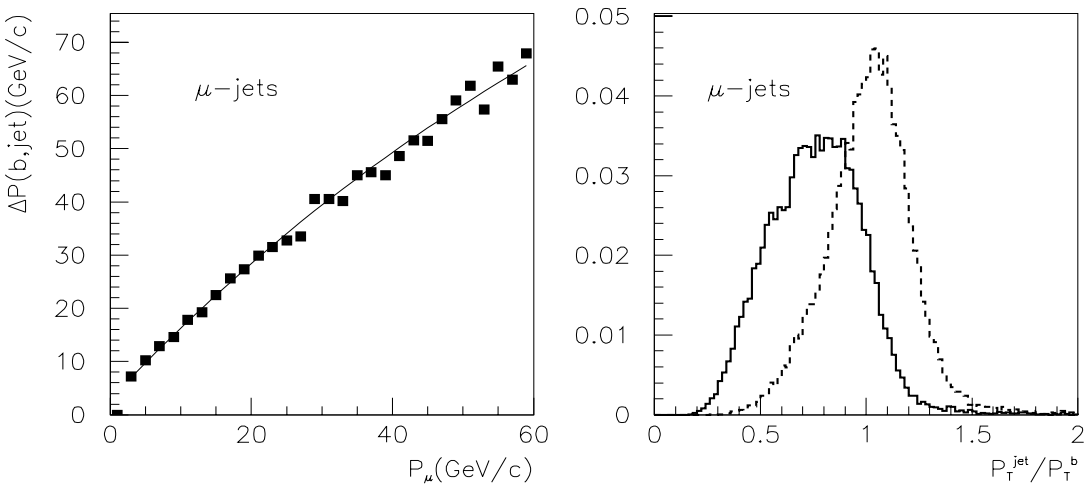

Figure 5.5: SLT *corrections (left) and effect on* P_T^{jet}/P_T^b *ratio (right) for* μ*-jets.*

make no use of the electron momentum, and to leave the task of centering the P_T distribution around its true value to the corrections we are going to discuss in the following subsections.

5.3.2 Charged Fraction Corrections

The P_T resolution of charged hadrons within CTC acceptance is much higher than the resolution of the energy deposit they leave in the calorimeter; however, the fluctuations in the momentum fraction carried by neutral particles in the jets and the relatively small pseudorapidity acceptance of the central tracking prevent a direct use of track P_T to infer the jet momentum. Nevertheless, some valuable information on the parton momentum is extractable from the sum of P_T of tracks included in the jet cones, when the jet falls within the CTC active region. We therefore studied the charged fraction, modifying its definition from the usual CHFR in the JETS bank. We define a corrected charged fraction as

$$CHFR_{corr.} = CHFR_{JETS} \times P_T^{raw}/P_T^{corr.}$$

where P_T^{raw} and $P_T^{corr.}$ are respectively the jet transverse momentum in the JETS bank (before the application of standard corrections) and after all the corrections described up to this point. Thus defined, the charged fraction is decoupled from the effects dealt with precedently, and shows a stronger correlation to the ΔP of the jets.

We observe that the average charged fraction is constant with jet pseudorapidity for $|\eta_{jet}| < 1.1$ (see Fig. 5.7), falling steeply outside that interval. We therefore correct for the charged fraction only the jets in the central region, $|\eta_{jet}| < 1.1$.

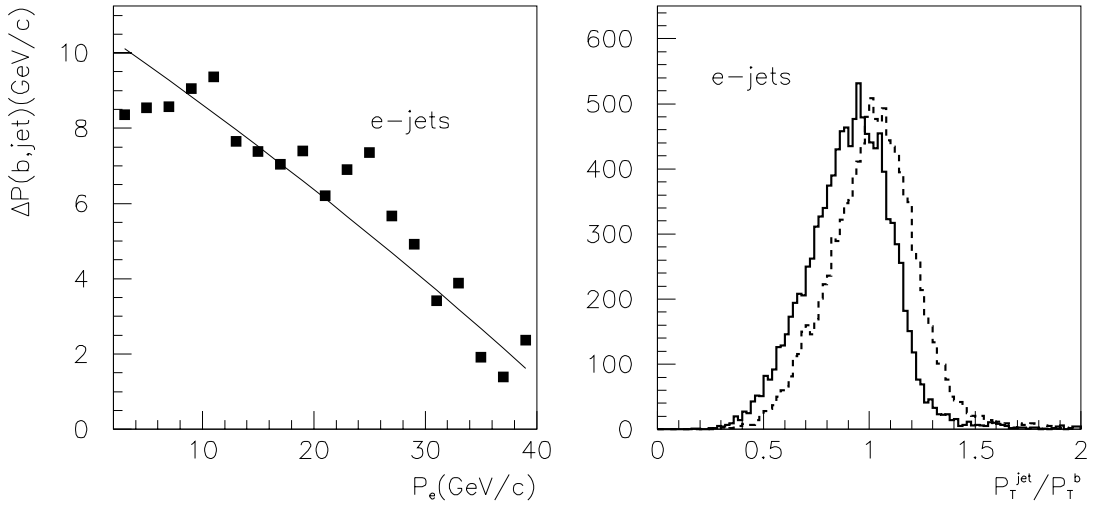

Figure 5.6: SLT *corrections (left) and effect on* P_T^{jet}/P_T^b *ratio (right) for e-jets.*

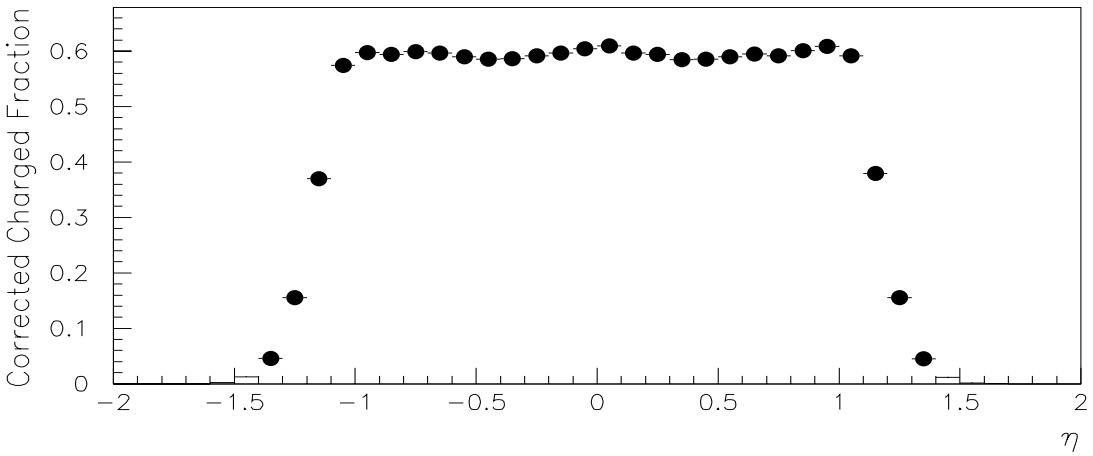

Figure 5.7: *Average charged fraction as a function of jet pseudorapidity.*

Finally, we correct the value of jet P_T by fitting its relative mismeasurement $(P_T^b - P_T^{jet})/P_T^b$ to a function

$$e^{p1+p2\cdot ChF} + p3$$

of the jet charged fraction ChF. Fit results are shown in Fig. 5.8 together with corrections effects on P_T^{jet}/P_T^b distribution. We find an improvement of about 10% (from $0.158 \cdot P_T^b$ to $0.142 \cdot P_T^b$) for generic jets and 4% (from $0.179 \cdot P_T^b$ to $0.172 \cdot P_T^b$) for μ-jets, while we have no improvement on P_T resolution for e-jets. However, since the charged fraction corrections do center the average value of jet P_T closer to the true value, we decide to keep them.

5.3.3 E_T Corrections

As a last correction we study $(E_T^b - E_T^{jet})/E_T^{jet}$ as a function of E_T^{jet}. We need to deal separately with generic jets having $|\eta| < 1.1$ and $|\eta| \geq 1.1$, since they have been corrected in a different way up to this point; e-jets and μ-jets do not need such a treatment since the soft lepton requirement essentially ensures that $|\eta| < 1.1$ for these jets. The functional form used in our fits is:

$$e^{p1+p2\cdot E_T^{jet}} + p3.$$

Fit results and correction effects on jet P_T are shown in Figs. 5.9 and 5.10 for generic and SLT jets respectively. The overall jet P_T resolution improvement turns out to be of about 8% (from $0.142 \cdot P_T$ to $0.130 \cdot P_T$) for generic jets with $|\eta| < 1.1$, 8% (from $0.162 \cdot P_T$ to $0.149 \cdot P_T$) for generic jets with $|\eta| \geq 1.1$, 7% (from $0.194 \cdot P_T$ to $0.180 \cdot P_T$) for e-jets and 3% (from $0.172 \cdot P_T$ to $0.166 \cdot P_T$) for μ jets.

Tab. 5.1 summarizes the performances of all our corrections on the jet P_T.

	mean		resolution	
	before corr.	after corr.	before corr.	after corr.
generic jets ($\|\eta\| < 1.1$)	1.00	1.01	0.158	0.130 (−18%)
generic jets ($\|\eta\| \geq 1.1$)	1.02	1.02	0.162	0.149 (−8%)
e-jets	0.92	1.01	0.194	0.180 (−7%)
μ-jets	0.76	1.01	0.232	0.166 (−28%)

Table 5.1: *Performances of all our corrections on the jet P_T.*

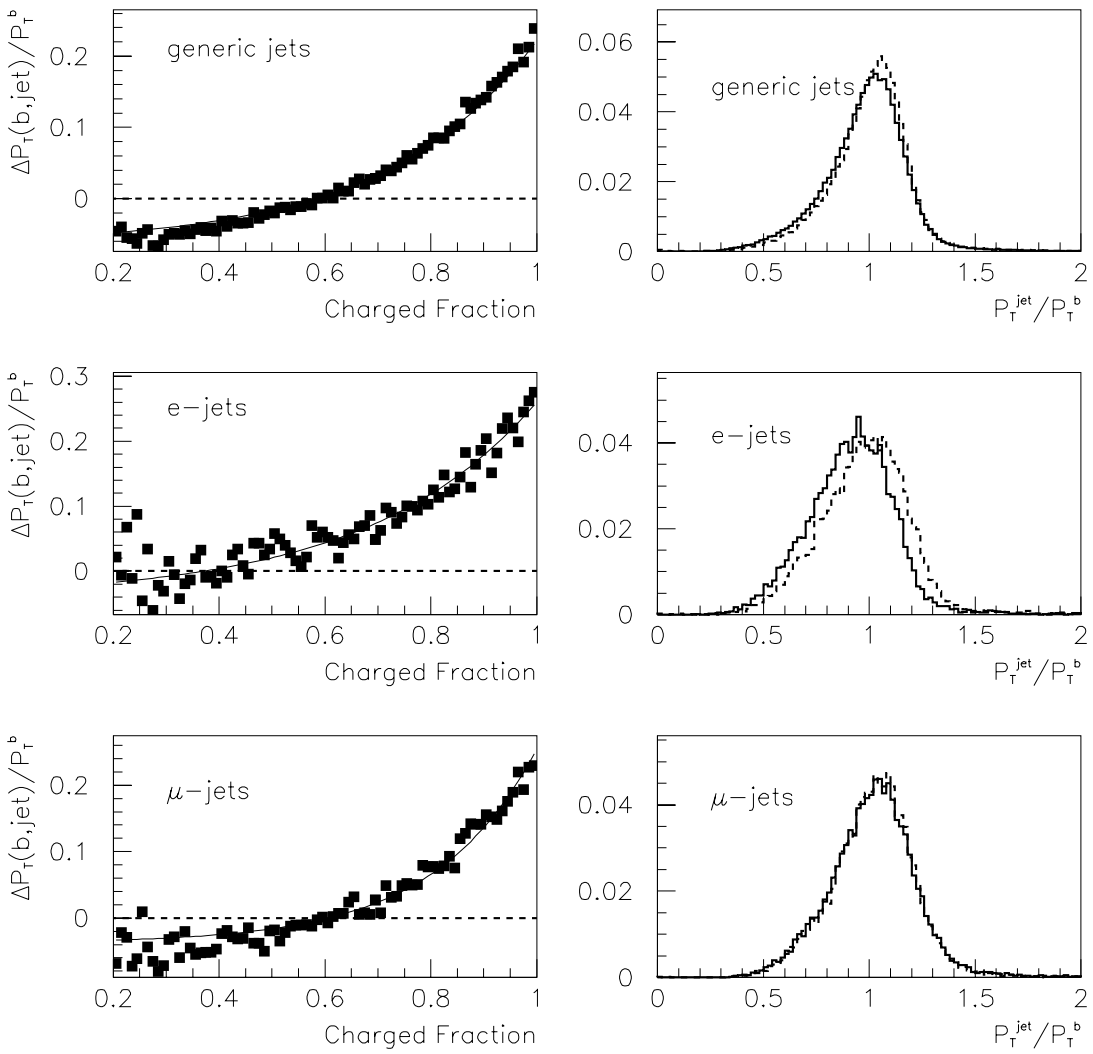

Figure 5.8: *Ch. F. corrections (left) and effect on P_T^{jet}/P_T^b ratio (right) for generic jets (top), e-jets (middle) and μ-jets (bottom).*

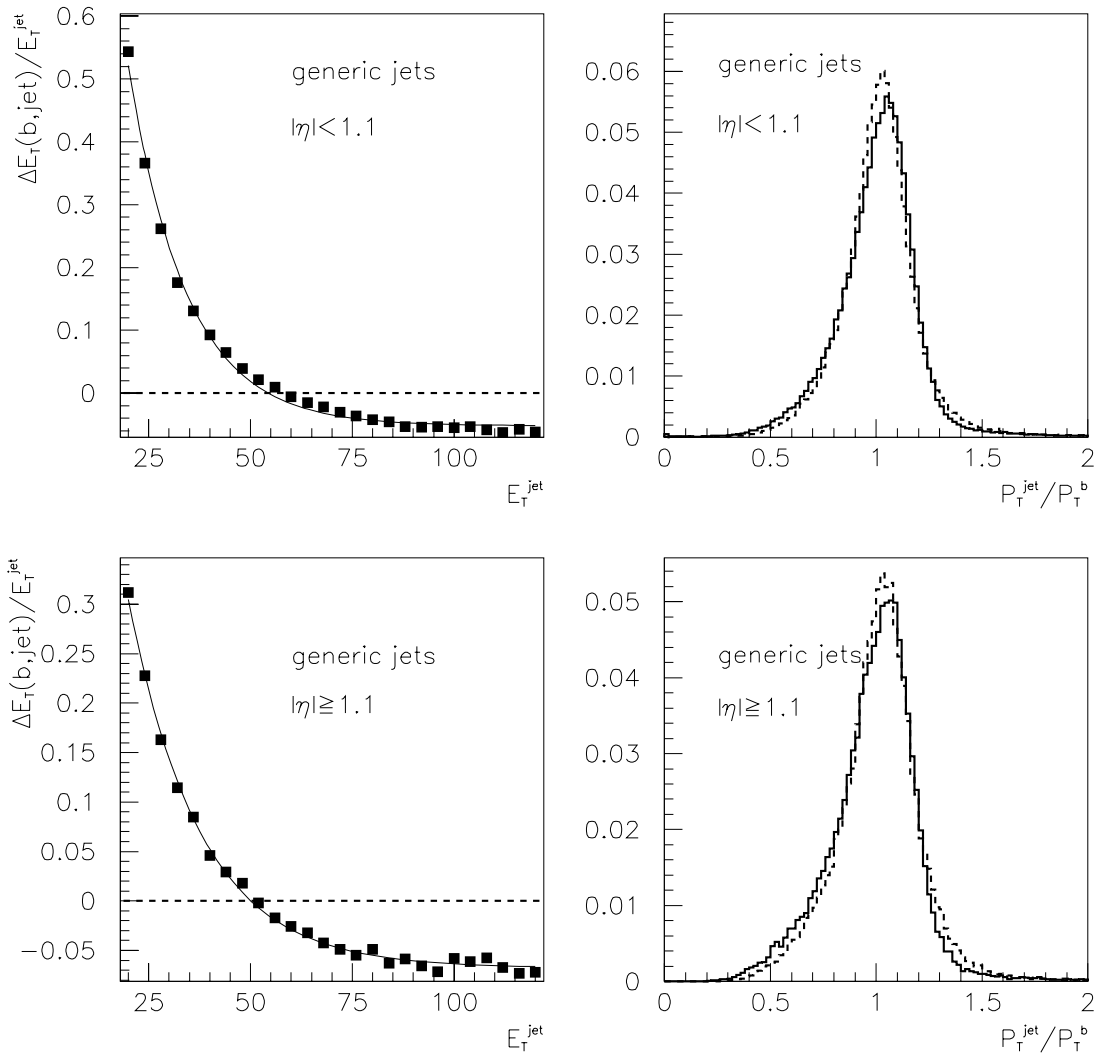

Figure 5.9: *E_T corrections (left) and effect on P_T^{jet}/P_T^b ratio (right) for generic jets with $|\eta| < 1.1$ (top) and with $|\eta| \geq 1.1$ (bottom).*

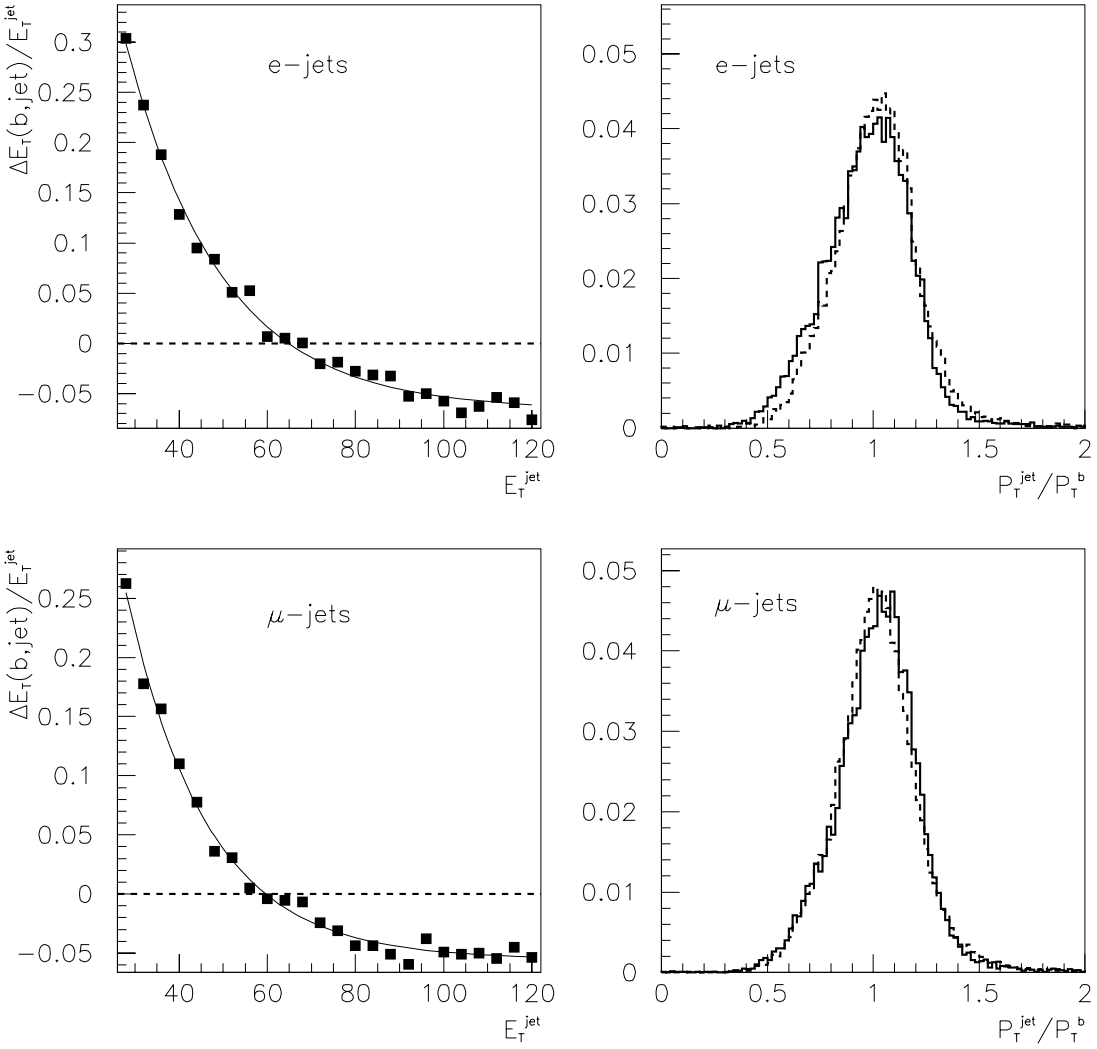

Figure 5.10: *E_T corrections (left) and effect on P_T^{jet}/P_T^b ratio (right) for e-jets (top) and μ-jets (bottom).*

5.4 Effects of the Corrections on Dijet Mass Spectra

In order to study the impact of our three different sets of jet corrections, we look separately at the reconstructed invariant mass of Higgs bosons for four dijet categories: dijets with a soft muon tag, dijets with a soft electron tag, dijets without soft leptons, and all categories together. The effects of the corrections on the spectra of these categories are shown in Figs. 5.11-5.14 (top) for $M_H = 120\ GeV/c^2$.

In order to evaluate the improvement on the dijet mass resolution, we proceed as for jet P_T and fit the spectra with a gaussian, again excluding from the fit the tails of the distributions by requiring that bins contain more then 20% of the entries of the most populated bin. As before, the resolution is defined as the gaussian σ. Figs. 5.11 to 5.14 (bottom) show the resolution versus the mean value of the mass distribution before and after each correction for all the samples with different Higgs mass. The improvement corresponds to the relative decrease in σ before and after our corrections; it is shown at the bottom of the same figures.

In summary, we find an improvement of about 23% on the dijet mass resolution for the whole sample selected by our trigger. It must be noted, though, that for hadronic jets the E_T resolution nearly scales with E_T: therefore, the figure of merit has to be estimated on the σ_M/M ratio, which shows an improvement of $\gtrsim 30\%$.

Finally, we look at the effects of our jet energy corrections on dijet mass spectra of Z and W vector bosons (see Fig 5.15). We find an improvement of about 11% (from 14.6 to 12.9 GeV/c^2) and 5% (from 11.9 to 11.2 GeV/c^2) on the dijet mass resolution of Z and W bosons respectively. However, our corrections have been studied on b-jets coming from Higgs boson decays and could be not the optimal tool to correct generic jets form vector boson. In particular, E_T corrections are dependent on E_T spectrum of the jet sample they are computed on. Due to the lower mass of the vector bosons, jets from W and Z have average E_T lower than ones from Higgs boson, so that their correction could be over estimated. Actually, the mean value of the dijet mass peak are shifted of about 6 GeV/c^2 after corrections both for Z (from 93.2 to 99.3 GeV/c^2) and W (from 84.2 to 90.3 GeV/c^2) boson. Therefore, we decide to compute a specific set of corrections for vector boson, in the same way we computed Higgs one. Fig 5.15 shows the effects of this new set of jet energy corrections: dijet mass resolution improves of about 14% (from 14.6 to 12.5 GeV/c^2) for Z boson and 10% (from 11.9 to 10.7 GeV/c^2) for W boson, while mass peak shift is reduced at about 2 GeV/c^2.

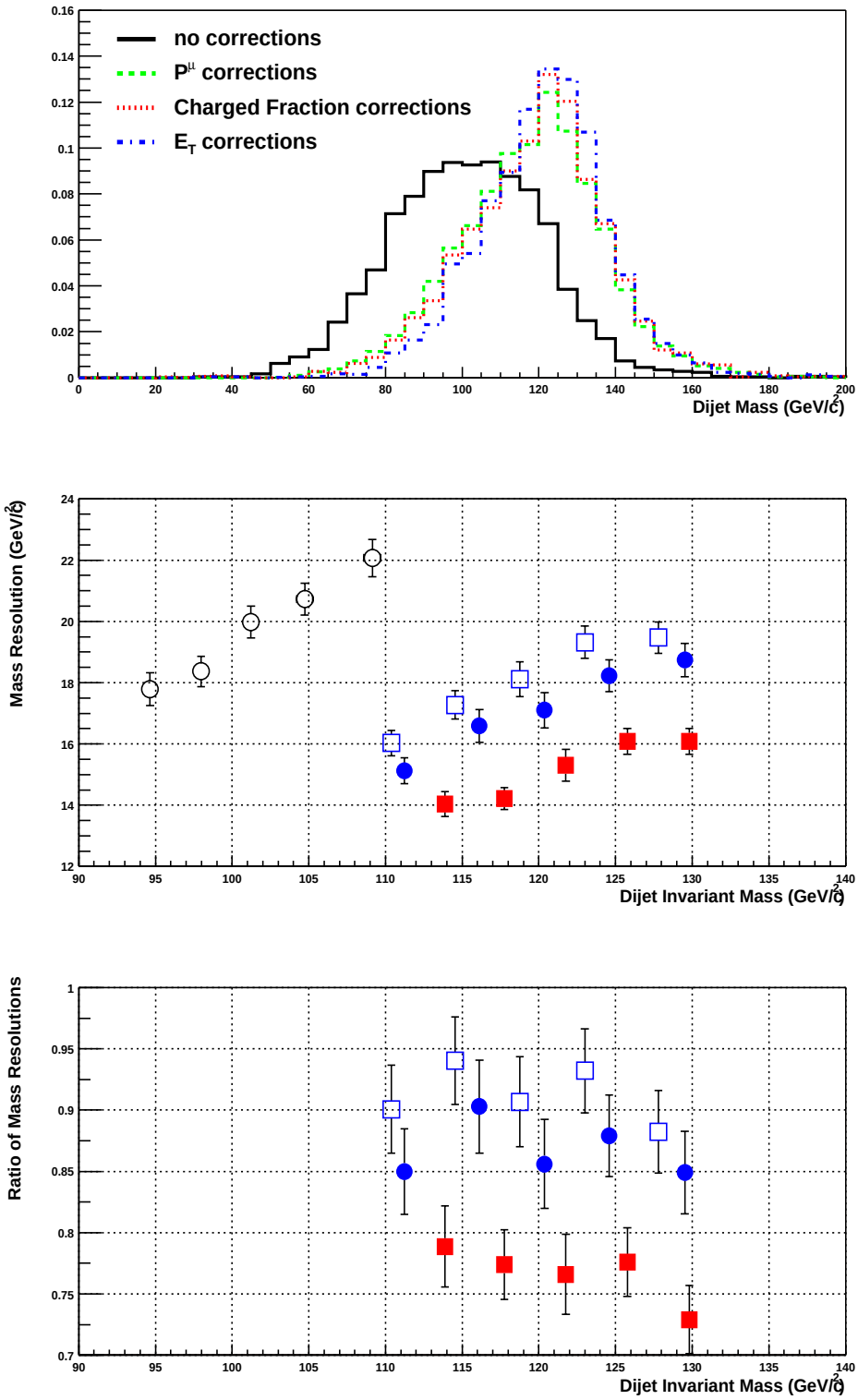

Figure 5.11: *Top: effects of the corrections on dijet invariant mass with soft muon for* $M_H = 120\ GeV/c^2$. *Bottom: mean and resolution improvement on dijet invariant mass with soft muon. The* ○ *is for uncorrected jet energies,* □ *is for jet energies after* P^μ *corrections,* ● *after Ch. F. corrections and* ■ *after* E_T *corrections.*

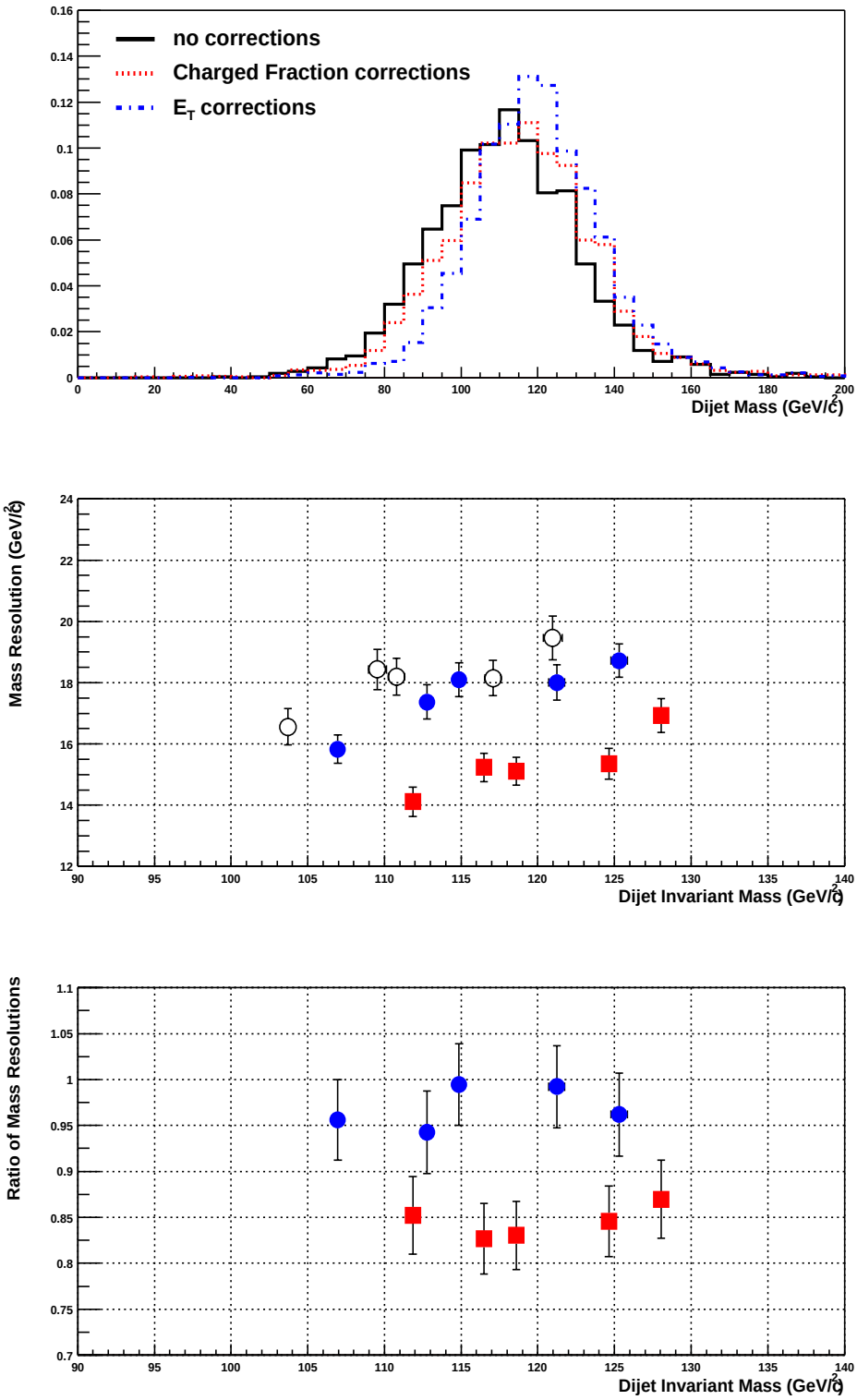

Figure 5.12: *Top: effects of the corrections on dijet invariant mass with soft electron for* $M_H = 120\ GeV/c^2$. *Bottom: mean and resolution improvement on dijet invariant mass with soft electron. The* $\circ$ *is for uncorrected jet energies,* $\square$ *is for jet energies after* P^μ *corrections,* $\bullet$ *after Ch. F. corrections and* $\blacksquare$ *after* E_T *corrections.*

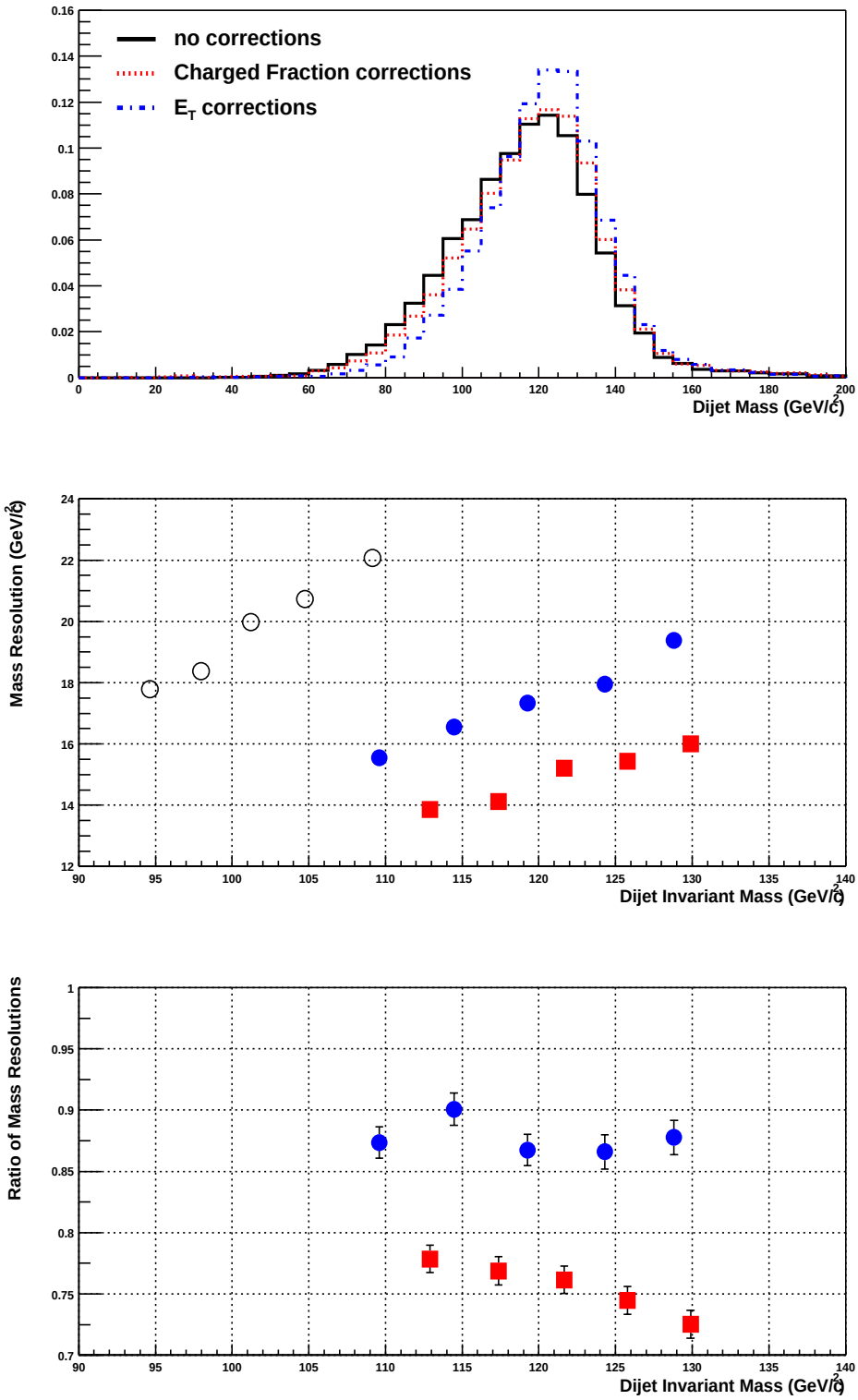

Figure 5.13: *Top: effects of the corrections on dijet invariant mass without soft leptons for* $M_H = 120\ GeV/c^2$. *Bottom: mean and resolution improvement on dijet invariant mass without soft leptons. The* $\circ$ *is for uncorrected jet energies,* $\square$ *is for jet energies after* P^μ *corrections,* $\bullet$ *after Ch. F. corrections and* $\blacksquare$ *after* E_T *corrections.*

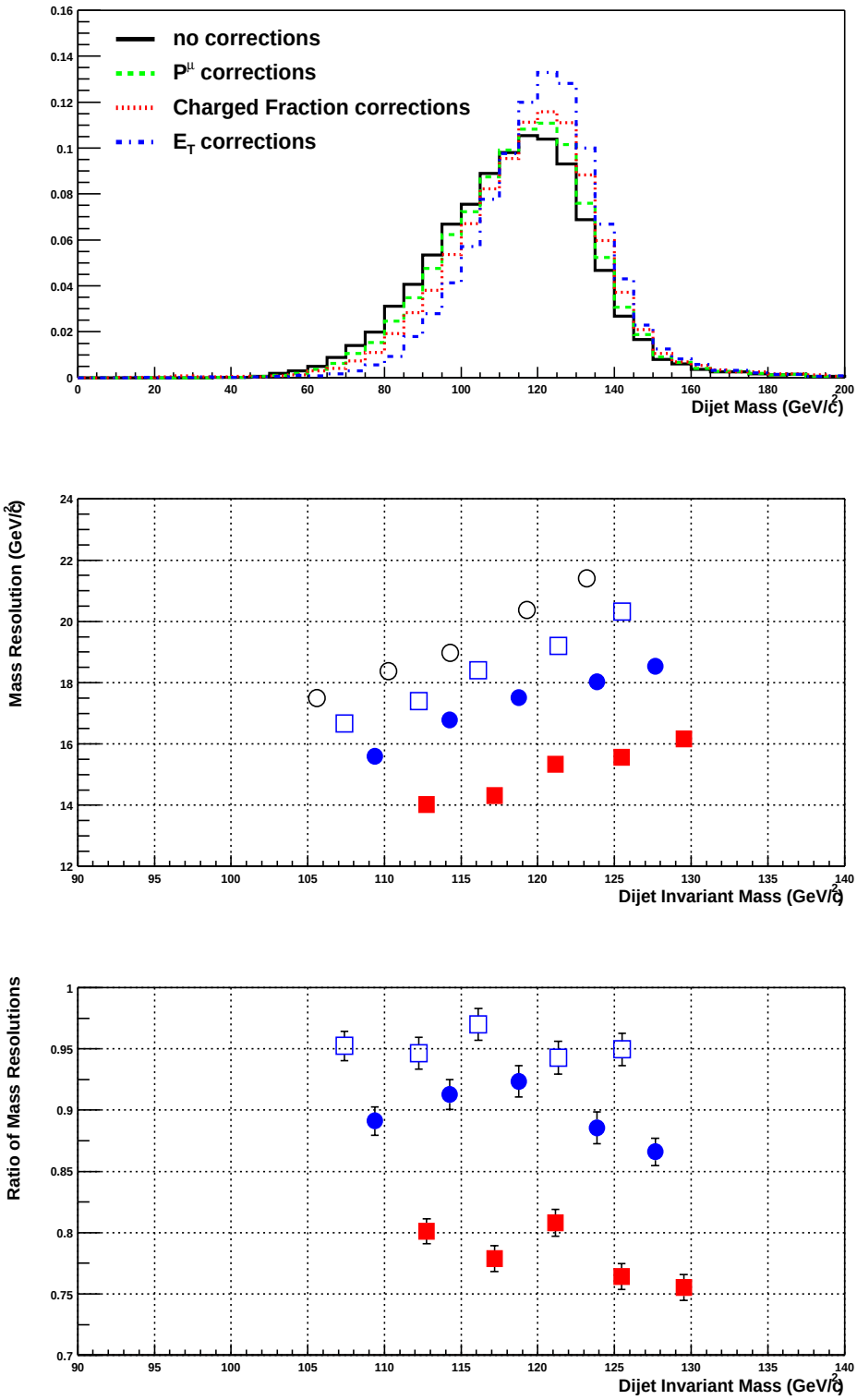

Figure 5.14: *Top: effects of the corrections on dijet invariant mass for* $M_H = 120\ GeV/c^2$ *(all categories together). Bottom: mean and resolution improvement on dijet invariant mass (all categories together). The* $\circ$ *is for uncorrected jet energies,* $\square$ *is for jet energies after* P^μ *corrections,* $\bullet$ *after Ch. F. corrections and* $\blacksquare$ *after* E_T *corrections.*

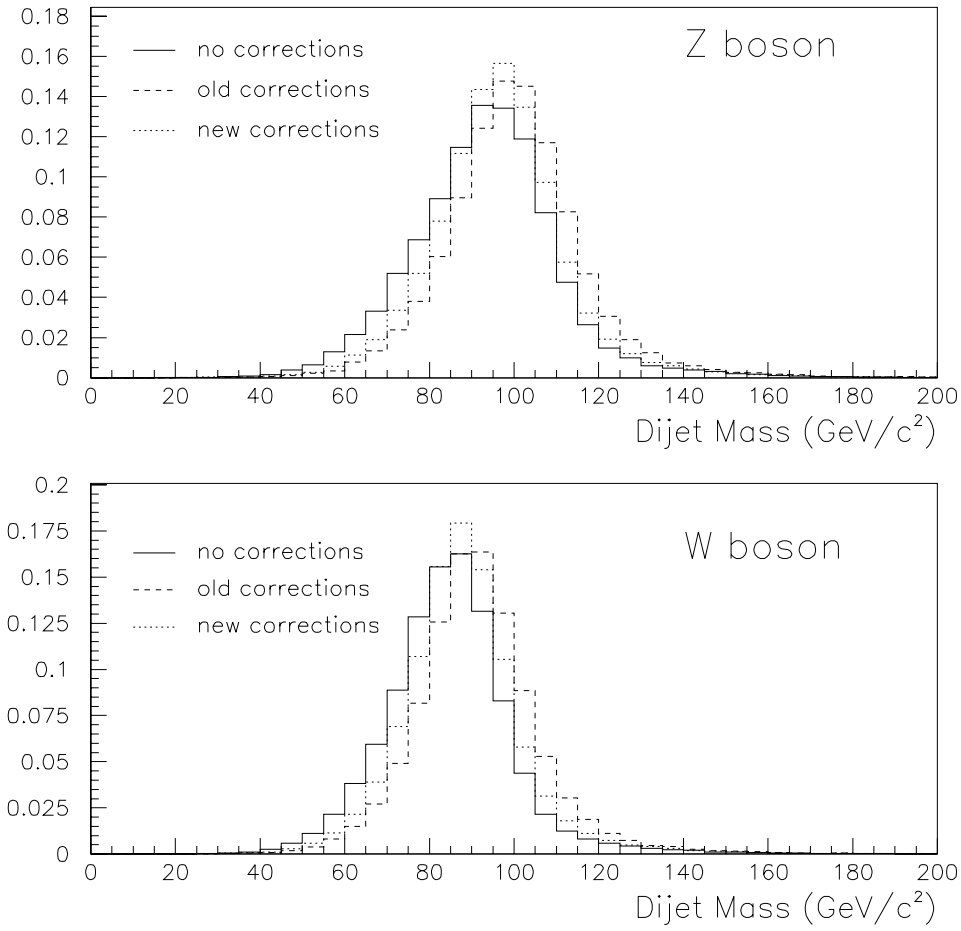

Figure 5.15: *Comparison of the effects of the old and new corrections on dijet invariant mass of Z (top) and W (bottom) bosons.*

5.5 Checks

5.5.1 Independence of the Corrections on the Input Mass

We used the same samples both to compute the parameters of the corrections and to study their effects on dijet mass spectra. In principle, this could be troublesome for at least two reasons:

- We could be measuring some bias in our samples and reappling it to them;
- The correlations between measurable quantities and jet mismeasurement we used could be simulated incorrectly by the MC or be dependent on the fragmentation model chosen.

The second point is discussed in the next subsection and in 5.5.5. The first one instead is essentially connected with the statistical significance of our MC samples. In order to study this potential bias, we compute new parameters for our corrections by excluding from the input mixture the sample of data generated with $M_H = 120\ GeV/c^2$, and then we compare their effects on Higgs boson dijet mass for this sample with the effects of preceding corrections. Fig. 5.16 show that there are no substantial differences.

5.5.2 Independence of the Corrections on the Fragmentation Model

As pointed out in the last section, the use of a specific Monte Carlo (PYTHIA 6.115 in this study) could introduce some bias in the jet corrections such as, for example, a dependence on the fragmentation model. To check this, we study the performances of our corrections on the sample of direct Higgs production events ($M_H = 120\ GeV/c^2$) generated with the HERWIG 5.6 Monte Carlo (see Fig. 5.17). We find that the resolution of the Higgs mass improves of about 20% (from 15.1 to 12.2 GeV/c^2), while the mean value of the dijet mass distribution increases from 118.0 to 122.1 GeV/c^2. This result achieves our initial task and suggests that our study could be useful also in processes different from the associated production of Higgs boson.

5.5.3 Effects of the Corrections on Backgrounds

We test the effect of our corrections on three different samples to check the behavior of backgrounds:

- Dijet pairs from HV events with at least one jet coming from vector boson decay or hard gluon radiation (combinatoric background);
- QCD simulation;
- Run I data (W+JETS sample).

We look at the invariant mass of dijet pairs with a tagged jet after trigger selection; however, in order to keep enough events, we do not apply the calorimetric requirements on W+JETS sample. Results are shown in Fig. 5.18: all dijet mass spectra shift to a larger value, without a sizeable change in shape. This assures an improvement in the S/N ratio, as we can see better in Fig. 5.19. Here the mass correction $\Delta M = M^{corr.} - M^{uncorr.}$ is plotted as a function of the uncorrected mass: background mass corrections are quite constant while Higgs boson dijet masses have corrections ΔM greater than those of background events for $M^{uncorr.} < M_H$ and less for $M^{uncorr.} > M_H$, so that after the corrections not only all the dijet mass resolutions improve, but the amount of background events under the signal region is reduced.

5.5.4 Stability of the Corrections for Analysis Cuts

Finally, we want to check the behavior of our corrections after analysis cuts. We study some standard selection variables, as the sum of jet transverse energies computed using all jets (ΣE_T) or excluding the two leading jets ($\Sigma_3 E_T$), and the transverse energy fraction of the event ($\Sigma E_T/\sqrt{\hat{s}}$), and we look at the corrected dijet mass spectra after appling some cuts. In particular, we choose:

- $\Sigma E_T > 150$, 200 and 250 GeV;
- $\Sigma_3 E_T > 50$, 70 and 90 GeV;
- $\Sigma E_T/\sqrt{\hat{s}} > 0.7$, 0.75 and 0.8;
- a jet with SECVTX tag and the second jet with SECVTX or SLT tag.

The differences between the mean values of the dijet mass distributions and the input mass of the Higgs boson and the resolutions of the Higgs mass are shown as a function of the hypothetical cuts in Fig. 5.20 and 5.21 respectively. After a selection based on ΣE_T or $\Sigma_3 E_T$ the resolutions seem to remain enough stable. Instead, mean values decrease slightly after the cuts on $\Sigma_3 E_T$. However, they are quite stable as far as the requirements on $\Sigma_3 E_T$ remain in a reasonable range. A selection based on $\Sigma E_T/\sqrt{\hat{s}}$ does not seem to affect the resolutions of the Higgs mass and shifts down only very slightly the mean values of the dijet mass distributions. Moreover, this effect is not sizeable for a conservative cut on the transverse energy fraction. Finally, the tagging requirement seems to improve the dijet mass resolutions, even if the mean values increase slightly. Actually this request enriches the total spectrum of dijets containing tagged soft leptons, that are better corrected than dijets containing leptons failing SLT requirements, since jets with such leptons are corrected as generic jets.

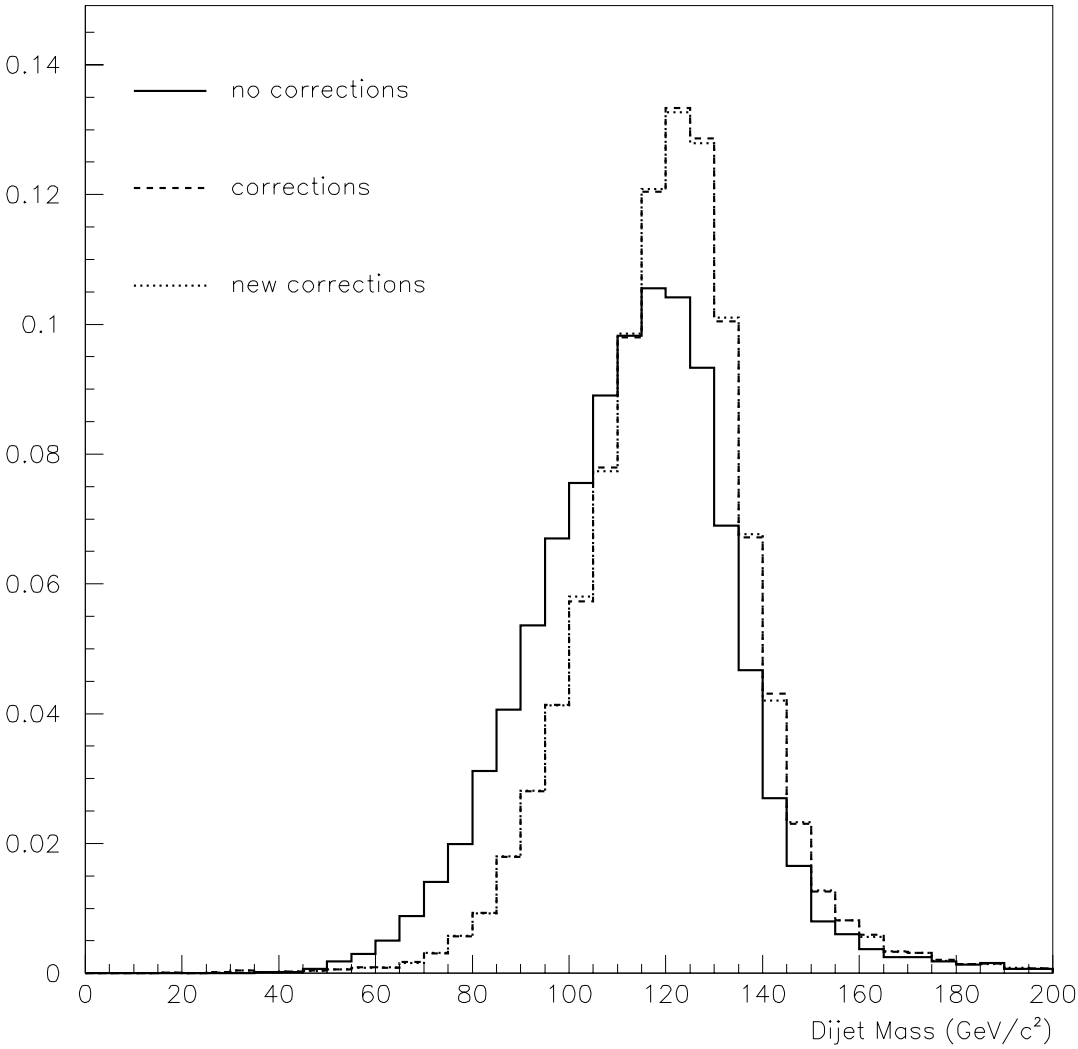

Figure 5.16: *Comparison between dijet mass spectra for* $M_H = 120\ GeV/c^2$ *before corrections and after corrections computed with and without the* $M_H = 120\ GeV/c^2$ *sample.*

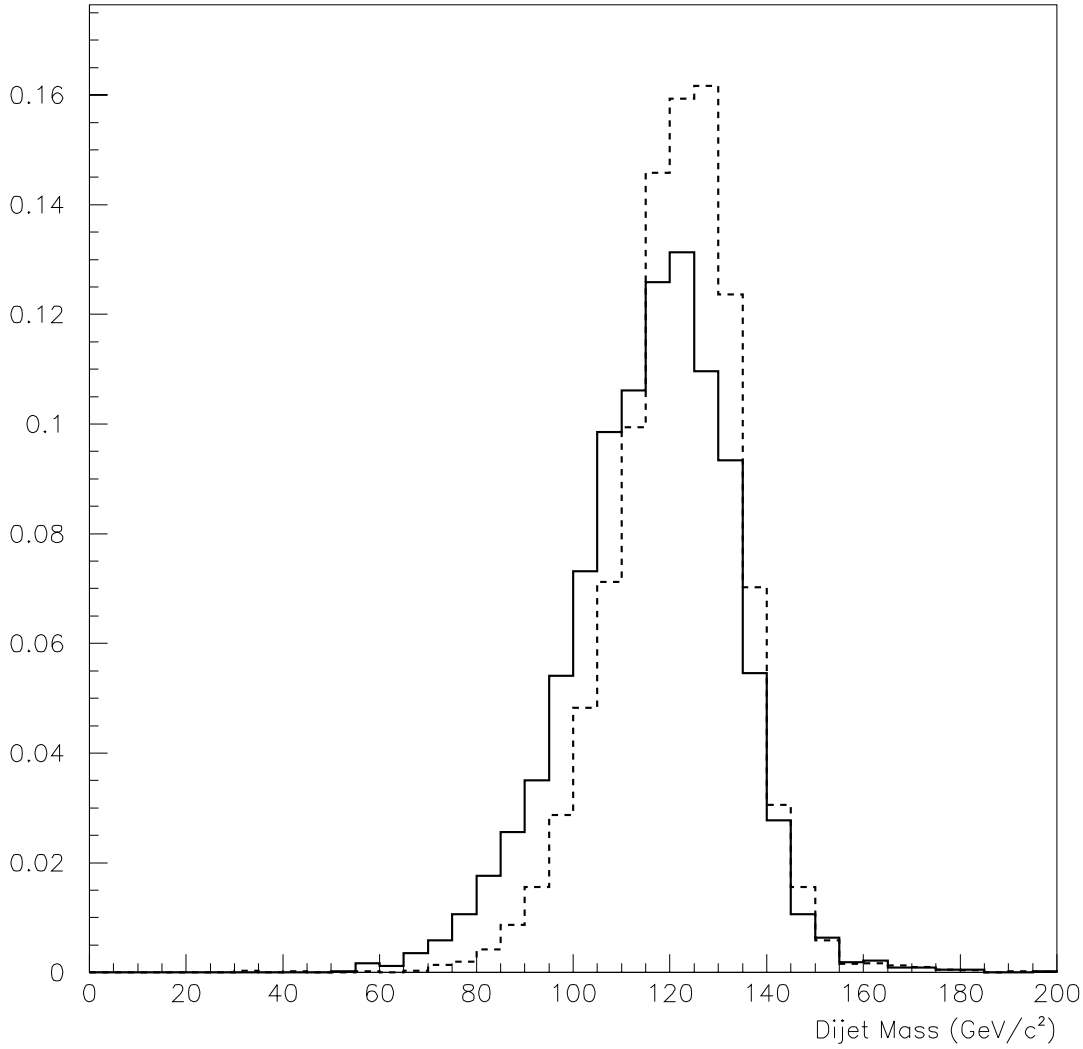

Figure 5.17: *Effects of our corrections on invariant mass spectrum of dijet pairs from Higgs decay as simulated from* HERWIG 5.6 *Monte Carlo* ($M_H = 120\ GeV/c^2$).

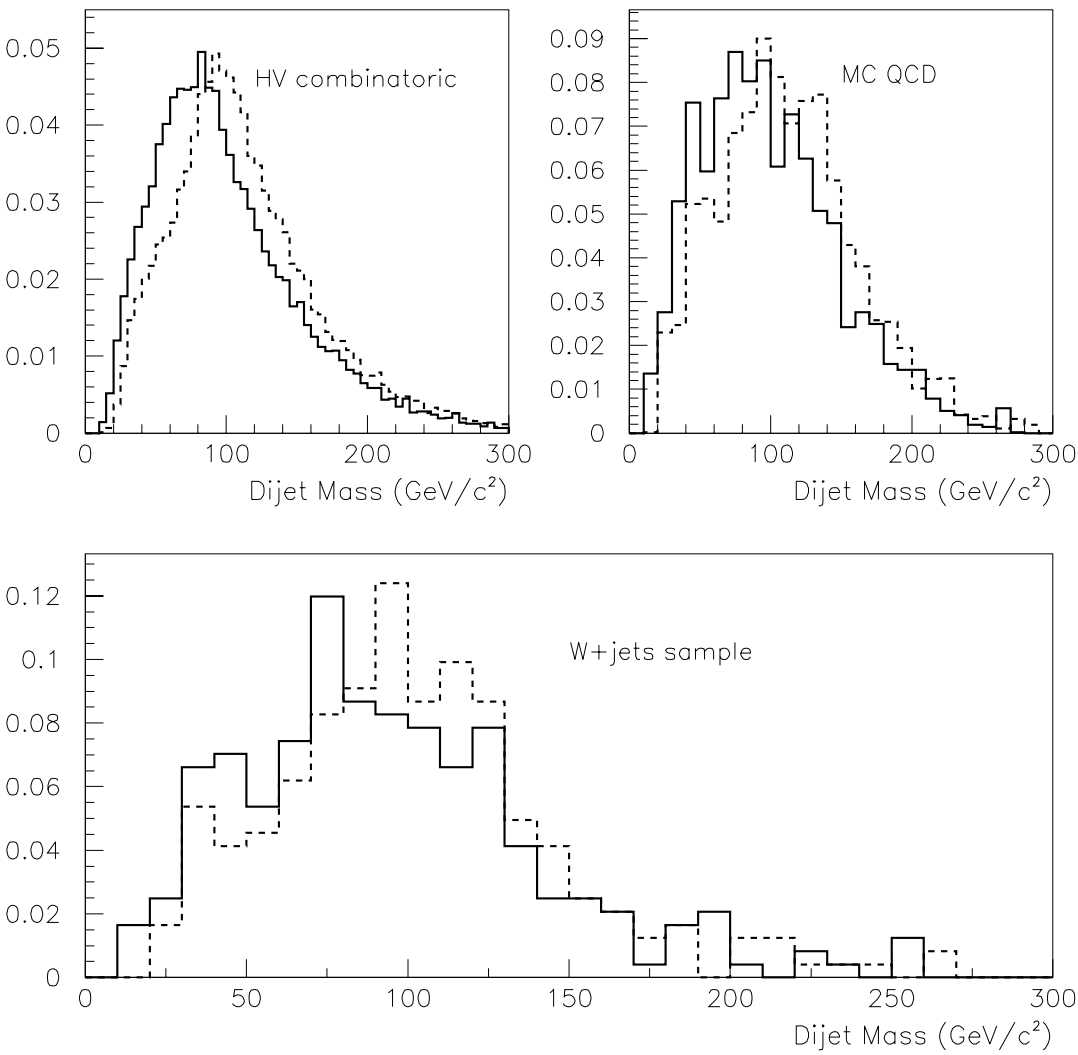

Figure 5.18: *Effects of the corrections on background dijet mass spectra. Full histogram: before corrections; hatched histogram: after corrections.*

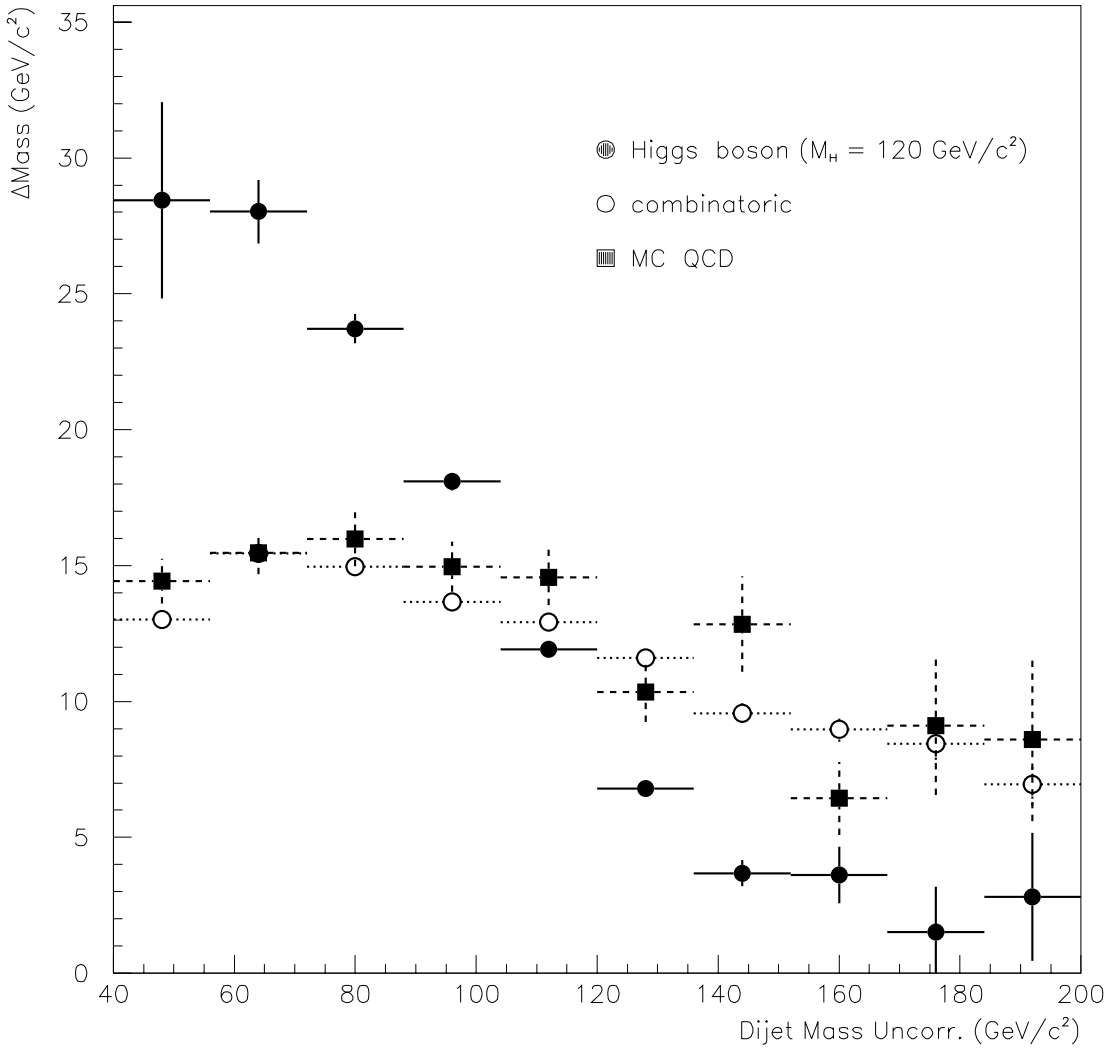

Figure 5.19: *Mass shift* $\Delta M = M^{corr.} - M^{uncorr.}$ *as a function of the mass before corrections, for dijet pairs from Higgs decay (•), wrong dijet combinations in HV events (○), and a sample of QCD MC events (■).*

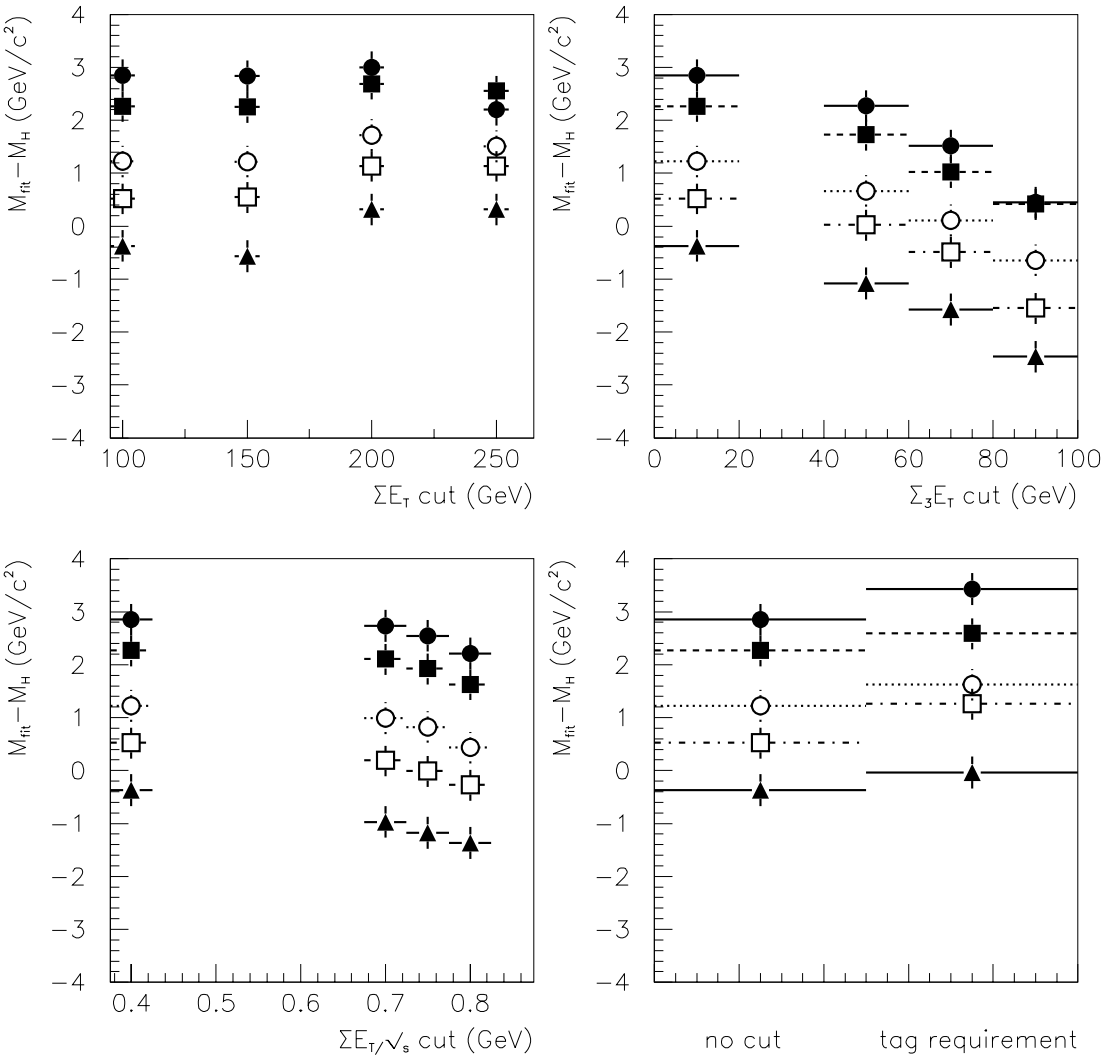

Figure 5.20: *Differences between the mean values of the dijet mass distributions and the input mass of the Higgs boson after some analysis cuts for* $M_H = 110$ *(•),* 115 *(■),* 120 *(○),* 125 *(□) and* 130 *(▲)* GeV/c^2.

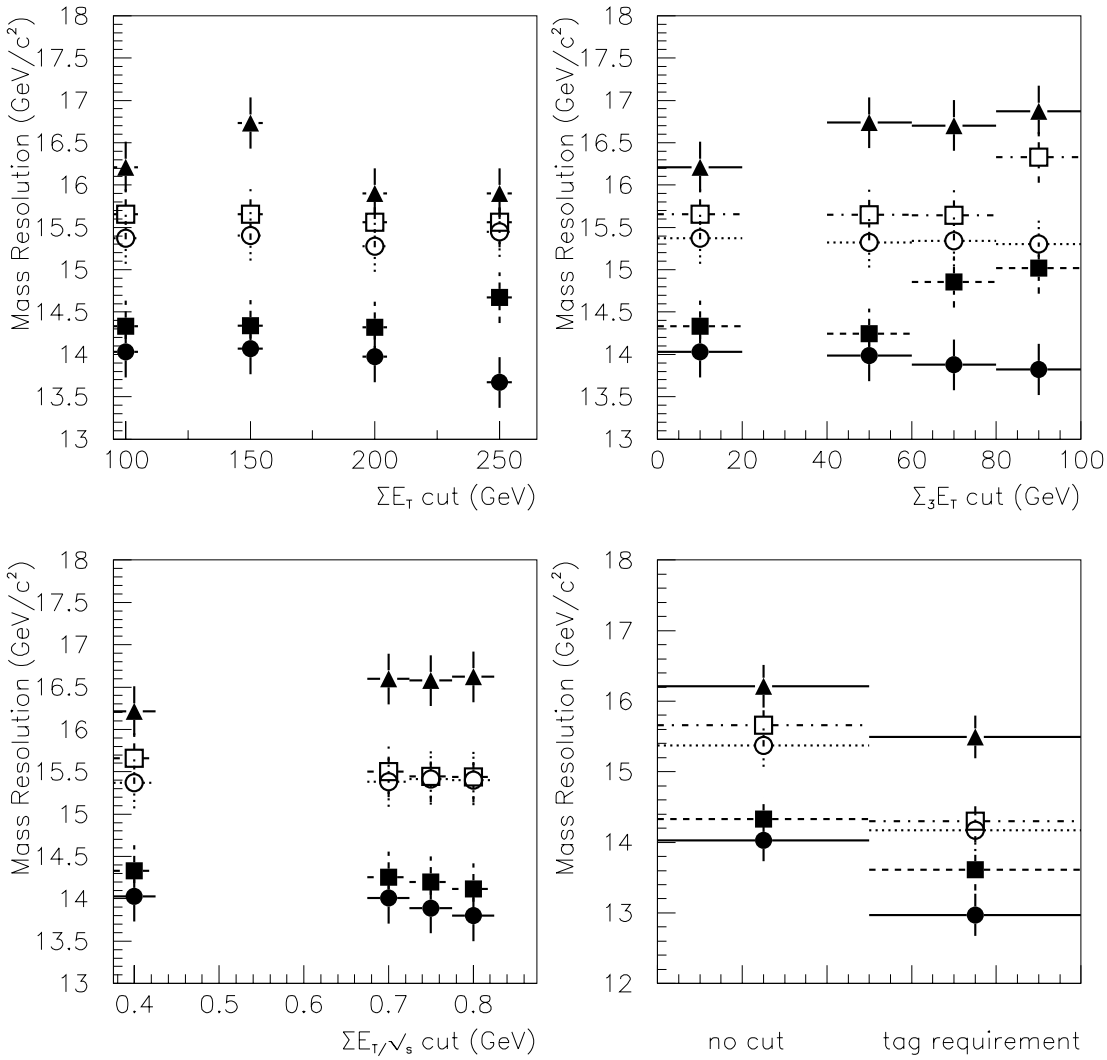

Figure 5.21: *Resolutions of the Higgs mass after some analysis cuts for* $M_H = 110$ *(•),* 115 *(■),* 120 *(○),* 125 *(□) and* 130 *(▲)* GeV/c^2.

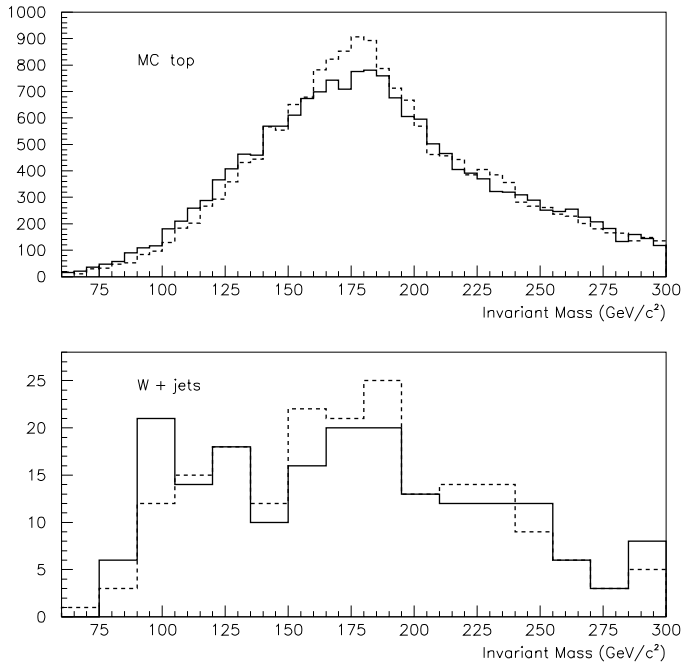

Figure 5.22: *Effects of the corrections on invariant mass spectra from $t\bar{t}$ MC and W + jets data. Full histogram: before corrections; hatched histogram: after corrections.*

5.5.5 Effects of the Corrections on Real Data

We test how our corrections work on real data by using the top mass signal in the $W + jets$ sample as a benchmark. In order to enrich the sample of $t\bar{t}$ events we select events with at least three jets with raw $E_T \geqslant 15\ GeV$. As a preliminary approach we use the four leading jets to reconstruct top decays by looking at the invariant mass of each combination of three jets with one tag (SLT or SVX tag): we keep one entry from events with three jets and one tag, two entries from events with at least four jets and two tags and three entries from events with at least four jets and one tag. We optimize our correction parameters on $t\bar{t}$ MC events in order to avoid possible biases due to the different process we are dealing with. In particular, jets from W decay (from $t \to bW$) are not originated from b quarks, so they need a different set of jet corrections. We compute these corrections in a manner similar to that discussed in Section 5.2. Fig. 5.22 compares correction effects on invariant mass spectra both for real data and MC sample. We see a similar behavior of these two samples; however, it is only a qualitative check at this point. Future studies using more detailed top mass fitters are possible.

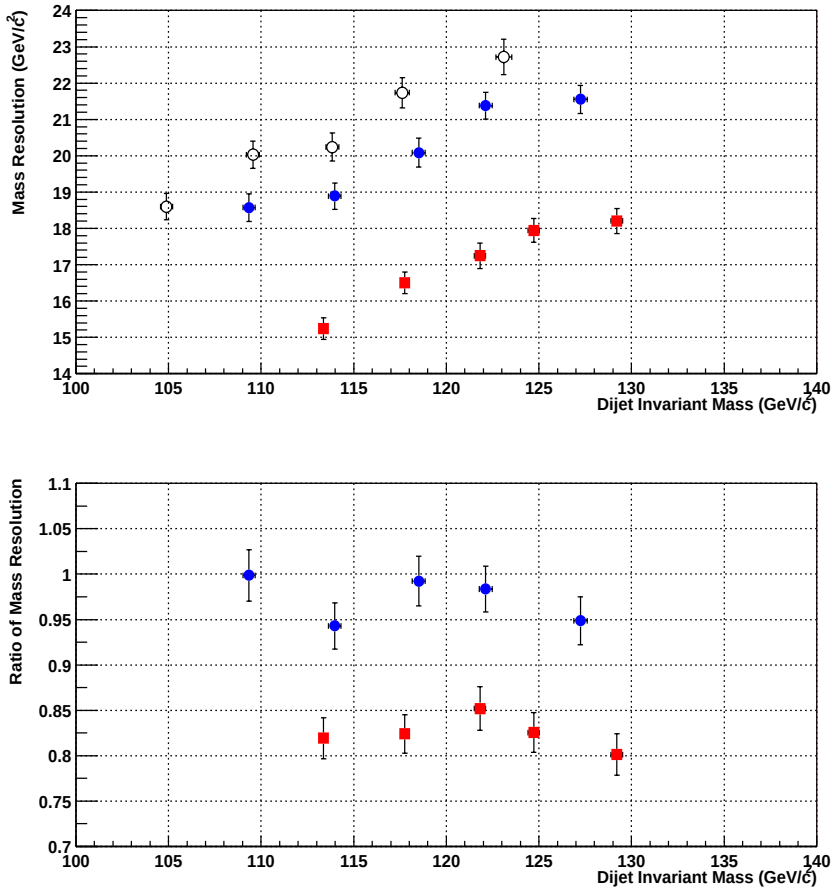

Figure 5.23: *Effects of preliminary jet energy corrections developed in* CDF II *environment on reconstructed Higgs mass spectrum. The* ○ *is for uncorrected jet energies,* • *is for jet energies after Ch. F. corrections and* ■ *after* E_T *corrections.*

5.6 Status of Jet Energy Corrections with CDF II Code

As stressed in the introduction, the status of CDF II software does not allow again a complete conversion of our work on jet energy corrections to a Run II environment. However, we can perform a first step by compute charged fraction and E_T-based corrections. To this purpose, we use 5 sample of $\sim$ 10000 VH events, generated with an Higgs mass ranging from 110 to 130 GeV/c^2 and filtered with trigger and 4-jets requirement after a full detector simulation. Results are shown in Fig 5.23. We find an improvement of about $15 \div 20\%$ on the dijet mass resolution for all the range of Higgs mass considered. It is a rather amazing result since we have not a SLT tagging algorithm to classify jets in muon, electron and generic jets and therefore we have to compute our corrections on an only jet category.

5.7 New Jet Energy Reconstruction Algorithm

The standard CDF jet reconstruction algorithm uses the calorimeter information only, and then apply corrections to take into account calorimeter non-linearity, detector cracks, and jet shower leakage.

The CDF Dijet Mass Group are studying a new strategy [9] to compute the energy of the calorimeter towers including also information from other CDF detector devices. For the first time the full granularity of the calorimeter and the track momenta measured by the tracking system are used to perform corrections at *tower level* rather than at *jet level*.

The calorimeter towers are grouped into four classes, depending on which kind of particles hit the tower. For each class, a different method to determine the energy collected in the tower has been studied. The four classes are:

- Track Tower: the tracks reconstructed in the COT are extrapolated to the calorimeter and associated to the towers. The towers hit by a track are flagged *Track Tower*. The adjacent towers in η are also considered Track Tower, in order to take in account leakage. The sum of the transverse momenta of the hitting tracks is used to determine the energy of the tower. To avoid double counting, no energy is attributed to leakage towers.

- Gamma Tower: The presence of an energetic cluster in the CES, interpretable as a photon, flags a *Gamma Tower*. If the photon falls near the tower edge, leakage towers are considered. The energy associated to these kind of towers is the energy collected by the electromagnetic calorimeter.

- Mixed Tower: if a tower satisfies both the prescriptions required to be flagged as track and gamma tower, it is labeled as *Mixed Tower*. The energy associated to these tower is a combination of track transverse momenta and electromagnetic calorimeter energy, after subtracting an estimation of the charged particle contribution to the calorimeter energy in order to avoid double counting.

- Not Assigned Tower: if a tower satisfies neither prescription, it is labeled as *Not Assignad Tower*. Monte Carlo studies show that these towers are usually hit by either low energy photon or neutral hadrons. The calorimetric response is then used to compute their energy.

A study of tower classification on the photon + jet data sample collected during Run I shows that, even if $\sim 60\%$ of the towers are flagged as Track Tower, the main fraction of energy ($\sim 60\%$) is carried by the Mixed Towers, due to both shower leakage outside the target tower and overlap of energetic particles in the core of the jet. Moreover, Not Assigned Towers turn out to carry a small amount of energy.

In order to compare the new jet energy reconstruction with the standard CDF method, direct photon data were used since it allow a photon-jet P_T balancing. In particular, a data semple was selected by using the standard CDF photon selection [10] for Run I and requiring a central jet. Furthermore, to extract a detector

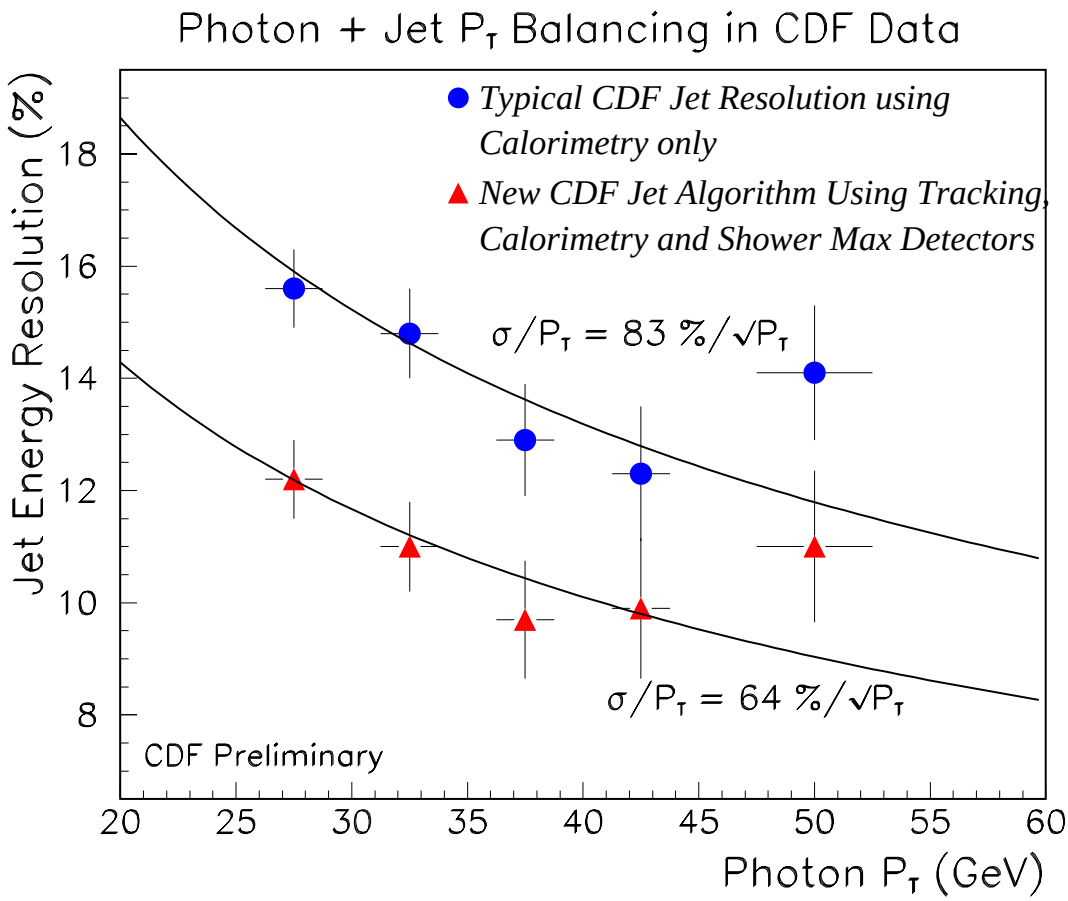

Figure 5.24: *Central detector resolution σ_D as a function of P_T^γ for the two jet energy reconstruction methods.*

resolution reducing the sensitivity to the physics effects, the projection of the imbalanced vector $\vec{P}_T = \vec{P}_T^{jet} + \vec{P}_T^\gamma$ along the azimuthal angular bisectors of the photon-jet system has been considered. The two resulting components, P_T^ξ and P_T^η, are sensitive to different effects: the detector energy resolution is the main source of the P_T^ξ component, while gluon radiation effects are common to both components. After hard gluon emission has been reduced by applying a cut on the second jet energy, an *effective* detector resolution σ_D for central jets was defined by subtracting in quadrature σ_η, carrying an estimate of the soft contribution, from the σ_ξ, where σ_η and σ_ξ denote the width of P_T^η and P_T^ξ respectively. Fig. 5.24 shows the relative resolution σ_D/P_T^γ as a function of P_T^γ. There is an improvement going from $\sigma/P_T \sim 83\%/\sqrt{P_T}$ using the standard CDF corrections to $\sigma/P_T \sim 64\%/\sqrt{P_T}$ obtained with the new jet energy reconstruction algorithm.

5.8 Perspectives on Jet Energy Corrections at CDF II

The simple algorithm for jet corrections we studied in this chapter, using P^μ, jet charged fraction, and E_T informations, achieves a $\sim 30\%$ improvement in σ_M/M on

the range of Higgs masses where the $H \to b\bar{b}$ decay is dominant. On the contrary, dijet mass distributions of the background processes do not substantially change their shapes.

Further improvements are expected to be coming from new jet correction algorithms currently to the study at CDF, showing an improvement on the jet energy resolution better than 20% with respect to the Standard CDF jet corrections when tested on a γ-*jet* data sample.

These approach is quite orthogonal to our one, since it use different variables and it has been conceived for generic jet, not specifically for b-jet carrying the problem of energy loss due to neutrinos.

Hopes are that an integration of the two algorithms assures a further improvement in the S/N ratio, and improves again the observability of the Higgs mass peak.

Bibliography

[1] N. Eddy, *New relative jet corrections for Run 1A and 1B data*, CDF internal note 3534.

[2] J. Troconiz et al., *Update in Search for a Neutral Heavy Scalar in the Multijet Data Sample*, CDF internal note 4129, Apr 1998.

[3] Higgs Working Group, *Report of the Higgs Working Group*, Mar 2000.

[4] M. P. Giordani, *A RunII Trigger Design for Higgs Boson Search at CDF*, Ph.D. thesis, Dec 2000.

[5] T. Dorigo et al., *Jet Corrections for Dijet Systems With a Muon*, CDF internal note 4527, Mar 1998.

[6] A. Caner et al., *Jet Corrections for top mass fitting*, CDF internal note 2469, Feb 1994.

[7] `http://www.thep.lu.se/tf2/staff/torbjorn/Pythia.html`.

[8] `http://hepwww.rl.ac.uk/theory/seymour/herwig/`.

[9] S. Lami et al., *Studies of jet energy resolution*, CDF internal note 5507, Dec 2000.

[10] F. Abe et al. (CDF Collaboration), *Prompt photon cross section measurement in p anti-p collisions at* $\sqrt{s} = 1.8\ TeV$, Phys. Rev. D **48** 2998 (1993).

Chapter 6

Characterization of the Events

The process of production of Higgs boson in association with a vector boson and their decays in all hadronic final states lead to events characterized by a high jet multiplicity and particularly enriched of heavy quarks. In addition to the events we are interested in, other processes present analogous characteristics and can therefore pass the trigger requirements. They then constitute a background *overlapping the signal.*

In this chapter we will describe the data sample the trigger is expected to collect. In the first two subsections, the main contributions will be presented and some basic *characteristics of signal events will be used to define an* analyzable *sample. Successively, the issue of the Higgs and vector boson decay reconstruction will be studied. Finally, we will provide a kinematical characterization of the main processes contributing to our sample with a view to a background discrimination.*

6.1 The Trigger Selected Sample

Several processes contribute to the trigger collected sample. Among them, the most important are:

- event production by means of strong interaction (QCD *processes*). At tree level, these events have two outgoing partons, yielding in most cases two final-state jets. However, due to the large cross section and to the additional jets coming from gluon radiation, they end up constituting the main contribution to the multijet trigger sample. Heavy flavour production through various processes (shown in Fig. 6.1) is expected to provide the bulk of these events. However, also processes involving light flavour only represent a consistent background to this search due to their higher cross section.

- $t\bar{t}$ events (see Fig. 6.3). The main contribution to the multijet sample comes from all hadronic $t\bar{t}$ decays ($t\bar{t} \to bW\bar{b}W \to bq\bar{q}'\bar{b}q\bar{q}'$). Events with only one W boson decaying into quarks can also contribute to the sample, but they can be ruled out by requiring high $\not{E}_T$ and an isolated lepton coming from $W \to l\nu_l$ decay.

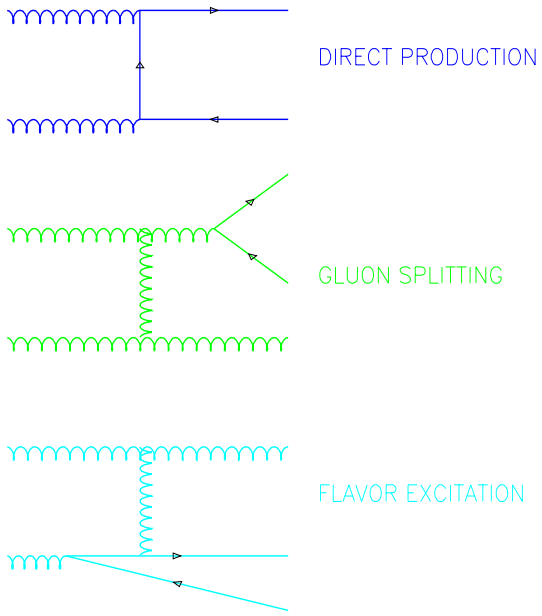

Figure 6.1: *Main contributions to* QCD *production of heavy quark pairs.*

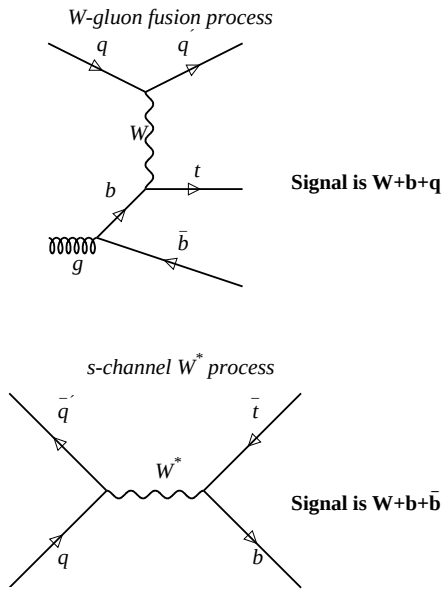

Figure 6.2: *Diagram for single top production.*

- single top production in association with a b quark. This process, whose dominant diagrams are shown in Fig. 6.2, lead to multijet final states for top quark decaying into hadrons.

- diboson production. All hadronic decay channels of WW, ZW and ZZ events are expected to yield to four jet final states. Heavy flavour comes from both $W \to cs$ and $Z \to b\bar{b}(c\bar{c})$ decays.

- Z/W direct production. Gluon radiation leads to an high jet multiplicity, while heavy flavour production is provided by vector boson decays or by gluon splitting (Fig. 6.4).

In order to estimate the cross section of signal production after trigger requirements, we use five samples of $5,000$ Higgs associated production events (forcing the $H^0 + Z^0/ W^{\pm} \to b\bar{b} + q^{(\prime)}\bar{q}$ decays) each generated at $\sqrt{s} = 2\ TeV$ with the PYTHIA 6.129 Monte Carlo [1]. The Higgs boson mass has been set to 110, 115, 120, 125, and 130 GeV/c^2, respectively. After a full detector and trigger simulation, we obtain the results summarized in Tab. 6.1.

We also generate $5,000$ events of $t\bar{t}$, single top and diboson production at $\sqrt{s} = 2\ TeV$ with the PYTHIA 6.129 Monte Carlo to compute the contributions of these background processes to the trigger sample. Again, a full detector and trigger simulation has been applied to the generated events. Results are shown in Tab. 6.2. The estimate of the QCD background cross section is provided by the trigger rate itself. Actually, contributions from other background processes are negligible at this level. In Chap. 3, we found a rate of $(1.5 \pm 0.2)\ Hz$ at the project luminosity of $10^{32}\ cm^{-2}s^{-1}$. The correspondent cross section is $15 \pm 2\ nb$. For the time being, no

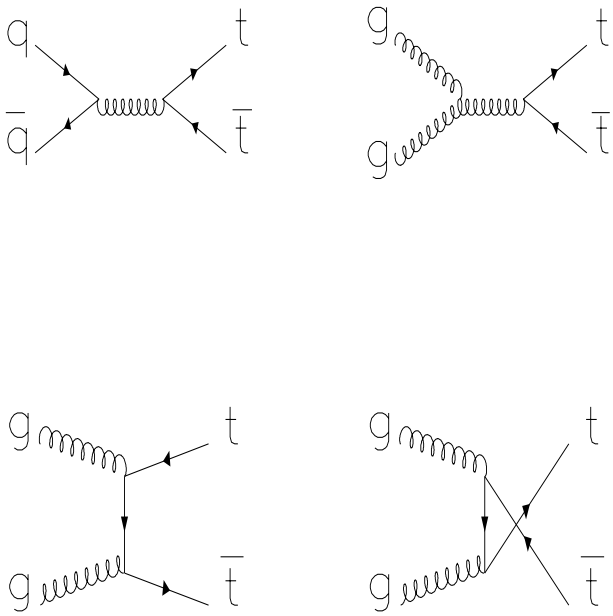

Figure 6.3: *Contributions to $t\bar{t}$ production.*

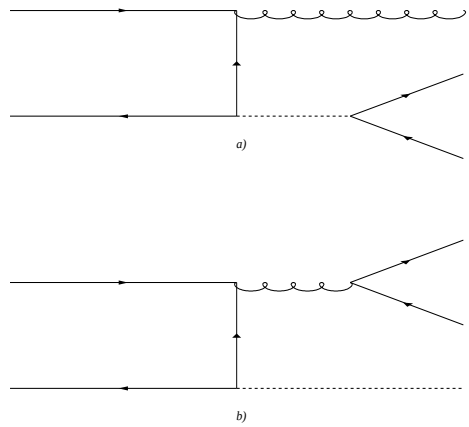

Figure 6.4: *Z/W direct production contributions to multijet sample.*

attempt to estimate the contribution of the Z/W direct production to the trigger collected sample will be made. Actually, the cross sections of these processes are not easy to calculate and the Monte Carlo generators are not able to reproduce correctly the specific contributions of the different processes involved in the single vector boson production. In fact, during Run I the contributions of the Z/W direct production to the different samples were computed through a comparison between real data and Monte Carlo predictions [3]. An effective estimate of the cross section of this source of background for our sample will be then a possible task only when a sizable sample of data is available.

Finally, multijet + heavy flavour trigger is expected to collect few tens of signal events for each fb^{-1} of integrated luminosity, while selecting several millions of background events. We need therefore a lot of statistic and powerful discrimination tools to obtain appreciable results: the CDF II experiment can reasonably be expected to collect about 15 fb^{-1} of integrated luminosity in the next few years, providing an increase of the achievable statistical significance by a factor of $\lesssim 4$; signal and background characteristics and discrimination strategy will be the arguments of the following sections.

6.2 Signal Topology and Analysis Sample Selection

All hadronic decay channel of Higgs boson associated production processes $VH \rightarrow q\bar{q}^{(\prime)}b\bar{b}$ is characterized by the presence of four quarks in the final states. After hadronization, four jets are then expected to populate the signal events, each car-

	110 GeV/c^2	115 GeV/c^2	120 GeV/c^2	125 GeV/c^2	130 GeV/c^2
$\sigma\beta$ (fb)	186	152	121	94	71
$\sigma\beta\epsilon_{trg.}$ (fb)	58 ± 2	50 ± 1	41 ± 1	33.4 ± 0.9	26.2 ± 0.7

Table 6.1: *Cross sections of the* $p\bar{p} \to HVX \to b\bar{b}q\bar{q}^{(\prime)}X$ *process before and after trigger requirements for some values of the Higgs boson mass* M_H. *Errors are statistical only.*

	QCD	$t\bar{t}$	single top	WW	WZ	ZZ
$\sigma\beta$ (fb)	–	2600	1670	4000	1400	490
$\sigma\beta\epsilon_{trg.}$ (fb)	$(15 \pm 2) \times 10^6$	1360 ± 40	340 ± 10	210 ± 10	107 ± 5	64 ± 2

Table 6.2: *Cross sections of background processes before and after trigger requirements. Branching ratios of hadronic decays are included. Errors are statistical only.*

rying information energy and direction of the originating parton. However, several factors can trouble this picture: jet can fail minimum E_T requirement (10 GeV for multijet trigger) or be lost outside calorimeter acceptance; moreover, two jets can be merged in only one jet due to a too small η-ϕ separation; on the contrary, gluon radiation can lead to new jets, not produced by the original partons. Finally, observed jet multiplicity is shown in Fig. 6.5 for VH (Higgs boson mass is assumed to be $M_H = 120$ GeV/c^2), and QCD events after trigger selection.

The requirement of at least four jets per event results to be $(83 \pm 2)\%$ efficient on the signal, while it rejects $(51 \pm 8)\%$ of the events due to QCD processes. Since we are interested in a full reconstruction of the $VH \to q\bar{q}^{(\prime)}b\bar{b}$ decay, we apply this requirement in defining our analysis sample. Quarks from boson decays are associated to the closest jet in the η-ϕ plane, within a radius $R = 0.4$. The four partons in the final states are then found to be all reconstructed in $(66 \pm 2)\%$ of the cases. The jet E_T distribution after standard jet corrections (see Sec. 2.4.2) is shown in Fig. 6.6.

The cross sections for signal and background production after ≥ 4 jet selection are summarized in Tab. 6.3 and 6.4 respectively. They have been computed on the same Monte Carlo samples we used in the Sec. 6.1 .

One of the most distinctive characteristics of the signal events we are considering is the presence of two b quarks in the final state. The main procedures for b-jet identification used by the CDF I experiment exploited two different characteristics of these particles' decays. The Soft Lepton Tagging (SLT) algorithm [4] was based on the search for electrons or muons originated in the semileptonic decays of heavy quark ($q \to q'l\nu_l$): these have different characteristics from the leptons produced in W boson decays since they have a lower transverse momentum and are usually embedded in a jet. The details of the SLT procedure have already been discussed in Sec. 2.4.4 and 2.5.1. The SECondary VerTeX (SECVTX) tagging algorithm [5, 6], on the other hand, exploits the high resolution of the silicon vertex detector to

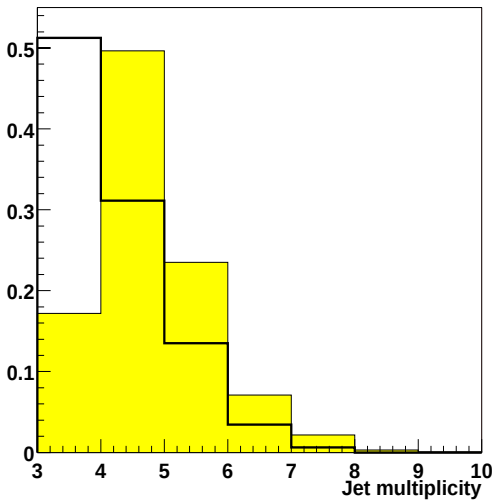

Figure 6.5: *Jet multeplicity for VH (shaded histogram) and* QCD *(white) events after trigger selection.*

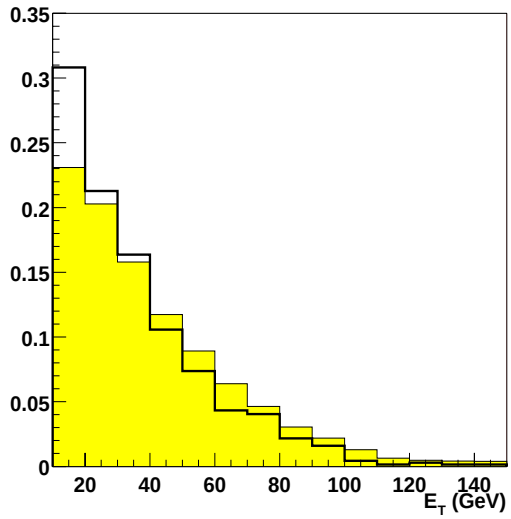

Figure 6.6: *Jet E_T distribution for VH (shaded histogram) and* QCD *(white) events after four jet requirement. Standard jet corrections have been applied.*

identify secondary vertices originated inside a jet by decays of long lifetime particles produced in heavy quark hadronization. This approach resulted to provide a greater discrimination of high-P_T b-jets from jets originated by light quarks or gluons, and it is therefore the most suitable tool to study Higgs boson production in all hadronic final state. Further details on SECVTX tagging algorithm are provided in Chap. 2.

So far, a Run II-based SECVTX tagging algorithm has been implemented following the guidelines of the Run I algorithm. In fact, the silicon tracking system of CDF II has been disegned to keep the performance of Run I detector in the higher luminosity environment expected during Run II. The silicon vertex detector has been subjected to several upgrades for Run II (see Sec. 2.3). In particular, it has been provided with double-sided silicon layers, making it capable of precise z measurenment of track position in addition to x and y coordinates. It should enable to perform a full three-dimensional reconstruction of the secondary vertices, leading to a more powerful b-jet identification. On the contrary, the higher instantaneous luminosity and the increased quantity of material around the interaction point contribute to degrade the resolution achievable by the silicon tracking system. Although the new Layer 00 detector has been designed to restore the same performance the silicon tracking system had during Run I, predictions are not easy to make. A mistag probability measurement[1], on the other hand, will be possible only when a large sample of data will be available [7]. Preliminary studies have been performed by means of a parametrized detector simulation. They estimated the mistag probability of a jet as a function of its transverse momentum. The obtained distributions are

[1]The mistag probability is the probability that a jet produced by light quark or gluon hadronization is tagged by the SECVTX algorithm (see Sec. 2.4.3).

	110 GeV/c^2	115 GeV/c^2	120 GeV/c^2	125 GeV/c^2	130 GeV/c^2
$\geq$ 4 jets (fb)	46 ± 1	41 ± 1	34 ± 1	28.0 ± 0.8	22.3 ± 0.7
$\geq$ 1 tag (fb)	36 ± 1	31 ± 1	25.7 ± 0.9	20.5 ± 0.7	16.8 ± 0.6
$\geq$ 2 tags (fb)	11.8 ± 0.7	11.2 ± 0.6	8.7 ± 0.5	7.1 ± 0.4	6.0 ± 0.3

Table 6.3: *Cross sections for signal production after sample selection cuts. Errors are statistical only.*

	QCD	W production	Z production
$\geq$ 4 jets (fb)	$(7 \pm 1) \times 10^6$	–	–
$\geq$ 1 tag (fb)	$(1.7 \pm 0.2) \times 10^6$	$(8 \pm 3) \times 10^3$	$(12 \pm 4) \times 10^3$
$\geq$ 2 tags (fb)	$(194 \pm 21) \times 10^3$	$(0.07 \pm 0.03) \times 10^3$	$(0.5 \pm 0.2) \times 10^3$

	$t\bar{t}$	single top	WW	WZ	ZZ
$\geq$ 4 jets (fb)	1340 ± 40	270 ± 9	170 ± 10	89 ± 5	52 ± 2
$\geq$ 1 tag (fb)	960 ± 50	167 ± 7	39 ± 6	39 ± 3	29 ± 2
$\geq$ 2 tags (fb)	320 ± 30	20 ± 3	0.8 ± 0.8	9 ± 1	9 ± 1

Table 6.4: *Cross sections for background production after sample selection cuts. Errors are statistical only.*

roughly the same as in Run I. As a preliminary approach, we assume this result. We assign heavy quarks in the event to the jets following the prescription described above. If a jet does not result associate to an heavy parton, we do not look at the SECVTX tagging information, but we simulate the tagging result according to the estimated mistag probabilty.

We compute expected cross sections after b-tagging requirements by using the same simulation as in the last section. Results are quoted in Tab. 6.3 and 6.4 for signal and background events respectively. The estimates of the cross sections of QCD and W/Z direct production require more work. For the same reasons we discussed in Sec. 6.1 about the single vector boson production, we can not compute the cross sections of these processes after b-tagging requirements by using only Monte Carlo simulation. Fully satisfactory estimates will can be possible only on experimental data. For the time being, we perform a rough estimate of these cross sections by extrapolating the obtained values for the Run I multijet trigger to the Run II framework. During Run IB, 10377 (783) events with at least 1 (2) tags were collected by the multijet trigger for an integrated luminosity $\mathcal{L}^{int.} = 90 \pm 7\ pb^{-1}$. Since this sample is dominated by the QCD production, we estimate a cross section of $(115 \pm 9) \times 10^3\ fb$ ($(8.7 \pm 0.7) \times 10^3\ fb$) for the QCD background after at least 1 (2) tag has been required. The main differences with respect to the Run II arise from the calorimetric requirements, b-tagging efficiency, center of mass energy of the $p\bar{p}$ collisions, and SVT requirements. We estimate the effect of the difference in the calorimetric requirements by using the Run I JET20 data sample we described in Sec. 3.3.1. We simulate the Run II calorimetric primitives through the parametriza-

tion of the increased acceptance [8] we used in Sec. 3.2 and 3.3.1. Successively, we compute the ratio R_c between the events passing Run II and Run I multijet calorimetric requirements. We find $R_c = 16 \pm 1$. Since too few events with SECVTX tags are found to pass Run I multijet requirements, we assume this ratio is valid also for tagged events[2]. The improvement in the b-tagging efficiency is expected to be about 1.3 [7]. The effect of the increase of the center of mass energy of the $p\bar{p}$ collisions is taken into account by generating two samples of $100,000$ events each by means of the PYTHIA Monte Carlo with $\sqrt{s} = 1.8$ and $\sqrt{s} = 2\ TeV$ respectively. Events are filtered by requiring an outcoming parton with transverse momentum $P_T \geq 40\ GeV/c$. The ratio $R_\sigma = 1.23$ between the cross sections predicted by PYTHIA for the two samples is used to estimate the increase of the QCD background cross section in Run II. Finally, we compute the efficiency ϵ_{svt} of the SVT requirements on tagged events passing calorimetric selection. The Monte Carlo sample used is described in Sec. 6.4. We find $\epsilon_{svt} = 58 \pm 2\%$ ($68 \pm 2\%$) for events with at least 1 (2) tag. By combining these estimates, we predict a cross section of $(1.7 \pm 0.2) \times 10^6\ fb$ and $(194 \pm 21) \times 10^3\ fb$ for QCD event production contributing to the multijet trigger sample with at least 1 or 2 SECVTX tag respectively. We must note that the quoted errors are statistical only. In order to test these results, we compute the QCD background cross section by starting from the value predicted by the PYTHIA Monte Carlo. We use again the sample described in Sec. 6.4. We obtain a cross section of $(1.62 \pm 0.02) \times 10^6\ fb$ and $(198 \pm 5.2) \times 10^3\ fb$ for events with 1 or 2 SECVTX tag respectively. The compatibility between the two results is very good. Finally, we estimate the cross section for W/Z direct production by following the same procedure described above. The R_c ratio is evaluated by means of two simulated samples of $5,000$ $W + jets$ and $Z + jets$ events generated with the HERWIG [9] Monte Carlo. A full CDF I detector simulation is applied to the generated events. The obtained results are summarized in Tab. 6.4. They have to be considered as purely indicative values.

Tagging requirements result to be a mandatory tool to discriminate signal production from QCD processes. Some observations can be done the effect of tagging requirements on the other background sources. WW production results to be strongly suppressed, according to the fact that no b quark production is expected by these processes. Signal discrimination power with respect to WZ and ZZ events, on the other hand, results to be increased by requiring a single SECVTX tag, but seems to suffer from a double tagging requirement. Actually, the first SECVTX tag selects events with vector boson decaying into heavy quarks (mainly $Z \to b\bar{b}$), and further tagging results no more discriminant. Finally, SECVTX tag requirements do not result to be useful to discriminate VH events from $t\bar{t}$ and single top production because these processes always yield two high-P_T b-jets ($\beta(t \to W^+ s(d)$ and $\beta(\bar{t}^- \to W^- \bar{s}(\bar{d})$ are CKM-suppressed). However a b-jet tagging would be a powerful tool for a correct event reconstruction. Everything considered, since QCD processes

[2]This is a conservative hypothesis since the SECVTX algorithm has been optimized to tag high-P_T jets, therefore tagging requirements are expected to decrease R_c. Actually, Run II calorimetric requirements are loose with respect to Run I ones, so that the fraction of events with a SECVTX tag is expected to be lower.

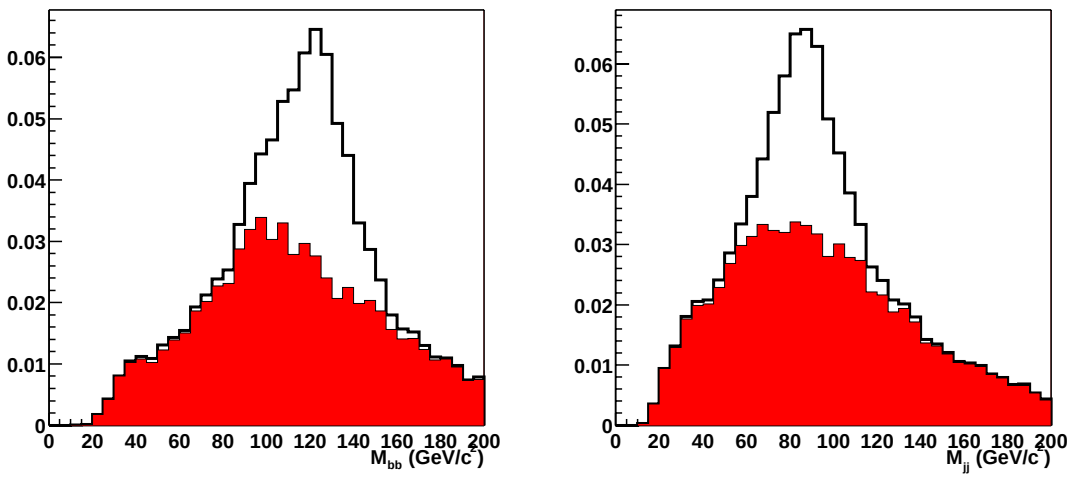

Figure 6.7: *Dijet mass distributions for Higgs (left) and vector (right) boson candidates. The four leading jets have been used. Tagged jets have been assigned to the Higgs boson decay. All combinations are included. The shaded histograms show the contributions from wrong combinations. Preliminary jet energy corrections we studied in Sec. 5.6 are been applied.*

are the dominant source of background, we define our analyzable sample by requiring at least one SECVTX tag. In the following, we will refer to a jet tagged by the SECVTX algorithm as a *tagged jet*.

6.3 Studies of $HV \to b\bar{b}q\bar{q}^{(\prime)}$ Decay Reconstruction

The reconstructed masses of the $b\bar{b}$ pair coming from Higgs boson decay is one of the most distinctive characteristics of VH production. A correct assignment of the reconstructed jets to the originating partons is then an important tool to discriminate signal from background events. In this section, we discuss a simple prescription to reconstruct the boson decays. A view to future improvements is also provided. As a reference, we set the Higgs boson mass to $M_H = 120\ GeV/c^2$.

In the sample with at least four jets and one SECVTX tag, we find that the reconstruction of all the four quarks originated by boson decays is achieved with an efficiency of $(67 \pm 1)\%$. In this situation, the produced jets result to correspond to the four leading jets in $(81 \pm 1)\%$ of the cases. Moreover, the identification of the tagged jets with a b quark from Higgs decay results to be correct $(86 \pm 1)\%$ of the times. Therefore, we reconstruct Higgs and vector boson decay by using the four leading jets in the event, and by assigning tagged jets to the Higgs particle. Fig. 6.7 shows mass distributions of all the jet pairs fulfilling requirements for Higgs and vector boson reconstruction. The distribution for correct and not correct jet assignments are also shown. The jet energy corrections we studied in Sec. 5.6 have been applied. Reconstruction efficiencies are $(74 \pm 1)\%$ for the Higgs boson and $(72 \pm 1)\%$ for the

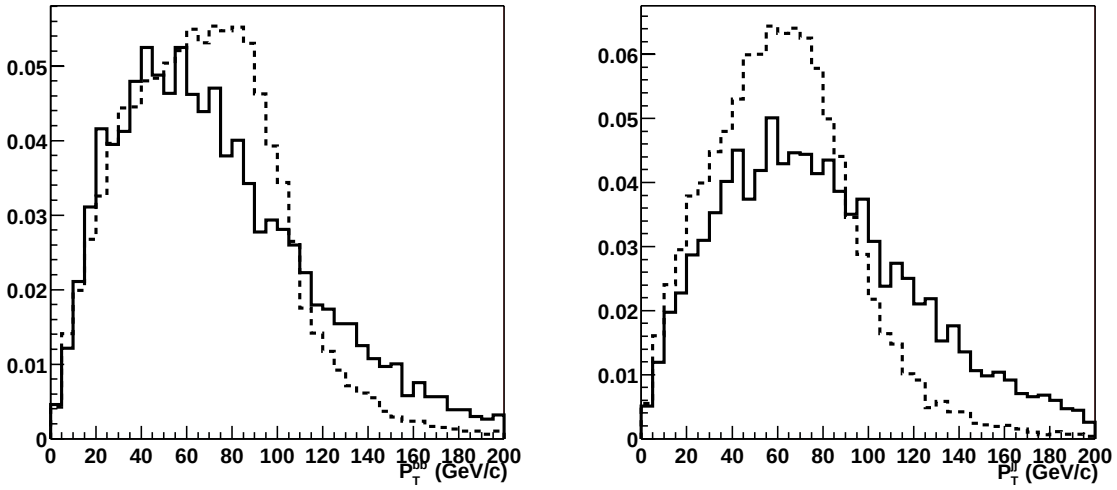

Figure 6.8: *Comparison of transverse momentum spectra of dijet system when right (full histograms) and wrong (hatched) combinations are considered for Higgs (left) and vector (right) boson reconstruction.*

vector boson. Due to the numerous combinations, purity of the boson reconstruction (*id est* the ratio between the right combinations and all the possible ones) is rather low: $(28.3 \pm 0.3)\%$ and $(23.4 \pm 0.3)\%$ for Higgs and vector bosons respectively. In order to increase the reconstruction purity, we study further requirements for jet-parton association, able to guarantee a single assignment per event. We begin by looking at kinematical variables, such as the transverse momentum of the dijet system and the angle between the two jets (see Fig. 6.8 and 6.9). These quantities exhibit a quite different behaviour, but it is not enough to provide an effective rejection of wrong combinations. Moreover, they are correlated with the mass value. Cuts on these variables could induce a bias in the dijet mass spectra of background events and eventually make them less separable from signal ones.

A more effective tool is the requirement of a second SECVTX tag in the event. Reconstructed mass distributions for Higgs and vector bosons are then shown in Fig. 6.10. Purity increases to $(43 \pm 1)\%$ for $W^{\pm}/Z^0$, and to $63 \pm 2)\%$ for H^0. Actually, the double tagging requirement selects a high fraction of events where both jets from Higgs decay have been reconstructed. The loss in efficiency ($(20.2 \pm 0.5)\%$ and $(16.1 \pm 0.4)\%$) is compensated from the high background rejection provided by the double tag requirement (see Tab. 6.3 and 6.4). Further studies are in progress to increase the efficiency of the boson decay reconstruction by improving the b-jet identification, while keeping high rejection factor on background events. A strategy consists of recovering efficiency by allowing to the second jet from Higgs boson decay to be tagged by a different algorithm, as for example the SLT one. More sophisticated analyses aim at merging all information from tagging algorithms by means of multivariate techniques. Preliminary studies within the Run I framework show the effectiveness of this strategy [10]. It could become a useful tool to increase the sensitivity on Higgs boson production in the multijet sample.

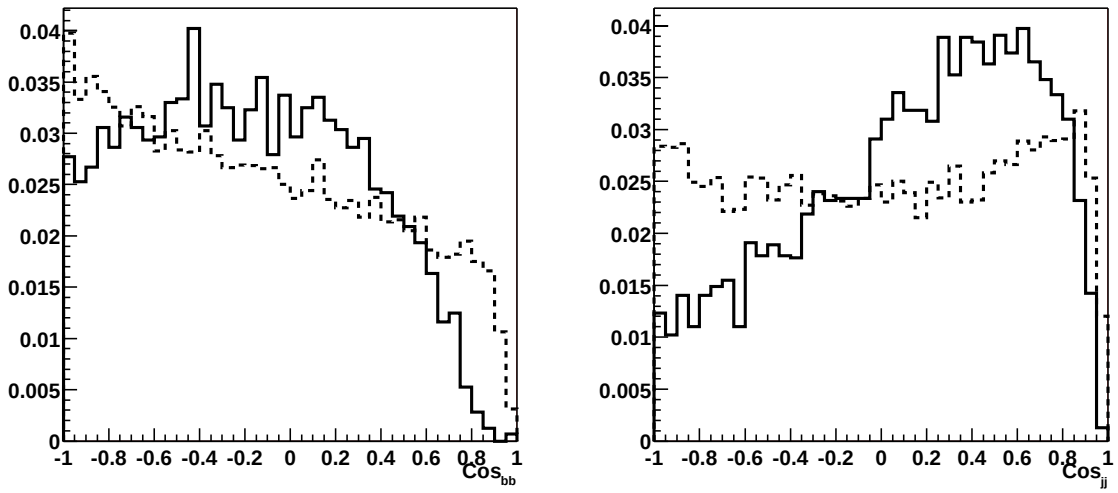

Figure 6.9: *Comparison of the angle of the jet pairs when right (full histograms) and wrong (hatched) combination are considered for Higgs (left) and vector (right) boson reconstruction.*

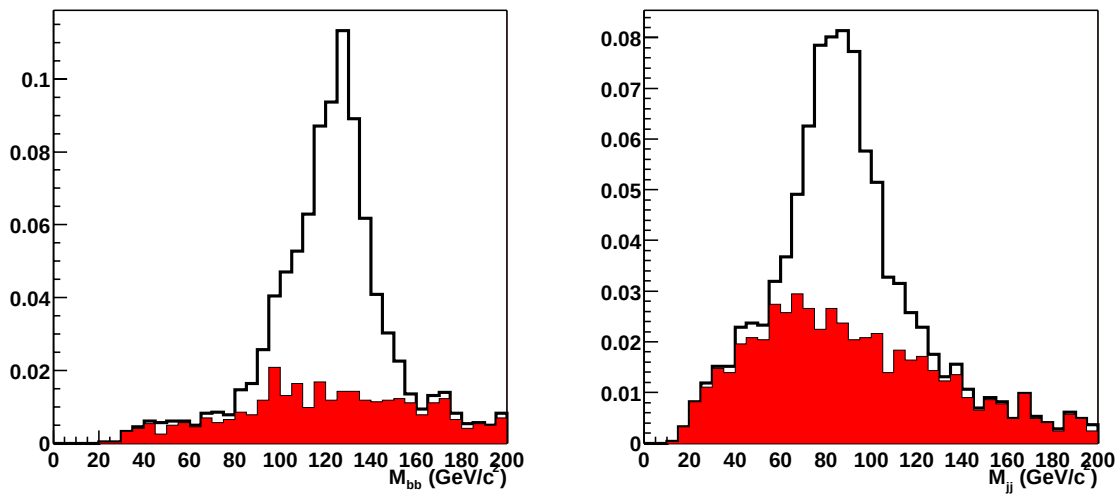

Figure 6.10: *Dijet mass distributions for Higgs (left) and vector (right) boson candidates. Two* SECVTX *tag are required. The four leading jets have been used and tagged jets have been assigned to Higgs boson: one combination per event is included. The shaded histograms show the contributions from wrong combinations. We observe that the vector boson reconstruction suffers from a high number of wrong combinations with respect to Higgs boson one. Actually, the double tagging requirement selects a high fraction of events where both jets from Higgs decay have been reconstructed.*

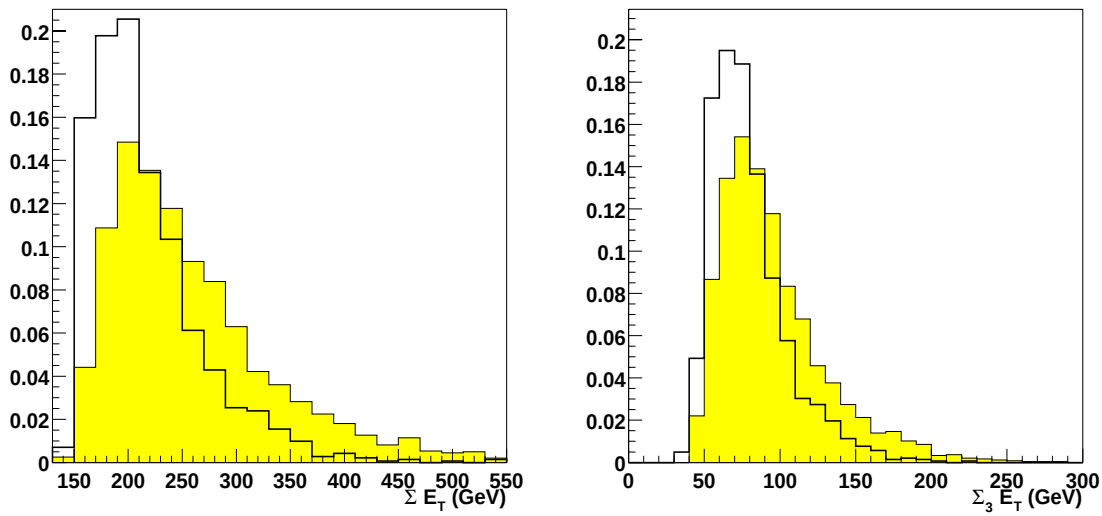

Figure 6.11: ΣE_T *(left) and* $\Sigma_3 E_T$ *(right) distributions for signal (shaded histograms) and* QCD *(white) events.*

6.4 Kinematical Characterization of the Events

Signal Discrimination from QCD Processes

QCD processes constitute the main source of background for Higgs boson search in the multijet sample (see Tab. 6.4). Other than the reconstructed masses of the bosons, we need additional variables to increase the signal-to-background ratio.

In order to characterize VH and QCD events, we generate 40,000 and 4,500,000 events of Higgs associated production and QCD pair production respectively. We use the PYTHIA 6.129 Monte Carlo. As a reference, we set the Higgs boson mass to $M_H = 120\ GeV/c^2$. Furthermore, QCD events are filtered by requiring an outcoming parton with transverse momentum $P_T \geq 40\ GeV/c$ and a heavy flavour quark with $P_T \geq 5\ GeV/c$. After a full detector and trigger simulation, we find 2,500 and 1,500 events contributing to our analyzable sample for VH and QCD production respectively.

Heavy particle production is characterized by a special kinematical topology, that can be summarized in specific event variables. The energy available in the hard scattering producing them is expected to flow mainly in the transverse plane. Moreover, the great amount of energy released in the successive decays of the heavy particles leads to jets with high energy. The most distinctive kinematical properties of VH production with respect to background events are then:

- total jet energy,
- centrality of the energy flux.

The total jet energy is effectively expressed by the scalar sum of the transverse energy of the jets, $\Sigma E_T = \Sigma_{i=1}^{N_{jet}} E_T^i$. Since sub-leading jets for QCD processes are

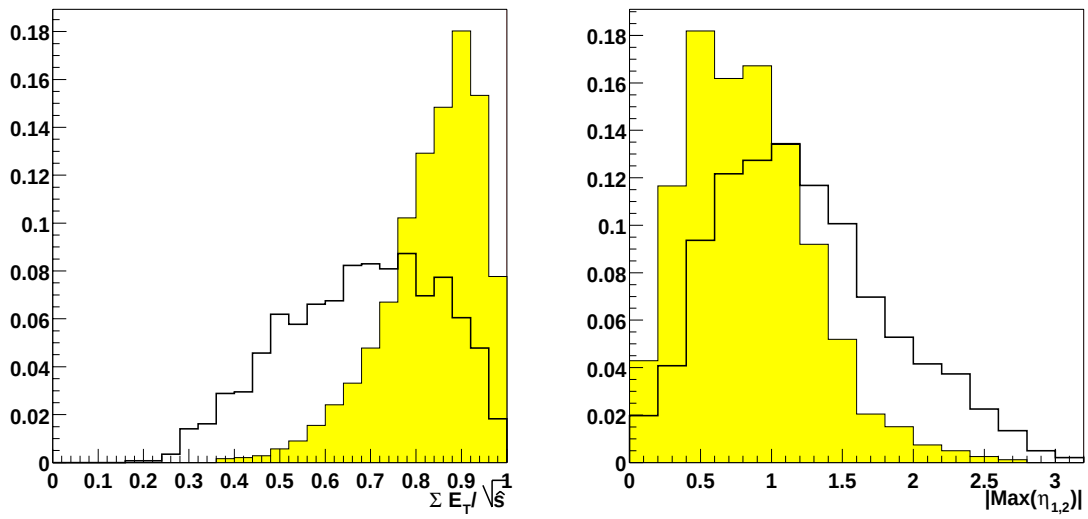

Figure 6.12: $\Sigma E_T/\sqrt{\hat{s}}$ *(left) and* $|\eta_{j2}|$ *(right) distributions for signal (shaded histograms) and* QCD *(white) events.*

expected to be originated from radiation phenomena with a softer energy than jets produced in heavy boson decays, we consider also the sum of the E_T jet for all jets excluding the leading two $\Sigma_3 E_T = \Sigma_{i=3}^{N_{jet}} E_T^i$. A comparison between the distributions of these variables for VH and background events is shown in Fig. 6.11. As expected, QCD production is characterized by a lower total energy with respect to signal one.

The centrality of the energy flux drives jets produced in $VH \rightarrow q\bar{q}^{(\prime)}b\bar{b}$ decays mainly in the perpendicular direction with respect to the beam line. Two variables have been chosen to describe this property: the fraction of transverse energy $\Sigma E_T/\sqrt{\hat{s}}$, where $\sqrt{\hat{s}} = \sqrt{x_1 x_2 s}$ is the energy in the center of mass of the process, x_1 and x_2 being the fraction of the beam energy carryed by the interacting partons ($x_{1,2} = (\Sigma E \pm \Sigma p_z)/\sqrt{s}$), and the absolute value of the pseudorapidity of the second leading jet in the event. Distribution of these quantities for both signal and background events are shown in Fig. 6.12. Again, the expected behaviour is observable. Another distinctive characteristic of multijet events is the spacial distribution of the jets. A useful variable carrying information about this distribution turns out to be the thrust value of the four leading jets in their center of mass

$$t_4 = max_{\vec{n}} \frac{\Sigma_{k=1}^4 \vec{P}^k \cdot \vec{n}}{\Sigma_{k=1}^4 P^k} \ ,$$

where $\vec{P}^k$ is the momentum of the jet k in such frame of reference. Distributions of t_4 values for VH and QCD production are compared in Fig. 6.13. The thrust value result to be correlated with the centrality of the event. This is put in evidence by plotting t_4 as a function of $\Sigma E_T/\sqrt{\hat{s}}$ (see Fig. 6.15) and the relation $t_4 - 0.82 \cdot \Sigma E_T/\sqrt{\hat{s}}$ [11] (see Fig. 6.15). Additional variables summarizing the jet distribution

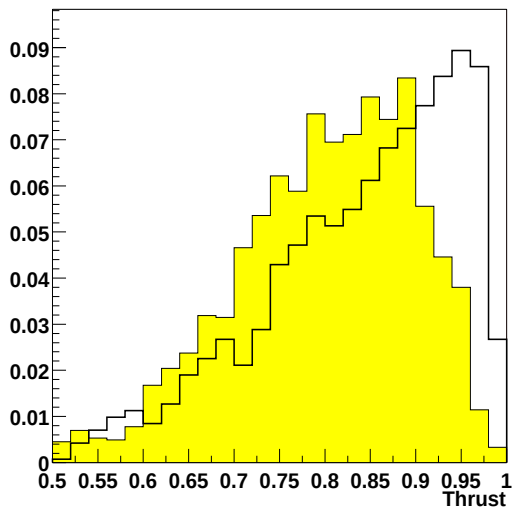

Figure 6.13: *t_4 distributions for signal (shaded histogram) and* QCD *background (white) production.*

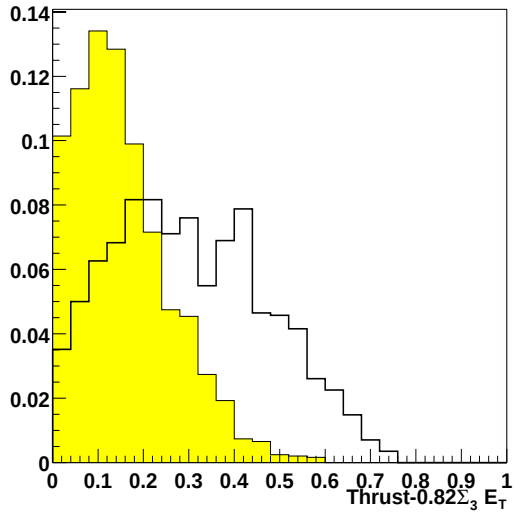

Figure 6.14: *$t_4 - 0.82 \cdot \Sigma E_T/\sqrt{\hat{s}}$ distribution for VH (shaded histogram) and* QCD *(white) events.*

can be obtained from the eigenvalues Q_i of the tensor

$$M_{a,b} = \frac{\Sigma_{k=1}^{N_{jet}} P_{k,a} P_{k,b}}{\Sigma_{k=1}^{N_{jet}} P_k} \ ,$$

where P_k is the quadrimomentum of the jet k and a and b label the spacial components. After the eigenvalues are ranked according to increasing values, we can define the aplanarity $\mathcal{A} = \frac{3}{2}Q_1$ and the sphericity $\mathcal{S} = \frac{3}{2}(Q_1 + Q_2)$, whose distributions for signal and background events are shown in Fig. 6.16 and 6.17. These variables turn out to have some discrimination power.

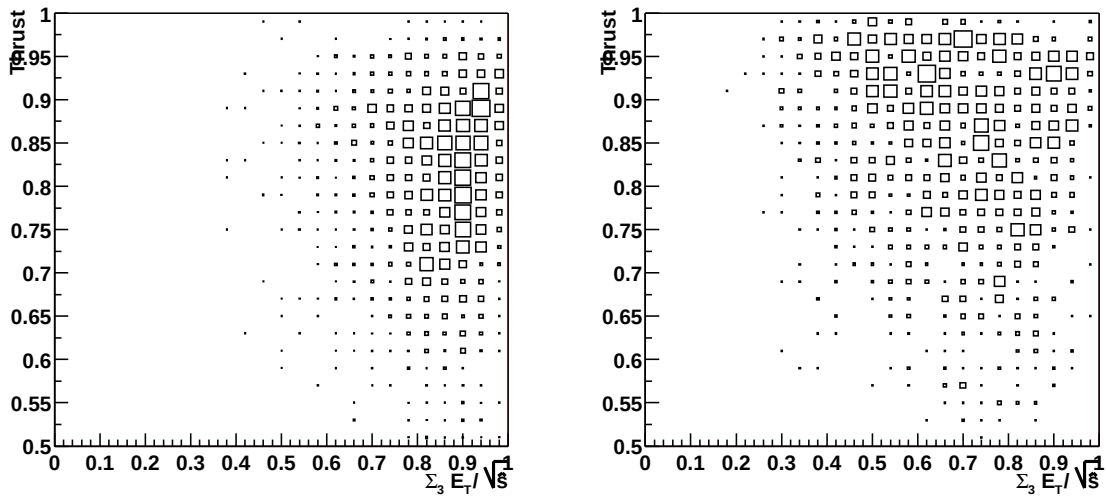

Figure 6.15: $t_4 - 0.82 \cdot \Sigma E_T /$ *as a function of* $\sqrt{\hat{s}}$ *for signal (shaded histograms) and* QCD *background (white) production.*

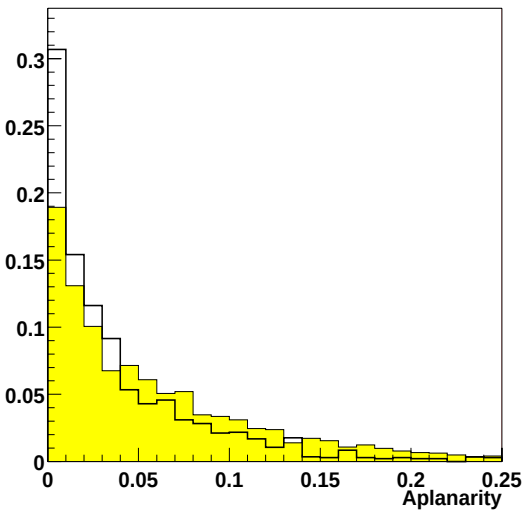

Figure 6.16: *Aplanarity distributions for signal (shaded histogram) and* QCD *background (white) events.*

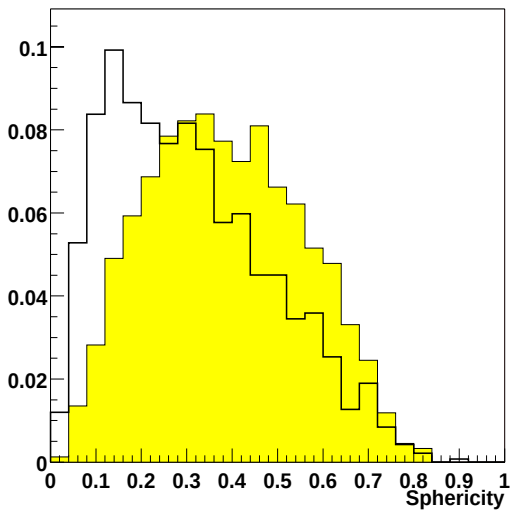

Figure 6.17: *Sphericity distributions for* VH *(shaded histogram) and* QCD *(white) production.*

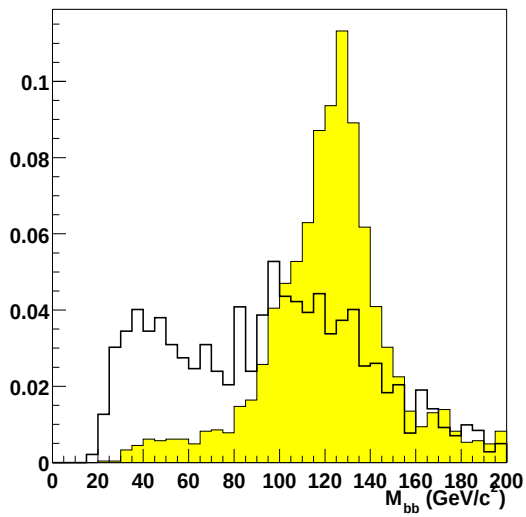

Figure 6.18: *Invariant mass distributions of the jet pairs associated to the Higgs boson decays for signal (shaded histogram) and* QCD *background (white) production.*

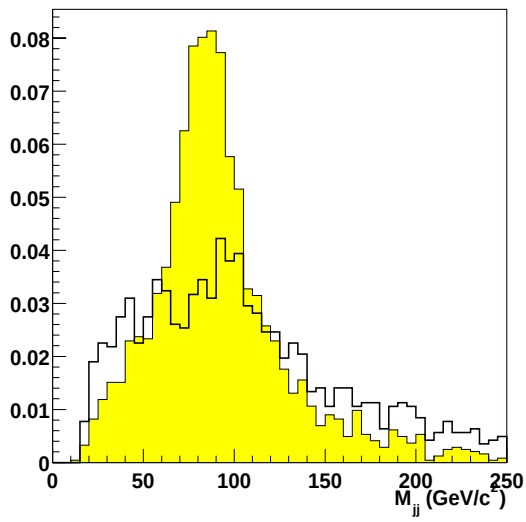

Figure 6.19: *Invariant mass distributions of the jet pairs associated to the vector boson decays for VH (shaded histogram) and* QCD *(white) events.*

Finally, we look at the masses of the reconstructed bosons. As discussed in Sec. 6.3, we reconstruct boson decays by assuming the jets originated from the outcoming partons are the four leading ones and by assigning tagged jets to the b-quarks from Higgs decay. Fig. 6.18 and 6.19 compare the obtained dijet mass spectra for signal and background production for the two tagged jets and the other two jets respectively. The high discrimination power is pointed out by the scatter plot of the two dijet invariant masses (see Fig. 6.20). Furthermore, the correlation between mass and transverse momentum of the two tagged jet system exhibits a marked difference between VH and QCD events [12] (see Fig. 6.21). The signal distribution is obviously characterized by mass values in the Higgs mass region and by transverse momentum values between 20 and 80 GeV/c. On the contrary, background events show two different populations: tagged jet pairs produced by means of gluon splitting processes are expected to be produced relatively close together, and result to have small invariant mass but large transverse momentum; on the contrary, direct production of heavy quark pairs lead to tagged jets recoiling against each other, so exhibiting larger invariant mass and smaller transverse momentum values. Moreover, background dijet systems whose invariant mass fall in the signal region turn out to have on average a smaller transverse momentum than signal ones. This is pointed out in Fig. 6.22, where the P_T distribution for jet pairs having mass between 100 and 140 GeV/c^2 is shown.

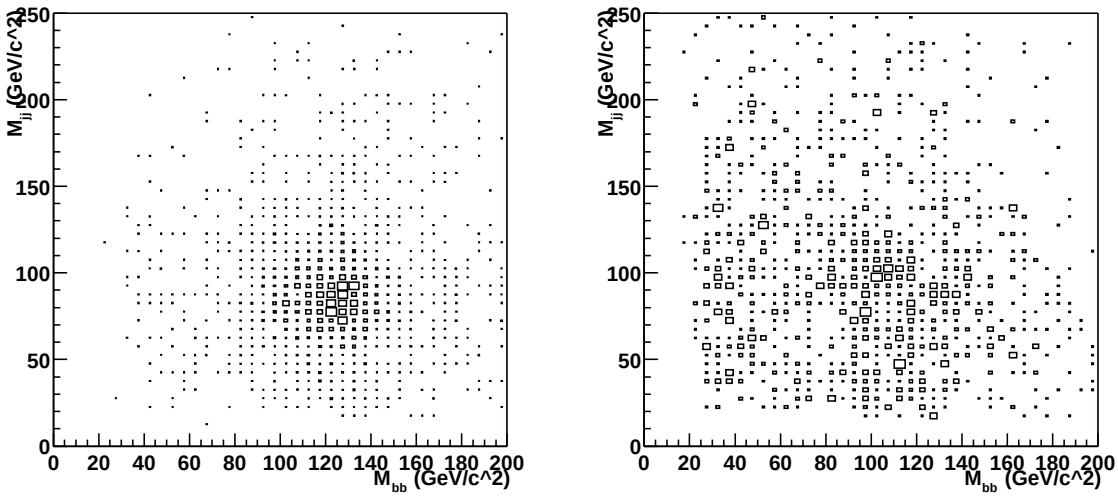

Figure 6.20: *Invariant mass of the two tagged jet system versus other two jets' one for signal (left) and* QCD *background (right) production.*

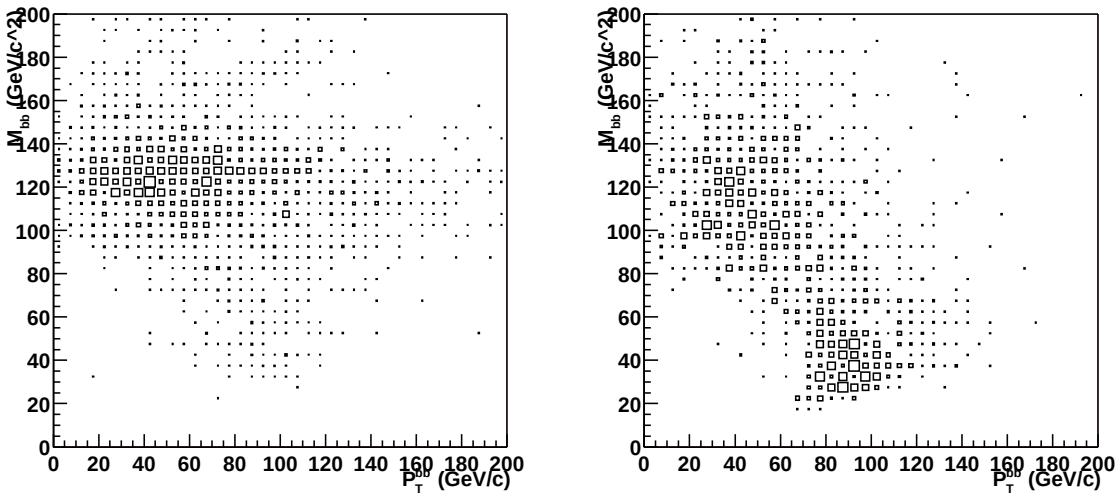

Figure 6.21: *Invariant mass versus transverse momentum of the two tagged jet system for VH (left) and* QCD *(right) events.*

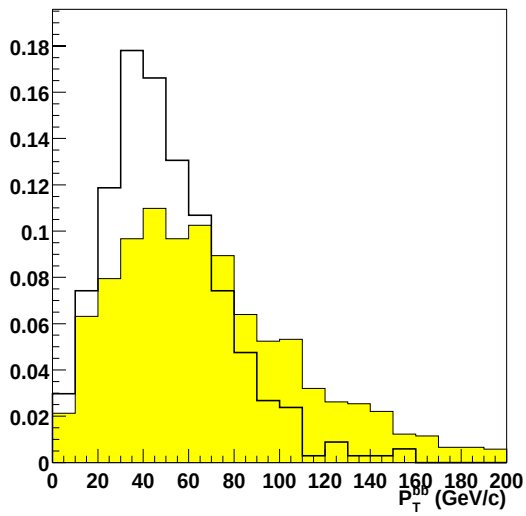

Figure 6.22: *P_T distributions of tagget jet pairs having invariant mass between* 100 *and* 140 *GeV/c^2 for signal (shaded histogram) and* QCD *background (white) production.*

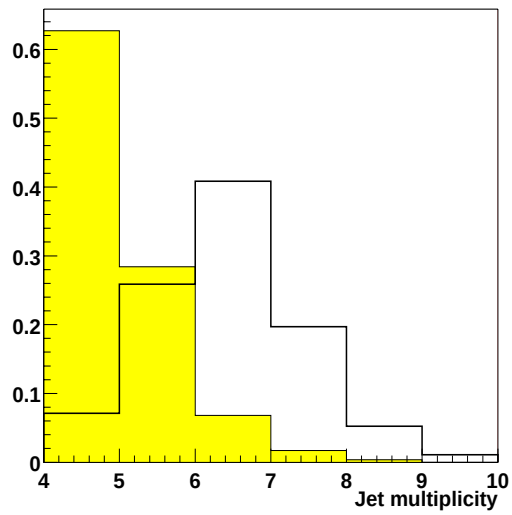

Figure 6.23: *Jet multeplicity for VH (shaded histogram) and $t\bar{t}$ (white) events.*

$t\bar{t}$ Event Characterization

$t\bar{t}$ production constitutes an important contribution to the multijet sample. Its cross section after analysis requirements has been estimed to be 0.32 ± 0.03 *pb* (see Tab. 6.4). Besides being an interesting matter of search, it could become a non-negligible contribution to the background for Higgs boson search after QCD events have been filtered by means of kinematical cuts. Therefore, we look for some characteristics of $t\bar{t}$ production able to discriminate it from the signal one. The main contribution to the multijet sample comes from all hadronic $t\bar{t}$ decays. Events with only one W boson decaying into quarks can also contribute to the sample, but they can be rejected by discarding events with high $\not{E}_T$ and an isolated lepton coming from $W \to l\nu_l$ decay.

The sample we use consists of $20,000$ $t\bar{t}$ events generated with the PYTHIA 6.129 Monte Carlo. After a full detector and trigger simulation, we find about $1,500$ events passing our analysis requirements.

The $t\bar{t} \to bq\bar{q}'\bar{b}q\bar{q}'$ decay is expected to lead to six jet final states. Jet multiplicity N_{jets} of $t\bar{t}$ events results then greater than signal one. Fig. 6.23 shows the great discrimination power of this variable.

In order to avoid the natural correlation between jet multiplicity and the other event variables, we perform the successive studies by requiring $N_{jets} < 6$. Results are summarized in Fig. 6.24. The high energy of the jets produced by top quark decays ($m_{top} = 175$ GeV/c^2) is effectively expressed by the ΣE_T and $\Sigma_3 E_T$ and provide a good discrimination between $t\bar{t}$ and VH events. On the contrary, the centrality

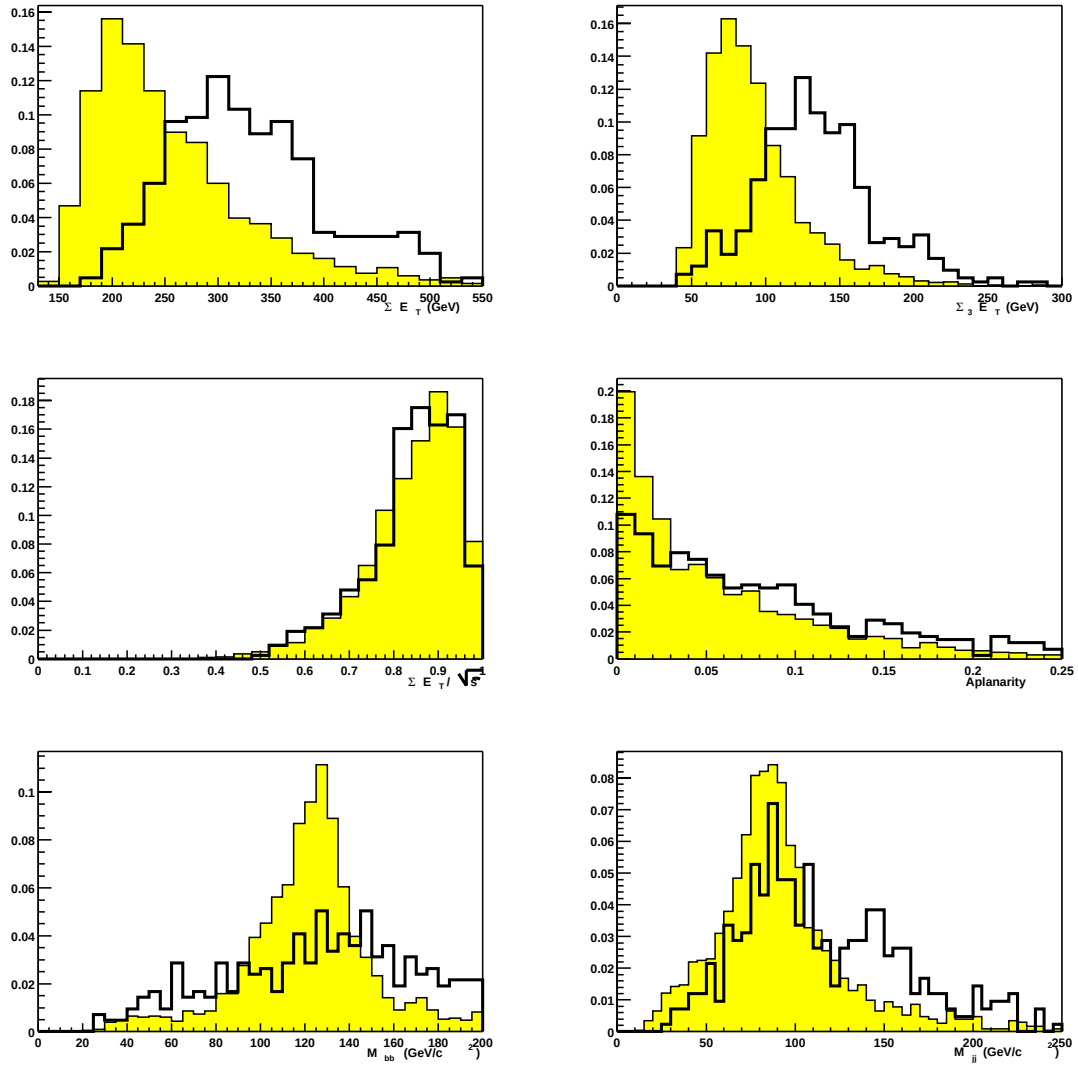

Figure 6.24: *Comparison of some kinematical variables for VH (shaded histogram) and $t\bar{t}$ (white) events after requiring $N_{jets} < 6$.*

of the energy flux and the jet spatial distribution do not exhibit a significantly different behavior, as shown by the $\Sigma E_T/\sqrt{\hat{s}}$ and aplanarity distributions. Finally, dijet mass spectra offer a powerful tool for the signal-to-background discrimination, even if the W boson production by top quark decays decreases the difference in the reconstructed mass distributions of the vector boson candidates.

Single Top and Diboson Production

After analysis selection, single top and diboson production cross sections are expected to be of the same size as the signal production one (see Tab. 6.3 and 6.4). These events could then become an issue only if a great QCD process rejection is reached.

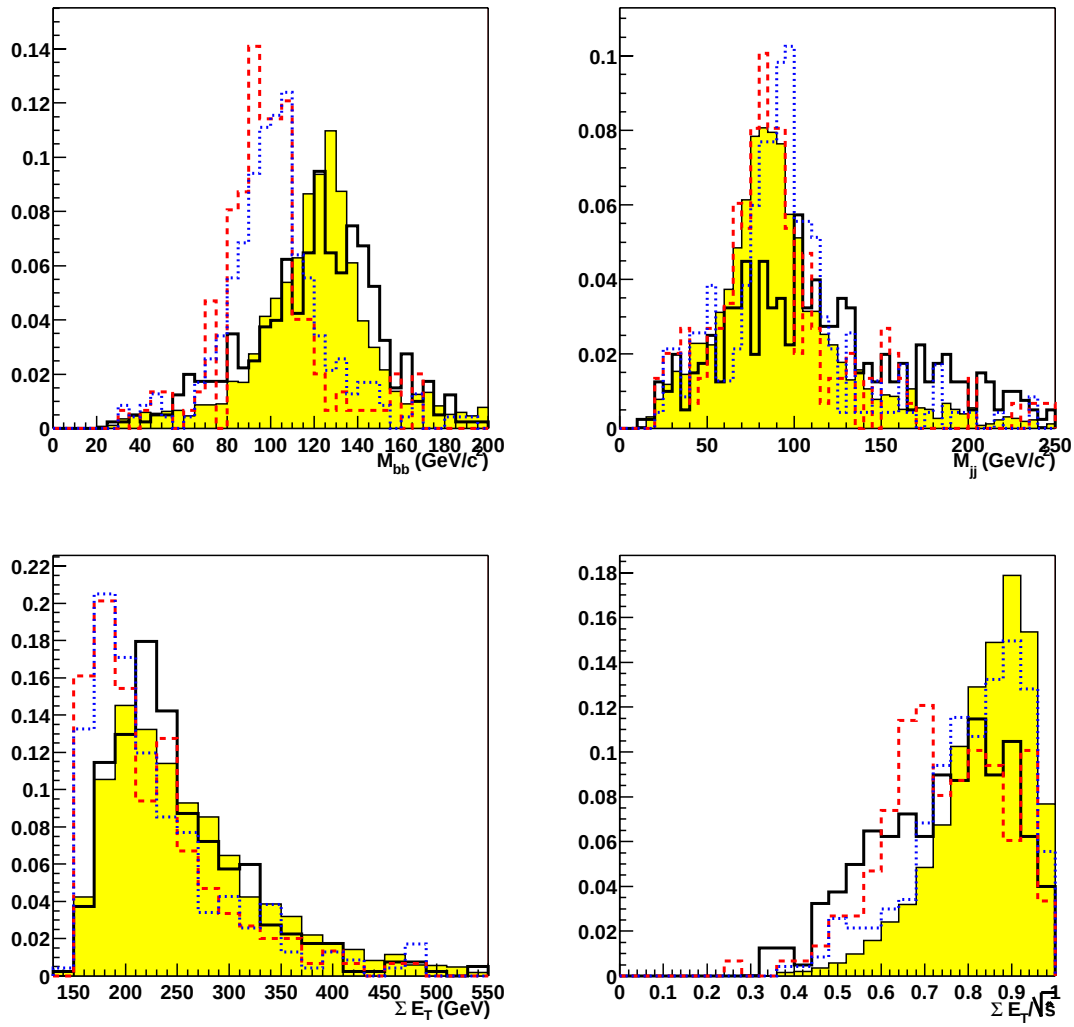

Figure 6.25: *Comparison of some kinematical variables for VH (shaded histogram), single top (white), WZ (hatched) and ZZ (pointed) events.*

The main characteristics of these events have been studied through three sample of about 30,000 simulated events of single top production and 40,000 events for both WZ and ZZ production. The PYTHIA 6.129 Monte Carlo has been used. A full detector and trigger simulation has been applied to generated events. Finally, we have about 400, 300 and 300 events for single top, WZ and ZZ production respectively.

Distributions for the most distinctive variables are shown in Fig. 6.25. Other than by dijet masses, we find that diboson production is characterized by a smaller total energy than signal production. ΣE_T distributions express well this behaviour. Finally, single top and WZ events exhibit a lower centrality of energy flux than VH events, as shown by the fraction of transverse energy $\Sigma E_T/\sqrt{\hat{s}}$.

Bibliography

[1] `http://www.thep.lu.se/tf2/staff/torbjorn/Pythia.html`.

[2] `http://hepwww.rl.ac.uk/theory/seymour/herwig/`.

[3] P. Azzi et al., *Evaluation of the W/Z + jets background for the top search in the all-hadronic channel*, CDF internal note 3428, Nov 1995.

[4] C. Campagnari et al., *Review of the SLT Algorithm for Run Ib*, CDF internal note 3682, May 1996.

[5] D. Glenzinsky et al., *A detailed study of the SECVTX algorithm*, CDF internal note 2925, Dec 1994.

[6] C. Cmiao et al., *Update of SECVTX tagging on Run 1B data*, CDF internal note 3178, Jun 1995.

[7] M. Carena, J. S. Conway, H. E. Haber, J. D. Hobbs, et al. (The Fermilab Higgs Working Group), *Report of the Tevatron Higgs Working Group*, HEP-PH/0010338, Oct 2000.

[8] J. Lewis et al., *Guide to Run II Trigger Simulations*, CDF internal note 4321, Sep 1997.

[9] `http://hepwww.rl.ac.uk/theory/seymour/herwig/`.

[10] D. Wolinsky et al., *Jet Flavour Tagging Using Tracking Variables*, CDF internal note 3711, Nov 1999.

[11] M. P. Giordani, *A Run II Trigger Design for Higgs Boson Search at CDF*, Ph.D. thesis, Dec 2000.

[12] J. F. Troconiz and J. A. Valls, *Search for Invariant Mass Resonances in the Multijet Data Sample*, CDF internal note 3711, Jun 1996.

Chapter 7

Strategies for an Estimate of the Sensitivity on VH Production

In this chapter, we study some tools to make an estimate of the sensitivity on VH production achievable with the multijet trigger sample. The characteristics of signal and background events pointed out in the last chapter are exploited to improve the statistical significance of the Higgs signal, defined as the $S/\sqrt{B}$ ratio, where S and B are the expected number of signal and background events respectively. Two possible approaches are investigated. The first one is based on a standard kinematical selection, id est *on a set of cuts on the most discriminating kinematical variables. The second strategy instead studies the effectiveness of a neural network technique to maximize the signal sensitivity.*

Finally, we discuss briefly the main sources of systematic uncertainties in our analysis and make a preliminary estimate of the achievable limits on the cross section for VH production at the Tevatron collider.

7.1 Estimate of $S/\sqrt{B}$

7.1.1 Standard Kinematical Selection

In this subsection we study how the statistical significance of the Higgs signal, $S/\sqrt{B}$, can be optimized by means of a standard kinematical selection. Since we will be interested to a dijet mass distribution fitting on data to extract signal evidence, we keep the following guidelines:

- choosing kinematical cuts that do not introduce undesired biases on the dijet mass distributions;
- keeping the efficiency as high as possible.

As a reference, we use a signal sample with $M_H = 120\ GeV/c^2$ and the QCD sample described in Sec. 6.4. Due to the higher cross section of the QCD event production, the contribution of the other competing processes (such as top quark and vector boson production) is not considered here. It will be briefly discussed in

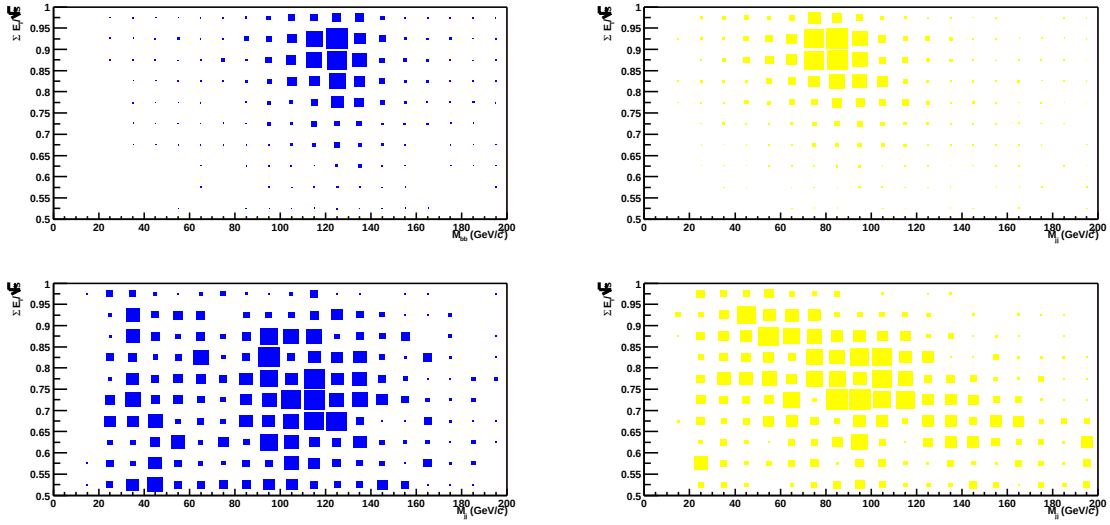

Figure 7.1: *Fraction of transverse energy as a function of the reconstructed mass of tagged (left) and not-tagged (right) jet pairs for VH (top) and* QCD *(bottom) events.*

Sec. 7.2. We study the correlation between the reconstructed dijet mass both of the tagged and not-tagged jet pairs and many kinematical variables. We find that the most interesting one is the fraction of transverse energy $\sum E_T/\sqrt{\hat{s}}$ in the event. Fig. 7.1 shows the value of this variable as a function of the invariant masses both for VH and QCD events. We note that a cut on highest values of $\sum E_T/\sqrt{\hat{s}}$ selects

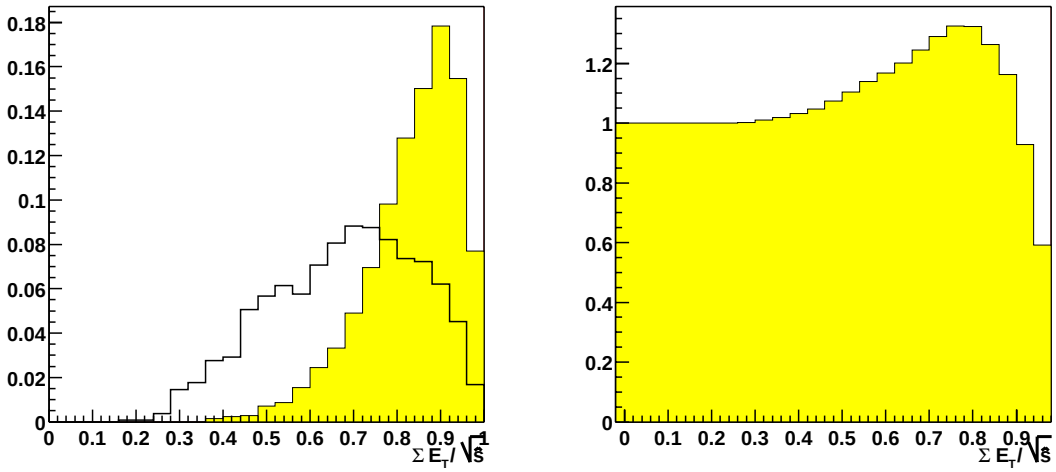

Figure 7.2: $\sum E_T/\sqrt{\hat{s}}$ *distribution (left) for signal (shaded histogram) and background (white) events, and cut optimization (right).*

background events with dijet masses away from the signal ones. This is particularly evident for not-tagged jet pairs. We decide therefore to cut on this variable to improve the $S/\sqrt{B}$ ratio. The value of the cut is established through a maximization criterion (see Fig. 7.2): all values are tested and the one that supplies the maximum increase of $\epsilon_S/\sqrt{\epsilon_B}$, where ϵ_S (ϵ_B) is the efficiency on signal (background) events, is

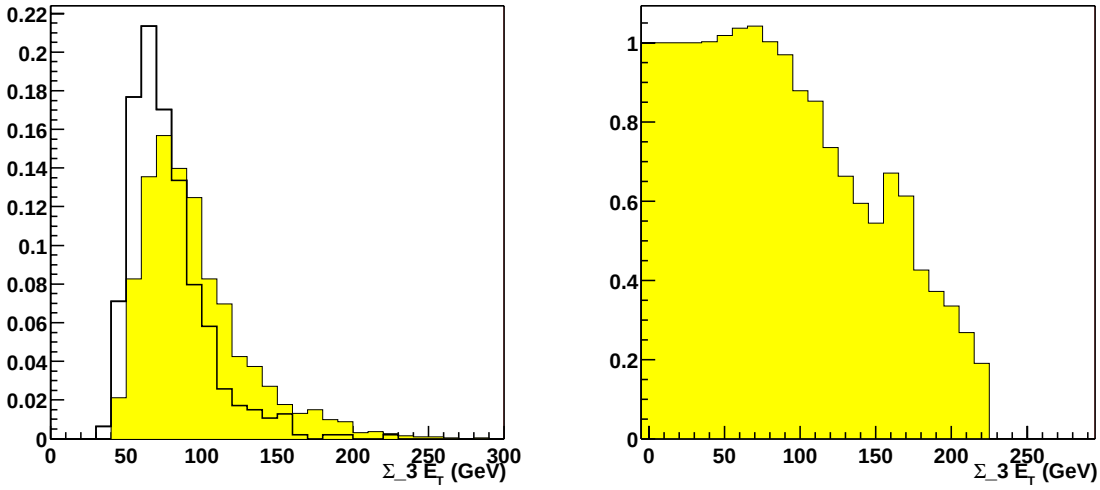

Figure 7.3: *$\sum_3 E_T$ distribution after cut on $\sum E_T/\sqrt{\hat{s}}$ for signal (shaded histogram) and background (white) events, and cut optimization (right).*

chosen (see Tab. 7.1).

Successively, no further significant correlations have been found. Then we decide to increase the signal significance $S/\sqrt{B}$ by exploiting the most discriminating kinematical variables we found in the last chapter:

- the scalar sum of the transverse energy of the jets $\sum E_T$,
- the sum of the E_T jet for all jets but the leading two $\Sigma_3 E_T$,
- the quantity $t_4 - 0.82 \cdot \Sigma E_T/\sqrt{\hat{s}}$, where t_4 is the thrust value of the four leading jets in their center of mass.

However, a cut on the total energy could introduce an undesired bias on the dijet mass distribution. Therefore, we cut only on $\sum_3 E_T$ and $t_4 - 0.82 \cdot \Sigma E_T/\sqrt{\hat{s}}$ values, according to the results of the maximization procedure (see Fig. 7.3 and 7.4). Selected cuts are quoted in Tab. 7.1.

Fig. 7.5 shows dijet mass spectra after kinematical selection. This distribution could be used for a fit to the data. Since we have no analyzable data yet, we make a preliminary estimate of the achievable signal significance by counting the fraction of signal and background events with $M_{bb} \geq M_H - 2\sigma_{M_H}$ and $|M_{jj} - M_V| \leq 2\sigma_{M_V}$, where $\sigma_{M_H} \sim 17\ GeV/c^2$ and $\sigma_{M_V} \sim 12.5\ GeV/c^2$ are the resolution for Higgs and vector boson masses respectively, and $M_V = 85\ GeV/c^2$ is the mean value of the W and Z boson masses.

An analogous procedure has been followed to estimate the signal sensitivity for Higgs boson mass $M_H = 110$, 115, 125 and 130 GeV/c^2. Monte Carlo samples have been generated with the PYTHIA 6.129 [1] generator. After a full detector and trigger simulation, the samples result to have each about 1500 events.

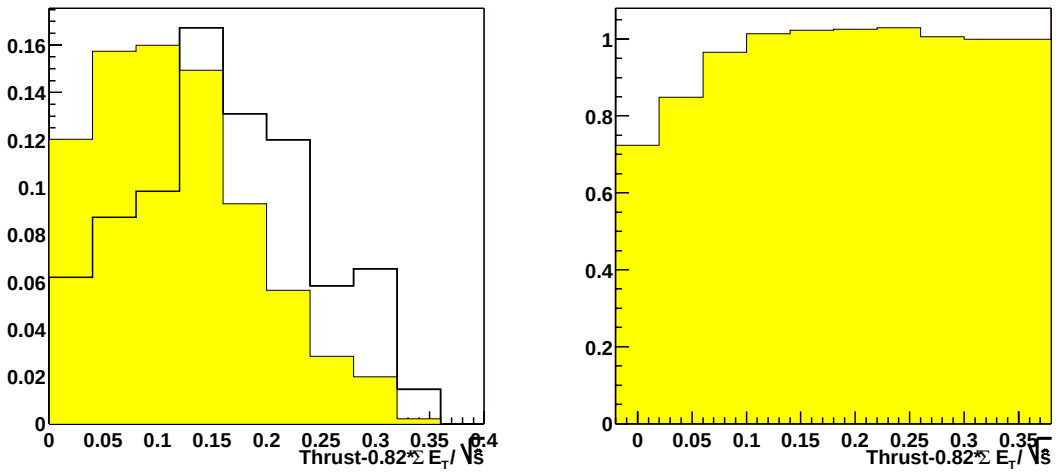

Figure 7.4: $t_4 - 0.82 \cdot \Sigma E_T/\sqrt{\hat{s}}$ *distribution after cuts on* $\sum E_T/\sqrt{\hat{s}}$ *and* $\sum_3 E_T$ *for signal (shaded histogram) and background (white) events, and cut optimization (right).*

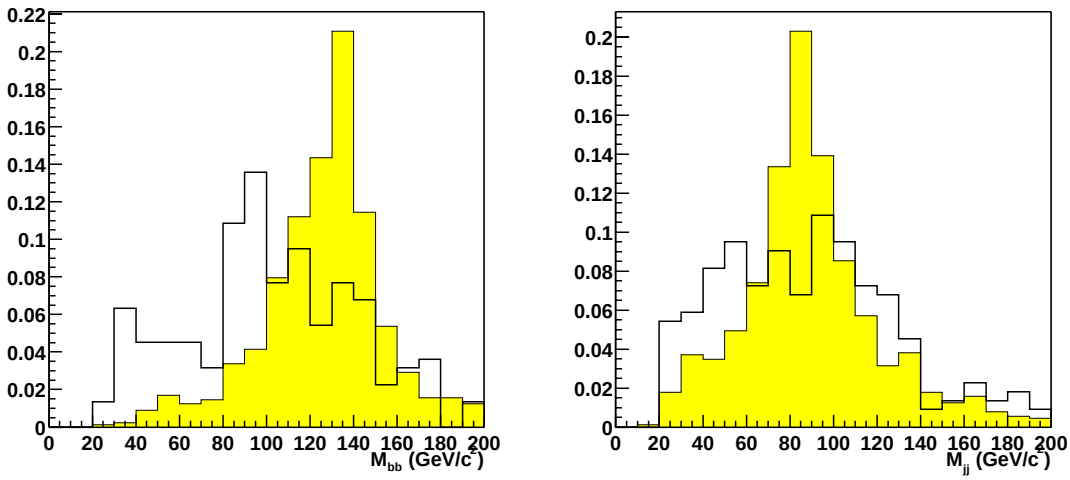

Figure 7.5: *Dijet mass distribution after kinematical selection for tagged (left) and not-tagged (right) jet pairs. Shaded histograms are for* VH *events, white ones for* QCD *processes.*

Cut	VH		QCD	
	ϵ (%)	σ (fb)	ϵ (%)	σ (fb)
$\sum E_T/\sqrt{\hat{s}} \geq 0.76$	79 ± 1	6.9 ± 0.4	36 ± 1	$(70 \pm 8) \times 10^3$
$\sum_3 E_T/\sqrt{\hat{s}} \geq 70\ GeV$	60 ± 1	5.2 ± 0.3	19 ± 1	$(36 \pm 5) \times 10^3$
$t_4 - 0.82 * \sum E_T/\sqrt{\hat{s}} \leq 0.24$	57 ± 1	5.0 ± 0.3	15 ± 1	$(29 \pm 4) \times 10^3$
Mass Requirements	35 ± 1	3.0 ± 0.2	5.2 ± 0.6	$(10 \pm 2) \times 10^3$

Table 7.1: *Summary of the kinematical selection performance. Efficiencies are computed with respect to the analysis samples. Errors are statistical only.*

$110\ GeV/c^2$	$115\ GeV/c^2$	$120\ GeV/c^2$	$125\ GeV/c^2$	$130\ GeV/c^2$
0.039 ± 0.005	0.035 ± 0.004	0.030 ± 0.004	0.026 ± 0.003	0.021 ± 0.003

Table 7.2: *Expected significances $S/\sqrt{B}$ achievable on Higgs associated production with 1 fb^{-1} of integrated luminosity. Errors are statistical only.*

Tab. 7.2 summarizes the expected statistical significances of the Higgs signal $S/\sqrt{B}$ achievable with 1 fb^{-1} of integrated luminosity for the different values of the Higgs boson mass. The sensitivity on Higgs production results poor. It would not allow the Standard Model Higgs boson observation even if the CDF II experiment collected several tens of fb^{-1} of integrated luminosity in many years of data taking. These results are preliminary and are expected to be improved by the development and tuning on real data of the reconstruction and analysis tools. However, we need a more powerful strategy to discriminate background events from signal ones. In the next subsection, a neural network approach will be investigated to increase the signal sensitivity.

7.1.2 Neural Network Approach

As an alternative strategy to the kinematical selection, we want to investigate the perspectives that a neural network analysis can offer to the search of Higgs associated production in the all hadronic channel. Analogous studies have been already performed for the other decay channels and seems to improve the achievable results for Run II Higgs search at the Tevatron [2].

A brief introduction to this field of analysis is given in Appendix A. For our study, we use the JETNET artificial neural net (ANN) code, version 3.0 [3]. We run it through the root interface package ROOT_TO_JETNET [4].

The same Monte Carlo samples we described in the last section are used. As a reference, we will study neural network performances on signal-to-background discrimination by assuming an Higgs boson mass of $M_H = 120\ GeV/c^2$. Results will be generalized to the range $110 \leq M_H \leq 130\ GeV/c^2$ in the last part of this section.

Input Variables and Neural Network Architecture

As input variables, those selected for the standard kinematical selection (see Subsec. 7.1.1) have been chosen. Moreover, dijet invariant mass distributions are used. A different strategy could consist in comparing signal and background mass spectra after a neural selection based on kinematical information only. However, we have no data the simulated distributions can be fitted to. For the time being, we can only perform a counting of the expected signal and background events. Moreover, using mass spectra as input variables to the network allows to exploit their correlations with the kinematical variables we discussed above.

We use a three-layered feed-forward perceptron with the standard activation function

$$\Phi(x) = \frac{1}{2}[1 + tanh(x)] = (1 + e^{-2x})^{-1} \ . \tag{7.1}$$

An input layer is required for each input variable. Only one output is instead needed to classify signal events (output value $NN_{out} = 1$) from background ones ($NN_{out} = 0$). Finally, there is no specific rule to set the number of nodes in the hidden layer. We tested the network performances with different numbers of hidden nodes, and we choose a 5-10-1 configuration, which provides the best event classification.

Neural Network Training and Testing

In order to train the network, two subsets of $1,000$ events each have been extracted from VH and QCD Monte Carlo samples respectively. The remaining events are used to test network performances.

We optimize the performances of the network by running $8,000$ training epochs with the selected configuration. Weights are updated through the standard back-propagation algorithm [5] with the default training parameters of the JETNET package. For each epoch, learning performances are estimated by computing the fraction of training and testing events assigned to the right class. The assignment is established according to the shortest distance between the neural network output of the

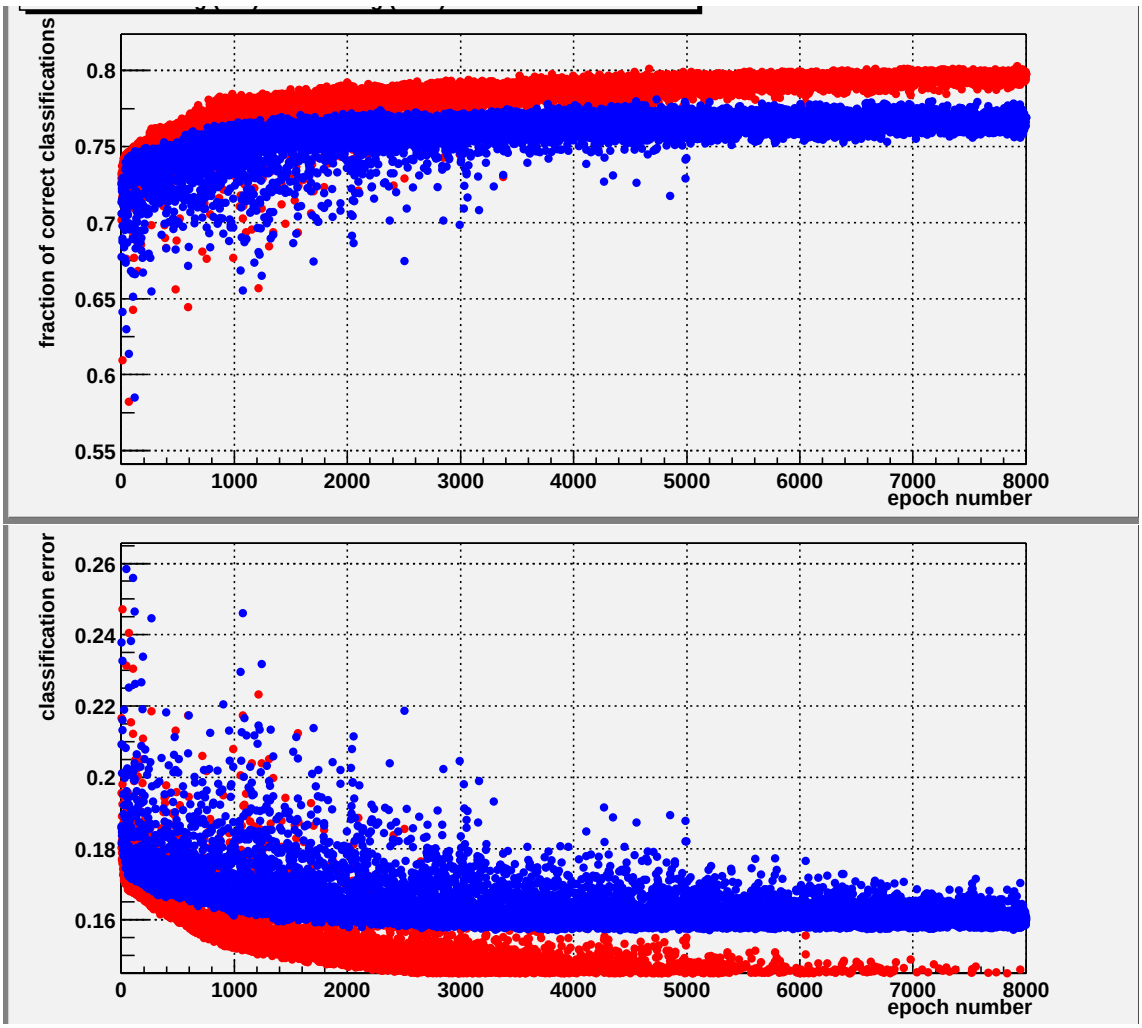

Figure 7.6: *Learning performances and errors for training (light bullets) and testing (dark) events as a function of the epoch number.*

event and the target for signal ($NN_{out} = 1$) and background ($NN_{out} = 0$) ones. Results are shown in Fig. 7.6 (top). Another useful parameter to evaluate learning progress is the error function value. For training events it is

$$E^{train} = \frac{1}{N^1_{train} + N^2_{train}} \sum_{k=1}^{2} \sum_{n=1}^{N^k_{train}} [O^k_n - T^k]^2 \ , \tag{7.2}$$

where N^1_{train} and N^2_{train} are the number of training events for the two different classes of events, O^k_n is the neural network output for the nth events of the class k and T^k is its target value. Analogously, we can define an *error* value for the kth testing sample as

$$E^k_{test} = \frac{1}{N^k_{test}} \sum_{n=1}^{N^k_{test}} [O^k_n - T^k]^2 \ . \tag{7.3}$$

Fig. 7.6 (bottom) shows training and average testing errors at each training epoch.

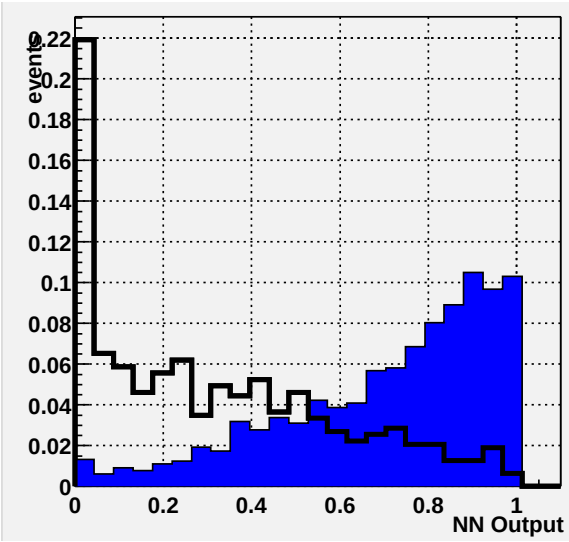

Figure 7.7: *Neural network output distributions for signal (shaded histogram) and background (white) events.*

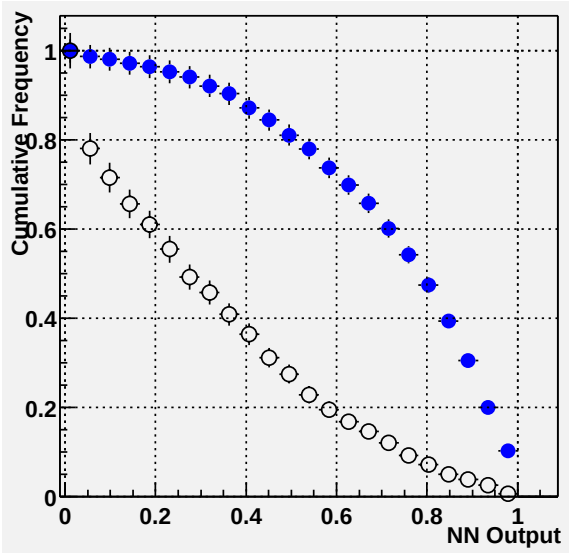

Figure 7.8: *Efficiencies on VH ($\bullet$) and* QCD *($\circ$) events as a function of the cut on the neural network output.*

We see the network performances on testing events become stable after about $2,000$ epochs, therefore we stop here the training and freeze the weights.

Finally, we look at the classification performances of the trained neural network. Fig. 7.7 shows the NN_{out} distributions for signal and background events. VH and QCD production can be discriminated by means of a cut on the network output. The obtained efficiencies for the two classes of events are shown in Fig. 7.8 as a function of the cut value. A useful way to evaluate the neural network performances is to plot the purity vs. the signal efficiency curve, where purity is defined as the ratio between the expected numbers of signal and total (signal + background) events selected by the NN_{out} cut (see Fig. 7.9).

Improvement of VH Sensitivity

The improvement of the sensitivity on Higgs associated production is estimated by maximizing the *quality factor* $\epsilon_s/\sqrt{(\epsilon_b)}$, where ϵ_s and ϵ_b are respectively the efficiencies on signal and background events for a fixed cut on the neural network output. The behaviour of the quality factor as a function of the cut value is shown in figure 7.10. We note a sizable improvement on the signal significance with respect to the value we obtained through the standard kinematical analysis.

An analogous procedure has been followed to estimate the signal sensitivity for Higgs boson mass $M_H = 110$, 115, 125 and 130 GeV/c^2 (Monte Carlo samples used have been described in the last subsection). Results are shown in Fig. 7.11. Finally, Tab. 7.3 summarizes the expected significances $S/\sqrt{B}$ achievable with 1 fb^{-1} of integrated luminosity for the different values of the Higgs boson mass.

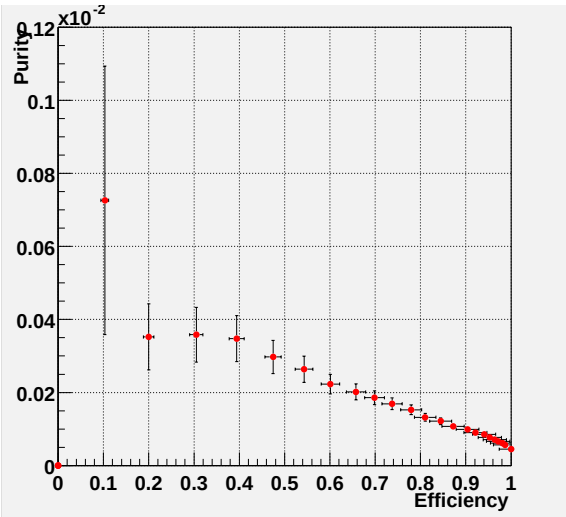

Figure 7.9: *Purity vs. signal efficiency curve.*

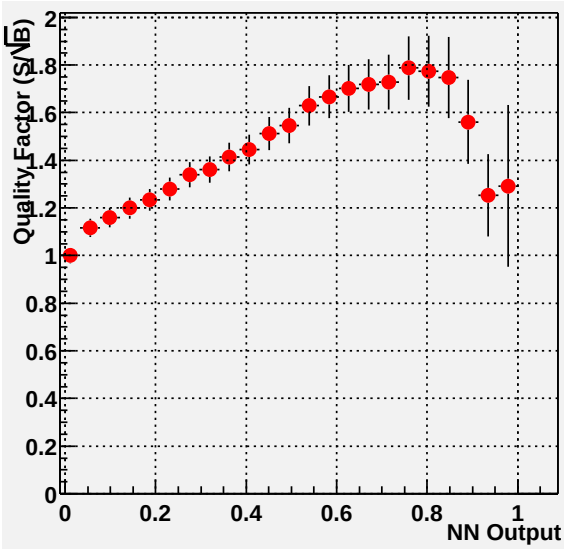

Figure 7.10: *Expected $S/\sqrt{B}$ improvement as a function of the cut on the neural network output.*

110 GeV/c^2	115 GeV/c^2	120 GeV/c^2	125 GeV/c^2	130 GeV/c^2
0.048 ± 0.007	0.046 ± 0.007	0.036 ± 0.006	0.031 ± 0.005	0.027 ± 0.004

Table 7.3: *Expected significances $S/\sqrt{B}$ achievable on Higgs associated production with 1 fb^{-1} of integrated luminosity. Errors are statistical only. They have been computed by assuming that the number of events passing a generic selection $NN_{out} \leq$ cut obeys a binomial distribution.*

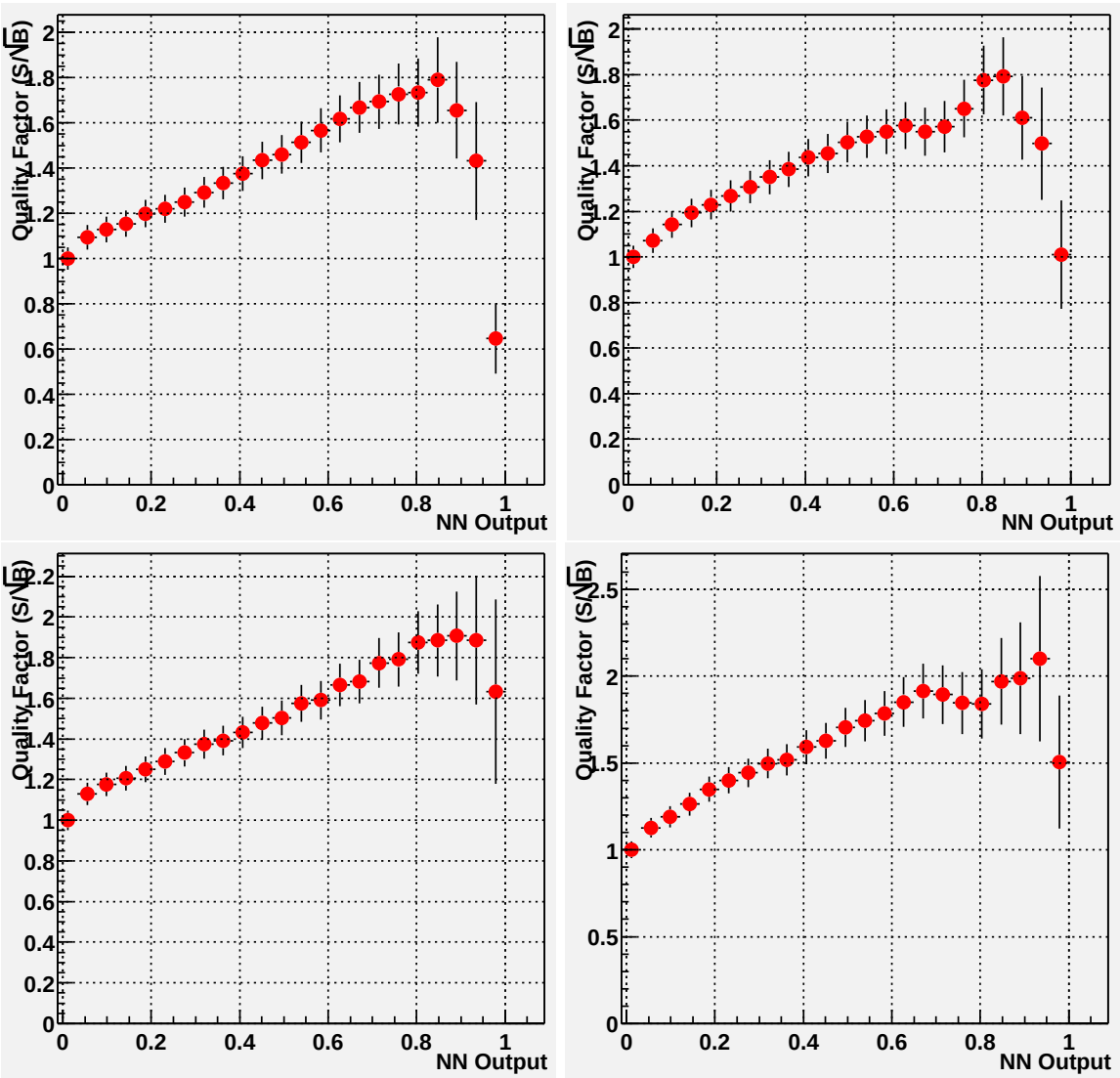

Figure 7.11: *Expected $S/\sqrt{B}$ improvement as a function of the cut on the neural network output for Higgs boson mass $M_H = 110$ GeV/c^2 (top-left), 115 GeV/c^2 (top-right), 125 GeV/c^2 (bottom-left) and 130 GeV/c^2 (bottom-right).*

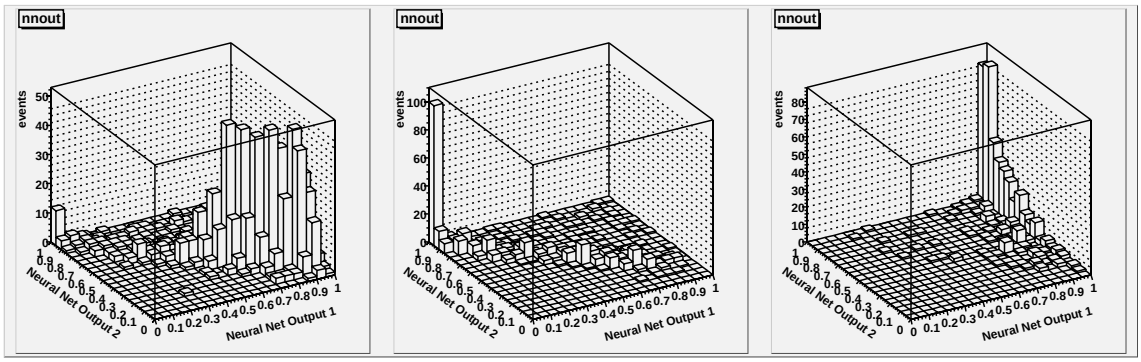

Figure 7.12: 2 *output neural network classification performances on VH (left),* QCD *(middle) and $t\bar{t}$ (right) events.*

7.2 Discussion of the Systematic Uncertainties

There are three main sources of systematic uncertainties in multijet sample analysis:

- *Estimate of the cross section for* QCD *processes with* 2 *tagged jets in the final states.* We have performed two independent evaluations based on Monte Carlo calculations and Run I data extrapolations respectively. Although our estimates are in agreement with each other, a lot of factors could bias our estimates. In fact, QCD processes need to be studied on real data. The evaluation of their contribution to the multijet sample will be one of the more important tasks when analyzable data are available.

- *Contribution of the competing processes to the background.* By means of the analysis cuts, we get a rejection factor of about 50 on the QCD production (see Fig. 7.8). This leads to an effective QCD cross section of ~ 3 *pb*. Other background processes are expected to have a cross section of the order $\sim 10^{-1}$ *pb* (see Tab. 6.4). Their contribution on the $S/\sqrt{B}$ ratio results then to be $\lesssim 10\%$. A more sophisticated strategy consists in exploiting a neural network with two or more output nodes. An example is shown in Fig. 7.12: a 5-10-2 configuration has been used to train the network to classify VH (target (1,0)), QCD (target (0,1)) and $t\bar{t}$ (target (1,1)) events. Training procedure follows the guidelines we described above (see Sec. 7.1.2) . The $t\bar{t}$ sample used has been described in Sec. 6.4. This could be an useful strategy if a stronger rejection of QCD processes is achieved.

- *Uncertainties on trigger acceptance and analysis selection efficiency.* In our preliminary studies we use a *in progress* simulation of CDF detector and reconstruction tools. In fact, the performances of the detector and reconstruction algorithms have to be studied and eventually re-tuned on data.

The systematic uncertainty affecting our analysis needs to be studied on experimental data samples, which will become available only in the next months. For the time being, only statistical effects are considered.

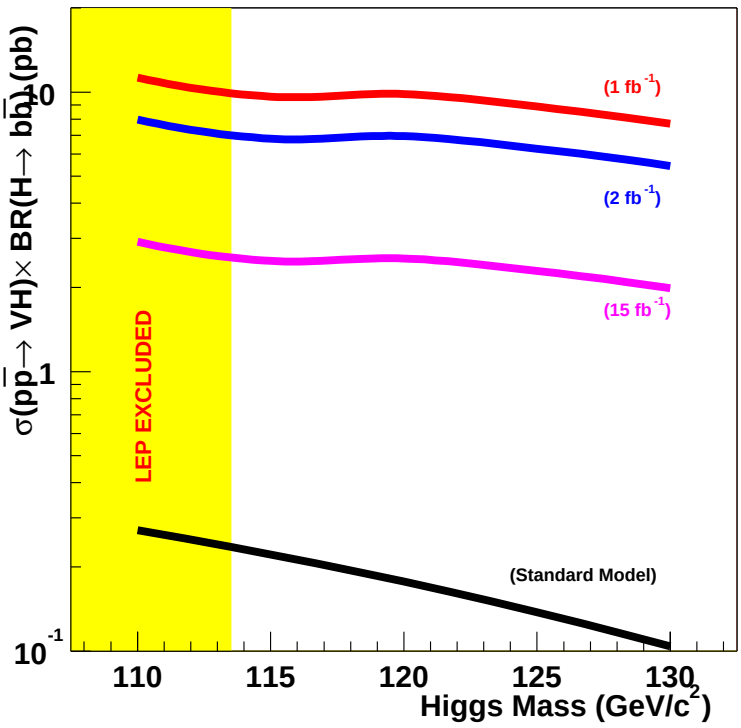

Figure 7.13: *Preliminary estimates of the limits on Higgs associated production cross section achievable with* $\mathcal{L}^{int.} = 1$, 2 *and* 15 fb^{-1}. *Also shown is the cross section predicted by the Standard Model.*

7.3 Preliminary Limits on the Cross Section of the VH Production

A preliminary estimate of the limit on the Higgs associated production cross section σ_{VH} at 95% C.L. achievable with a fixed integrated luminosity can be obtained by scaling the statistical significance of the Higgs signal $S/\sqrt{B}$ expected for the theoretical cross section to 2, according to the formula:

$$\sigma_{VH} = \frac{2\sigma_{VH}^{theor.}}{S/\sqrt{B}} \ . \tag{7.4}$$

Fig. 7.13 shows the preliminary limits on σ_{VH} achievable with 1, 2 and 15 fb^{-1} of integrated luminosity. For comparison, the cross section predicted by the Standard Model is also shown. We can see that a Standard Model Higgs boson would not be observable in full hadronic final states in the present conditions. Moreover, a non-standard Higgs production would be detectable only if its cross section were an order of magnitude higher than the standard one. However, this analysis has to be considered as a work *in progress*. Obtained limits reflect the present status of this study, and are expected to improve with the development of the various used tools.

Bibliography

[1] `http://www.thep.lu.se/tf2/staff/torbjorn/Pythia.html`.

[2] M. Carena, J. S. Conway, H. E. Haber, J. D. Hobbs, et al. (The Fermilab Higgs Working Group), *Report of the Tevatron Higgs Working Group*, HEP-PH/0010338, Oct 2000.

[3] C. Peterson and T. Rognvaldsson, JETNET 3.0 - *A Versati le Artificial Neural Network Package*, CERN-TH 7135/94.

[4] C. Ciobanu et al., *A* ROOT *Interface to* JETNET , CDF internal note 5434, Nov 2001.

[5] P. J. Werbos, *PhD thesis*, Harvard University, 1974.

Conclusions

The work described in this thesis concerns a very important theme for the CDF II experiment. However, it is also a very complex topic. The Higgs boson search constitutes the mainline for the analysis at this experiment in the next years and all the possible ways to develop such a search have to be studied in detail. In particular, the main urgency is the identification of trigger criteria to define the characteristics of the experimental data to collect. A sizable part of this work has been dedicated to this topic, and has led to the definition of a trigger topology that will be used by the CDF II experiment in the next months.

The definition of a strategy for an offline analysis of the collected events resulted a more complex task. Actually, signal of Higgs boson production, besides suffering from the production of events with similar final states and several orders of magnitude more probable, is also confused with other important competing processes of top quark and vector boson production. Besides, many tools for this analysis need to be studied on experimental data samples, that will become available only in the next months. In particular, the reconstruction algorithms and the techniques to identify the jets produced by heavy quark hadronization have to be set on real data in order to optimize the selection of multijet events with heavy flavour contents and to allow a better characterization of their kinematical behaviour. However, important tools for the event reconstruction and background discrimination have been developed. For instance, a simple algorithm for jet energy corrections, designed to improve the observability of the Higgs mass peak, has been studied. Moreover, the heavy flavour contents and the kinematical characteristics of the processes contributing to the trigger selected sample have been analyzed to allow a background discrimination capable to increase the sensitivity on Higgs boson production.

In the last chapter of this thesis, we have estimated the lower limits on the cross section of the Higgs associated production achievable at the CDF II experiment. We found that a Standard Model Higgs boson would not be observable in the present conditions. Besides, a non-standard Higgs production would be detectable only if its cross section is an order of magnitude higher than the standard one. However, these limits have to be considered as preliminary results. Actually, they reflect the present status of this study, and are expected to improve with the development of the various used tools.

In many respects, this is a work in progress; all the described tools (like the b-tagging algorithms) have to be optimized on real data again and others (such as jet energy corrections and the SLT algorithm) have to be implemented within the Run II framework yet. Many efforts will be made by the CDF II collaboration in the

next years in order to achieve these results.

Acknowledgements

This thesis, and the underlying research, would not have been completed without the contribution of many friends and colleagues. I need to thank them for the suggestions and the encouragement they offered to me during the years I spent on the present work.

First of all, I thank my family, whose support and patience have been invaluable during all the time I studied at university.

I would also thank all the members of the CDF group at Padova University. In particular, I must thank my official and non-official advisors, Giovanni and Tommaso, for all the help they have given me during these three years of Ph.D. studies. Their suggestions and their availability have been very important for my work.

I need to acknowledge Giorgio, *my* undergraduate student, who shared my work on the multijet trigger. I am grateful to him for the help and friendship he has given me. I hope he could continue his work as a Ph.D. student.

A lot persons supported my work with useful discussions and friendly encouragements. In particular, I have to thank Donatella, Irene, Andrea, Antonio, Patrizia, Dario and Maurizio. I am very grateful to them.

Finally, I want to acknowledge Roberto, Elisa, Saverio, Daniele, Francesco, Davis, Matteo, Jeff, Piero, Mario, Andrea, and Riccardo. Their friendship has been very important in the difficult moments.

Appendix A

Introduction to Neural Networks

Neural networks belong to a branch of statistics named multivariate analysis. *The feature of this devices is to map a vector of variables in a single scalar variable. In the recent years, they have arisen a growing attention in the high energy physics experiments [1, 2, 3] thanks to the interesting perspectives their ability in pattern recognition offers in the analysis of data to discriminate interesting events from background ones.*

In this chapter, a brief introduction to the neural networks and to their application is provided.

A.1 Neural Network Architecture

The most commonly used neural network architecture in high energy physics experiments is the *feed-forward*, *multi-layer perceptron* (MLP) network. A perceptron is a model of a single biological neuron [4]. Its task is to map a set of N input variables $\vec{\xi}=(\xi_1,..., \xi_N)$ in an output value ν according to the expression (see Fig. A.1):

$$\nu = \Phi\left(\frac{1}{N}\sum_{j=1}^{N}\omega_j\xi_j - \theta\right) \quad , \tag{A.1}$$

where ω_j is a *weight* characterizing the jth input connection of the perceptron, $\Phi(x)$ is an *activation* function and θ is a threshold. This operation has a simple geometrical interpretation: it provides a two-class discrimination in the N-dimensional input variable hyper-space by cutting with a hyper-plane whose direction are given by the connection weights. In a feed-forward neural network (FFNN), the output of a perceptron (*node*) is influenced (*connected*) only by the perceptrons (*nodes*) in the immediately preceding layer. In such a way, only input connections of the nodes in the first layer and the output of the last one are accessible from outside. The nodes in the intermediate layers are then called *hidden* (see Fig. A.2). In many pattern recognition problems encountered in high energy physics only one output node is needed. In this case, output is usually taken to be in the interval $[0, 1]$, and can be used as a discriminator between signal ($f = 1$) and background ($f = 0$).

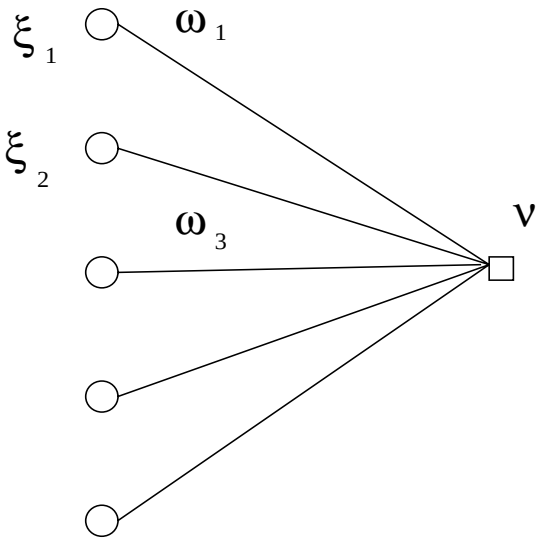

Figure A.1: *Schematic view of a perceptron with* 5 *input connections.*

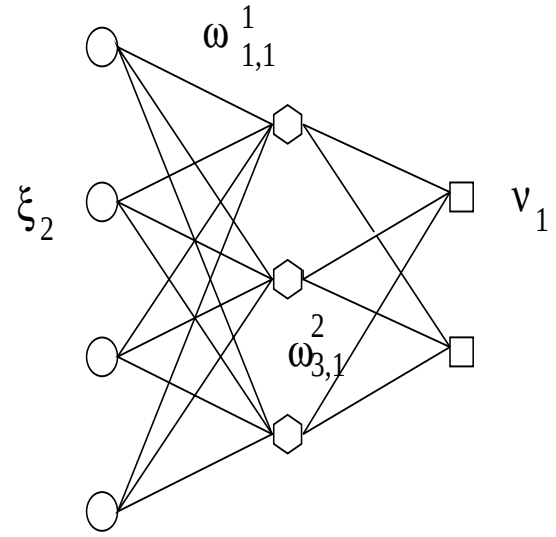

Figure A.2: *Feed-forward neural network with* 4 *input nodes,* 3 *hiddem nodes and* 2 *output nodes.*

A.2 Training

To use a FFNN as a discriminator, the weights and thresholds have to be determined, that is the neural network has to be *trained.* Many training strategies have been proposed. The most common ones, *supervised training*, are based on a direct comparison of the neural network response on sets of events of known type (signal or background training samples). The weights and thresholds are then adjusted by minimizing an error function, usually defined as:

$$E(\omega, \theta) = \frac{1}{M} \sum_{j=1}^{M} (f^j(\omega, \theta) - t^j)^2 \ , \tag{A.2}$$

where f^j is the output value obtained from the network for the jth training event, t^j its expected value (*target*), and M the number of training events.

Finding the minimum of the error function is a very difficult problem. For this reason, many training algorithms have been developed. The most used one is the *back-propagation learning rule* [5]. This method minimizes the error function by changing the weights in the network in an iterative fashion. It is known as the gradient descent method, because the weights ω and the thresholds θ are changed according to the functions direction of the greatest descent:

$$\Delta\omega(t+1) = -\eta \frac{\partial E}{\partial \omega} + \alpha \Delta\omega(t) \ , \tag{A.3}$$

and $\omega(t)$ refers to the preceding iteraction. The learning weight parameter, η, determines how the gradient effects the change. The momentum term, α, is used to prevent oscillation around a minimum and thereby interfere with the convergence.

These parameters are highly problem-dependent and there is no general criteria to determine them.

On the pratical side, the user have to be careful to some problems:

- If the training sample is not representative enough, the obtained weights will be biases and the FFNN will assign different output values to events that actually belong to the same class. This occurs for example when the training events are too few.
- A certain number of interaction on the training samples (*epochs*) is necessary to get the minimum of the error function.
- On the contrary, too many epochs or too many hidden layers can lead to an *over-fitting*, *id est* to a situation in which the classifying hyper-planes are too close to the training points (the cuts have too fine a grain).

A.3 Testing and Generalization

The ability of a trained neural network to discriminate signal from background events can be studied by *testing* its performance on samples of events belonging to known classes [6]. An useful plot is the *purity* $\eta(cut)$ vs. *efficiency* $\epsilon(cut)$ curve, where $\eta(cut)$ is the ratio between the number of signal and the total (signal + background) events passing the requirement $NN_{out} \geq cut$ on the FFNN output NN_{out}, while $\epsilon(cut)$ is the fraction of signal events in the testing sample with $NN_{out} \geq cut$.

When applying the neural networks on data, one does not know *a priori* the output values. A *generalization* is then performed by processing events we want to classify, and NN_{out} distribution can be compared with expected signal and background ones.

Bibliography

[1] P. Abreu et al., *Classification of the Hadronic Decays of the Z^0 into b and c Quark pairs using a Neural Network*, Physics Letters B**295**, 383 (1992).

[2] B. Abbott et al., *Neural Networks for Analysis of Top Quark Production*, hepex/9907041.

[3] P. Azzi et al., *Measurement of the $t\bar{t}$ cross section and mass in the all hadronic channel using a neural network*, CDF internal note 4722, Mar 1999.

[4] F. Rosenblatt, *Principles of Neurodinamics*, Spartan, New York, 1962.

[5] P. J. Werbos, *PhD thesis*, Harvard University, 1974.

[6] L. Garrido et al., *Proc. Conf. Computing in High Energy Physics '92*, 661, (1992).

List of Figures

1.1 *Diagrams for WW elastic scattering: (a) mere dynamic of gauge bosons, (b) exchange of a scalar boson.* 6
1.2 *One-loop contributions to Higgs boson mass within the* SM. 10
1.3 *Running of λ as a function of the energy scale Λ.* 11
1.4 *Limits on Higgs boson mass from top quark and W boson mass measurements at* CDF, D0, LEP *and* SLC. 11
1.5 *Diagrams contributing to the running of the selfinteraction constant λ of the Higgs field.* 12
1.6 *Higgs branching ratios as a function of M_H. Shaded bands result from the uncertainties on input parameters (m_b, m_c, m_t, α_s).* 13
1.7 *Total width of the Higgs boson as a function of its mass.* 13
1.8 *Standard Model Higgs boson dominant production modes at the* LEP *collider.* 14
1.9 *Observed behaviour of $-2ln(Q(M_H))$ as a function of M_H; green and yellow bands correspond to a 68% and 95% compatibility with an exclusive background production.* 15
1.10 *Value of $1-CL_b$ as a function of M_H obtained by the four* LEP *experiment; excesses above the expected background are shown on the right axis.* 15
1.11 SM *Higgs boson dominant production processes at the Tevatron collider: from left to right, gluon fusion, Higgsstrahlung and vector boson fusion.* 16
1.12 *Cross sections for* SM *Higgs boson production at the Tevatron collider.* 17
1.13 CDF *limits on the cross section for* SM *Higgs boson associated production [21].* 17
1.14 *Integrated luminosity thresholds for Standard Model Higgs boson discovery at the Tevatron collider.* 18

2.1 *Average number of interactions per beam cross for various beam conditions.* 22
2.2 CDF II *detector section.* 25
2.3 *$r-\phi$ view of the* CDF II *detector.* 26
2.4 *Convention for the sign of impact parameter.* 27
2.5 *Sector of* COT *($\Delta\phi = 60°$).* 28
2.6 *Perspective view of* ISL. 28
2.7 *Perspective view of* SVX II. 29

2.8 *$r-\phi$ view of* SVX II. 29
2.9 *$r-\phi$ view of silicon detectors.* 30
2.10 *$r-z$ view of silicon detectors.* 30
2.11 *$r-z$ view of* CDF. 30
2.12 *Expected resolutions on tracking parameters in Run II.* 31
2.13 *Expected P_T resolutions in Run II.* 32
2.14 Performance of the Time-of-flight detector 33
2.15 *Perspective view of a* CEM *module.* 35
2.16 *$r-z$ view of the plug calorimeter.* 36
2.17 *Perspective view of* SMD. 36
2.18 *Reconstruction of the primary and secondary vertices in the r-ϕ plane. The impact parameter d for some representative tracks and the distance L_{xy} between the vertices on the transverse plane are shown.* . . 40
2.19 *η-ϕ coverage of the Run II muon system.* 43
2.20 CDF *three level pipelined and buffered trigger architecture.* 47
2.21 *Schematic diagram of trigger paths and datasets.* 47
2.22 *The Run II trigger system block diagram.* 48
2.23 *Cluster finding procedure.* 50
2.24 *The* SVT *architecture.* 51

3.1 *Run I multijet trigger efficiency for Level 2 calorimetric requirements.* 56
3.2 *Level 2 efficiencies and rates for different calorimetric requirements.* . 58
3.3 *$\Sigma E_T 10$ and number of clusters ($E_T^{cl} \geqslant 10GeV$) distributions.* 58
3.4 *Impact parameter distribution of good* SVT *tracks in multijet events, for the default simulation (0.5% of noisy silicon strips, χ^2 cut set at 12.6). In dark (open circles) tracks in* QCD *events; in red (full circles) tracks in HV events.* 61
3.5 *Impact parameter distributions of* SVT *tracks in* QCD *events, for the default χ^2 cut and four different noise levels in the silicon microstrips; the rejection of multiple tracks from the same* XFT *seed described in Sec. 3.3.2 is not applied, and no beam spot smearing is operated. Notice the worsening of prompt track IP resolution as the noise level increases. A summary of the impact parameter resolutions fitted from these curves is presented in Fig. 3.17.* 62
3.6 *Impact parameter distributions of* SVT *tracks belonging to three different categories: tracks univocally associated to an* XFT *seed (open dark circles), tracks belonging to a multiplet associated to the same seed that have been selected as the right one by the prescription discussed in Sec. 3.3.2 (full red circles), and tracks belonging to a multiplet that have been discarded by the prescription (open black squares). For this plot,* QCD *events and a 2% noise level (see Sec. 3.3.2) have been used; the χ^2 cut was set at its default value; a finite beam spot was simulated as discussed in the text.* 63

3.7 *Average number of* SVT *tracks as a function of SVX noise with and without multiple track removal. Top left: average number of tracks (red) and tracks with* $|d| < 100\mu m$ *(dark) when the prescription for the removal of multiple tracks is applied. Top right: same when no removal is operated. Bottom: comparison of the fraction of displaced tracks (*$|d| > 100\mu m$*) as a function of noise before (black) and after (magenta) the removal.* 64

3.8 *Effect of the simulation of a finite beam spot size on track impact parameters. Left: impact parameter of tracks before vs after the smearing; right: the same quantities are overlayed. For this plot,* QCD *events and the default values of noise and* χ^2 *cut have been used.* . . 65

3.9 *Distribution of the largest (left) and second-largest (right) impact parameter in VH (open light circles) and* QCD *events (dark circles). The default values of* χ^2 *cut and noise level have been used; track impact parameters have been smeared with a finite beam spot size (see Sec. 3.3.2).* 68

3.10 *Optimization of the selection based on the highest-IP track in the event. Top left: highest impact parameter in* QCD *(dark) and HV (light) events. Top right: efficiency as a function of the cut on the highest IP. Bottom left: ratio between signal and background efficiency. Bottom right: quality factor (see text). The default values of* χ^2 *cut and noise level have been used.* 69

3.11 *Optimization of the selection based on the second-highest-IP track in the event. Top left:* 2nd*-highest impact parameter in* QCD *(dark) and HV (light) events. Top right: efficiency as a function of the cut on the* 2nd*-highest IP. Bottom left: ratio between signal and background efficiency. Bottom right: quality factor (see text). The default values of* χ^2 *cut and noise level have been used.* 70

3.12 *Optimization of the selection based on the second-highest-IP track in the event, when no removal of multiple* SVT *tracks extrapolating to the same azimuth on* SL6 *is performed. Top left:* 2nd*-highest impact parameter in* QCD *(dark) and HV (light) events. Top right: efficiency as a function of the cut on the* 2nd*-highest IP. Bottom left: ratio between signal and background efficiency. Bottom right: quality factor (see text). The default values of* χ^2 *cut and noise level have been used.* 71

3.13 *Optimization of the selection based on the third-highest-IP track in the event. Top left:* 3rd*-highest impact parameter in* QCD *(dark) and HV (light) events. Top right: efficiency as a function of the cut on the* 3rd*-highest I.P.. Bottom left: ratio between signal and background efficiency. Bottom right: quality factor (see text). The default values of* χ^2 *cut and noise level have been used.* 72

3.14 *Optimization of the selection based on the sum of impact parameters of all tracks with $d > 50$ μm. Top left: sum of impact parameters in* QCD *(dark) and HV (light) events. Top right: efficiency as a function of the cut on the sum. Bottom left: ratio between signal and background efficiency. Bottom right: quality factor (see text). The default values of χ^2 cut and noise level have been used.* 73

3.15 *Optimization of a selection based on the quadrature sum of impact parameter significances of* SVT *tracks (see text). The quality factor attainable is not larger than those obtained with simpler approaches.* 74

3.16 *Optimization of the selection based on the second-highest-IP track in the event, for tracks selected by* SVT *with a χ^2 cut at 8. Top left: 2nd-highest impact parameter in* QCD *(dark) and HV (light) events. Top right: efficiency as a function of the cut on the 2nd-highest IP. Bottom left: ratio between signal and background efficiency. Bottom right: quality factor (see text). The default value of noise level has been used.* 76

3.17 *Impact parameter resolution of prompt tracks reconstructed by* SVT *as a function of the noise level in the silicon.* QCD *events have been used (see the fits in Fig. 3.5).* 77

3.18 *Variation of quality factor with the choice of the χ^2 cut on* SVT *tracks. Bins 1 to 7 in the abscissa denote cuts at 6, 8, 10, 12.6, 15, 20 and 50, respectively. Top left: quality factor for a selection based on the impact parameter of the highest-IP track. Top right: Q values for a selection based on the impact parameter of the second-highest-IP track. Bottom left: Q values for a selection based on the impact parameter of the 2nd-highest-IP track for events having at least one track with $|d| > 100$ μm. Bottom right: Q values for a selection based on the sum of impact parameters of all tracks with $|d| > 50$ μm. The default value of noise (0.5%) has been used for all plots.* 78

3.19 *Variation of quality factor with the choice of the χ^2 cut on* SVT *tracks. Bins 1 to 7 in the abscissa denote cuts at 6, 8, 10, 12.6, 15, 20 and 50, respectively. Top left: quality factor for a selection based on the impact parameter of the highest-IP track. Top right: Q values for a selection based on the impact parameter of the second-highest-IP track. Bottom left: Q values for a selection based on the impact parameter of the 2nd-highest-IP track for events having at least one track with $|d| > 100$ μm. Bottom right: Q values for a selection based on the sum of impact parameters of all tracks with $|d| > 50$ μm. The highest value of noise (2.0%) has been used for all plots.* 79

3.20 *Degradation of the effectiveness of a selection based on the 2nd-largest impact parameter in VH events ($|d_{2^{nd}}| > 100$ μm) with the noise level in the silicon strips. Left: signal efficiency (light) and background acceptance (dark); center: gain of the selection (S/N); right: quality factor.* 80

3.21 *A schematic view of the block model of the* SVT *system used for timing estimates (from Ref. [11]).* 81

3.22 *Total processing time for different categories of* SVT *output. Top row: events with no found roads (left); events with at least one found road (right). Middle row: events with zero found* SVT *track (left); events with one found track (right). Bottom row: events with two found* SVT *tracks (left); events with three or more found tracks (right). The default value of noise level has been used.* 83

3.23 *Cumulative processing time of each* SVT *functional block for* $VH \rightarrow q\bar{q}^{(\prime)}b\bar{b}$ *events. The default value of noise level has been used.* 84

3.24 *This bar chart shows which* SVT *block is processing signal events as a function of time from Level 1 accept. Each thick red bar has extrema at the average value of* t_1^{in} *and* t_2^{out} *(see text), while the dark bar extends to the minimum and maximum of those values among the 12 parallel streams. The thin magenta line extends to the point when events have a 95% chance of having been finished processing from each block. A 0.5% electronic noise has been used.* 86

3.25 *This bar chart shows which* SVT *block is processing background events as a function of time from Level 1 accept. Each thick red bar has extrema at the average value of* t_1^{in} *and* t_2^{out} *(see text), while the dark bar extends to the minimum and maximum of those values among the 12 parallel streams. The thin magenta line extends to the point when events have a 95% chance of having been finished processing from each block. A 0.5% electronic noise has been used.* 87

3.26 *Cumulative time necessary to process signal events through the various blocks of* SVT *a given fraction of the events. The default value of noise in the silicon strips has been used.* 88

3.27 *Cumulative time necessary to process background events through the various blocks of* SVT *a given fraction of the events. The default value of noise in the silicon strips has been used.* 89

3.28 *Dependence of the average processing time of* SVT *on the amount of hits due to electronic noise in the silicon microstrips.* VH *events have been used.* 90

3.29 *These plots show the total time to process a given fraction of* VH *signal with* $M_H = 120\ GeV/c^2$ *(on the top), and a given fraction of background events (on the bottom), as a function of the noise set on the silicon strips.* 91

3.30 *Top:* ΣE_T *distribution for signal (shaded histogram) and background (white) events. Bottom: Efficiencies of the requirements* $\Sigma E_T \geq cut$ *on* VH *(light bullets) and* QCD *(dark) production as a function of the cut value.* 93

3.31 *Top: Efficiency of single (full line) and double (hatched) soft lepton requirement on VH events where a semileptonic decay occurred (left) and on all the all hadronic final state events. Bottom: expected rate after single (full line) and double (hatched) soft lepton requirement. Efficiency and rates are shown as a function of the requirements on the $\sum E_T$.* 96

4.1 *Top: Level 1 cross section as a function of the run number N_{run} (left) and of the instantaneous luminosity (right). Bottom: Level 1 cross section as a function of the instantaneous luminosity for $N_{run} <=$ 126005 (left) and for $N_{run} >$ 126005 (right).* 100

4.2 *Level 2 calorimetric primitive distributions for events selected by the* SingleTower10 *trigger path. From top left clockwise: number of Level 2 clusters in the event, transverse energy of the clusters, number of clusters with $E_T \leq 10$ GeV in the event, and sum of their transverse energy.* 101

4.3 *Top: Level 2 cross section and extrapolated rate as a function of the run number N_{run} (left) and of the instantaneous luminosity (right). Bottom: Level 2 cross section and extrapolated rate as a function of the instantaneous luminosity for $N_{run} <=$ 126005 (left) and for $N_{run} >$ 126005 (right).* 102

4.4 *Effect of a beam displacement from the z axis on impact parameter determination.* 103

4.5 *Distribution of the reconstructed hits in the* SVX II *detector for a specific run (*123901*). The x (y) axis shows the number of* SVX II *sector (layer) where the hit has been detected. The active layers are well recognizable.* 104

4.6 *Impact parameter correction for the considered runs. Top: correlation between impact parameter d_0 and azimuthal angle ϕ of the* SVT *tracks. On the left, all the track have been considered. In the middle, only tracks reconstructed with $\chi^2 < 12.6$ and $P_T \geq 2$ GeV/c are shown. On the right, same as the middle plot after the correction on the impact parameter. Bottom: distribution of the corrected impact parameters.* . 105

4.7 *Estimated Level 2 rate on real data. The extrapolation to the complete detector has been performed. Top: distributions of the highest (left) and 2nd highest (right) track impact parameter in the event. Bottom: expected Level 2 rate as a function of the requirement on the highest (left) ans 2nd highest (right) track impact parameter.* 106

5.1 *Ratio between transverse momentum of jet and originating b-quark before (histogram) and after (bullets) standard jet corrections are applied. Events were generated with $M_H = 120$ GeV/c^2.* 110

5.2 *Comparison between reconstructed Higgs mass distribution when a muon (pointed histogram), an electron (hatched) or no lepton (full) is found inside Higgs jet.* 110

5.3 *ΔR spectrum of b-quarks from Higgs decays and their nearest jet.* . . 112

5.4 *Comparison of P_T^{jet}/P_T^b ratio for generic jets, e-jets and μ-jets.* 112
5.5 SLT *corrections (left) and effect on P_T^{jet}/P_T^b ratio (right) for μ-jets.* . . 114
5.6 SLT *corrections (left) and effect on P_T^{jet}/P_T^b ratio (right) for e-jets.* . . 115
5.7 *Average charged fraction as a function of jet pseudorapidity.* 115
5.8 *Ch. F. corrections (left) and effect on P_T^{jet}/P_T^b ratio (right) for generic jets (top), e-jets (middle) and μ-jets (bottom).* 117
5.9 *E_T corrections (left) and effect on P_T^{jet}/P_T^b ratio (right) for generic jets with $|\eta| < 1.1$ (top) and with $|\eta| \geq 1.1$ (bottom).* 118
5.10 *E_T corrections (left) and effect on P_T^{jet}/P_T^b ratio (right) for e-jets (top) and μ-jets (bottom).* 119
5.11 *Top: effects of the corrections on dijet invariant mass with soft muon for $M_H = 120\ GeV/c^2$. Bottom: mean and resolution improvement on dijet invariant mass with soft muon. The $\circ$ is for uncorrected jet energies, $\square$ is for jet energies after P^μ corrections, $\bullet$ after Ch. F. corrections and $\blacksquare$ after E_T corrections.* 121
5.12 *Top: effects of the corrections on dijet invariant mass with soft electron for $M_H = 120\ GeV/c^2$. Bottom: mean and resolution improvement on dijet invariant mass with soft electron. The $\circ$ is for uncorrected jet energies, $\square$ is for jet energies after P^μ corrections, $\bullet$ after Ch. F. corrections and $\blacksquare$ after E_T corrections.* 122
5.13 *Top: effects of the corrections on dijet invariant mass without soft leptons for $M_H = 120\ GeV/c^2$. Bottom: mean and resolution improvement on dijet invariant mass without soft leptons. The $\circ$ is for uncorrected jet energies, $\square$ is for jet energies after P^μ corrections, $\bullet$ after Ch. F. corrections and $\blacksquare$ after E_T corrections.* 123
5.14 *Top: effects of the corrections on dijet invariant mass for $M_H = 120\ GeV/c^2$ (all categories together). Bottom: mean and resolution improvement on dijet invariant mass (all categories together). The $\circ$ is for uncorrected jet energies, $\square$ is for jet energies after P^μ corrections, $\bullet$ after Ch. F. corrections and $\blacksquare$ after E_T corrections.* 124
5.15 *Comparison of the effects of the old and new corrections on dijet invariant mass of Z (top) and W (bottom) bosons.* 125
5.16 *Comparison between dijet mass spectra for $M_H = 120\ GeV/c^2$ before corrections and after corrections computed with and without the $M_H = 120\ GeV/c^2$ sample.* 128
5.17 *Effects of our corrections on invariant mass spectrum of dijet pairs from Higgs decay as simulated from* HERWIG 5.6 *Monte Carlo ($M_H = 120\ GeV/c^2$).* 129
5.18 *Effects of the corrections on background dijet mass spectra. Full histogram: before corrections; hatched histogram: after corrections.* . . . 130
5.19 *Mass shift $\Delta M = M^{corr.} - M^{uncorr.}$ as a function of the mass before corrections, for dijet pairs from Higgs decay ($\bullet$), wrong dijet combinations in HV events ($\circ$), and a sample of QCD MC events ($\blacksquare$).* . . 131

5.20 *Differences between the mean values of the dijet mass distributions and the input mass of the Higgs boson after some analysis cuts for* $M_H = 110$ *(•),* 115 *(■),* 120 *(∘),* 125 *(□) and* 130 *(▲)* GeV/c^2. . . . 132
5.21 *Resolutions of the Higgs mass after some analysis cuts for* $M_H = 110$ *(•),* 115 *(■),* 120 *(∘),* 125 *(□) and* 130 *(▲)* GeV/c^2. 133
5.22 *Effects of the corrections on invariant mass spectra from* $t\bar{t}$ *MC and* $W +$ *jets data. Full histogram: before corrections; hatched histogram: after corrections.* 134
5.23 *Effects of preliminary jet energy corrections developed in* CDF II *environment on reconstructed Higgs mass spectrum. The ∘ is for uncorrected jet energies, • is for jet energies after Ch. F. corrections and ■ after* E_T *corrections.* 135
5.24 *Central detector resolution* σ_D *as a function of* P_T^γ *for the two jet energy reconstruction methods.* 137

6.1 *Main contributions to* QCD *production of heavy quark pairs.* 142
6.2 *Diagram for single top production.* 142
6.3 *Contributions to* $t\bar{t}$ *production.* 143
6.4 Z/W *direct production contributions to multijet sample.* 143
6.5 *Jet multeplicity for* VH *(shaded histogram) and* QCD *(white) events after trigger selection.* 145
6.6 *Jet* E_T *distribution for* VH *(shaded histogram) and* QCD *(white) events after four jet requirement. Standard jet corrections have been applied.* 145
6.7 *Dijet mass distributions for Higgs (left) and vector (right) boson candidates. The four leading jets have been used. Tagged jets have been assigned to the Higgs boson decay. All combinations are included. The shaded histograms show the contributions from wrong combinations. Preliminary jet energy corrections we studied in Sec. 5.6 are been applied.* 148
6.8 *Comparison of transverse momentum spectra of dijet system when right (full histograms) and wrong (hatched) combinations are considered for Higgs (left) and vector (right) boson reconstruction.* 149
6.9 *Comparison of the angle of the jet pairs when right (full histograms) and wrong (hatched) combination are considered for Higgs (left) and vector (right) boson reconstruction.* 150
6.10 *Dijet mass distributions for Higgs (left) and vector (right) boson candidates. Two* SECVTX *tag are required. The four leading jets have been used and tagged jets have been assigned to Higgs boson: one combination per event is included. The shaded histograms show the contributions from wrong combinations. We observe that the vector boson reconstruction suffers from a high number of wrong combinations with respect to Higgs boson one. Actually, the double tagging requirement selects a high fraction of events where both jets from Higgs decay have been reconstructed.* 150

6.11 ΣE_T *(left) and* $\Sigma_3 E_T$ *(right) distributions for signal (shaded histograms) and* QCD *(white) events.* . . . 151
6.12 $\Sigma E_T/\sqrt{\hat{s}}$ *(left) and* $|\eta_{j2}|$ *(right) distributions for signal (shaded histograms) and* QCD *(white) events.* . . . 152
6.13 t_4 *distributions for signal (shaded histogram) and* QCD *background (white) production.* . . . 153
6.14 $t_4 - 0.82 \cdot \Sigma E_T/\sqrt{\hat{s}}$ *distribution for* VH *(shaded histogram) and* QCD *(white) events.* . . . 153
6.15 $t_4 - 0.82 \cdot \Sigma E_T/$ *as a function of* $\sqrt{\hat{s}}$ *for signal (shaded histograms) and* QCD *background (white) production.* . . . 154
6.16 *Aplanarity distributions for signal (shaded histogram) and* QCD *background (white) events.* . . . 154
6.17 *Sphericity distributions for* VH *(shaded histogram) and* QCD *(white) production.* . . . 154
6.18 *Invariant mass distributions of the jet pairs associated to the Higgs boson decays for signal (shaded histogram) and* QCD *background (white) production.* . . . 155
6.19 *Invariant mass distributions of the jet pairs associated to the vector boson decays for* VH *(shaded histogram) and* QCD *(white) events.* . . . 155
6.20 *Invariant mass of the two tagged jet system versus other two jets' one for signal (left) and* QCD *background (right) production.* . . . 156
6.21 *Invariant mass versus transverse momentum of the two tagged jet system for* VH *(left) and* QCD *(right) events.* . . . 156
6.22 P_T *distributions of tagget jet pairs having invariant mass between* 100 *and* 140 GeV/c^2 *for signal (shaded histogram) and* QCD *background (white) production.* . . . 157
6.23 *Jet multeplicity for* VH *(shaded histogram) and* $t\bar{t}$ *(white) events.* . . . 157
6.24 *Comparison of some kinematical variables for* VH *(shaded histogram) and* $t\bar{t}$ *(white) events after requiring* $N_{jets} < 6$. . . . 158
6.25 *Comparison of some kinematical variables for* VH *(shaded histogram), single top (white),* WZ *(hatched) and* ZZ *(pointed) events.* . . . 159

7.1 *Fraction of transverse energy as a function of the reconstructed mass of tagged (left) and not-tagged (right) jet pairs for* VH *(top) and* QCD *(bottom) events.* . . . 164
7.2 $\sum E_T/\sqrt{\hat{s}}$ *distribution (left) for signal (shaded histogram) and background (white) events, and cut optimization (right).* . . . 164
7.3 $\sum_3 E_T$ *distribution after cut on* $\sum E_T/\sqrt{\hat{s}}$ *for signal (shaded histogram) and background (white) events, and cut optimization (right).* 165
7.4 $t_4 - 0.82 \cdot \Sigma E_T/\sqrt{\hat{s}}$ *distribution after cuts on* $\sum E_T/\sqrt{\hat{s}}$ *and* $\sum_3 E_T$ *for signal (shaded histogram) and background (white) events, and cut optimization (right).* . . . 166
7.5 *Dijet mass distribution after kinematical selection for tagged (left) and not-tagged (right) jet pairs. Shaded histograms are for* VH *events, white ones for* QCD *processes.* . . . 166

7.6 *Learning performances and errors for training (light bullets) and testing (dark) events as a function of the epoch number.* 169
7.7 *Neural network output distributions for signal (shaded histogram) and background (white) events.* 170
7.8 *Efficiencies on VH ($\bullet$) and* QCD *($\circ$) events as a function of the cut on the neural network output.* 170
7.9 *Purity vs. signal efficiency curve.* 171
7.10 *Expected $S/\sqrt{B}$ improvement as a function of the cut on the neural network output.* 171
7.11 *Expected $S/\sqrt{B}$ improvement as a function of the cut on the neural network output for Higgs boson mass $M_H = 110\ GeV/c^2$ (top-left), $115\ GeV/c^2$ (top-right), $125\ GeV/c^2$ (bottom-left) and $130\ GeV/c^2$ (bottom-right).* 172
7.12 *2 output neural network classification performances on VH (left),* QCD *(middle) and $t\bar{t}$ (right) events.* 173
7.13 *Preliminary estimates of the limits on Higgs associated production cross section achievable with $\mathcal{L}^{int.} = 1$, 2 and 15 fb^{-1}. Also shown is the cross section predicted by the Standard Model.* 174

A.1 *Schematic view of a perceptron with 5 input connections.* 182
A.2 *Feed-forward neural network with 4 input nodes, 3 hiddem nodes and 2 output nodes.* 182

List of Tables

1.1 *Organization and characteristics of fermions in the Standard Model.* . . . 4

1.2 *Vector bosons in the electroweak sector of the Standard Model.* 8

1.3 *Theoretical limits on Higgs boson mass M_H for two specific values of the cut-off energy Λ.* 12

2.1 *Summary of resolutions on various track parameters as obtained in Run I and as expected in Run II.* 32

2.2 Characteristics of the CDF II calorimeter. 34

2.3 *Standard electron selection compared to soft electron requirements for Run I.* 42

2.4 *Soft muon requirements for Run I.* 45

3.1 *Average processing time of each* SVT *functional block for different datasets: all hadronic decays of WH and ZH events (with M_H = 120 GeV), and B production simulations at P_T^{min} = 10 GeV and 20 GeV from Ref. [11]. Note: noise in the silicon strips was generated differently in the studies of Ref. [11]; therefore, the values most dependent on the total number of hits in the silicon strips (MR1 in particular) do not warrant a direct comparison. See below for a description of noise effects on the timing.* 84

3.2 *Average processing time of each* SVT *functional block for 4-jet decays of WH and ZH events (M_H = 120 GeV/c^2), for the four different noise levels. See also Fig. 3.28.* 85

3.3 *Average processing time of each* SVT *functional block for* QCD *background events for the four different noise levels.* 85

3.4 *Total time necessary to process a given fraction of VH events of signal with M_H = 120 GeV/c^2 or of* QCD *background passing Level 1 calorimetric requirements as a function of the noise level.* 85

3.5 *Trigger rate and efficiency on VH production for some values of the Higgs boson mass M_H. Errors are statistical only.* 94

3.6 *Trigger rate and efficiency on VH production for some values of the Higgs boson mass M_H. Errors are statistical only.* 95

5.1 *Performances of all our corrections on the jet P_T.* 116

6.1 *Cross sections of the* $p\bar{p} \to HVX \to b\bar{b}q\bar{q}^{(\prime)}X$ *process before and after trigger requirements for some values of the Higgs boson mass* M_H*. Errors are statistical only.* 144
6.2 *Cross sections of background processes before and after trigger requirements. Branching ratios of hadronic decays are included. Errors are statistical only.* 144
6.3 *Cross sections for signal production after sample selection cuts. Errors are statistical only.* 146
6.4 *Cross sections for background production after sample selection cuts. Errors are statistical only.* 146

7.1 *Summary of the kinematical selection performance. Efficiencies are computed with respect to the analysis samples. Errors are statistical only.* 167
7.2 *Expected significances* $S/\sqrt{B}$ *achievable on Higgs associated production with* $1\ fb^{-1}$ *of integrated luminosity. Errors are statistical only.* . 167
7.3 *Expected significances* $S/\sqrt{B}$ *achievable on Higgs associated production with* $1\ fb^{-1}$ *of integrated luminosity. Errors are statistical only. They have been computed by assuming that the number of events passing a generic selection* $NN_{out} \leq cut$ *obeys a binomial distribution.* . . 171